ROMA TRE
UNIVERSITÀ DEGLI STUDI

Doctoral School of Engineering
Branch of Biomedical Electronics, Electromagnetism and Telecommunications

27th Doctoral Year

MODAL TECHNIQUES FOR MICROWAVE COMPONENTS IN FUSION ENGINEERING AND FOR PERIODIC STRUCTURES APPLIED TO DIRECTIVE ANTENNAS

Candidate: Silvio Ceccuzzi

Supervisor: Prof. Giuseppe Schettini

Coordinator: Prof. Alessandro Salvini

To my parents

Preface

The present doctoral dissertation deals with different microwave structures, the leitmotif of which is the modal expansion of the electromagnetic field inside them. Some devices, conceived for either radiation or guiding purpose of the electromagnetic waves, are considered by either exploiting them in unconventional ways or building up effective tools for their study. Such advancement in the electromagnetics research is attained by adopting a fully modal viewpoint in addressing the microwave structures.

In recent years, the widespread use of volumetric solvers such as the finite element method and the finite-difference time-domain, boosted by the growing availability of computational resources, has greatly simplified the solution of electromagnetic problems, which previously required remarkable mathematical skills and physical understanding. As a drawback, the functional dependences between input parameters and performance, as well as the insight on the laws ruling electromagnetic phenomena, have been partially obscured. It is this author's opinion that, in the electromagnetics research, *quantity* has prevailed on *quality* in the sense that the increase of simulation runs is often preferred to the effort and time necessary to the development of specialist knowledge on a topic. The philosophy this work supports is that solid mathematical and physical background will only redeem the research in the branches of engineering.

It is worth clarifying that the aforementioned viewpoint is not contrary to the numerical solution of Maxwell equations. The latter is a significant breakthrough in the electromagnetics research and is undoubtedly helpful in any research activity. Commercial tools, with their solvers based on domain discretization, have been indeed employed also in the present work; they have been mostly used for the validation of developed codes and for the study of some components and antennas. Nevertheless such tools have intrinsic limitations, which the present document is aimed at overcoming by means of full-wave or approximate mathematical models. The modal behaviour of all structures under consideration is the key-element in this sense: it is exploited to reveal new perspectives of their physical mechanisms and unprecedented ways of employment as well as to build up effective tools for their analysis and design.

The first chapter, which concerns antennas based on electromagnetic

band-gap (EBG) structures, is exemplary with respect to previous remarks. Two methods are recalled: the plane wave expansion method and the cylindrical wave approach. The one, after enhancing the code available at the electromagnetic field laboratory of the "Roma Tre" university, allows the understanding of a physical property which is used in a novel concept of dual-feed EBG-based antennas. The other, enhanced in comparison with previous scientific papers and implemented in a flexible and reliable code, is run to quickly analyse two-dimensional arrangements of cylinders, leading to the design of a compact, efficient, cheap and easy-to-fabricate antennas. Both radiating structures share a common mechanism, which received scarce attention in the scientific literature: they rely on particular Bloch waves. A comprehensive benchmark of this approach with the more widely known resonator antenna is reported in the chapter against EBG structures made of alumina rods, discussing strengths and weaknesses of the two mechanisms.

The second chapter recalls the formulation of the coupled-mode theory, i.e. an approximate semi-analytical method for the analysis and design of waveguides with varying cross-section. An approach of this kind is mandatory to study oversized components for high-power applications such as Bragg reflectors or converters for cyclotron auto-resonance masers. Most commercial softwares are indeed unsuitable when the size of the waveguide cross-section is electrically large. The coupled-mode theory is coded and successfully validated using corrugated waveguides with sinusoidal or rectangular ripple profiles. A rigorous calculation, which is beyond the state of the art, is implemented to compute the quality factor of Bragg resonators.

The third chapter describes the mode-matching (MM) method, i.e. a full-wave semi-analytical formulation for the study of step-type discontinuity in waveguides. The standard method is enhanced, in combination with the resonator technique, to generate a powerful tool for mode filters based on corrugations partially filled with absorbers. The net improvement in terms of computation time, with respect to commercial CAD programs, allows the use of the MM method under the control of heuristic optimizers techniques as demonstrated through several examples. Moreover simple models of a corrugation are developed to understand the physical relations between filter performance and geometrical parameters as well as to provide guidelines for designers.

The last chapter describes some areas of application where previous modal approaches for oversized waveguides are useful. A 250 GHz cyclotron auto-resonance maser is firstly considered: a feasibility study of its development has been recently undertaken at the Italian national agency for new technologies, energy and sustainable economic development (ENEA). Then a possible lower hybrid system for reactor-relevant tokamaks is addressed, focusing on the technological needs and issues associated with its realization such as the materials of the launcher and the oversized components of the main transmission line.

Contents

Chapter 1

Antennas Based on Lattice Eigenmodes

The emission by simple radiators can be shaped using electromagnetic band-gap (EBG) materials that exploit proper Bloch waves supported by the lattice rather than using its band-gaps. The latter approach, which is implemented in the so-called resonator (or Fabry-Pérot) antennas, is more widely known and used than the former one, which is addressed here in detail. The two mechanisms are initially compared under the radiative and electrical viewpoint for both 2D and 3D configurations of dielectric cylinders. Then antennas based on lattice eigenmodes are studied under an unprecedented perspective, highlighting new capabilities and potentials of this kind of EBG structures.

1.1 Methods and Tools for Periodic Structures

1.1.1 Introduction

Periodic physical properties in space allow to control particle motion: this principle applies to electrons within a periodic electrostatic potential as well as to photons, i.e. electromagnetic waves, in photonic crystals [1]. The latter feature spatially periodic electromagnetic properties and may exhibit some frequency ranges, called band-gaps, where light propagation is forbidden. Although this phenomenon is known since 1887, when Lord Rayleigh explained it in terms of multiple reflection for the quarter-wave stack, the first three-dimensional periodic structure, utterly preventing microwave propagation in any direction, was realized about a century later by Yablonovitch [2]. This breakthrough opened new, unimaginable possibilities, triggering a remarkable interest and an intense research towards the so-called electromagnetic band-gap (EBG) materials.

The last three decades have seen EBG materials finding useful application in a wide range of devices such as shields, filters, waveguides, oscillators and antennas [3, 4]. Concerning the latter, EBG structures have been successfully employed in combination with several types of radiators, e.g. printed [5], slot [6], reflector [7], aperture coupled patches [8], curl [9] or dipole [10] antennas with different roles. Among the most attended ones, there is the use of EBG materials as substrates, avoiding trapped radiation and increasing antenna efficiency, and as ground planes, realizing high impedance surfaces or proper phase reflections, so as to prevent surface wave propagation or to attain low profile antennas [11, 12]. Furthermore, EBGs can be designed to be a passive medium able to shape the antenna radiation pattern [13, 14], standing out as an attractive solution when the use of several radiators with their cumbersome feeding networks is not suggested. Antennas implementing multiple approaches, based on a combination of different EBG geometries, have been also studied [15].

This chapter addresses the employment of EBG materials to enhance the directivity of antennas with particular attention to the mechanism that exploits Bloch waves. The analysis and design of periodic structures have been commonly addressed with manifold methods such as plane wave expansion [1], finite difference [16, 17], finite element [18, 19, 20], transfer matrix [21], coupled equations [22], equivalent circuits [23, 24], lattice sums [25], Fourier modal approach [26], cylindrical waves [27], combined methods [28, 29, 30]. Meanwhile the fabrication of EBG materials considerably improved, becoming feasible even at sub-millimeter waves [31].

In this chapter three numerical methods are adopted: the finite integration technique (FIT) of a commercial software [32], the plane wave expansion (PWE) [1] and the cylindrical wave approach (CWA) [27]. The first one, known as “transient solver”, is not explained because it is a widespread time-

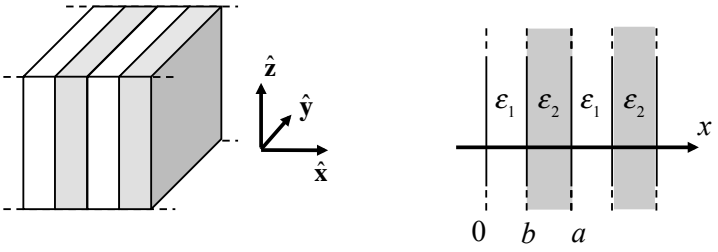

Figure 1.1: Geometry of the multilayer.

domain technique. The second one, despite being well known, is addressed in section 1.1.2 because the classical method has been extended to take into account the presence of an excitation term. With reference to the CWA, a description is given in section 1.1.3 because some improvements have been introduced with respect to the theoretical model described in [27] for similar applications. In detail, the present version of the code can deal at the same time with metal and dielectric cylinders, multiple sources and infinite ground planes under a two-dimensional approximation. Moreover, in [27] the demonstration presents some errors and wrong values of directivities are provided for calculated geometries.

1.1.2 Plane wave expansion method

One-dimensional photonic crystals

We initially refer to the reference geometry of Fig. 1.1, which represents a one-dimensional structure obtained by periodically staking multiple layers of different materials and usually referred to as multilayer. We assume a time dependence $\mathrm{e}^{\iota\omega t}$ and refer to the polarization (E_z, H_y); other choices would lead to the same conclusions.

Owing to the translational invariance along y and z, the master equation on the electric field reduces to

$$\frac{1}{\varepsilon_r(x)}\frac{\partial^2 E_z}{\partial x^2} + \left(\frac{\omega}{c}\right)^2 E_z = 0 \tag{1.1}$$

The relative permittivity ε_r is periodic and its reciprocal is written as a Fourier series with coefficients κ_n:

$$\frac{1}{\varepsilon_r(x)} = \sum_{n=-\infty}^{\infty} \kappa_n \mathrm{e}^{\iota n g x} \qquad \text{with} \quad g = \frac{2\pi}{a}, \tag{1.2}$$

while the electric field can be expressed as an expansion of Floquet harmonics

$$E_z(k,x) = f(k,x) esp{-}\iota k x = \sum_{m=-\infty}^{\infty} \tilde{f}_m(k) esp\imath m g x esp{-}\iota k x \tag{1.3}$$

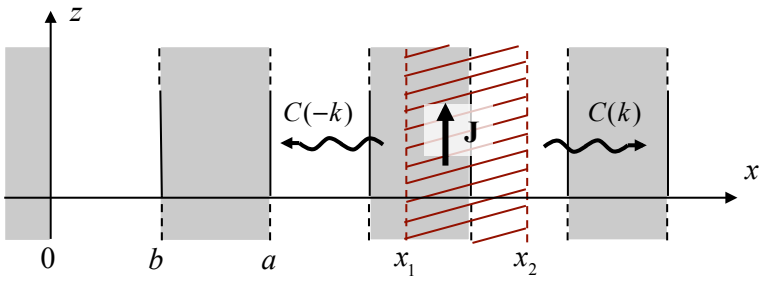

Figure 1.2: Multilayer with a current distribution.

being $f(k, x+a) = f(k, x)$. Both summations must be truncated to an order M to allow numerical computation. After replacing (1.2) and (1.3) into (1.1) and performing some mathematical manipulations, the wave equation becomes

$$\sum_{m=-M}^{M} (mg - k)^2 \kappa_{n-m} \tilde{f}_m(k) = \left(\frac{\omega}{c}\right)^2 \tilde{f}_n(k) \tag{1.4}$$

with $n = -M, -M+1, \ldots, M$. Once fixed k, the (1.1) returns a standard eigenvalue problem of the form

$$\underline{\mathbf{A}} \cdot \mathbf{x} = \lambda \mathbf{x}$$

Each eigenvector $\mathbf{x}$, corresponding to a particular λ, consists in a set of $\tilde{f}_m$ that define the spatial dependence of the crystal mode according to the (1.3). The magnetic field can be derived as

$$H_y(k, x) = \frac{1}{\iota\omega\mu_0} \frac{\partial E_z}{\partial x} = h(k, x) esp{-\iota kx} \tag{1.5}$$

and the ratio between the field components of forward and backward waves satisfy the following relation

$$\frac{f(k, x)}{h(k, x)} = -\frac{f(-k, x)}{h(-k, x)} \tag{1.6}$$

The non-homogeneous problem of a current sheet in a one-dimensional lattice can be qualitatively addressed following a similar approach to a current source in a waveguide [33]. The excitation of crystal modes by a current distribution $J_z(x, \omega)$ is projected into the crystal eigenmodes derived with the PWE method. The Lorentz reciprocity formula

$$\int_V (\mathbf{E}_2 \cdot \mathbf{J}_1 - \mathbf{E}_1 \cdot \mathbf{J}_2) dV = \oint_S (\mathbf{E}_1 \times \mathbf{H}_2 - \mathbf{E}_2 \times \mathbf{H}_1) \cdot \hat{\mathbf{n}} dS \tag{1.7}$$

is applied to the geometry depicted in Fig. 1.2. The field $\mathbf{E}_1$, $\mathbf{H}_1$ is a superposition of lattice modes with amplitudes $C(q)$, excited by $\mathbf{J}_2 = J_z(x, \omega)\hat{\mathbf{z}}$,

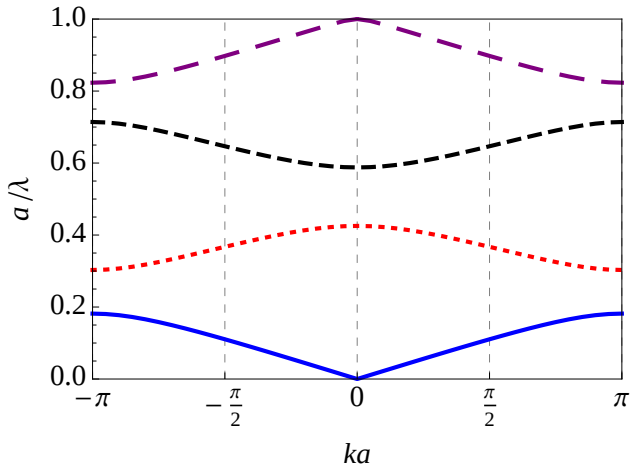

Figure 1.3: Band diagram of a multilayer with $b = a/2$, $\varepsilon_1 = 1$ and $\varepsilon_2 = 9$.

whereas the field $\mathbf{E}_2$, $\mathbf{H}_2$ is a source-free solution ($\mathbf{J}_2 = 0$) represented by the k-th backward propagating mode. Omitting the dependence on x to simplify the notation, the (1.7) becomes

$$\begin{aligned}\int_{x_1}^{x_2} E(-k)J_z(\omega)dx =& C(-q)\left[E(-q)H(-k) - E(-k)H(-q)\right]_{x=x_1} + \\ &- C(q)\left[E(q)H(-k) - E(-k)H(q)\right]_{x=x_2}\end{aligned} \tag{1.8}$$

The spectrum of modes is continuous in the q-space, but for a monochromatic current distribution $J_z(x)\delta(\omega - \omega_r)$, only the k-th modes with $\lambda = \omega_r^2/c^2$ can propagate. By taking $q = k$, the first term in the rhs of (1.8) vanishes and, using (1.6), the modal amplitude $C(k)$ can be expressed as

$$C(k) = \frac{\int_{x_1}^{x_2} f(-k,x)J_z(x)esp\imath kxdx}{2f(-k,x_2)h(k,x_2)} \tag{1.9}$$

Hence, in the case of a current sheet $J_z(x) = I_0\delta(x - x_0)$,

$$|C(k)| \propto |f(-k,x_0)| \tag{1.10}$$

i.e. the amplitude of the excited eigenmode depends on the value of the eigenfunction of the electric field where the source is located.

Fig. 1.3 shows the typical band diagram for a stack of vacuum and Alumina layers with the same widths. In the case of $ka = 0.8\pi$, the envelope of the first three modes inside the primitive cell is depicted in Fig. 1.4 after normalizing each function by its maximum. The mode in the dielectric band is maximally excited when the current sheet is located in the centre of the Alumina layer, whereas the source in $x_0 = a/4$ mainly supports the mode in the air band.

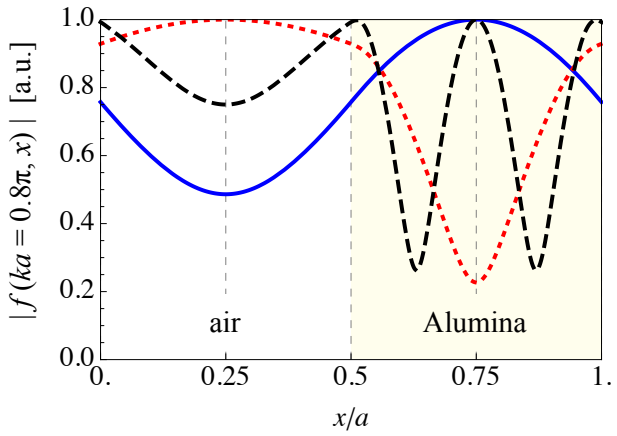

Figure 1.4: Normalized amplitude of the electric field eigenfunctions for the first three modes of the lattice in Fig. 1.3 when $ka = 0.8\pi$.

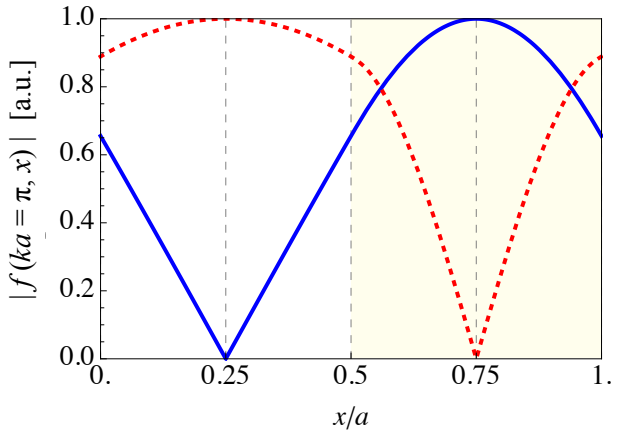

Figure 1.5: Normalized amplitude of the electric field eigenfunctions for the first two modes of the lattice in Fig. 1.3 when $ka = \pi$.

Fig. 1.5 shows the same plot of Fig. 1.4 when $ka = \pi$. Under this condition, which is particularly attractive for antenna applications, a standing wave pattern sets up in the crystal because the group velocity $v_g = \nabla_k \omega$ vanishes, as can be seen from Fig. 1.3. The rhs of (1.7) also vanishes in absence of propagation, but the amplitude of the standing wave can be related to the electric (W_e) and magnetic (W_m) energy by the Poynting theorem:

$$\int_V \mathbf{E} \cdot \mathbf{J}^* dV = 4\iota\omega(W_m - W_e) + \oint_S \mathbf{E} \times \mathbf{H}^* \cdot \hat{\mathbf{n}} dS + \int_V \sigma |\mathbf{E}|^2 dV \qquad (1.11)$$

In a lossless medium with a standing wave, the last two terms of (1.11) are

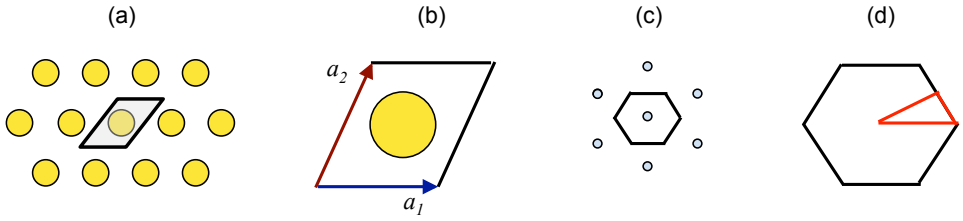

Figure 1.6: Lattice (a), unit cell (b), reciprocal lattice (c) and irreducible Brillouin zone (d) for a triangular arrangement of cylinders.

null, so we get

$$\int_{x_1}^{x_2} E_z J_z^* dx = \iota\omega \int_{x_1}^{x_2} \left(\varepsilon |E_z|^2 + \mu |H_y|^2\right) dx \tag{1.12}$$

By replacing (1.3) and (1.5) into (1.12), for a current sheet and a stationary wave with amplitude C_{sw}, we find

$$C_{sw}^* = \frac{I_0^* esp\iota \frac{\pi}{2} x_0 f\left(\frac{\pi}{2}, x_0\right)}{\iota\omega \int_{x_1}^{x_2} \left[\varepsilon \left|f\left(\frac{\pi}{2}, x_0\right)\right|^2 + \mu \left|h\left(\frac{\pi}{2}, x_0\right)\right|^2\right] dx}$$

which confirms the validity of (1.10) also when $v_g = 0$.

Two-dimensional photonic crystals

The application of the plane wave expansion to two-dimensional periodic structures is briefly recalled to illustrate how unit cells in the form of parallelograms can be treated analytically. The MATLAB [34] code available at "Roma Tre" University at the beginning of this work (`pweRm3` v.1.0) could handle square lattice only, but it has been enhanced into the `pweRm3` v.2.0 to solve unit cells with a given inclination angle. This improvement is worth being described because the demonstration of the PWE method given in [27] does not work for triangular lattices. Moreover the eigenvalue solver of some commercial software like CST MICROWAVE STUDIO [32] can calculate the dispersion diagram of a square lattice, but it does not support the definition of the unit cell for triangular ones. The latter is depicted in Fig. 1.6 together with the corresponding reciprocal lattice and irreducible Brillouin zone (IBZ).

A test geometry has been chosen from literature as a benchmark and an oversized unit cell has been studied with CST MICROWAVE STUDIO (MWS). The comparison between the dispersion diagrams is reported in Fig. 1.7, showing that in the oversized cell the commercial software finds some fake bands that are not present in the primitive one; the same curves are obtained using the `pweRm3` v.1.0. A feature of such fake bands is that they

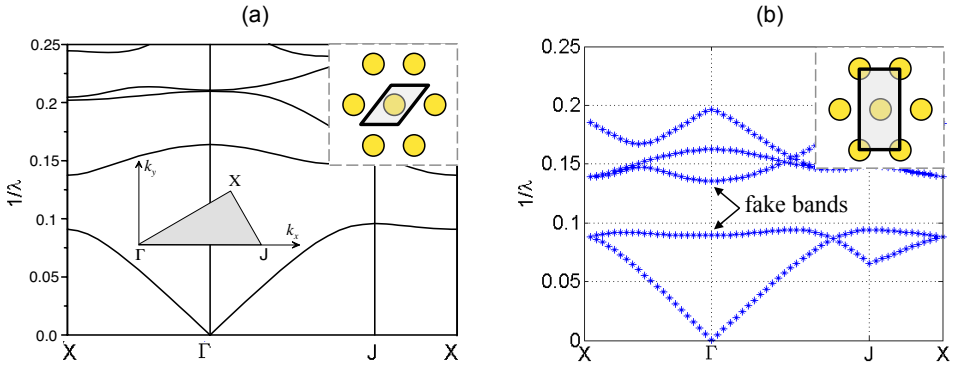

Figure 1.7: Dispersion plot taken from [14] (a) and calculated with CST MWS (b) for a triangular lattice of dielectric cylinders in a vacuum with lattice period = 4 m, cylinder radius = 0.4 m and $\varepsilon_r = 8.41$.

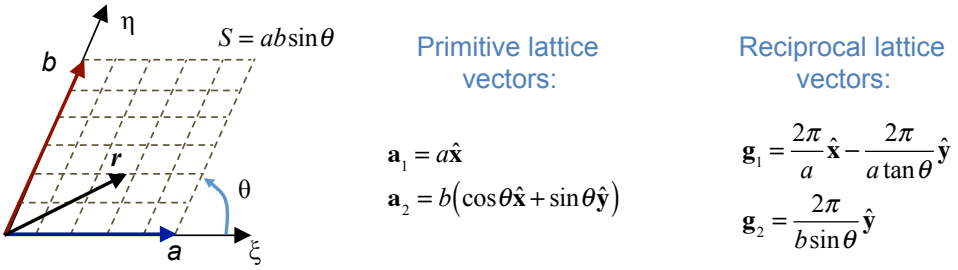

Figure 1.8: Primitive cell with the form of a parallelogram and relevant lattice vectors.

are not symmetric with respect to the IBZ; it follows that, when plotting the dispersion curves of two different irreducible Brillouin zones, only the modes of the primitive cell hold steady, while the fake ones change. In principle real and wrong bands can be discriminated according to this feature, but such an approach requires heavy additional processing and it is not suitable for three-dimensional plots.

The analytical formulation of the PWE for two-dimensional lattices has been thus faced to look for a rigorous solution to the problem. We refer to a lattice, the primitive cell of which is depicted in Fig. 1.8. The plane wave expansion method consists of two steps:

1. The Fourier transform of the inverse of the dielectric constant in the primitive cell:

$$\kappa(\mathbf{G}) = \frac{1}{S}\int_S \varepsilon_r^{-1}(\mathbf{r})\mathrm{e}^{-\iota\mathbf{G}\cdot\mathbf{r}}d\xi d\eta$$

where $\mathbf{G} = m_1\mathbf{g}_1 + m_2\mathbf{g}_2$ is the connecting vector of the cells in the

reciprocal lattice and

$$\mathbf{r} = \xi\frac{\mathbf{a}_1}{a_1} + \eta\frac{\mathbf{a}_2}{a_2} = \frac{n_1}{N_1}\mathbf{a}_1 + \frac{n_2}{N_2}\mathbf{a}_2$$

is the position vector inside the primitive cell. This vector is discretized into $N_1 \times N_2$ subcells, justifying the last equality in the previous equation.

2. The solution of the eigenvalue equation for TM polarization given a set of k_x and k_y:

$$\sum_{\mathbf{G}} \kappa(\mathbf{G}' - \mathbf{G})(\mathbf{G} - \mathbf{k})^2 V(\mathbf{k}, \mathbf{G}) = k_0^2 V(\mathbf{k}, \mathbf{G}')$$

where k_0^2 is ω/c and V is the amplitude of the two-dimensional Floquet modes. This form of the eigenvalue equation is not convenient to compute the eigenvectors because the matrix on the lhs is not hermitian. A suitable form can be obtained multiplying both sides by $(\mathbf{G}'-\mathbf{k})$ and calculating $W(\mathbf{k}, \mathbf{G}') = |\mathbf{G}' - \mathbf{k}|V(\mathbf{k}, \mathbf{G}')$ from the following system:

$$\sum_{\mathbf{G}} |\mathbf{G}' - \mathbf{k}|\kappa(\mathbf{G}' - \mathbf{G})|\mathbf{G} - \mathbf{k}|W(\mathbf{k}, \mathbf{G}) = k_0^2 W(\mathbf{k}, \mathbf{G}')$$

For the primitive cell of Fig. 1.8, the first step becomes

$$\kappa(m_1, m_2) = \frac{1}{ab\sin\theta}\int_0^b\int_0^a \frac{1}{\varepsilon_r(\xi,\eta)} \mathrm{e}^{-\iota(m_1\mathbf{g}_1 + m_2\mathbf{g}_2)\cdot\left(\frac{n_1}{N_1}\mathbf{a}_1 + \frac{n_2}{N_2}\mathbf{a}_2\right)} \sin\theta d\xi d\eta$$

where the exponential can be developed as follows

$$\begin{aligned} &\mathrm{e}^{-\iota\left(\frac{2\pi m_1}{a}\hat{\mathbf{x}} - \frac{2\pi m_1}{a\tan\theta}\hat{\mathbf{y}} + \frac{2\pi m_2}{b\sin\theta}\hat{\mathbf{y}}\right)\cdot\left(\frac{n_1}{N_1}a\hat{\mathbf{x}} - \frac{n_2}{N_2}b\cos\theta\hat{\mathbf{x}} + \frac{n_2}{N_2}b\sin\theta\hat{\mathbf{y}}\right)} = \\ &= \mathrm{e}^{-\iota 2\pi\left(\frac{m_1 n_1}{N_1} + \cancel{\frac{m_1 n_2 b}{2N_2 a}\cos\theta} - \cancel{\frac{m_1 n_2 b}{2N_2 a}\cos\theta} + \frac{m_2 n_2}{N_2}\right)} \end{aligned}$$

leading to

$$\begin{aligned} \kappa(m_1, m_2) &= \frac{1}{ab\sin\theta}\int_0^b\int_0^a \frac{1}{\varepsilon_r(\xi,\eta)} \mathrm{e}^{-\iota 2\pi\left(\frac{m_1 n_1}{N_1} + \frac{m_2 n_2}{N_2}\right)} \sin\theta d\xi d\eta = \\ &\approx \frac{1}{N_1 N_2}\sum_{n_1}\sum_{n_2} \frac{1}{\varepsilon_r(n_1, n_2)} \mathrm{e}^{-\iota 2\pi\left(\frac{m_1 n_1}{N_1} + \frac{m_2 n_2}{N_2}\right)} \end{aligned} \tag{1.13}$$

The latter expression is the same of a rectangular lattice with unit cell $a_1 \times a_2$; in other words, the Fourier coefficients for a parallelogram primitive cell can be computed by calculating the ones of an equivalent orthogonal (i.e. rectangular) cell, where the length of the edges is the same as in the tilted cell. In one of its modules, the `pweRm3` v.1.0 actually implements a more

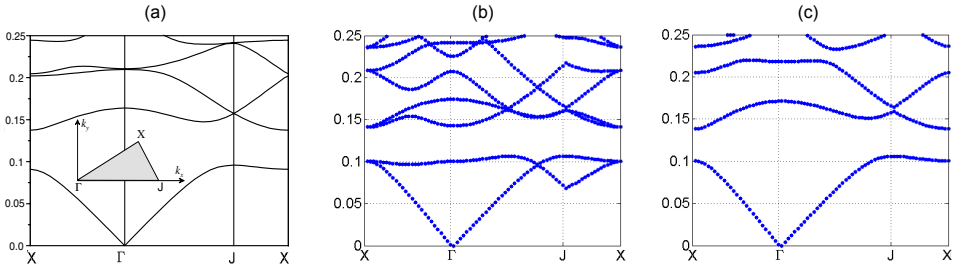

Figure 1.9: Dispersion plots obtained from [14] (a), `pweRm3` v.1.0 (b) and `pweRm3` v.2.0 (c) for the triangular lattice of Fig. 1.7.

complicated algorithm than expression (1.13) in order to avoid numerical instabilities and errors related to the discretization of the unit cell [35, 36]. Such module can be applied without modification to parallelogram primitive cells provided that previous indications are followed.

With reference to the second step, the squared term can be developed as follows

$$\begin{aligned}(\mathbf{G}-\mathbf{k})^2 &= \left(\frac{2\pi m_1}{a}\hat{\mathbf{x}} - \frac{2\pi m_1}{a\tan\theta}\hat{\mathbf{y}} + \frac{2\pi m_2}{b\sin\theta}\hat{\mathbf{y}} - k_x\hat{\mathbf{x}} - k_y\hat{\mathbf{y}}\right)^2 = \\ &= \left[\left(\frac{2\pi m_1}{a} - k_x\right)\hat{\mathbf{x}} + \left(-\frac{2\pi m_1}{a\tan\theta} + \frac{2\pi m_2}{b\sin\theta} - k_y\right)\hat{\mathbf{y}}\right]^2 = \\ &= \left[\left(\frac{2\pi m_1}{a} - k_x\right)^2 \hat{\mathbf{x}}\cdot\hat{\mathbf{x}} + \left(\frac{2\pi m_2}{b\sin\theta} - \frac{2\pi m_1}{a\tan\theta} - k_y\right)^2 \hat{\mathbf{y}}\cdot\hat{\mathbf{y}}\right]\end{aligned}$$

and the eigenvalue equation becomes

$$\begin{aligned}\sum_{m_1}^{\infty}\sum_{m_2}^{\infty}\kappa(\mathbf{G}'-\mathbf{G})\left[\left(\frac{2\pi m_1}{a} - k_x\right)^2 + \left(\frac{2\pi m_2}{b\sin\theta} - \frac{2\pi m_1}{a\tan\theta} - k_y\right)^2\right]\cdot \\ \cdot V(\mathbf{k},\mathbf{G}) = k_0^2 V(\mathbf{k},\mathbf{G}')\end{aligned} \tag{1.14}$$

From (1.14), the equation for square lattices is readily derived by taking $\theta = \pi/2$ and $a = b$, giving the linear system that was coded in `pweRm3` v.1.0. The release v.2.0 of the code instead implements the (1.14) as well as many other improvements. For example, hermitian matrices are used, tricks have been introduced to speed up the calculation, and the derivation of eigenvectors, not allowed in the previous version of the code, has been implemented. Fig. 1.9 shows the benchmark with the test case from [14] and the outcomes of the two versions of `pweRm3`, demonstrating the reliability of the new release.

1.1.3 Cylindrical wave approach

The cylindrical wave approach employs a multipole expansion based on cylindrical functions; it is mostly fast and effective in addressing scattering problems from cylindrical objects with circular cross section. A two-dimensional formulation for TM-polarized waves is given here by referring to the geometry shown in Fig. 1.10. It consists of N cylinders and M current wires with negligible radius (i.e. line sources), both invariant along z, in a vacuum background. All dimensions and coordinates are normalized using the vacuum wavenumber $k_0 = 2\pi/\lambda$, so that $\xi = k_0 x$ and $\eta = k_0 y$; besides the main reference frame, polar local coordinate systems are also introduced for each object, e.g. $\rho_q = k_0 r_q$ and θ_q for the q-th cylinder. The latter, which has a normalized radius α_q, can be made of either a perfect metal conductor or a linear, isotropic, homogeneous, dielectric material with $\varepsilon_q = \varepsilon_0 n_q^2$, being n_q the refractive index. A time dependence $\mathrm{e}^{\iota\omega t}$ is assumed throughout the demonstration. The scattering problem reduces to the determination of a scalar function $V(\xi, \eta)$, which is the total electric component E_z given by the superposition of the three terms: V_i, V_s, V_q.

The first term is the incident field, namely the one radiated by the sources in absence of cylinders. By superposition principle, it can be written as

$$V_i(\sigma_m, \phi_m) = -\sum_{m=1}^{M} V_m H_0^{(2)}(\sigma_m) \tag{1.15}$$

being σ_m as in Fig. 1.10, $H_0^{(2)}$ the 0-th order Hankel function of the second kind and V_m the complex amplitude of the m-th source. The latter radiates a field that does not depend on ϕ_m because thin current wires feature an omnidirectional radiation pattern on the H-plane. It is convenient to express

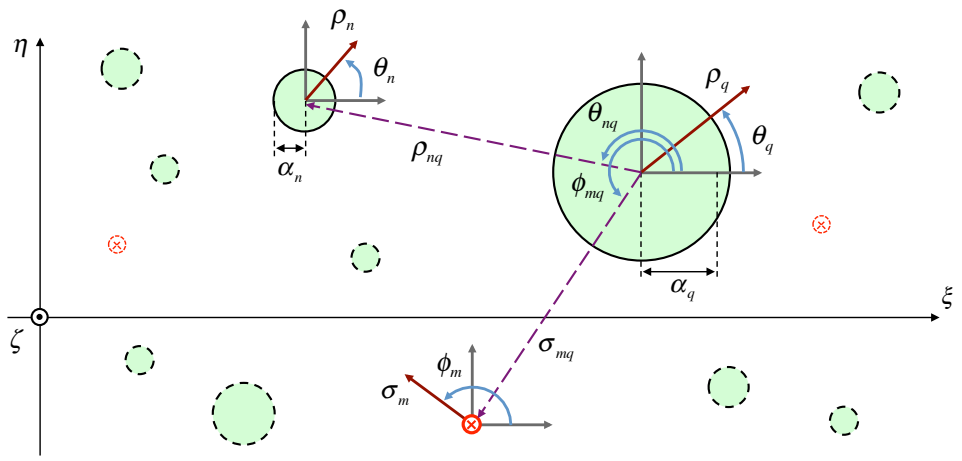

Figure 1.10: Geometry of the scattering problem.

the (1.15) through the local coordinate system of each q-th scatterer by using the Graf's addition theorem [37] and noticing that $\sigma_m = \|\underline{\rho}_q - \underline{\sigma}_{mq}\|$. After applying some properties of the Hankel functions, the (1.15) becomes

$$V_i(\rho_q, \theta_q) = -\sum_{m=1}^{M} \sum_{k=-\infty}^{\infty} \mathrm{CW}_{-k}(\sigma_{mq}, \phi_{mq})\, J_k(\rho_q)\, \mathrm{e}^{\iota k \theta_q} \tag{1.16}$$

where J_k is the k-th order Bessel function of the first kind and the cylindrical function $\mathrm{CW}_k(r, \varphi) = H_k^{(2)}(r)\mathrm{e}^{\iota k \varphi}$ has been introduced.

The term V_s is the superposition of the scattering due to any cylinder. If the field scattered by the n-th rod is expressed as an expansion of cylindrical waves with unknown coefficients $c_{n\ell}$, we have

$$V_s(\rho_n, \theta_n) = \sum_{n=1}^{N} \sum_{\ell=-\infty}^{\infty} c_{n\ell} H_\ell^{(2)}(\rho_n) \mathrm{e}^{\iota \ell \theta_n} \tag{1.17}$$

The Graf's formula can be rearranged to write the Hankel functions with the q-th local coordinates as follows

$$\begin{aligned} H_\ell^{(2)}(\rho_n)\mathrm{e}^{\iota \ell \theta_n} &= H_\ell^{(2)}(\|\rho_q - \rho_{nq}\|)\mathrm{e}^{\iota \ell \theta_n} = \\ &= \sum_{k=-\infty}^{\infty} (-1)^{\ell+k} \mathrm{CW}_{\ell-k}(\rho_{nq}, \theta_{nq}) J_k(\rho_q) \mathrm{e}^{\iota k \theta_q} \end{aligned} \tag{1.18}$$

Taking into account the case $n = q$, the (1.17) becomes, after some manipulations,

$$\begin{aligned} V_s(\rho_q, \theta_q) = \sum_{n=1}^{N} \sum_{\ell=-\infty}^{\infty} \sum_{k=-\infty}^{\infty} c_{n\ell} (-1)^{\ell+k} \big[H_k^{(2)}(\rho_n)\, \delta_{nq} \delta_{\ell k} + \\ + \mathrm{CW}_{\ell-k}(\rho_{nq}, \theta_{nq})\, J_k(\rho_q)\, (1 - \delta_{nq}) \big] \mathrm{e}^{\iota k \theta_q} \end{aligned}$$

The last term is the field inside the metallic and dielectric q-th cylinder. In the fist case, it vanishes, whereas in the second case, it is expressed as a superposition of standing cylindrical waves with unknown coefficients d_{qk}:

$$V_q(\rho_q, \theta_q) = \sum_{k=-\infty}^{\infty} d_{qk} (-1)^k J_k(n_q \rho_q) \mathrm{e}^{\iota k \theta_q} \tag{1.19}$$

where $(-1)^k$ has been inserted for convenience. We introduce the function τ_q equal to 0 or 1 for metallic or dielectric cylinders, respectively.

The boundary condition on E_z over the cylinders surface is

$$V_i(\alpha_q, \theta_q) + V_s(\alpha_q, \theta_q) = V_q(\alpha_q, \theta_q), \qquad \forall \theta_q \tag{1.20}$$

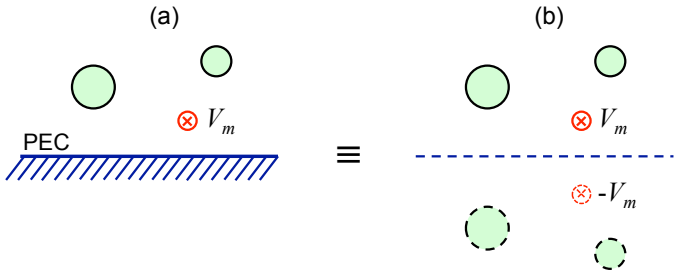

Figure 1.11: Application of the image principle; after calculating the equivalent geometry (b) the field in the bottom half-space is set to zero.

for $q = 1, 2, \ldots, N$. In the case of dielectric cylinders, the term V_q contains the unknowns d_{qk}, which can be derived using the boundary condition on the tangential component of the magnetic field H_θ:

$$\frac{\partial \left[V_i(\rho_q, \theta_q) + V_s(\rho_q, \theta_q)\right]}{\partial \rho_q} = \frac{\partial V_q(\rho_q, \theta_q)}{\partial \rho_q}, \qquad \begin{cases} \forall \theta_q \\ \rho_q = \alpha_q \end{cases} \tag{1.21}$$

for $q = 1, 2, \ldots, N$. After using the orthogonality property of the exponential function and combining (1.21) with (1.20), the following equation for the q-th cylinder and the k-th cylindrical harmonic is obtained:

$$\begin{aligned} \sum_{n=1}^{N} \sum_{\ell=-\infty}^{\infty} c_{n\ell} (-1)^{\ell} \left[(1 - Q_{qk}) U_{n\ell qk} + T_{n\ell qk} Q_{qk} T'_{n\ell qk} \right] = \\ = (1 - Q_{qk}) P_{qk} \end{aligned} \tag{1.22}$$

with

$$\begin{aligned} U_{n\ell qk} &= \mathrm{CW}_{\ell - k}(\rho_{nq}, \theta_{nq}) \, (1 - \delta_{nq}) \\ P_{qk} &= \sum_{m=1}^{M} V_m \mathrm{CW}_{-k}(\sigma_{mq}, \phi_{mq}) \\ T_{n\ell qk} &= \delta_{nq} \delta_{\ell k} H_k^{(2)}(\alpha_q) / J_k(\alpha_q) \\ T'_{n\ell qk} &= \delta_{nq} \delta_{\ell k} H_k^{(2)\prime}(\alpha_q) / J'_k(\alpha_q) \\ Q_{qk} &= \begin{cases} 0, & \text{for } \tau_q = 0 \\ \dfrac{1}{n_q} \dfrac{J_k(n_q \alpha_q)}{J'_k(n_q \alpha_q)} \dfrac{J'_k(\alpha_q)}{J_k(\alpha_q)}, & \text{for } \tau_q = 1 \end{cases} \end{aligned} \tag{1.23}$$

where the symbols $H_k^{(2)\prime}$ and J'_k represent the total derivative of the relevant functions with respect to ρ_q.

After choosing a truncation index L for the harmonic expansions ($k = -L, -L+1, \ldots, L$, $\ell = -L, -L+1, \ldots, L$), a linear system of the form

$$\underline{\mathbf{A}} \cdot \mathbf{x} = \mathbf{B} \tag{1.24}$$

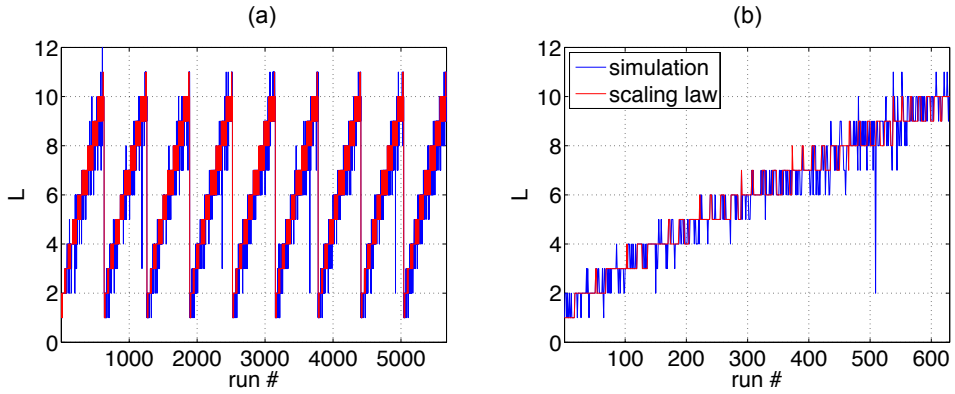

Figure 1.12: Convergence studies for dielectric (a) and metallic (b) cylinders.

for the coefficients $c_{n\ell}$ is obtained. By using the standard algorithms of LU factorization and partial pivoting, the (1.24) can be solved and the electromagnetic field outside the cylinders univocally determined. The presence of a ground plane can be handled by applying the image principle, solving the equivalent geometry and retaining only the electric field of the actual half-space, as illustrated in Fig. 1.11. In addition, no assumptions have been made on the refractive index of dielectric cylinders: it can be a complex number, allowing for lossy materials.

A fundamental parameter is the truncation index L, whose choice is a trade-off between accuracy and computational load. Its impact on the linear value of the directivity has been investigated using two test cases, made of either dielectric or metallic cylinders, in order to derive an empirical convergence rule. In detail, the test geometry consists of a current wire and three cylinders with the same radius; several preliminary calculations have been performed to identify the most important parameters affecting convergence. The number of sources and the distance between them or with the cylinders was found to have a negligible impact, whereas the minimum distance between cylinders and the maximum radius affect the truncation order. The convergence has been therefore studied for a large set of geometries obtained by varying the previous parameters and, in the case of dielectric cylinders, the relative permittivity. The directivity of each geometry is calculated increasing L step-by-step and checking its variation with the previous computation. When two consecutive checks return a variation lower than 0.01, the value of L corresponding to the first positive check is stored and another geometry is analysed.

In the case of dielectric scatterers with the same radius α_d, an accuracy of 0.01 on the directivity has been fulfilled with the following scaling law

$$L_d = \text{ceil}\left\{0.5 + 828\,\alpha_d^{0.8}\,\rho_{min}^{-0.12}\right\} \tag{1.25}$$

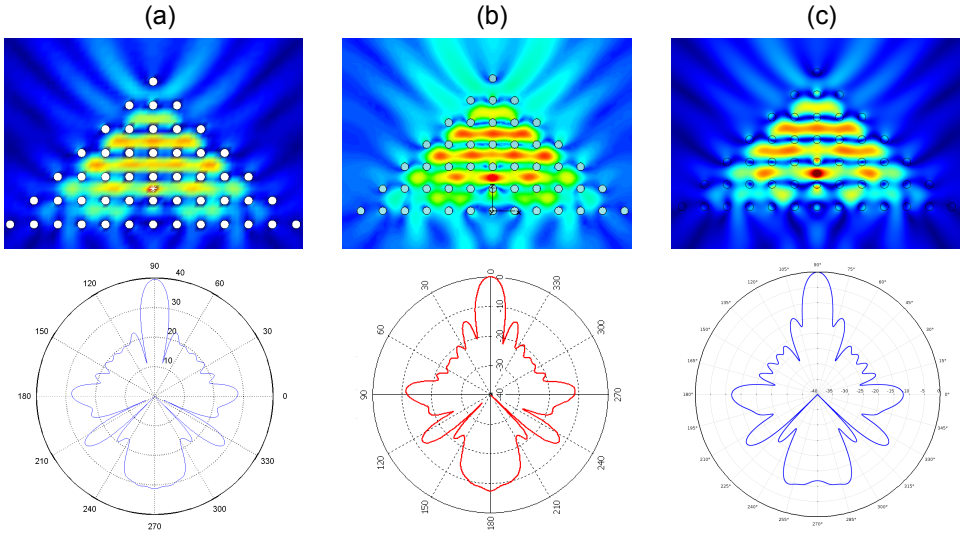

Figure 1.13: Electric field and radiation patterns in dB scale calculated with CWA (a), CST MWS (b) and COMSOL Multiphysics (c) at 5 GHz for a geometry taken from [27]. There are 49 dielectric rods with radius = 0.26 cm, Px = Py = 1.48 cm, $\varepsilon_r = 9$, arranged in a square lattice in a vacuum.

where ceil(x) gives the smallest integer $\geq x$ and ρ_{min} is the minimum distance between two elements in the geometry. The (1.25) has been overlapped to the calculated L of all geometries in Fig. 1.12a: the form resembling a sawtooth wave is due to the change of ε_r, which is found to play no role in the convergence. With reference to metallic cylinders with radius α_d, the same accuracy has been achieved according to the law

$$L_m = \text{ceil}\left\{547\,\alpha_d^{0.72}\,\rho_{min}^{-0.11}\right\} \tag{1.26}$$

The corresponding convergence plot is shown in Fig. 1.12b and exhibits a stair form, the steps of which mostly correspond to a change of the radius. As far as the structures dealt in this chapter are concerned, extensive parametric analyses provided sound confidence that the choice $L = \max\{L_d, L_m\}$ represents a satisfactory criterion.

The CWA has been coded in MATLAB and validated against other commercial softwares like CST MICROWAVE STUDIO and COMSOL Multiphysics [39] as well as against results from [38], where a method based on the T-matrix and lattice sum [25] is adopted. These tools intrinsically assume two-dimensional symmetry, i.e. translational invariance with respect to the z-axis. Fig. 1.13 shows a comparison for an antenna based on dielectric cylinders: the directivity, side lobe level and half-power beam width computed with CST MWS are 12.1 dB, -8 dB and 11.5 deg, respectively; the ones computed with CWA are 12.1 dB, -8 dB and 11.0 deg. Fig. 1.14 shows

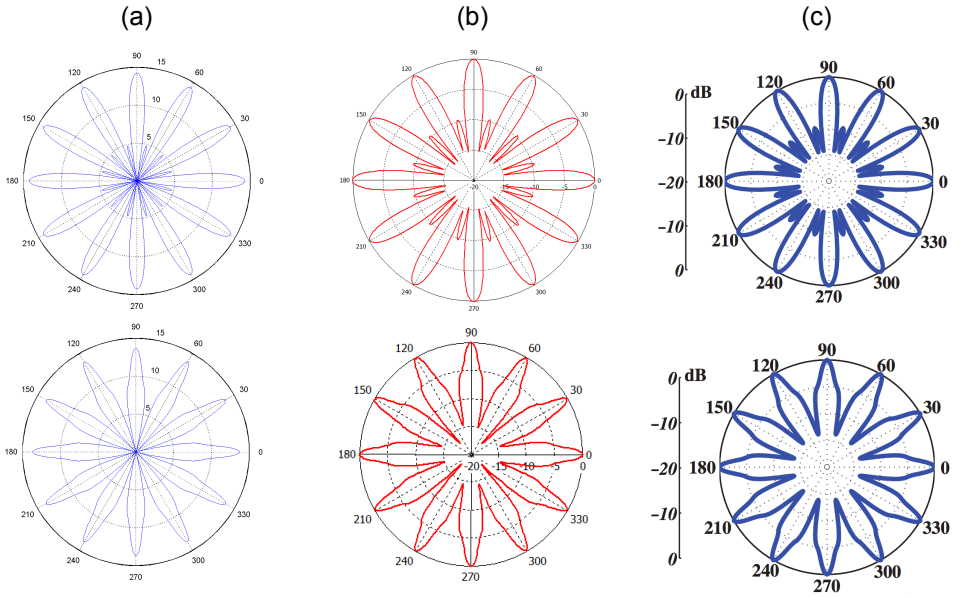

Figure 1.14: Radiation patterns calculated with CWA (a), CST MWS (b) and with the lattice sum technique (c) for the geometries reported in figures 7c (top) and 7e (bottom) of reference [38].

a comparison between H-plane radiation patterns for a structure based on metallic cylinders; such figures represent only a few examples of the exhaustive benchmark activity that was carried out. A very good agreement has been obtained between the outcomes of CST MWS and the analytical techniques; a good, despite slightly worse, matching was obtained with COMSOL Multiphysics.

1.2 Two Types of EBG-based Antennas: a Comparison

1.2.1 Background and motivations

This section deals with the mechanisms proposed to enhance the directivity of a single radiator by means of EBG structures. In this sense two approaches have been theoretically demonstrated and experimentally proven to be particularly effective. In the first one, i.e. the so-called *cavity method* [40, 41, 42, 43, 44], the primary radiator is located in between a ground plane and an EBG material working inside the band-gap. Such a configuration behaves like a resonator and the radiation is the result of a leakage from the EBG cover, which acts as a partially reflecting surface [45, 46]. In the second mechanism, which will be referred to as *embedded source method* [14, 47, 27], the radiating element is embedded within a crystal working at the edge of the band-gap, namely, in a region where the electromagnetic propagation is supported along only a few particular directions. The relevant layouts are depicted in Fig. 1.15.

Both methods are widely documented in scientific literature, but an exhaustive benchmark between them was never carried out. Here a detailed study of merits and limits and a comprehensive comparison of the two methods are presented. In details, two-dimensional periodic structures, arranged in either triangular or square lattices of infinitely long, dielectric rods are initially considered. The cylinders are excited by a 8 GHz electric line source, i.e. a thin current wire, infinite in extent, which radiates a TM-polarized wave, namely with the electric field parallel to the rod axis in order to maximize the interaction with the EBG structure. The main results have been published [48, 49, 50].

Despite based on different mechanisms, both the cavity and the embedded source methods act as spatial filters in the spectrum of the in-plane wavevector, being the one contained in the plane orthogonal to the cylinder axis, i.e. the H-plane radiation pattern of the line source. This concept can be better elucidated by referring to the radiation properties of a cur-

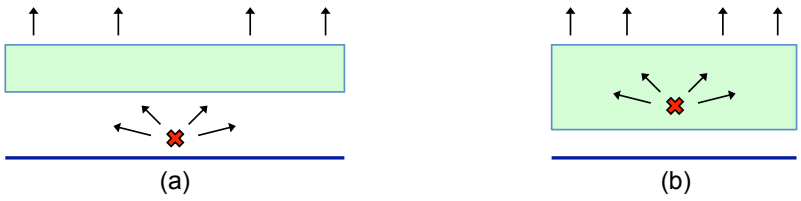

Figure 1.15: Layouts of the cavity (a) and embedded source (b) methods: rectangles, horizontal lines and X-points represent EBG materials, ground planes and primary radiators, respectively.

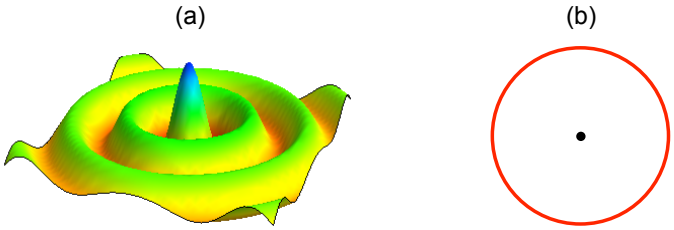

Figure 1.16: Real part of E_z (a) and H-plane radiation pattern (b) for a line source.

rent wire, which is assumed to be aligned with the z-axis and to have the following time and space dependence

$$I = I_0 \mathrm{e}^{\iota(\omega t - k_z z)}$$

The fields radiated by this source, placed in the origin, are TM^z-polarized and can be expressed through the vector potential, showing a family of solutions of the Helmholtz equation in cylindrical coordinates with the following form:

$$\begin{aligned}\mathbf{A} = \hat{\mathbf{z}} A_z(\rho, \phi, z) = \hat{\mathbf{z}}[C_1 H_m^{(1)}(k_t \rho) + C_2 H_m^{(2)}(k_t \rho)] \times \\ \times [D_1 \cos(m\phi) + D_2 \sin(m\phi)] \mathrm{e}^{-\iota k_z z}\end{aligned} \tag{1.27}$$

being ρ and ϕ the polar in-plane coordinates, k_t the modulus of the in-plane wavevector and $H_m^{(1)}$ and $H_m^{(2)}$ the m-th Hankel functions of the first and second kind, respectively. In an unbounded vacuum without scatterers, a line source features $C_1 = 0$ and $m = 0$, while the integration constants are $C_2 D_1 = A_0 = -\iota 0.25 \mu_0 I_0$. So in far zone:

$$\mathbf{E} = -I_0 \sqrt{\frac{\iota k_t \mu_0}{8\pi\varepsilon_0}} \frac{\mathrm{e}^{-\iota k_t \rho}}{\sqrt{\rho}} \hat{\mathbf{z}}, \quad \mathbf{H} = \sqrt{\frac{\varepsilon_0}{\mu_0}} \hat{\rho} \times \mathbf{E} \tag{1.28}$$

which is a TEM$^\rho$ wave that does not depend on ϕ. The line source uniformly excites the k_t space, generating an omnidirectional radiation pattern in the H-plane as shown in Fig. 1.16

The EBG-based techniques for directivity enhancement have the effect of shaping this uniform spectrum. In the case of the cavity method, the structure indeed behaves like a Fabry-Pérot interferometer, so that very few components of the wavevector are enhanced, while the others are impaired [51, 52]. With reference to the embedded source approach, instead, it is the crystal itself that works in a region of the Brillouin diagram, where only a very small portion of the wavevector spectrum is allowed. The same behaviour occurs in the H-plane of three-dimensional structures.

1.2.2 From lattice to finite-size geometries

The first step to be performed is a preliminary design of the lattices, based on infinite periodic arrangements of cylinders. The lattices under consideration consist of dielectric cylinders with circular cross-section, diameter $d = 5.6$ mm and relative permittivity $\varepsilon_r = 9$, whereas they differ in lattice periods and the type of arrangement, i.e. square or triangular. All structures are excited at a central frequency of 8 GHz and placed in a vacuum.

As far as the cavity method is concerned, the figure-of-merit to be considered is the transmission efficiency η_T of a plane wave impinging on stacked layers of infinite dielectric rods, arranged according to the lattice symmetry and provided with an interruption of periodicity. The transmission efficiency, defined as the ratio between transmitted and incident power, has been calculated with CST MICROWAVE STUDIO for the square and tri-

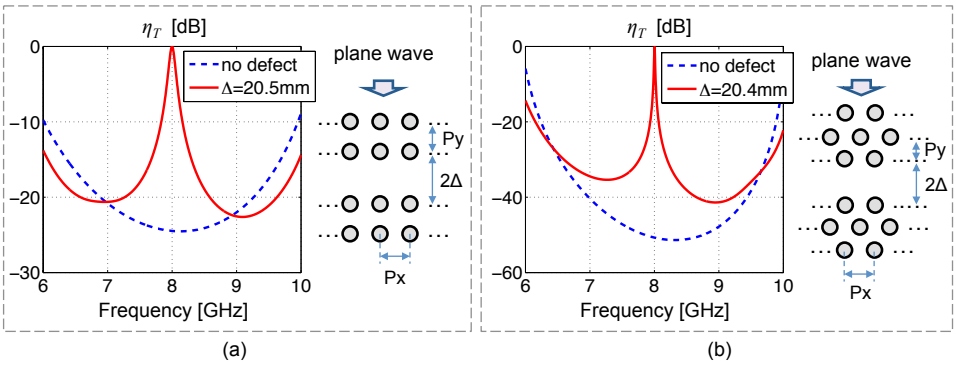

Figure 1.17: Transmission efficiency versus frequency for the square (a) and triangular (b) arrangements of dielectric rods in a vacuum with Px = Py = 13 mm for the former and Px = 15.4 mm, Py = 13.4 mm for the latter.

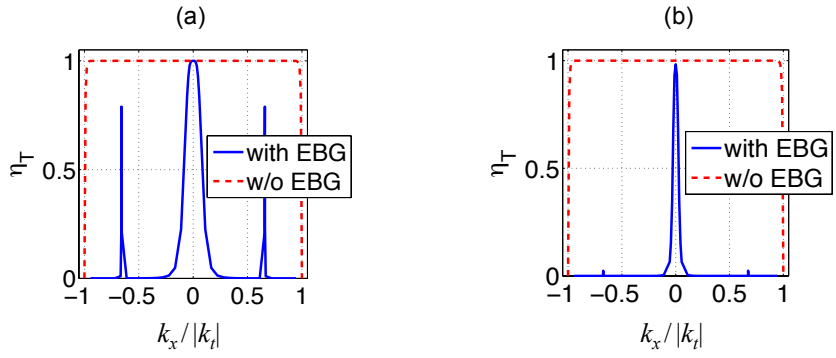

Figure 1.18: Transmission efficiency versus angular spectrum in the square (a) and triangular (b) arrangements of dielectric rods of Fig. 1.17 and in absence of scatterers.

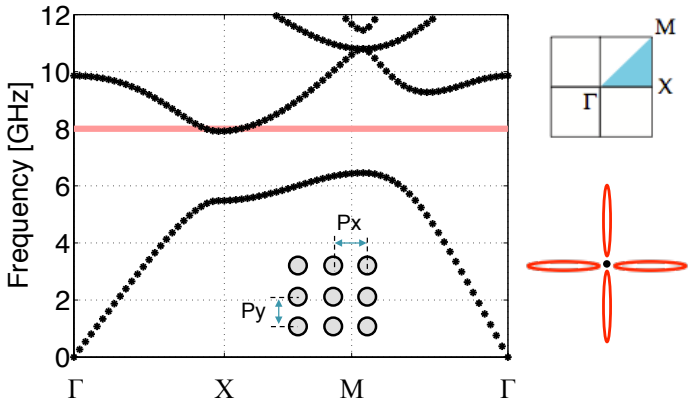

Figure 1.19: Two-dimensional band diagram of a square lattice with period Px = Py = 18.5 mm; at 8 GHz four directions of propagation are allowed as sketched aside.

angular arrangements of cylinders; their plots are given in Fig. 1.17 with the sketches of the relevant geometries. As reported in [51], several parameters can be adjusted to obtain a transmission peak at 8 GHz; here the cavity width has been used to this aim. In absence of defect, the structure holds its periodicity and the plane wave is totally reflected in the forbidden band (dashed curve), whereas a transmission peak appears in the band-gap (solid curve) after removing a layer and increasing the spacing between the two consecutive layers of rods. This behaviour applies to normal incidence: other propagation directions lead to negligible transmitted power in the band-gap as depicted in Fig. 1.18, where η_T is plotted at 8 GHz changing the propagation directions of the impinging plane wave from normal to grazing incidence.

With reference to the scheme using lattice modes, the band diagram of the crystal, calculated through the in-house code `pweRm3` v.2.0 described in section 1.1.2, is considered to select the proper mode. In the case of square arrangements of cylinders, the relevant dispersion plot is depicted in Fig. 1.19: at 8 GHz there are four allowed direction of propagations aligned with the Cartesian axes because the lattice properties are invariant by rotation or mirror operations in the first Brillouin zone according to the square symmetry. This behaviour can be better appreciated in Fig. 1.20, where the three-dimensional Brillouin diagram is shown together with the isofrequency plot at 8 GHz. The plane at constant frequency intersects the lower edge of the second band where $k_x = 0$ and $k_y = 0$, implying that only the Bloch waves propagating along the x and y axes are supported at this frequency. In the antenna configuration, the infinite perfect electric conductor (PEC) cancels the horizontal lobes and the bottom vertical one; therefore

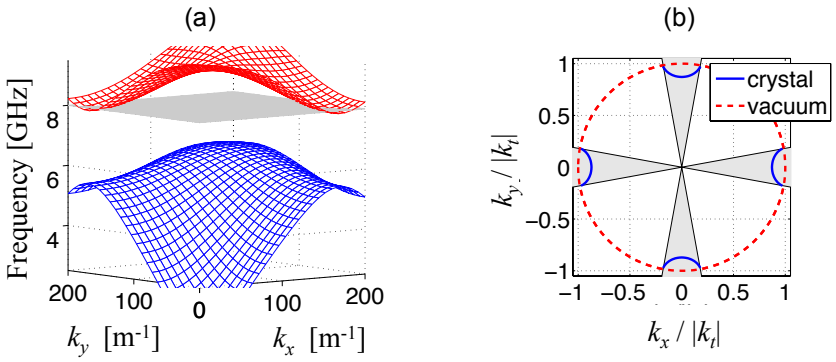

Figure 1.20: (a) Three-dimensional band diagram of the square lattice of Fig. 1.19. (b) Isofrequency dispersion diagram in the same lattice and in a vacuum; shaded regions represent allowed propagation directions inside the crystal.

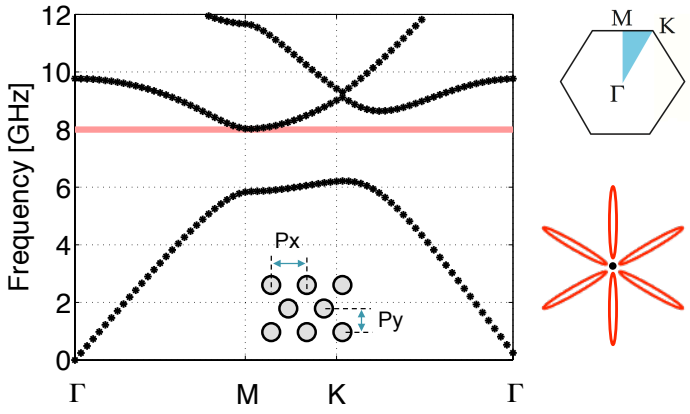

Figure 1.21: Two-dimensional band diagram of a standard triangular lattice with period of 21.3 mm (Px = 21.3 mm, Py = 18.4 mm); at 8 GHz six directions of propagation are allowed as sketched aside.

only upward propagating Bloch waves are allowed in the final structure.

As far as the triangular lattice is concerned, the band diagram along the IBZ of a standard arrangement, is shown in Fig. 1.21. At the lower edge of the second band only waves propagating toward the M point are allowed, that, according to the hexagonal symmetry of the reciprocal lattice, correspond to six allowed directions of propagation. We can suppress those with $k_x \neq 0$ by slightly decreasing the horizontal distance between rods to break the hexagonal symmetry of the reciprocal lattice. The three-dimensional band diagram that is obtained following this approach is depicted in Fig. 1.22, leading to only upward and downward propagating waves as clarified by

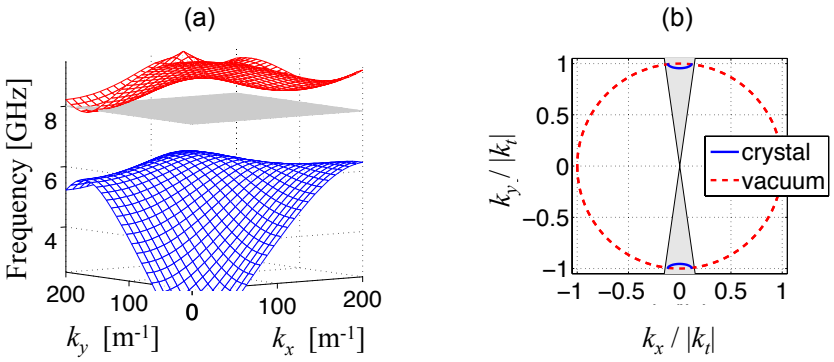

Figure 1.22: (a) Three-dimensional band diagram of the triangular lattice of Fig. 1.21 with Px decreased from 21.3 to 18.8 mm. (b) Isofrequency dispersion diagram in the same lattice and in a vacuum; shaded regions represent allowed propagation directions inside the crystal.

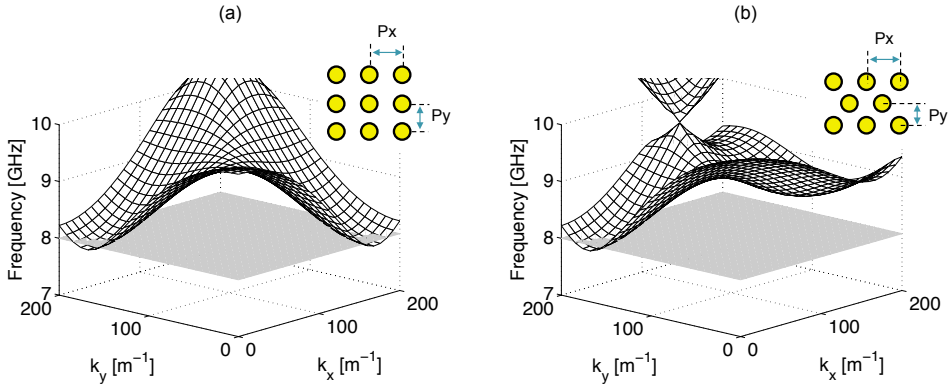

Figure 1.23: Three-dimensional band diagram of the square (a) and triangular (b) lattice of Figs. 1.19 and 1.22, respectively.

the isofrequency dispersion diagram shown in the same figure. Bloch waves propagating toward $y < 0$ are suppressed by a PEC plane in the finite-size antenna. An enlargement of the three-dimensional dispersion diagrams of both square and triangular lattices is reported in Fig. 1.23.

Since real antennas have finite dimensions, previous lattices must be truncated to a finite number of rods, moreover perfect electric conductors can be used to prevent wave propagation along unwanted directions and line sources are inserted to feed the device. Finite-size geometries, parametric with respect to the number of layers (NL) and the number of rods in the longest layer (NN), are depicted in Fig. 1.24.

Resonator antennas are realized splitting the structure in two halves, by placing an infinite PEC surface in the midplane of the cavity, and removing

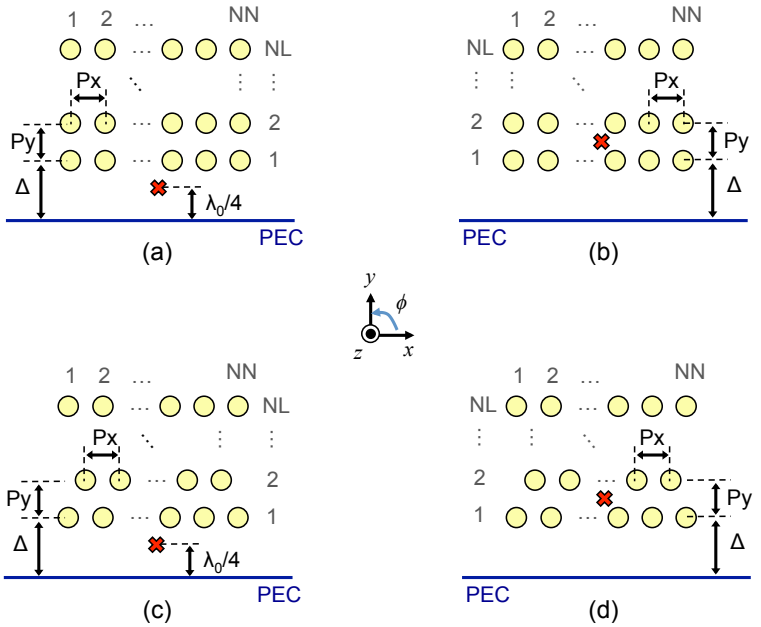

Figure 1.24: Finite-size geometries for the square arrangements of rods in the cavity (a) and the embedded source (b) method and for the triangular case in the former (c) and the latter (d) method. The PEC plane is infinite and the X-points stand for the location of the line sources.

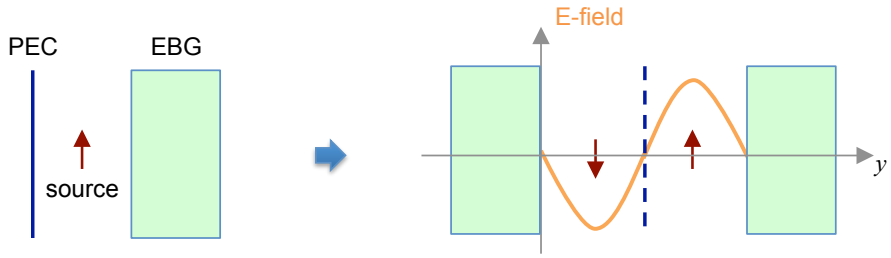

Figure 1.25: Excitation of the defect mode in the cavity.

the bottom part. The line source is located at a quarter wavelength ($\lambda_0/4$ in vacuum) from the ground plane; the radiation parameters were found to be almost insensitive to this distance, provided that a minimum spacing (about $\lambda_0/20$) from the PEC is preserved. At a first glance, one could believe that a line source, which is oriented parallel to the PEC, should appear shorted as it approaches the PEC, and at a distance of $\lambda_0/20$ is bound to produce very little radiated power. More precisely, this phenomenon happens when line sources radiating in a free half-space are considered because, by applying image theory, an array of two very close sources with opposite phasing destructively interferes along the array axis, while the scope is to maximize

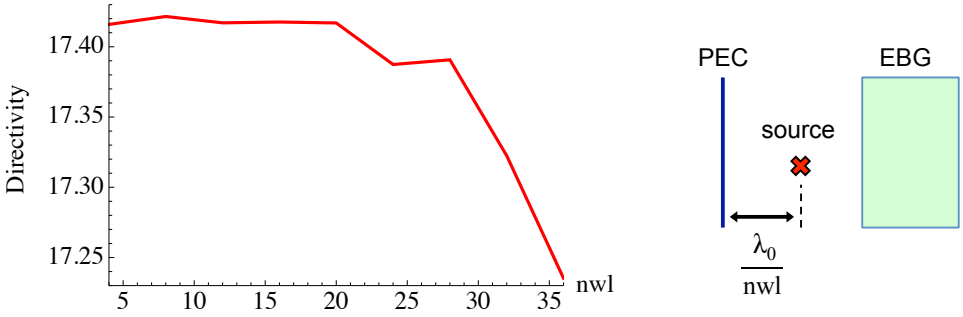

Figure 1.26: Two-dimensional directivity [dB] for the geometry of Fig. 1.24c with NN = 3, NL = 26, Δ = 20.43 mm, Px = 15.4 mm, Py = 13.4 mm.

the power radiated far away, i.e. in far field. In the present case the situation is somewhat different because the source has a local role, which is the excitation of a defect mode inside the cavity. This mode must be odd and the image source contributes to the excitation even when real and image sources are very close. The radiation performance starts deteriorating very close to the PEC, where the source is practically shorted or, under a different viewpoint, where the electric field pattern of the defect mode exhibits a null, so the mode is not excited. The situation is shown in Fig. 1.25 for clarity, while the behaviour of the directivity as a function of the PEC-source distance is given in Fig. 1.26.

As for the EBG materials working at the edge of the band-gap, a ground plane is also used at the bottom to obstruct downward propagating modes in the modified triangular lattice, whereas, for the square lattices, it also suppresses the horizontal lobes due to waves traveling along the x-axis. A thin, infinite current wire is embedded inside the crystal, between the first and the second layer of rods: this location was proven to be a good choice on the basis of several full-wave simulations; further details on the positioning of the source have been given section 1.1.2.

Lattice truncation slightly modifies the behaviour of infinite structures, e.g. leading to a detuning of the transmission peak in the cavity method. To compensate this effect, each finite configuration was optimized with respect to the directivity along the y-axis (see the reference coordinate system in Fig. 1.24). A local optimizing technique interpolates the objective function within a trusted region of the domain and updates the latter step-by-step according to the quality of the approximation model. The optimization domain consists of the geometrical parameters with the highest impact on the performance. They are the cavity width Δ in the resonator antenna and the lattice periods Px and Py in the other mechanism. The preliminary design presented in this section provides the starting values for these parameters to the optimizer.

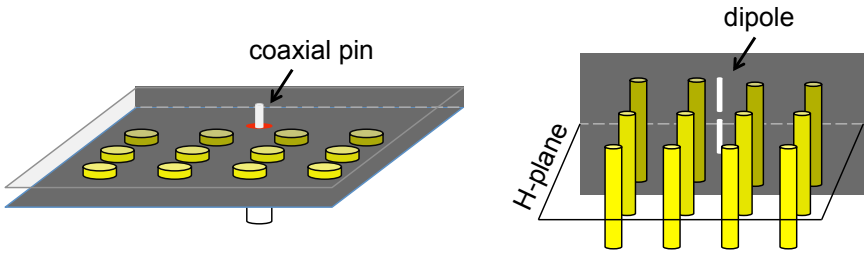

Figure 1.27: Realistic structures emulating the ideal two-dimensional geometries.

Two possible experimental setups can be conceived to physically implement previous two-dimensional structures. The one consists in arranging the dielectric rods in a parallel plate waveguide with height $\ll \lambda_0$ and using a coaxial cable with the outer conductor grounded to one plate. The coaxial pin emulates the current wire, while the parallel plates force the TM polarization; absorbers at the borders can act as open boundaries, while an electrically small sensor can measure the radiation pattern. Another implementation, which is instead useful in view of realistic applications, could be the fully three-dimensional setup made of finite-height bars and fed by a half-wave dipole. The H-plane radiation pattern of this structure matches the one of the corresponding two-dimensional geometry, provided that cylinders are tall enough. Both experimental setups are sketched in Fig. 1.27.

1.2.3 Comparison for two-dimensional structures

The optimization of finite-size two-dimensional geometries has been performed with the frequency solver of CST MWS, using one of its local optimizers, that is the Trust Region Framework. The structures, which would actually have infinite height, have been studied in the opposite limit of electrically short cylinders. More precisely, the height of the rods was taken $\leq \lambda_0/50$, enclosing all structures in between two PEC planes to enforce TM^z polarization and using a Hertz dipole as radiator. The feasibility of this approach, conceptually justified by the translational symmetry of the structure along z, was successfully benchmarked in terms of radiation parameters with other techniques like the CWA and the lattice sum technique (see Figs. 1.13 and 1.14). The optimization has been carried out with respect to the two-dimensional directivity defined as follows

$$\mathrm{Dmax} = 2\pi \frac{U(\theta = \frac{\pi}{2}, \phi = \frac{\pi}{2})}{\int_{-\pi}^{\pi} U(\theta = \frac{\pi}{2}, \phi) d\phi} \tag{1.29}$$

where $U(\theta = \frac{\pi}{2}, \phi)$ is the in-plane radiation intensity (see the reference coordinate system in Fig. 1.24).

Radiation properties

The directivity of the optimized geometries is plotted in Fig. 1.28, omitting the results from structures which do not lead to maximum radiation towards $\phi = \pi/2$. As a term of reference, it must be kept in mind that the directivity of a line source without cylinders, but with a ground plane, calculated according to (1.29), is 4.9 dB.

By comparing the curves with the same number of layers, like c2 with e2 or c3 with e3, it stands out that the method with the embedded source usually exhibits higher performance than the cavity method when a low number of cylinders per layer is used. Nevertheless the former mechanism is always outranked by the latter at higher abscissa values. Taking the square

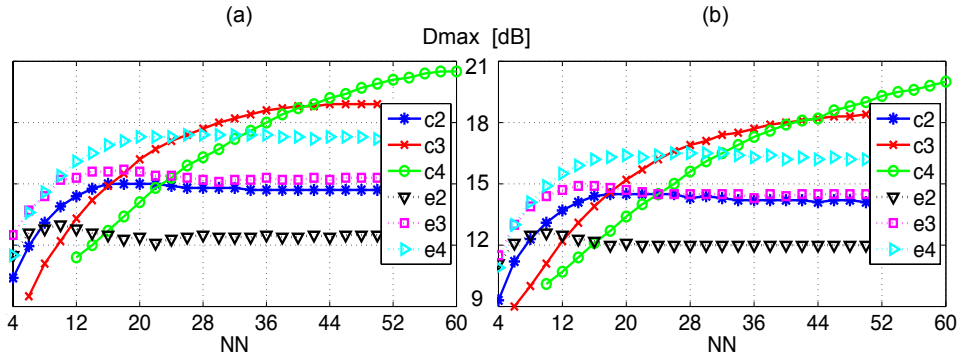

Figure 1.28: Maximum directivity versus the number of rods per longest layer for triangular (a) and square (b) lattices. Curve acronyms are in the form of a letter plus a number, which respectively represent used method (c=cavity, e=embedded source) and number of layers (NL).

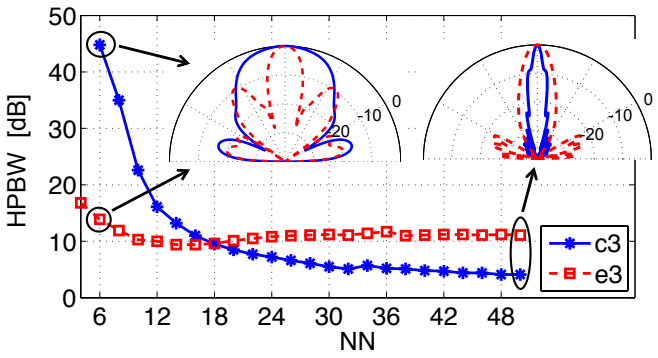

Figure 1.29: Half-power beam width for the square arrangements of 3 layers of rods for the cavity (c3) and the embedded source method (e3). On the top, the H-plane radiation patterns of circled geometries are shown in dB scale.

ID	geometry	lattice	NL	NN	optimized parameters [mm]	Size [λ_0] x [λ_0]
A	source with PEC				Δ=9.38	
B	cav	triangular	2	16	Δ=20.57	6.3 x 1.0
C	cav	triangular	3	26	Δ=20.47	10.4 x 1.3
D	cav	triangular	4	58	Δ=20.43	23.6 x 1.7
E	emb	triangular	2	6	Px=20.3, Py=19.4	2.9 x 0.8
F	emb	triangular	3	10	Px=20.3, Py=18.8	5.0 x 1.3
G	emb	triangular	4	20	Px=20.6, Py=18.5	10.6 x 1.8

Table 1.1: Main geometrical parameters of selected configurations

lattice as example, the resonator antenna with NL×NN = 2×16 presents a directivity enhancement of about 10 dB with respect to the single line source with ground plane; this value is comparable to the embedded source method with a similar number of rods arranged as 3×10.

In general, moving from short to long layers, the directivity initially increases till a sort of saturation point, after which it keeps constant or presents very little variation. For the same value of NL, this knee-point occurs at lower NN in the embedded source method, allowing the resonator antenna to overpass its competitor and become more and more directive. This behaviour is evident also looking at the half-power beam width (HPBW) of the structures, which is plotted in Fig. 1.29 for the square configurations with NL=3. The H-plane radiation patterns relevant to the shortest and longest geometries are reported in the same figure: they are left-right symmetric and there is no back radiation owing to the infinite ground plane.

Unlike the embedded source method, where the EBG structure requires at least two layers to host the source, the resonator antenna can be studied also with a single layer. Despite not plotted in Fig. 1.28, this configuration has been studied too; it does not create an actual partially reflecting cover, but it equally produces some beneficial effect on the radiation pattern. The larger the number of layers, the sharper the transmission peak of the cavity, making device tuning difficult; this phenomenon implies a bandwidth reduction, unless additional defects are inserted [52] but with the undesirable effect of increasing structure size.

On the basis of this behaviour, some configurations featuring the best trade-off between radiation performances and geometrical parameters (i.e. dimensions and number of scatterers) have been selected among the full set of results in order to pursue a deeper comparison. The main geometrical and radiative features of these structures are summarized in Tables 1.1 and 1.2 together with the performances of a single line source with ground plane. As for the latter the value given under the column for optimized parameters is actually the distance between the current wire and the ground plane, which

ID	geometry	NL	NN	Dmax [dB]	HPBW [deg]	SLL [dB]	η_{AP} [%]
A	source with PEC			4.9	120		
B	cav	2	16	14.8	8.5	-17.2	19
C	cav	3	26	17.4	5.3	-14.6	13
D	cav	4	58	20.5	2.8	-18.0	7
E	emb	2	6	12.6	14.4	-9.6	35
F	emb	3	10	14.9	8.7	-9.9	24
G	emb	4	20	17.3	5.5	-23.0	13

Table 1.2: Main radiation parameters of selected configurations

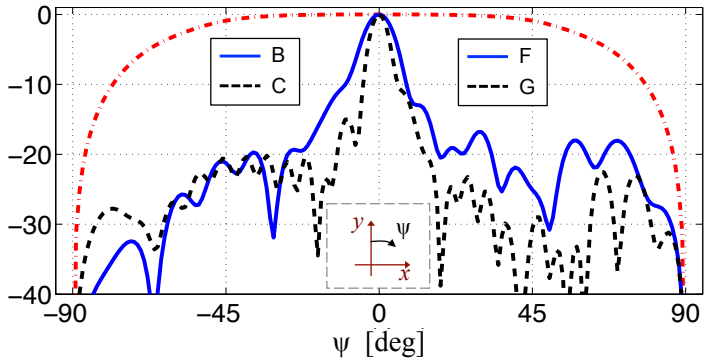

Figure 1.30: H-plane normalized radiation patterns [dB] of some configurations of Table 1.1 identified by their ID. The red line represents a line source with ground plane and no cylinders.

was set to a quarter of wavelength without any optimization. The abbreviations "cav" and "emb" stand for the cavity and the embedded source methods, respectively. According to the figures reported in the table, it emerges more clearly that the cavity method achieves the highest performances, provided that the number of layers is fixed. If the configurations with the same number of cylinders are instead considered, the directivity enhancements achieved by the two methods result almost comparable, while differing only in the rod arrangement. In details the resonator antenna appears more suitable for low-profile devices, while the embedded source method is attractive for more compact, i.e. taller but less extended, structures.

The radiation pattern on the H-plane of some configurations is plotted in Fig. 1.30; due to the symmetry only half of the pattern is shown: on the left there are the cases with the resonator antenna, while on the right there are the ones with the other scheme. Fig. 1.31 instead shows the average electric field for the configurations C and G. On the top of these overlays an almost planar wavefront, resembling that of a plane wave, can be easily recognized.

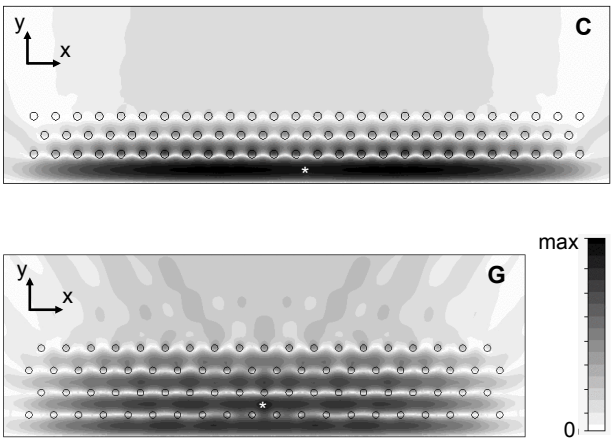

Figure 1.31: Overlays of the average E-field for two configurations of Table 1.1 with a similar number of rods. White asterisks represent the line sources.

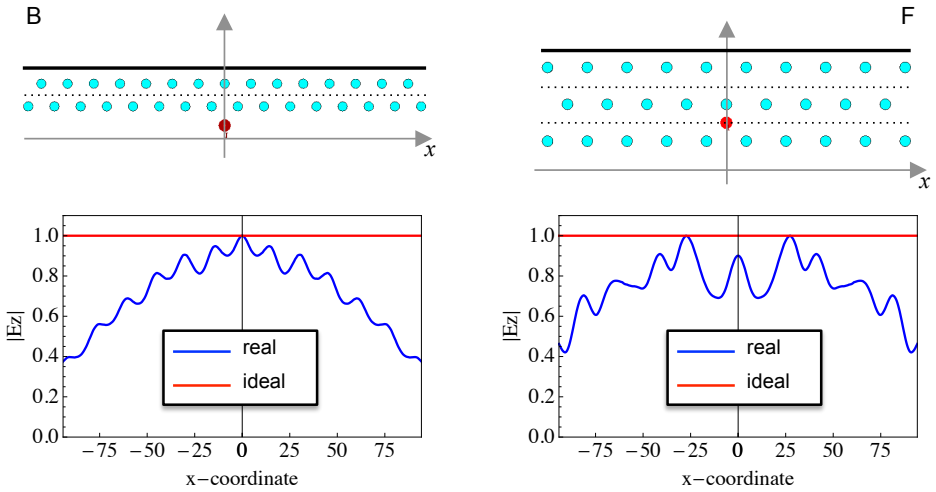

Figure 1.32: E_z amplitude along the black lines of the geometries shown on the top.

The EBG structures modify the radiation pattern, making it more directive, as expected. Nevertheless in the cavity method the wave passes through a crystal working in the band-gap by constructive interference in the resonator, while in the other mechanism a mode of the crystal is allowed to propagate.

Table 1.2 also gives the aperture efficiency of the structures, computed as the ratio between Dmax and the directivity of a uniform aperture with the same size, namely

$$\eta_{AP} = \frac{D_{\text{real}}}{D_{\text{ideal}}} = \frac{\text{Dmax}}{\frac{4\pi}{\lambda_0^2} A_{\text{geo}}} \tag{1.30}$$

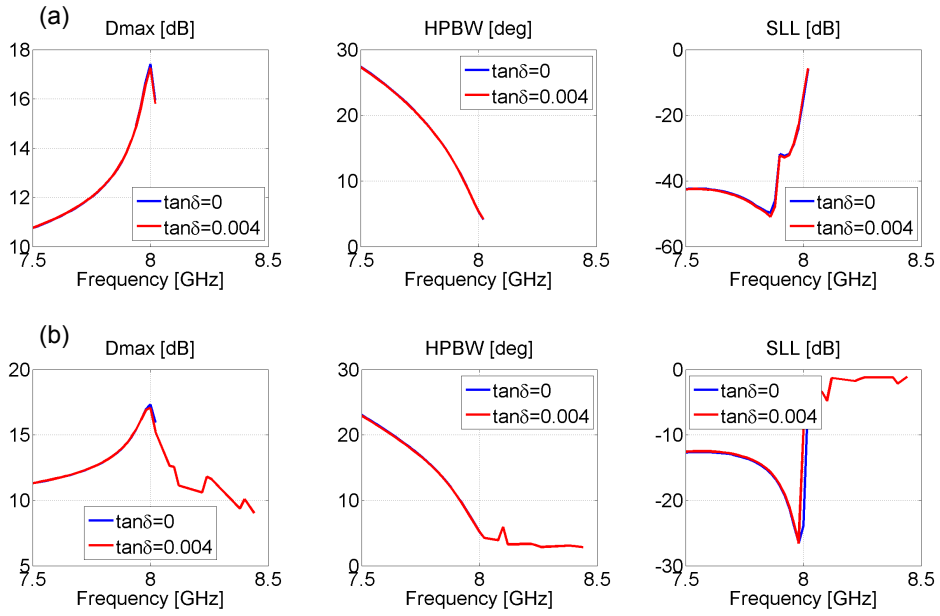

Figure 1.33: Radiation parameters versus frequency for the geometries C (a) and G (b) of Table 1.1.

where A_{geo} the geometrical area of the aperture. The latter is taken as large as the geometry and with height along z equal to a wavelength. Owing to the nonuniform field distribution at the interface EBG–freespace, the aperture efficiency assumes quite reduced values. In Fig. 1.32, we have reported the field amplitude for the cases B and F of Table 1.1, computed at the upper border of the periodic structure. Such EBG-based antennas have rather low aperture efficiency; their advantage is that the enhancement is achieved by employing a very simple structure composed by a passive medium and an omnidirectional radiator.

As far as the frequency behaviour of the radiation parameters is concerned, the directivity (Dmax), side lobe level (SLL) and the half-power beam width (HPBW) have been plotted as a function of the frequency in Fig. 1.33 for two proof configurations. Curves have been interrupted when the main lobe was no longer aligned with the y-axis. If an acceptable degradation larger than the 10% of its maximum value is defined for the directivity, the bandwidths are almost similar for the two methods; they are also negatively affected by the number of scatterers. In the plots of Fig. 1.33, the curves obtained in the case of lossy cylinders are also given, assuming a $\tan\delta = 0.004$ (see discussion later on): in presence of dielectric losses, radiation parameters exhibit negligible changes.

Electrical properties

Although the input impedance of the radiating element is an unphysical parameter in such simulations, it gives useful information on the role played by rods over the frequency behaviour of a real source. The rods are found to have a significant impact on the input impedance of the dipole which generally exhibits a not negligible reactive part. Unless a resonant condition is searched while running the optimizer, a matching network is generally needed to match a 50 Ω line. To perform the study, we introduced a simple microwave network consisting of an open stub connected in series to the dipole plus a quarter-wavelength transformer.

By a proper design, the reflection coefficient can be minimized at 8 GHz and the curves in Fig. 1.34 are obtained: from geometry A to G, the bandwidths at −10 dB in MHz are 703, 79, 10, 2, 91, 63 and 35. As a matter of fact, the bandwidth comes out to decrease as the number of scatterers increases because the higher the number of employed cylinders in a geometry, the faster the variation of the input impedance. This behaviour becomes more pronounced for the cavity method at high NL values since this mechanism relies on a resonant effect and the Q-factor of the cavity (i.e. the steepness of the transmission peak) increases with the number of layers. A similar effect occurs for the radiation properties: the directivity is very peaked for the configuration D of Table 1.1 and, moving away from 8 GHz, drops more quickly for geometries with many cylinders.

When realistic dielectrics are considered, a small imaginary part of the rod permittivity must be introduced. The number of cylinders becomes

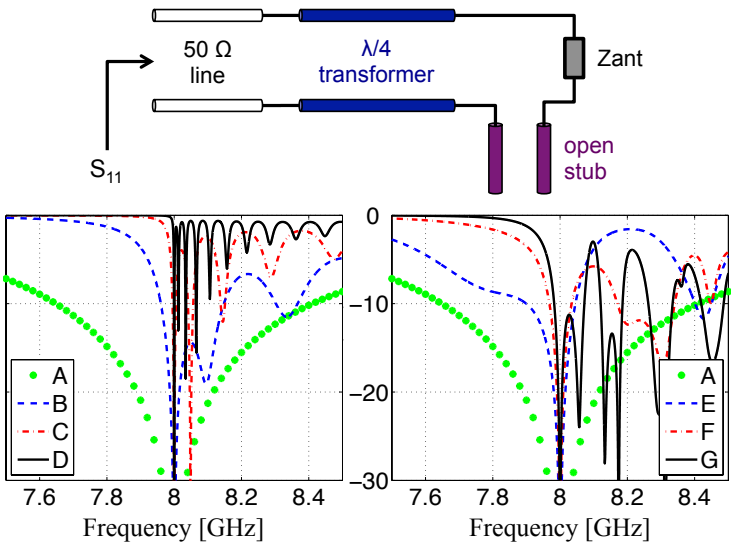

Figure 1.34: S_{11} [dB] versus frequency at the input of the matching network depicted on the top of the picture for the configurations of Table 1.1.

ID	method	number of rods	η_A ($\tan\delta = 0.0002$)	η_A ($\tan\delta = 0.004$)
B	cav	31	0.996	0.92
C	cav	77	0.97	0.65
D	cav	230	0.85	0.21
E	emb	11	0.997	0.96
F	emb	29	0.996	0.93
G	emb	78	0.99	0.88

Table 1.3: Antenna efficiency

therefore a fundamental parameter, being tightly related to the structure efficiency. Here the antenna efficiency η_A is analysed using two different loss tangent values for the cylinders, i.e. 0.0002 and 0.004. The former value resembles the $\tan\delta$ of a low-loss dielectric like alumina [53], which, according to its purity, features similar relative permittivities to the ones used here. The latter value was instead chosen to investigate the effect of a material with medium performance in terms of losses, such as beryllium oxide [54] or some types of glasses [55]. The antenna efficiencies have been calculated as follows

$$\eta_A = 1 - \frac{P_{\text{diel}}}{P_{\text{tot}}} \tag{1.31}$$

where P_{diel} is the power dissipated inside the dielectric rods, while

$$P_{\text{tot}} = \frac{1}{2} R_{in} |I_d|^2$$

being R_{in} and I_d the input resistance and the current of the dipole, respectively. CST MWS has a built-in routine for the calculation of the antenna efficiency, which gives almost identical value to (1.31).

The outcomes are reported in Table 1.3: the cavity is more affected by cylinder losses in comparison to the embedded source method. This phenomenon can be intuitively explained if the pattern of the electric field is considered in the relevant lattices, as sketched in Fig. 1.35. Ideally, waves in the band-gap are evanescent and an exponentially attenuated electric field passes through the rods. On the contrary Bloch waves, excited at the edge of the band-gap, feature a node along the horizontal lines crossing the axes of the cylinders. As far as finite-size geometries are concerned, the E_z pattern is altered by the presence of other boundary conditions, but the above mentioned concept still holds some validity. This can be appreciated from Fig. 1.31: the average electric field in configurations G is localized outside the rods to a larger extent than in configuration C, therefore it leads to a lower dissipation.

Regarding the modifications to the frequency behaviour due to dielectric losses, radiation parameters exhibit minimal changes, whereas the in-

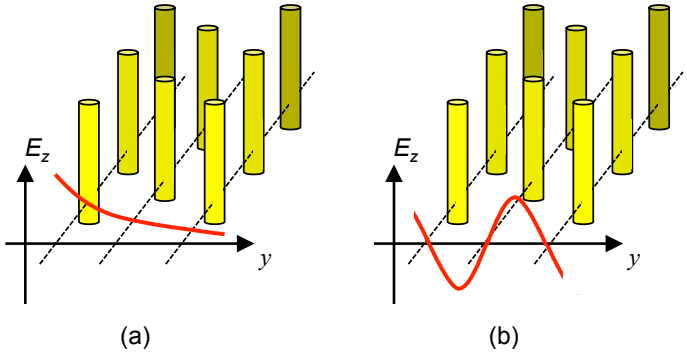

Figure 1.35: Sketch of the electric field in a triangular lattice working inside the band-gap (a) and in an expanded triangular lattice working at the lower edge of the second band (b).

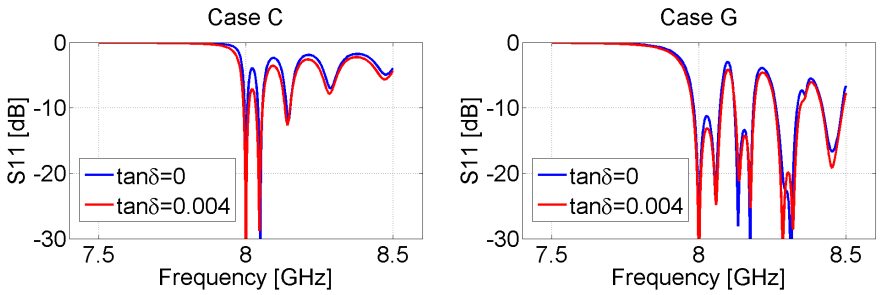

Figure 1.36: S_{11} versus frequency at the input of the matching network of Fig. 1.34 using ideal or lossy cylinders.

put impedance becomes less steep, experiencing a bandwidth increase. The larger the number of rods in the geometries, the higher the bandwidth enhancement, going from 6% for structure E to more than 300% for case D when $\tan\delta = 0.004$.

The aforementioned outcomes directly apply to frequencies other than 8 GHz due to the scaling properties of EBG materials. Preliminary comparisons using different rod diameters led to similar results, increasing their representativeness with respect to the variation of the filling factor in the primitive lattice cell. The same remark holds for small deviations of the dielectric constant from the simulated value, whereas a significant decrease needs to be studied, despite it is expected to only reduce antenna performances without modifying strengths and weaknesses of the two methods. Finally the analysis of both square and triangular lattices provides some confidence that previous outcomes do not depend on the type of arrangement.

1.2.4 Comparison for three-dimensional structures

The optimization of finite-size three-dimensional geometries has been similarly performed. The transient solver of CST MWS has been used in place of the frequency one and the three-dimensional directivity has been maximized. The structures we studied consist of alumina rods with finite height; the latter has been set to four wavelengths, a value that provides similar H-plane radiation patterns to the two-dimensional case. The dielectric cylinders is excited by a half-wave dipole, the centre of which is at the midplane of the rod height. The ground plane is also finite with horizontal and vertical extensions equal to the full EBG structures. A resonator antenna based on a triangular lattice is sketched in Fig. 1.37 as example.

The directivity of the optimized structures is plotted in Fig. 1.38 for configurations with maximum along y. The behaviour is similar to the two-dimensional case, but curves are steeper at lower NN. For a given number of layers, by increasing the number of rods, the antenna with the embedded source initially exhibits better performance, but, at a point, its directivity is always exceeded by the resonator antenna. To perform a deeper comparison,

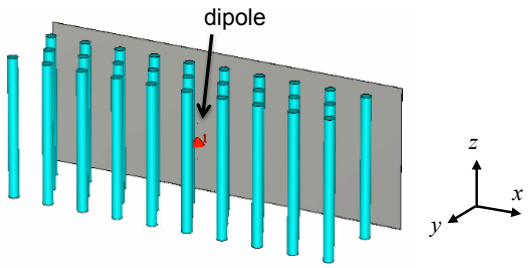

Figure 1.37: Example of a three-dimensional geometry.

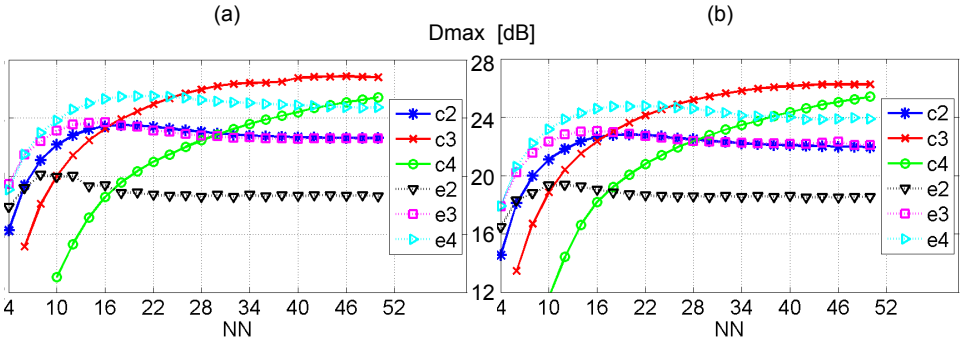

Figure 1.38: Maximum directivity versus the number of rods in the first layer for triangular (a) and square (b) lattices. Curve acronyms have the same meaning of Fig. 1.28.

	A	B	C	D	E
geometry	dipole with PEC	cav	cav	emb	emb
NL		2	3	3	4
NN		18	24	12	18
number of rods		35	71	35	70
optimized parameters [mm]	Δ = 9.38	Δ = 20.52	Δ = 20.46	Px=20.3 Py=18.7	Px=20.6 Py=18.4
Dmax [dB]	7.5	23.5	25.4	23.5	25.5
H-plane HPBW [deg]	70	10.1	8.0	9.6	7.6
H-plane SLL [dB]	-26.2	-23.8	-15.8	-20.3	-18.1
E-plane HPBW [deg]	118.1	14.6	13.7	13.5	12.7
E-plane SLL [dB]	n.a.	-23.8	-15.8	-20.3	-18.1
η_A [%] ($\tan\delta$=0.0002, P_{diel})		99.6	97.7	99.6	99.3
η_A [%] ($\tan\delta$=0.0002, CST)		99.6	93.1	>1	99.7
η_A [%] ($\tan\delta$=0.004, P_{diel})		91.5	71	93.2	88
η_A [%] ($\tan\delta$=0.004, CST)		93.4	60	93	90.5

Table 1.4: Main parameters of selected three-dimensional configurations

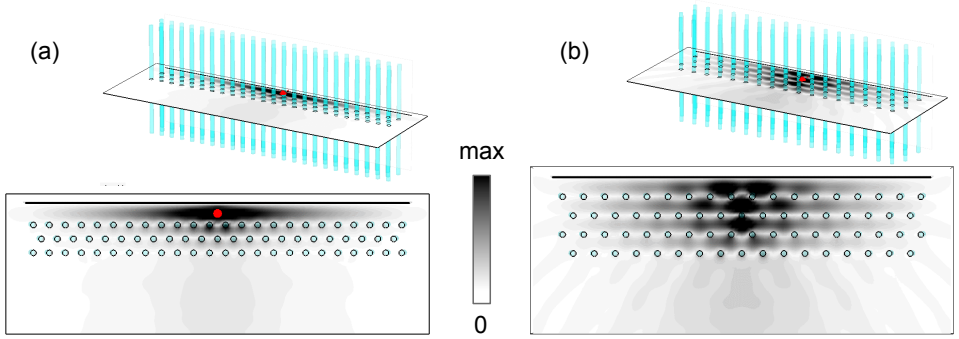

Figure 1.39: Average electric field for the configurations C (a) and E (b) of Table 1.4 on the midplane orthogonal to the rod axis.

two geometries with similar performance and total number of rods have been selected for each method. The triangular arrangements, being slightly more effective, and the geometries with the best trade-off between directivity and size were preferred. Table 1.4 gives a detailed benchmark of selected geometries, also reporting a dipole with a PEC plane a quarter wavelength apart. Such table confirms that the cavity method is more suitable for low-profile antennas, whereas the embedded source method is more appropriate for compact configurations, emulating a lattice to a larger extent.

An important parameter of Table 1.4 is the antenna efficiency η_A, which has been calculated through both the built-in function of the commercial

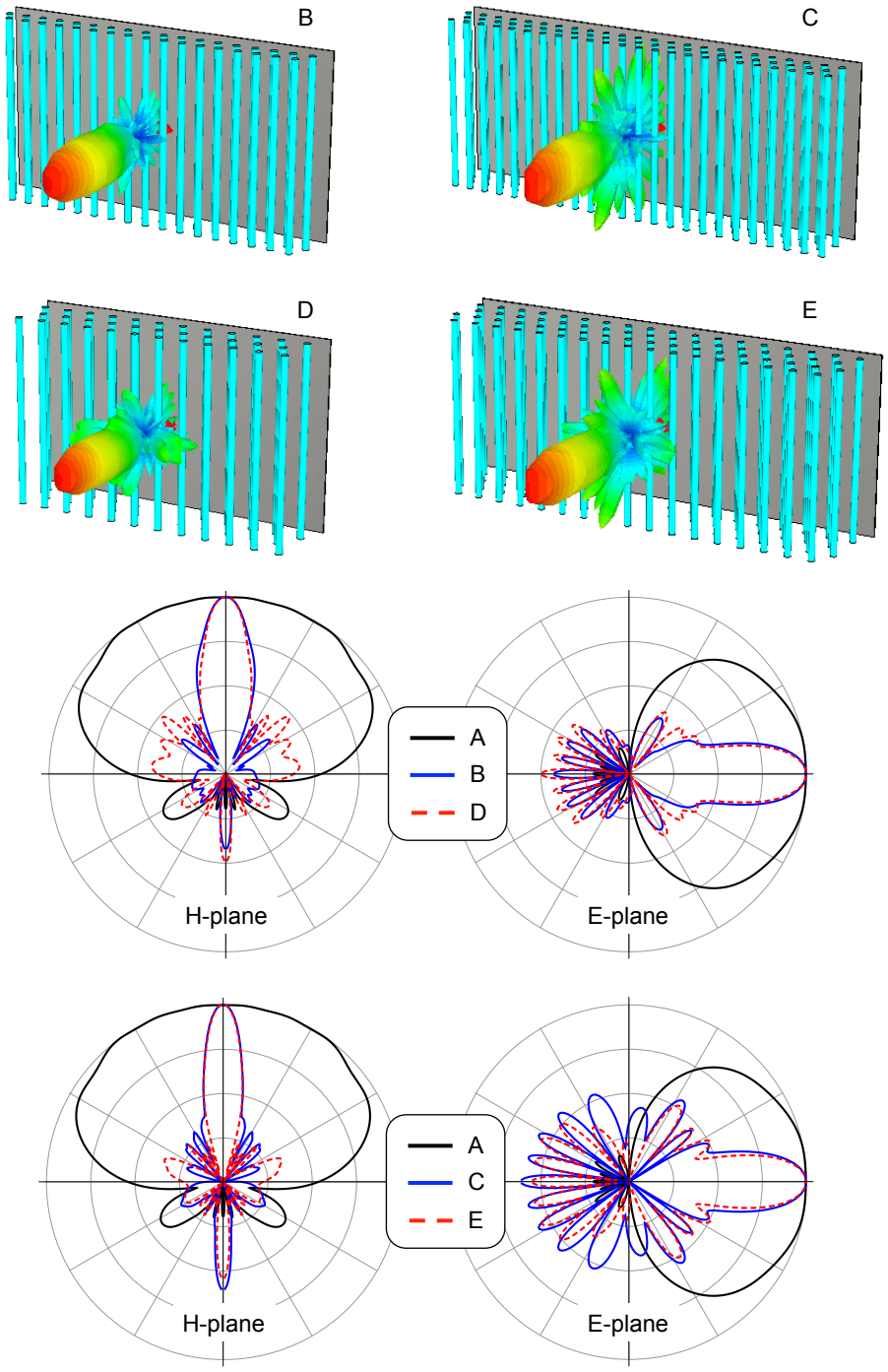

Figure 1.40: Three-dimensional radiation patterns and cuts on the H- and E-plane for the configurations of Table 1.4.

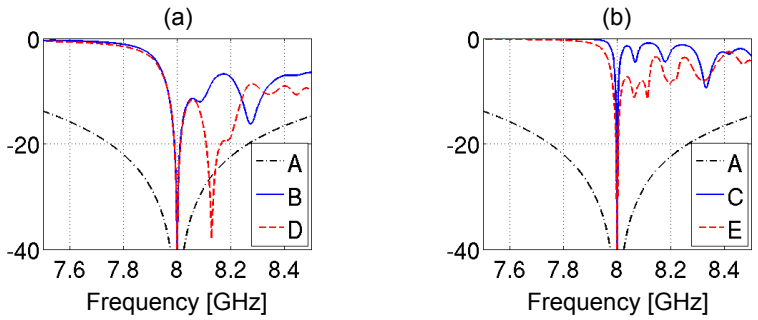

Figure 1.41: S_{11} [dB] versus frequency at the input of the matching network of Fig. 1.34 for the configurations of Table 1.4.

software and the dielectric losses P_{diel} as in the two-dimensional case. The two calculations give different results for some configurations; in our opinion the latter approach is less reliable because it integrates the radiated power, which could be very small if the input port is not matched. Independently from the type of calculation, the figures of η_A confirm a property pointed out in the two-dimensional comparison: the embedded source method working at the lower edge of the dielectric band is more efficient. Fig. 1.39 provides an explanation to this phenomenon in terms of average electric field, which is localized inside the rods to a larger extent in the cavity method.

The three-dimensional radiation patterns of the configurations in Table 1.4 are depicted in Fig. 1.40 together with the two-dimensional cuts on both H- and E-plane. As in the two-dimensional study, the effect of losses on such patterns is negligible. The SLL is due to the backward radiation, thus explaining why it is equal on both planes. Neglecting the backscattering, the two methods achieve similar directivities with a different combination of radiation parameters. For example, in the case of the mechanism with the embedded source, the optimal geometries have higher side lobes and lower HPBW on the H-plane. It is worth noticing that the periodic structures in both methods profitably shape the emission on the E-plane too, despite no attention has been paid to this effect during the lattice design. Since the height of the rods is fixed, the differences in the E-plane patterns must be ascribed to the number of layers and to the distance between cylinders.

As far as the antenna impedance is concerned, the frequency behaviour has been studied assuming the same kind of matching network of the two-dimensional comparison. It consisted of a stub and a quarter-wavelength transformer connected to a transmission line with a characteristic impedance of 50 Ω. The reflection coefficients are plotted in Fig. 1.41: the bandwidths at -15 dB for the configurations of Table 1.4 from A to E are 878, 38.6, 6.3, 37.6 and 15.8 MHz. The values are very similar for the cases B and D; in general, a higher number of cylinders results in a faster variation of the antenna impedance and, accordingly, in a smaller bandwidth.

1.3 Antenna Design Through Lattice Eigenmodes

1.3.1 A new perspective of the embedded source method

Among the most successful employments of periodic structures, there are the emulation of high impedance surfaces [56, 10], realization of reflectors [7], reduction of the coupling between patch antennas [57, 58] and the enhancement of the directivity of simple primary radiators [13, 52]. They can prevent wave propagation within some frequency bands and this feature was mostly exploited so far. In particular we have studied the directivity enhancement by comparing the cavity with the embedded source method. The former has undergone significant development and advancement in terms of efficiency, reduction of dimensions, frequency tuning, bandwidth increase or multiple beams [15, 59, 12, 60, 44, 61]. Resonator (or Fabry-Pérot) antennas rely on metallic grids and EBGs working in the band-gap and acting as spatial filters. A periodic structure can behave as spatial filter and shape the radiation pattern of antennas also working outside the band-gap, namely by using the latter method. Enoch et al. [14, 47] proposed and experimentally demonstrated this alternative approach, which has been explored to a modest extent [27], despite it can reveal unprecedented and profitable usage of EBG materials.

The alternative approach to Fabry-Pérot antennas works with a crystal mode excited by a source embedded in the lattice, as shown in Fig. 1.42. The directivity enhancement was generally explained by similarity with the behaviour of epsilon near zero (ENZ) materials, nevertheless a different physics rules the phenomenon, enabling the exploitation of peculiar properties that ENZ or other metamaterials do not share. More precisely, the excited mode is a solution of the lattice eigenvalue equation with its own dispersion relation and eigenfunction. By adopting this viewpoint, deeper understanding as well as improvements to this kind of "lattice antennas" are explored in this section.

We refer to a classical geometry dealt in literature: a square lattice of alumina cylinders with circular cross-section and infinite length in a vacuum background. The dispersion diagram for TM modes (electric field parallel

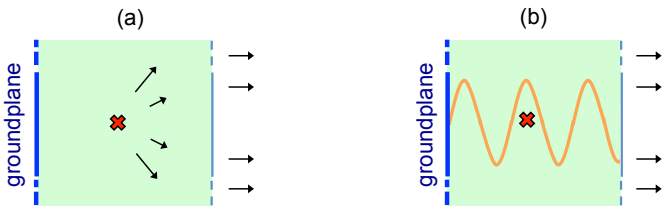

Figure 1.42: Schematics of the method with embedded sources (= X-points), viewed as an ENZ material (a) or as a crystal with its own modes (b).

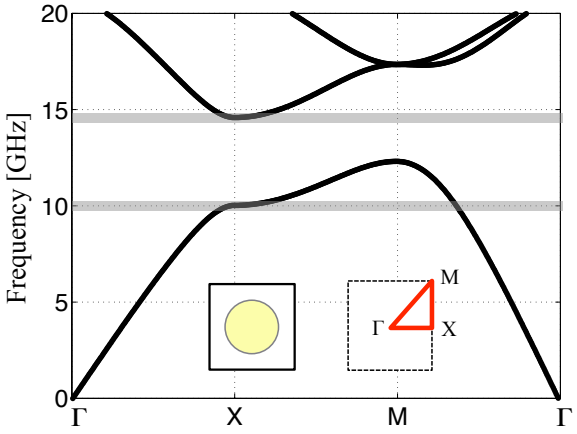

Figure 1.43: Dispersion diagram along the edge of the IBZ for a square lattice of dielectric cylinders with $\varepsilon_r = 9$, lattice period $a = 6.2$ mm and diameter $d = 0.7a$.

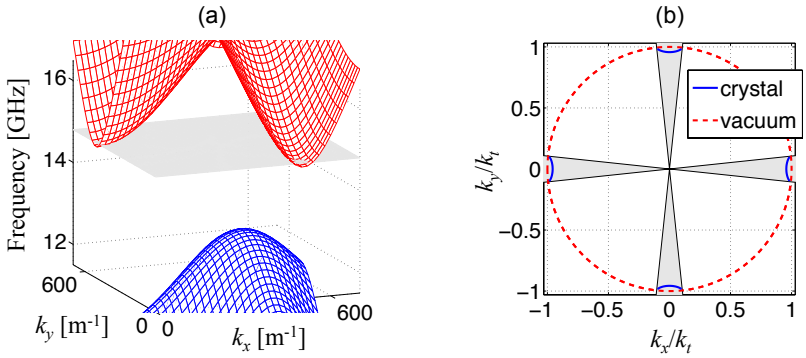

Figure 1.44: (a) Three-dimensional dispersion diagram of the square lattice of Fig. 1.43 and constant plane at 14.8 GHz. (b) Isofrequency dispersion diagram at 14.8 GHz in the same lattice and in a vacuum; shaded regions represent allowed propagation directions inside the crystal.

with the cylinder axis), calculated along the border of the irreducible Brillouin zone, is shown in Fig. 1.43.

Each Bloch wave is allowed to propagate along a given direction so that, if an omnidirectional source excites only a few crystal modes, the radiation is spatially filtered. This phenomenon has been used to realize directive antennas by working at the lower edge of the air band, i.e. at about 14.8 GHz in the dispersion diagram of Fig. 1.43. The eigenvalues of such region, which have been shaded in the figure, are in proximity of the X-point of the IBZ, that is, owing to the lattice symmetry, the corresponding eigenmodes propagate along the two coordinate axes. This behaviour is clarified in Fig. 1.44,

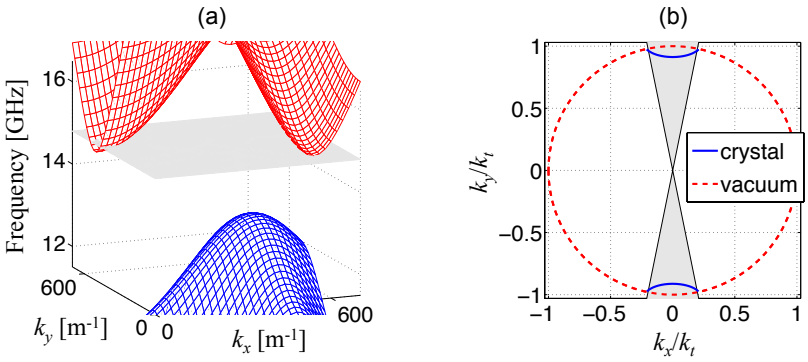

Figure 1.45: Same plots as in Fig. 1.44 for a lattice with horizontal period decreased from 6.2 to 5.8 mm.

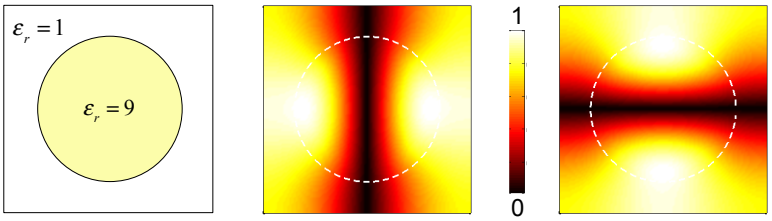

Figure 1.46: Primitive cell and normalized eigenfunctions of the modes at the lower edge of the air band for the lattice of Fig. 1.43.

where two plots are shown. The former is the three-dimensional dispersion diagram for positive spatial harmonics inside a cell of the reciprocal lattice; the constant plane corresponding to the working frequency is also depicted. The latter is the isofrequency plot at 14.8 GHz, showing the intersection of the aforementioned plane with the air band; negative spatial harmonics are also considered here.

Two directions of propagation can be suppressed by breaking the square symmetry of the lattice. For example, with a proper decrease of the horizontal period, the air band rises above the working frequency in proximity of $k_y = 0$. The new dispersion diagram is depicted in Fig. 1.45 together with the in-plane angular spectrum at 14.8 GHz. A similar approach was applied to triangular lattices in [47]: it consists in shaping the bands of eigenvalues.

Directive antennas based on square lattices can be actually realized without relying on such a strategy since all angular lobes apart from the upper one ($k_x \cong 0$, $k_y > 0$) can be seriously impaired by using a ground plane. To provide an intuitive explanation, we refer to the eigenfunctions of the crystal modes supported at 14.8 GHz and, more precisely, to the electric field patterns inside a primitive lattice cell, which are depicted in Fig. 1.46. The modes are degenerate and their eigenfunctions only differ in a rotation

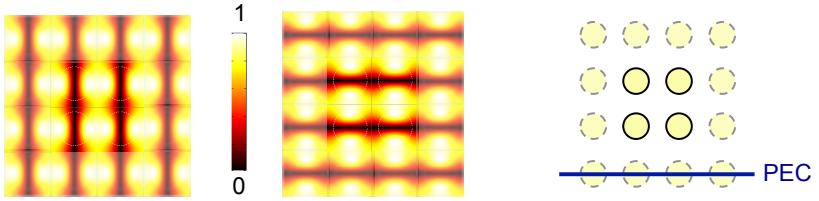

Figure 1.47: Normalized eigenfunctions of the modes of Fig. 1.46 spanning several lattice cells and geometry with a PEC plane.

by 90 deg. The one on the left presents little variation in vertical direction, i.e. $k_y \cong 0$, so it is responsible for the horizontal lobes of Fig. 1.44b, whereas the one on the right is associated with vertical propagation. Being at the edge of the band, both modes feature a group velocity $v_g \cong 0$, namely they are similar to standing waves with fixed nodal and anti-nodal lines.

Similar electric field patterns are expected in periodic structures with finite dimensions, provided that their size is large enough to emulate a lattice. They are depicted in Fig. 1.47 together with a sketch of the corresponding geometry, where a horizontal infinite PEC has been also inserted across the centres of a row of cylinders. The PEC plane perfectly matches the pattern of a mode, whereas it violates the one of the other mode. Assuming the presence of a source that excites both modes, the net effect is an impairment of the horizontal lobes and the suppression of the bottom one. A directive antenna featuring a single main lobe on the top is finally obtained; a good choice for the source location is where the eigenfunction of the desired mode exhibits a maximum.

The importance of crystal eigenfunctions in designing antennas is clarified here by showing how a lattice mode far from the band-gap can profitably shape the radiation pattern of an omnidirectional radiator. The CWA is adopted in the following by exciting the square arrangements of dielectric cylinders with a current wire of negligible radius. Both cylinders and source are aligned with the z-axis and translational invariance with respect to such direction is assumed.

By considering again Fig. 1.43, other eigenmodes in correspondence of the X-point can be noticed at 10 GHz, besides the ones in the upper shaded region. Those Bloch waves are suitable to realize directive antennas, but at such frequency the crystal supports other spurious (unwanted) waves. The plane at 10 GHz indeed intersects the dielectric band along continuous lines as depicted in Fig. 1.48, resulting in a continuous angular spectrum.

The pattern of the electric field for the desired mode is shown in Fig. 1.49 together with the radiating structure of finite dimensions, conceived to work with such mode. The antenna is realized by truncating the lattice to a number of layers NL and a number of rods per layer NN; ground plane

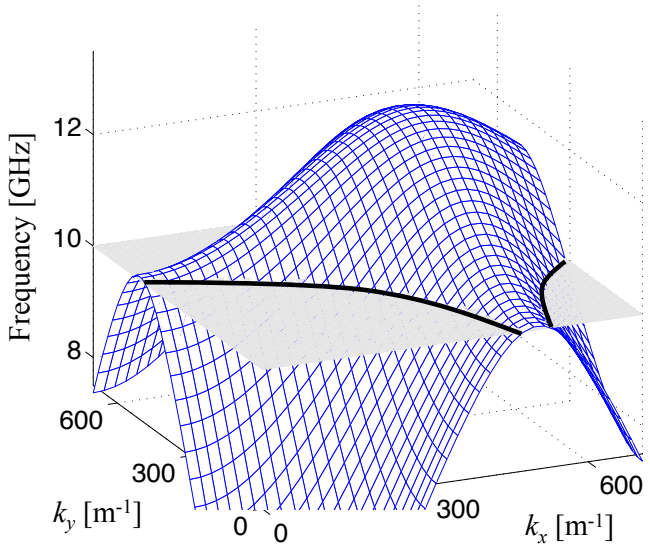

Figure 1.48: Three-dimensional dispersion diagram of the square lattice of Fig. 1.43 and constant plane at 10 GHz. Black lines represent allowed Bloch waves.

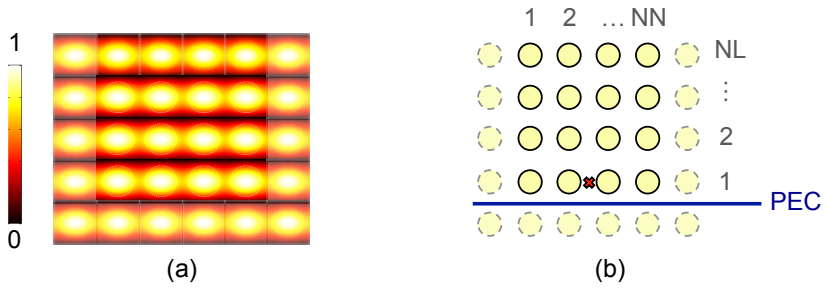

Figure 1.49: (a) Normalized magnitude of the electric field in the square lattice of Fig. 1.43 at 10 GHz for $k_y = 0$; (b) layout of the finite-size antenna.

and line source are respectively placed in correspondence of a nodal line and a field maximum of the eigenfunction. A structure of this kind, employing from 3 to 5 layers with 8 cylinders, can achieve directivity of the order of 10 dB after optimizing the lattice period. The optimization is required to cope with the side effects due to the lattice truncation, namely finite dimensions and new boundary conditions. Although the location of ground plane and line source has a beneficial effect in enhancing the purity of the desired Bloch wave, some spurious modes are always excited. The latter produce grating lobes, which become dominant for some configurations with many cylinders per layer.

A directive antenna can be realised using of a truncated lattice working

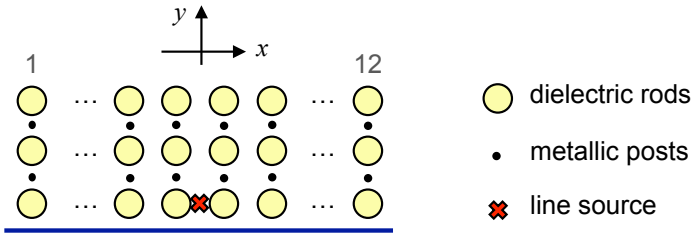

Figure 1.50: Antenna with alternating layers of alumina and metallic rods.

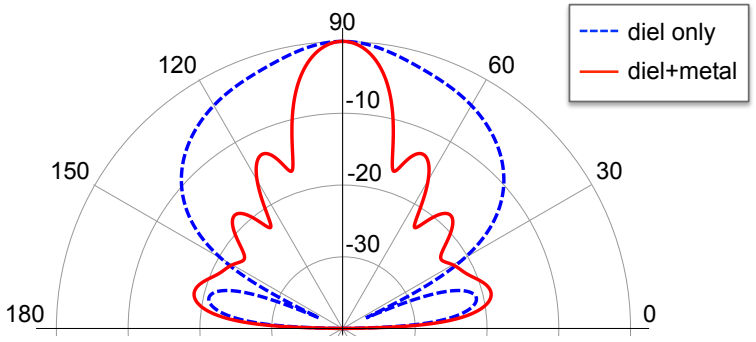

Figure 1.51: Normalized radiation pattern in dB scale for the geometry of Fig. 1.50 after optimizing the lattice period with and without metallic posts.

at 10 GHz by exploiting the eigenfunction of the desired Bloch wave. We consider the antenna of Fig. 1.50, where layers of metallic posts with a diameter of 0.5 mm have been inserted between the layers of dielectric cylinders. The former comply with the boundary conditions of the wanted eigenmode (see Fig. 1.49a), whereas they suppress spurious waves, whose pattern does not vanish in their position. The lattice periods of the structure in Fig. 1.50 with and without metallic posts have been optimized with respect to the directivity, which is maximized at $a = 6.0$ and 5.7 mm, respectively; the corresponding H-plane radiation patterns are compared in Fig. 1.51. The case with metallic posts is more directive, exhibiting a gain enhancement from 8.5 dB to about 13 dB, with the half-power beam width decreasing from 46 deg to 16 deg. This improvement must be attributed to the presence of metallic posts that increases the purity of the desired crystal mode, making the electric field on the top of the structure more uniform.

A meaningful parameter in this sense is the aperture efficiency calculated according to (1.30). In absence of metallic cylinders, $\eta_{AP} = 25\%$, whereas in the other case it almost reaches 70%. An explicative plot is presented in Fig. 1.52, showing the electric field magnitude (a) and phase (b) taken at a distance of a lattice period above the top layer of the optimized geometries. In the case with dielectric cylinders only, the amplitude of the electric field

decays more rapidly and its phase presents higher variation. In the same plot, the ideal pattern in a lattice is also shown as a term of comparison; such a distribution of electric field would give an aperture efficiency of 98.3%. The purity enhancement of the wanted mode by metallic posts is also proved by a negative consequence on the antenna efficiency. When the mode is purer, the pattern of the electric field becomes close to the one of Fig. 1.49, i.e. localized to a larger extent inside the dielectric cylinders. Assuming a loss tangent of 2×10^{-4} for alumina, the antenna efficiency decreases from 99.2% to 97.9% in the optimized configuration with metallic cylinders. This drawback can be overcome working with the lattice mode in the upper shaded line of Fig. 1.43, where the nodal lines of the relevant eigenfunction pass through cylinders axes.

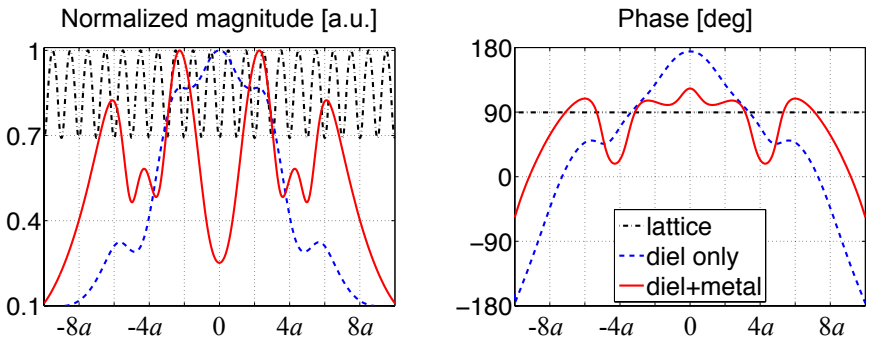

Figure 1.52: Normalized magnitude and phase of the electric field along x, calculated a lattice period above the top layer of the optimized structures with and without metallic posts; the ideal pattern in a lattice is also plotted.

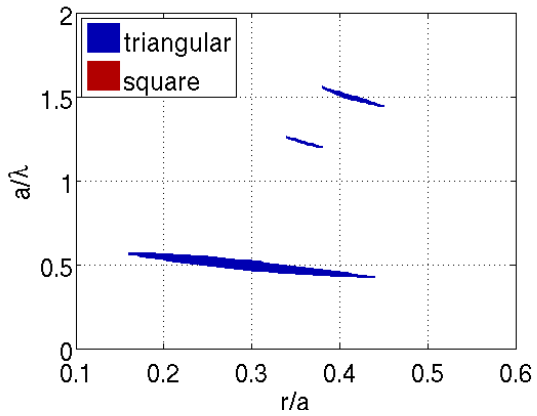

Figure 1.53: Gap map of a lattice of ABS cylinders with period a and radius r in a vacuum.

1.3.2 Antennas with 3D printable EBG structures

Two-dimensional explanation

At the lower edge of the air band, the lattice of Fig. 1.43 is nearly monomodal and the employment of metallic posts in the proper positions produces a minor improvement on the antenna gain. Previous concepts find instead useful application in a lattice with low dielectric contrast, where the band-gap is very short or even absent. For example Fig. 1.53 shows the gap map for square and triangular lattices of cylinders made of acrylonitrile butadiene styrene (ABS). The latter is a lossy plastic material, commonly used by consumer 3D printers; its electromagnetic properties at 10 GHz are approximately $\varepsilon_r = 2.8$ and $\tan\delta = 0.01$ [62]. The dispersion diagram along the border of the irriducible Brillouin zone for a square lattice of ABS cylinders is shown in Fig. 1.54. The use of typical plastic materials of 3D printers such as ABS allows the realization of cheap easy-to-manufacture efficient antenna.

The electric field of the working mode presents an almost complementary pattern in comparison to the one in Fig. 1.49. The normalized magnitude in a lattice section is depicted in Fig. 1.55, where the relevant finite-size antenna, provided with ground plane, source and metallic cylinders, is shown too. These elements have been located to match the desired pattern. A diameter of 0.5 mm has been used for the metallic posts.

A set of structures with different number of layers and cylinders in each layer has been optimized with respect to the lattice period, aiming at the maximization of the gain. The outcome of this study is depicted in Fig.

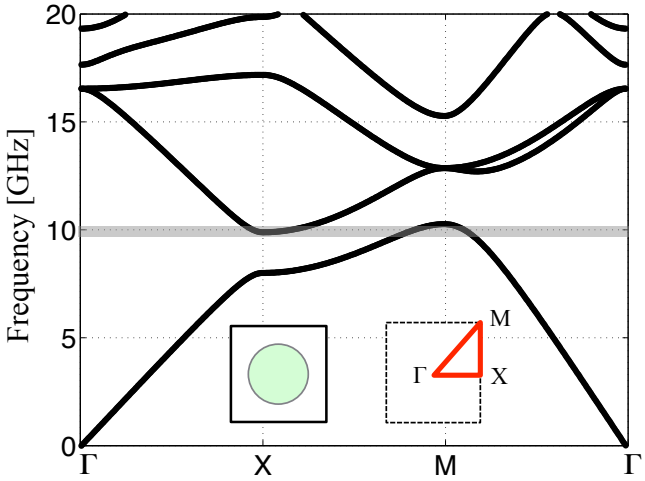

Figure 1.54: Dispersion diagram along the edge of the IBZ for a square lattice of dielectric cylinders with $\varepsilon_r = 2.8$, lattice period $a = 13$ mm and diameter $d = 0.7a$.

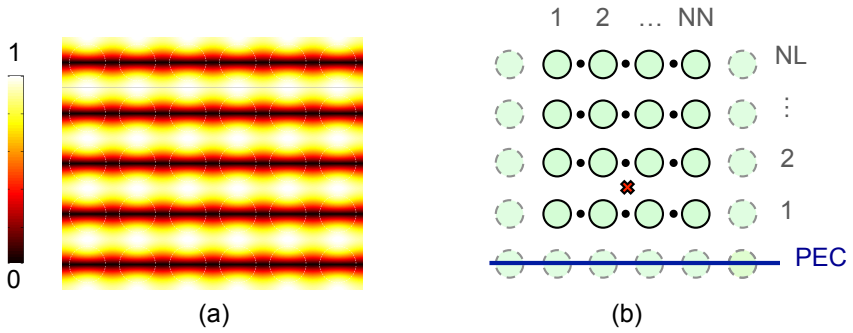

Figure 1.55: (a) Normalized magnitude of the electric field at 10 GHz in the square lattice of Fig. 1.54 when $k_y = 0$; (b) layout of the finite-size antenna.

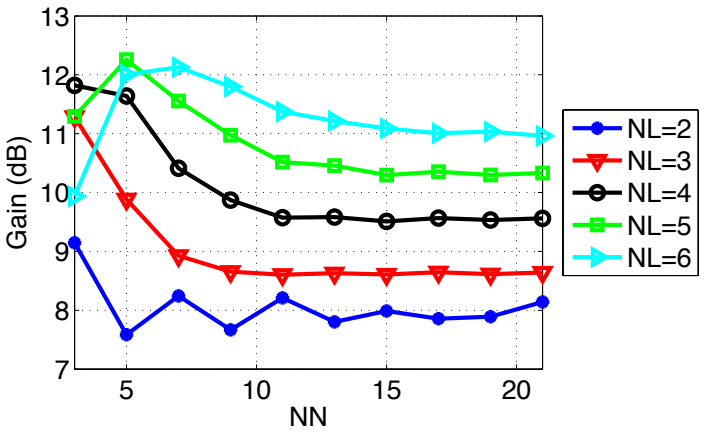

Figure 1.56: Optimized gain versus the number of dielectric cylinders per layer for geometries with 2 to 6 layers.

1.56; it must be noted that the gain of the line source is 0 dB, therefore the figures in the plot can be interpreted as the gain enhancement achieved by the periodic arrangement of cylinders. After a given layer length (NN>15), the gain approaches an asymptotic value, which increases by stacking more and more layers. At the same time the optimal lattice period approaches 13 mm, which is the value found considering an infinite lattice. As far as the geometry with 5 layers of 5 dielectric cylinders is concerned, a gain of 12.3 dB is achieved with a lattice period of 13.93 mm; aperture and antenna efficiencies are respectively 51.1% and 88.2%. It is worth noticing that, despite the very high loss tangent, the power lost due to dielectric losses is moderate.

Three-dimensional implementation

A realistic antennas based on lattice modes has been conceived following the scheme of Fig. 1.27, based on the parallel plate waveguide, fed by a coaxial cable. The geometry of the antenna is depicted in Fig. 1.57. It is a relatively compact structure made of 5×5 cylinders: the base is less than $2.3\lambda \times 2.6\lambda$ and its height is half a wavelength.

The lattice period has been optimized with respect to the antenna gain at 10 GHz, achieving an optimal value of 10.5 dB. The directivity is mostly constrained by the emission on the E-plane where, being the structure short, diffraction effects are significant: the HPBW on such plane is indeed around 102 deg. The square arrangement of cylinders instead affects the radiation pattern on the H-plane that is depicted in Fig. 1.58. In the same plot the emission of a half-wave dipole with a metallic reflector placed a quarter wavelength from it is also shown: the reflector has the same width and height of the backplane in the antenna with ABS rods.

Concerning the input impedance of the antenna with dielectric cylinders, the feeding line can be easily matched to standard coaxial cables, e.g. with an impedance transformer or a combination of shifter and stub. To appreciate the antenna behaviour independently from the particular frequency response of a matching network, the S_{11} parameter under ideal matching conditions is plotted in Fig. 1.59. The resonant frequency is tuned by adjusting the

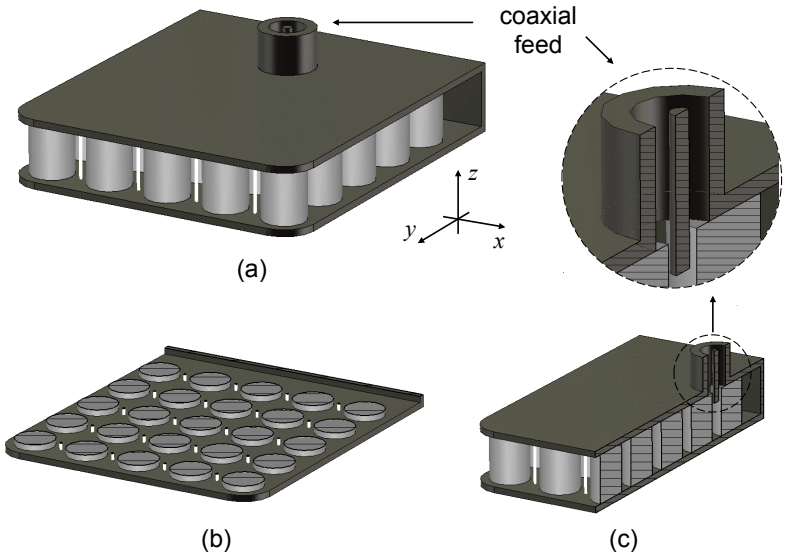

Figure 1.57: Full (a), H-plane cut (a) and E-plane (b) cut views of a three-dimensional antenna based on lattice modes. Parts in dark gray, light gray and white respectively represent the metallic box (PEC), the dielectric cylinders (ABS) and the metallic posts (PEC).

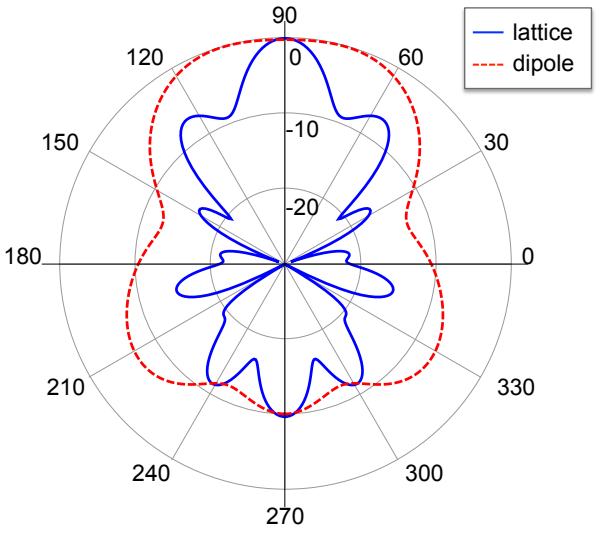

Figure 1.58: Normalized H-plane radiation pattern of the geometry in Fig. 1.57 and a dipole with a groundplane at a quarter wavelength; the latter structure is equal in size to the backplane of the EBG antenna.

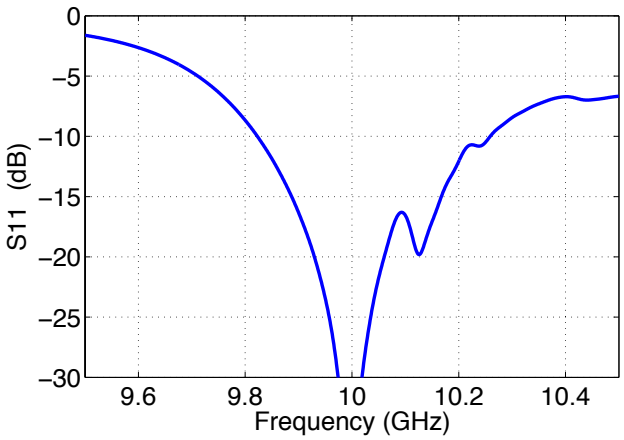

Figure 1.59: S_{11} versus frequency for the antenna of Fig. 1.57, matched at 10 GHz.

insertion of the coaxial pin in the structure and a transmission line with characteristic impedance equal to the antenna impedance $(838 + \imath 0\ \Omega)$ at 10 GHz is assumed. The bandwidth calculated at -10 dB is 4.4%.

The previous structure is aimed at providing confidence about the realistic implementation of antennas based on lattice modes. Further enhancements and developments are viable such as a reduction of backward radiation by acting on the backplane design or a directivity enhancement by increasing

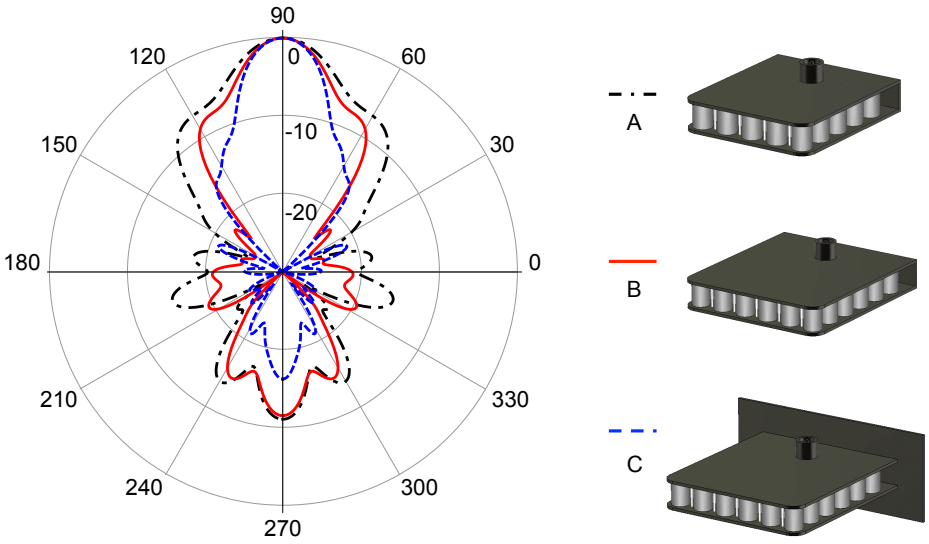

Figure 1.60: Normalized H-plane radiation pattern of three variations of the geometry in Fig. 1.57 with respectively improved SLL (A), 6×6 cylinders (B) and 6×6 rods with enlarged backplane (C).

	Gain [dB]	SLL [dB]	HPBW [deg]	Size [λ] × [λ] × [λ]
Ref.	10.5	−6.8	19.4	2.3 × 2.6 × 0.5
A	9.8	−11.1	25	2.2 × 2.5 × 0.5
B	10.9	−11.6	21	2.7 × 3.0 × 0.5
C	12.7	−16.3	18.7	3.7 × 3.0 × 1.5

Table 1.5: Performances of three variations

the number of cylinders or performing multi-dimensional optimization (e.g. on rod radius and spacing in the two directions). We present three possible variations of the previous structure to convey an idea of the flexibility in tailoring the radiation diagram through small changes in the geometrical configuration. The emission of these variations on the H-plane are reported in Fig. 1.60 and identified as cases A, B and C. The first one originates from relaxing the performance in terms of directivity to improve the SLL; the second one is an optimized structure with 6×6 rods; the last case has 6×6 cylinders and a backplane with enlarged dimensions of $\lambda/2$ along each direction. The main radiation parameters are summarized in Table 1.5, where the reference geometry of Fig. 1.57 is also reported; the values of SLL and HPBW are taken on the H-plane.

1.3.3 Dual-feed antenna exploiting degenerate modes

Two-dimensional explanation

The excitation of crystal modes in two-dimensional lattices fed by a current wire follows similar rules to the (1.10) explained in section 1.1.2. Nevertheless, due to the lattice symmetry, several modes can be excited by a monochromatic source, whose location plays a fundamental role in discriminating between modes. In the following, dielectric cylinders with circular cross-section, $\varepsilon_r = 11.4$ and filling ratio $r/a = 0.35$ are analysed considering TM polarization. The radiating structures are computed by means of the cylindrical wave approach of section 1.1.3.

The band diagram of a square lattice along the edge of the irreducible Brillouin zone is depicted in Fig. 1.61. The crystal modes at the lower edge of the air band, i.e. approximately at 8.4 GHz, can be employed to achieve directive antennas because only a few spatial harmonics are allowed in this frequency region. The lattice behaves like a filter in the wavenumber spectrum as explained in Fig. 1.44; the corresponding plots for the present lattice are depicted in Fig. 1.62. Two approaches can be followed to suppress the modes that propagate along the x-axis, without employing reflectors such as other EBG structures or perfect electric conductors. The one consists in breaking the square symmetry of the lattice as done in Fig. 1.45: the effect is a variation in the eigenvalues of the crystal modes. The other approach consists instead in acting on the eigenfunctions of the modes and their excitation.

At the lower edge of the air band of a square lattice, two degenerate

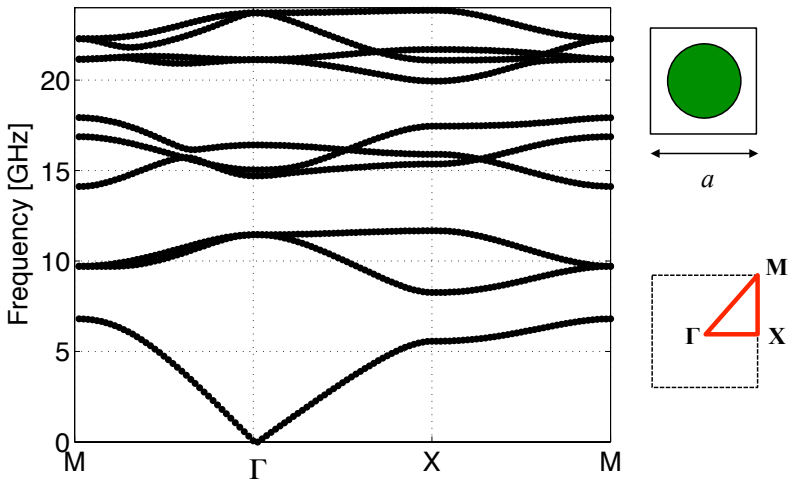

Figure 1.61: Band diagram along the edge of the IBZ for a square lattice of dielectric cylinders with $\varepsilon_r = 11.4$ and lattice period $a = 10$ mm.

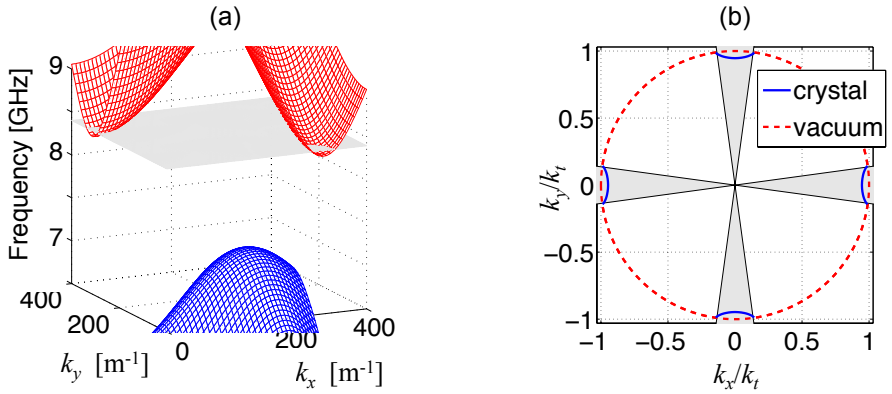

Figure 1.62: (a) Three-dimensional band diagram of the square lattice of Fig. 1.61 and constant plane at 8.4 GHz. (b) Constant-frequency dispersion diagram in the same lattice and in a vacuum; shaded regions represent allowed propagation directions inside the crystal.

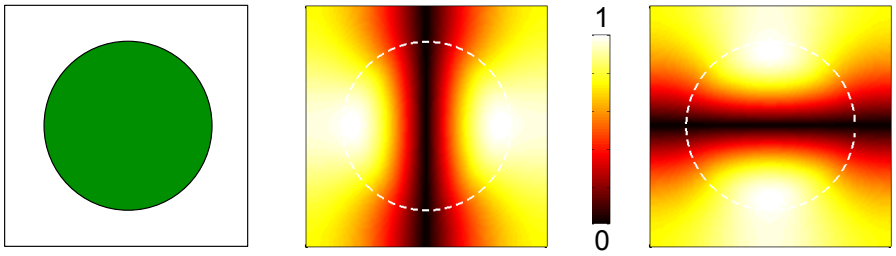

Figure 1.63: Primitive cell and normalized patterns of the two degenerate modes at the lower edge of the air band for the lattice of Fig. 1.61: they have identical eigenfunctions rotated by 90 deg.

modes are allowed; they are standing waves whose patterns in the primitive cell are depicted in Fig. 1.63. By moving a line source across the nodal and anti-nodal lines of the eigenmodes, their excitation can be controlled with some flexibility. In particular some locations of the source maximize the excitation of either both modes or a single one. These situations are analysed here by considering a finite-size periodic structure, with the same properties of the previous lattice, and an 8.4 GHz current wire with infinite length and negligible radius. Such a source uniformly excites the spatial spectrum in the H-plane, which is filtered by the square arrangement of cylinders; albeit finite, the latter is indeed large enough to resemble a lattice and support its modes. When the source is located at the corner of the primitive cell, like in Fig. 1.64a, both modes are equally excited and the radiation pattern on the H-plane presents four main lobes aligned with the coordinate axes. The far-field radiation along one of the coordinate axes

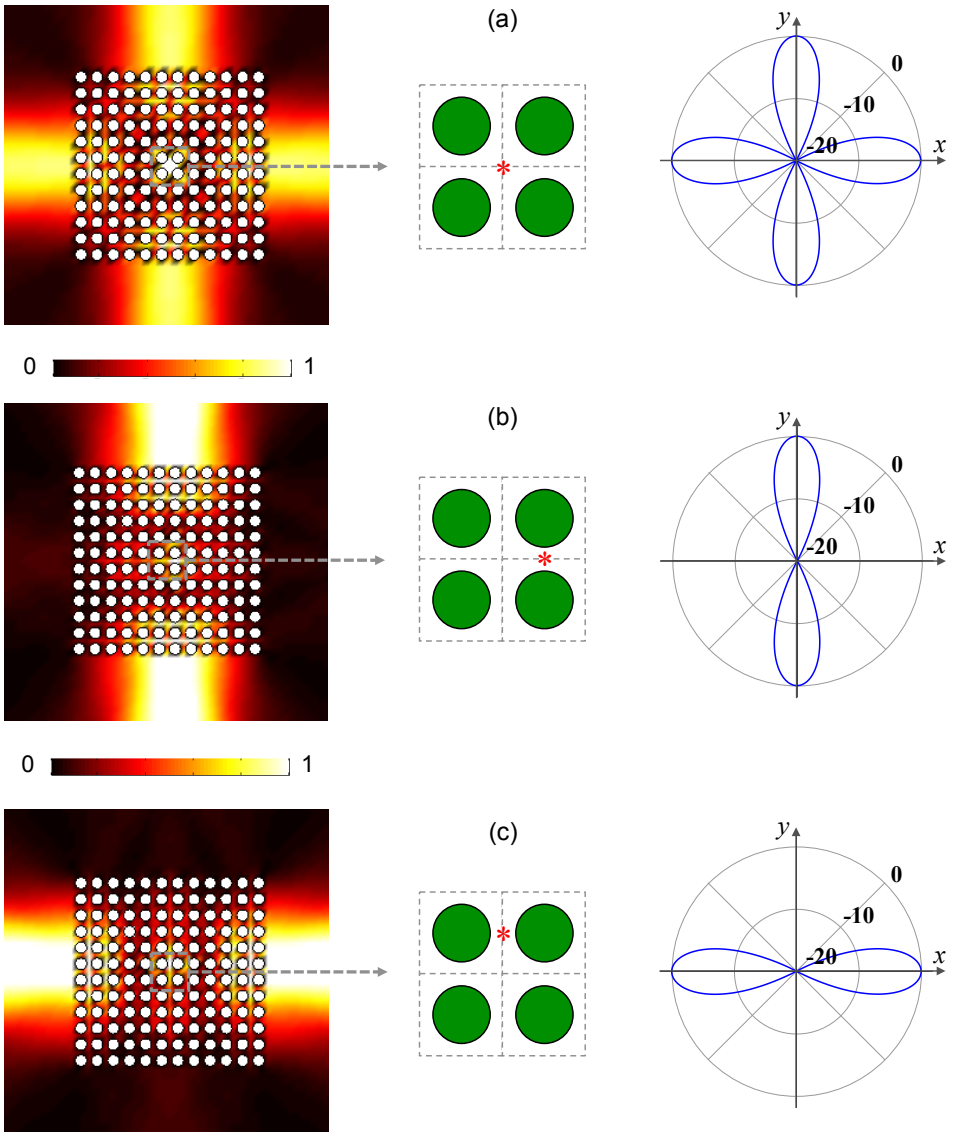

Figure 1.64: Electric field amplitudes, normalized to the same value, and H-plane radiation patterns in dB scale for three different situations. All cases are based on a square arrangements of 12×12 dielectric cylinders in a vacuum fed by an 8.4 GHz current wire and differ in the position of the source, which is indicated in the middle figures with an asterisk.

disappears when the source is located along the nodal line of the mode that generates those lobes (Fig. 1.64b and Fig. 1.64c); a 3 dB improvement in the directivity occurs.

Three-dimensional implementations

A three-dimensional implementation of the previous concepts can be conceived by means of electric dipoles, dielectric rods ($\varepsilon_r = 11.4$, $\tan\delta = 2 \times 10^{-4}$) and a finite ground plane. A typical value of high-quality ceramic materials has been chosen for the loss tangent. The structure depicted in Fig. 1.65 is considered: it consists of 49 cylinders arranged in a tilted square lattice with period $a = 10$ mm. The finite dimensions entail different boundary conditions and cause a detuning of the assembly, which exhibits the best performance at 8 GHz. The height of the cylinders and the ground plane is set to 6λ, being a high enough value to emulate a two-dimensional configuration; the dipoles are centred at their mid-height.

The H-plane radiation pattern of the finite-size geometry at 8 GHz is given in Fig. 1.66, together with the overlay of the electric field at the mid-plane, when the two dipoles are excited in turn. In comparison to the same geometry in absence of cylinders, the EBG structure shapes the radiation patterns of the two primary sources into two distinct main lobes pointing at about ± 40 deg with respect to the y-axis. The side lobe level and half-power beam width on the H-plane are around -20 dB and 32 deg, respectively, whereas the total gain is 11.6 dB.

Regarding the electrical properties of the geometry with finite height, the coupling between the dipoles could appear a major concern since the sources are less than a wavelength apart. Contrariwise the S_{21} is about -20 dB at 8 GHz and never exceeds -15 dB within the bandwidth of interest, as shown in Fig. 1.67. Dipoles are designed to be resonant at 8 GHz but their input impedance Z_{in} exhibits a high real part at the operational frequency (see again Fig. 1.67). Here a transmission line with characteristic impedance matched to the real part of Z_{in} has been used to assess the coupling in the

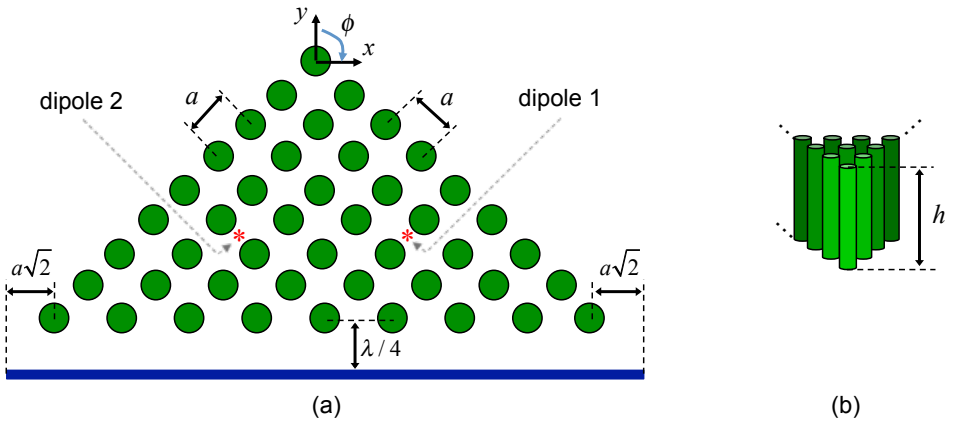

Figure 1.65: Top (a) and front (b) views of the 3D demonstrative structure.

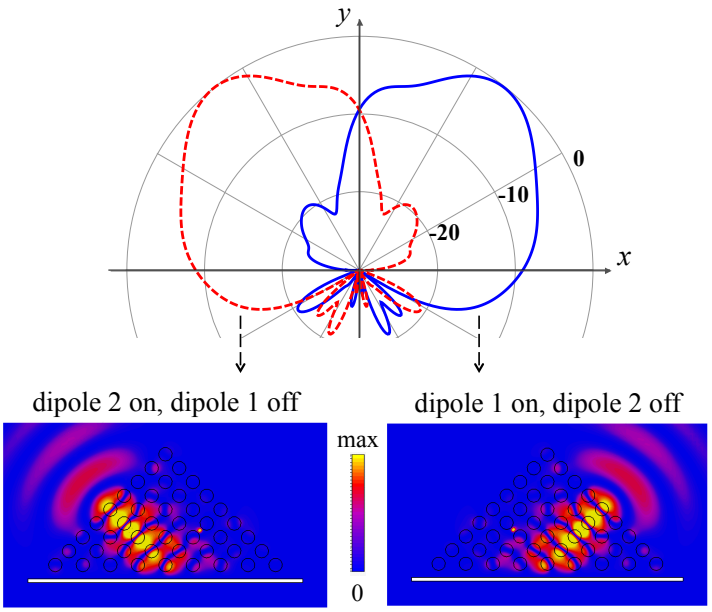

Figure 1.66: H-plane radiation pattern (top) and absolute value of the electric field in log scale (bottom) when either dipole 1 or 2 is radiating.

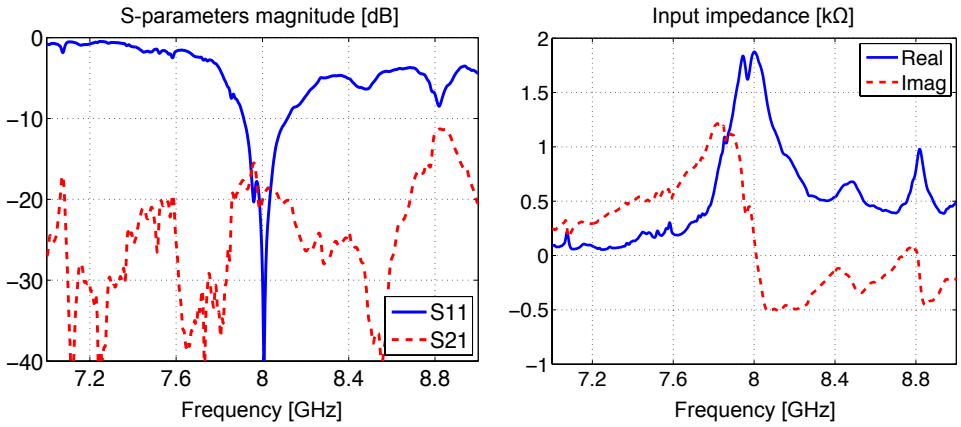

Figure 1.67: Reflection and coupling between dipoles in the case of a feeding line matched at 8 GHz and input impedance of the dipoles.

worst conditions. This choice gives the reflection coefficient given in Fig. 1.67 with a bandwidth at −15 dB of about 110 MHz; the real bandwidth in the case of a standard transmission line with a quarter-wavelength transformer would be lower. Yet, the bandwidth is also constrained by the deterioration of the radiation properties, primarily the SLL, which is plotted versus frequency in Fig. 1.68. If 10% is considered as an acceptable deterioration on the SLL, a bandwidth of about 30 MHz is obtained.

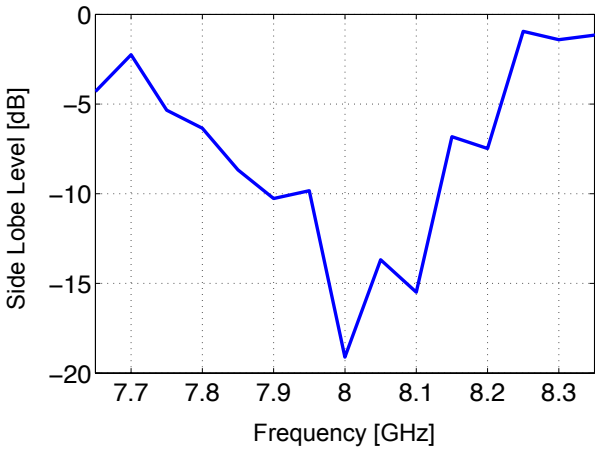

Figure 1.68: SLL versus frequency; outside the plotted range the orientation of the main lobe undergoes significant variations.

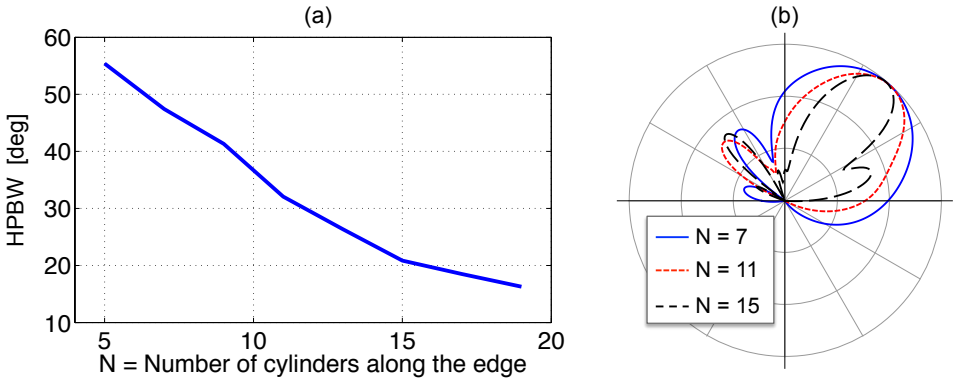

Figure 1.69: HPBW variation (a) at 8 GHz for the structure of Fig. 1.65 with infinite height when increasing the number of cylinders along the edge; H-plane radiation patterns (b) of three configurations.

The use of dielectric materials is often associated with losses. Their tan δ entails some dissipation of power by Joule effect, but the present employment of the periodic structure makes the power lost inside the cylinders small, leading to a predicted efficiency of 99.1%. As pointed out in the previous section, the nodal lines of the excited eigenmode run across the centres of the cylinders, implying low amplitude of the electric field in the dielectric material. This situation is partially verified also in the finite-size geometries, where the mode is not pure, as can be appreciated in Fig. 1.66.

Some improvements can be pursued in the previous structure. As example, the size of the ground plane has not been optimized, the HPBW can be reduced increasing the number of cylinders, some rods at the corners give

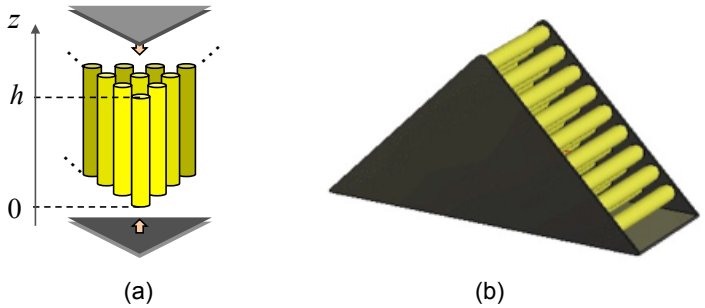

Figure 1.70: Front (a) and perspective (b) view of a structure similar to Fig. 1.65 with $h = 1.25\lambda$ at 8 GHz.

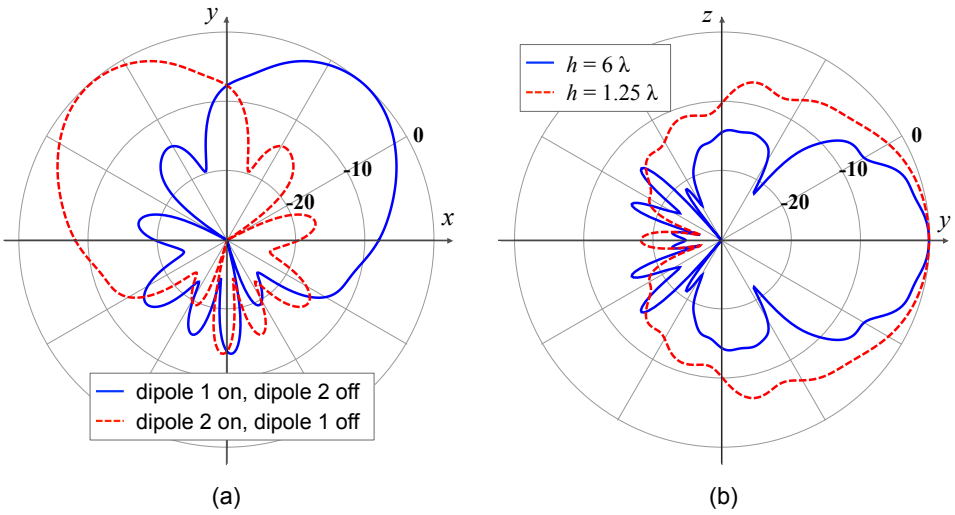

Figure 1.71: H-plane (a) and E-plane (b) radiation patterns of the structure of Fig. 1.70; the former shows the emission when dipoles are powered on separately, whereas the latter also shows the pattern of the antenna without metallic closure at the end of the rods (Fig. 1.37).

little contribution to the performance and can be removed. The HPBW is plotted in Fig. 1.69 versus the number of rods; two-dimensional structures with the same form as in Fig. 1.65 and fed by line sources have been used for this example. The SLL keeps similar values, whereas, once fixed the number of cylinders, a trade-off between HPBW and SLL can be set with some flexibility playing on the lattice period.

The demonstrative antenna presents useful features for cellular networks, e.g. to split coverage areas and increase frequency reuse, but its height is a major drawback. A compact solution is proposed in Fig. 1.70, where two PEC plane are placed on the top and bottom of the cylinder, whose height h is less than 50 mm. The transversal layout is the same as in Fig. 1.37.

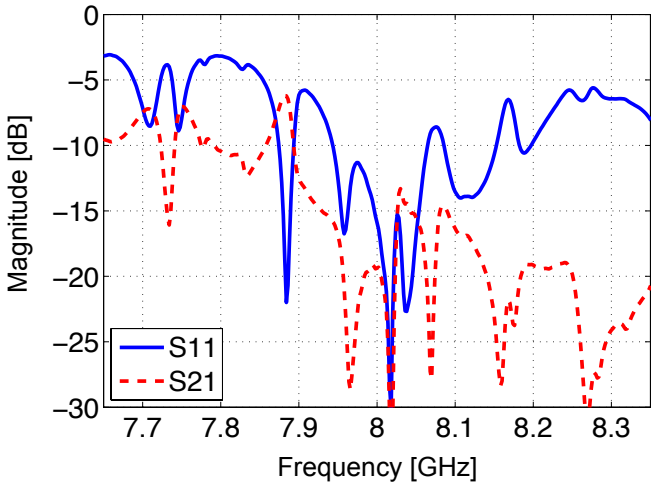

Figure 1.72: Reflection and coupling between dipoles in the case of 50Ω feeding line for the structure of Fig. 1.70.

Since the behaviour of this structure resembles the previous one, only the main outcomes are described here. The emission on the H-plane is shaped by the lattice similarly to Fig. 1.66: the radiation pattern is reported in Fig. 1.71a, achieving a half-power beam width of 46 deg and a side lobe level of -14 dB. The radiation is instead less directive in the vertical plane where the shorter height implies a larger lobe. The E-plane patterns of both configurations are overlapped in Fig. 1.71b. The total antenna gain is 9.14 dB for the single radiating dipole and the efficiency is 98.3%. The conductive enclosure realizes a sort of resonator, increasing the electric field inside the structure. This phenomenon causes a lower bandwidth and explains the slightly higher losses. Adopting the previous criterion, the SLL performance are kept within the acceptable threshold for about 25 MHz.

The input impedance of the dipoles, which are designed to resonate at 8 GHz, is slightly lower than 50 Ω, simplifying the matching to feeding lines with standard characteristic impedance. By assuming the direct use of 50 Ω transmission line, the same bandwidth of the previous case is achieved at −10 dB. The isolation between the two dipoles is close to −20 dB in the working bandwidth. Coupling and reflection curves are plotted in Fig. 1.72.

Previous examples have demonstrated that the position of the source plays a major role in EBG antennas based on Bloch waves. The amplitudes of the excited modes is proportional to the eigenfunction of their electric field taken at the point where the radiator is placed, allowing the isolation of sources placed less than a wavelength apart. Moreover the eigenfunctions, corresponding to the lower edge of the air band in square lattices of dielectric cylinders in a vacuum, enhances the radiation performance of the primary radiators and assures high antenna efficiency.

1.3.4 Excitation of dual-band structures

The resonator antenna is surely more inclined to realize dual-band structures: the same arrangement of cylinders and position of the source can attain band-pass behaviour also at different frequencies from the operational one. The transmission efficiency across layers of dielectric rods similar to Fig. 1.17a is plotted over a broader frequency range in Fig. 1.73 for a six-layers structure. Besides, by playing with both cavity width and multiple defects, additional transmission peaks can be easily inserted in either the same or different band-gaps and adjusted with some flexibility.

With reference to the EBG structure hosting the source, a completely different situation occurs because dual-band behaviours must be attained using additional band-gap edges, namely relying on different Bloch waves. This fact hinders a flexible tuning of the operational frequencies and makes troublesome even the simple achievement of a dual-band performance. A square lattice with useful properties in this sense has been designed by increasing the filling factor in the unit cell and the dielectric constant of the rods; then lattice periods have been adjusted to set the first working frequency at 8 GHz. The relevant band diagram is shown in Fig. 1.74.

Two major difficulties can impair the performance at the higher working frequency: firstly the pattern of relevant crystal mode may not shape effectively the radiation pattern of the line source. Secondly the field of this higher-order mode may be largely localized just inside the rods, leading to an efficiency reduction. Both issues apply to the case taken as example. The mode pattern shown on the upper left of Fig. 1.74 indeed presents two high field spots inside the cylinder. By placing the line source in one of these two points, the mode is well excited. The radiation pattern for a finite-size structure has been calculated without the ground plane using the cylindrical wave approach. Results are reported in Fig. 1.75 together with the overlay

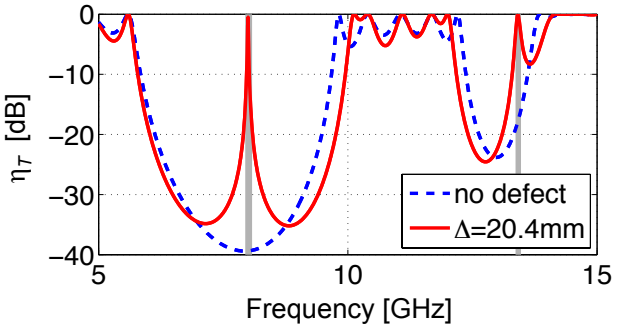

Figure 1.73: Transmission efficiency versus frequency of a square arrangement of dielectric rods in a vacuum similar to Fig. 1.17a, but with six layers, Px = Py = 14 mm, $d = 5.5$ mm and $\varepsilon_r = 9$.

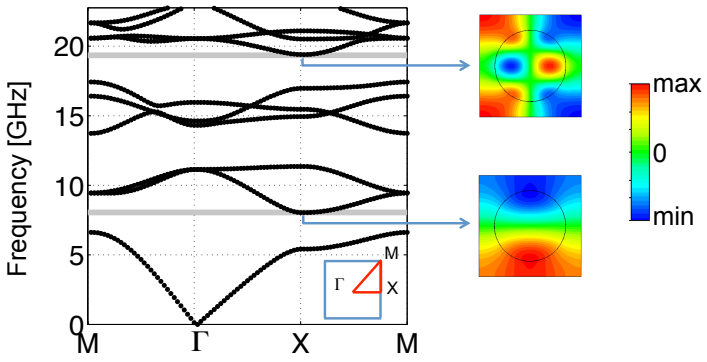

Figure 1.74: Two-dimensional band diagram along the irreducible Brillouin zone of a square lattice of dielectric rods in a vacuum, having Px = Py = 10.3 mm, d = 7.2 mm and ε_r = 11.4. E-field patterns of the modes at the shaded band-gap edges are shown aside.

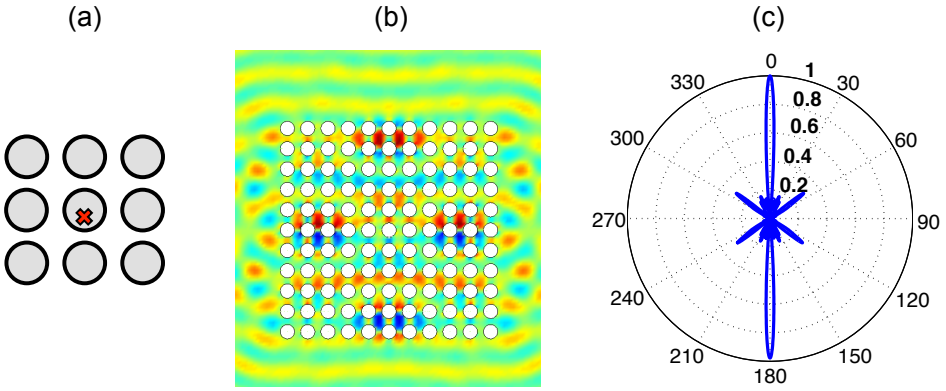

Figure 1.75: Behaviour at the edge of the second band-gap of Fig. 1.74 for a finite-size geometry of 11×11 rods without ground plane: (a) source location (X-point); (b) real part of the electric field; (c) normalized linear H-plane radiation pattern.

of the electric field, where a planar wavefront can be recognized at both the top and the bottom of the picture. This antenna achieves a two-dimensional directivity of 10 dB with a HPBW of 6 deg.

Chapter 2

Coupled-Mode Theory for Circular Waveguide

The coupled-mode equations are initially derived for a cylindrical metal Bragg reflector. Starting from Maxwell equations, the theory of non-uniform waveguides by Solymar is demonstrated and the Bragg condition is applied. The final formulation and the expression of the coupling coefficients are compared to the formulas provided by Bratman et al. and benchmarked with results from literature as well as from other numerical methods. The theory is further developed to perform a rigorous calculation of the Q-factor in resonators made of Bragg mirrors as well as to analyse and design mode converters.

2.1 Generalized Telegraphist's Equations

We derive the generalized telegraphist's equations for waveguides with varying cross-section, giving full details of a demonstration sketched by G. Reiter in 1959 [63]. We begin with the Maxwell's curl equations in a linear, isotropic, homogeneous, time-invariant, sourceless material with permittivity ε and permeability μ, assuming a time dependence $\mathrm{e}^{\iota\omega t}$:

$$\nabla \times \mathbf{E} = -\iota\omega\mu\mathbf{H} \tag{2.1}$$

$$\nabla \times \mathbf{H} = \iota\omega\varepsilon\mathbf{E} \tag{2.2}$$

The waveguide is assumed to have a varying cross-section along the z-axis and the fields can be written in terms of transversal and longitudinal components introducing the following positions:

$$\mathbf{E} = \mathbf{E_t} + \hat{\mathbf{z}}E_z$$
$$\mathbf{H} = \mathbf{H_t} + \hat{\mathbf{z}}H_z$$
$$\nabla = \nabla_t + \hat{\mathbf{z}}\frac{\partial}{\partial z}$$

The (2.1) becomes

$$\left(\nabla_t + \hat{\mathbf{z}}\frac{\partial}{\partial z}\right) \times (\mathbf{E_t} + \hat{\mathbf{z}}E_z) = -\iota\omega\mu\left(\mathbf{H_t} + \hat{\mathbf{z}}H_z\right)$$
$$\nabla_t \times \mathbf{E_t} + \nabla_t \times (\hat{\mathbf{z}}E_z) + \hat{\mathbf{z}} \times \frac{\partial \mathbf{E_t}}{\partial z} + \hat{\mathbf{z}} \times \hat{\mathbf{z}}\frac{\partial E_z}{\partial z} = -\iota\omega\mu\mathbf{H_t} - \iota\omega\mu H_z\hat{\mathbf{z}}$$
$$\nabla_t \times \mathbf{E_t} - \hat{\mathbf{z}} \times \nabla_t E_z + \hat{\mathbf{z}} \times \frac{\partial \mathbf{E_t}}{\partial z} = -\iota\omega\mu\mathbf{H_t} - \iota\omega\mu H_z\hat{\mathbf{z}}$$

since $\hat{\mathbf{z}} \times \hat{\mathbf{z}} = 0$ and $\nabla_t \times (\hat{\mathbf{z}}E_z) = \nabla_t E_z \times \hat{\mathbf{z}} + E_z\nabla_t \times \hat{\mathbf{z}} = -\hat{\mathbf{z}} \times \nabla_t E_z$. By collecting terms that are parallel or perpendicular to z, two equations are obtained:

$$\nabla_t \times \mathbf{E_t} = -\iota\omega\mu H_z\hat{\mathbf{z}} \tag{2.3}$$

$$-\hat{\mathbf{z}} \times \nabla_t E_z + \hat{\mathbf{z}} \times \frac{\partial \mathbf{E_t}}{\partial z} = -\iota\omega\mu\mathbf{H_t} \tag{2.4}$$

The (2.3) can be rearranged taking the scalar product with $\hat{\mathbf{z}}$

$$\hat{\mathbf{z}} \cdot \nabla_t \times \mathbf{E_t} = -\iota\omega\mu H_z$$

and using the rule of scalar triple product $\hat{\mathbf{z}} \cdot (\nabla_t \times \mathbf{E_t}) = \nabla_t \cdot (\mathbf{E_t} \times \hat{\mathbf{z}})$:

$$\nabla_t H_z = \frac{1}{\iota\omega\mu}\nabla_t\nabla_t \cdot (\hat{\mathbf{z}} \times \mathbf{E_t})$$

The (2.4) can be rearranged taking the vector product with $-\hat{\mathbf{z}}$ as

$$\frac{\partial \mathbf{E_t}}{\partial z} = \nabla_t E_z - \iota\omega\mu\mathbf{H_t} \times \hat{\mathbf{z}}$$

Similar equations can be derived from (2.2) by duality, i.e. changing $\mathbf{E}$ with $\mathbf{H}$, $\mathbf{H}$ with $-\mathbf{E}$ and μ with ε, leading to the following system of differential equations relating transversal and longitudinal field components:

$$\frac{\partial \mathbf{E_t}}{\partial z} = \nabla_t E_z - \iota\omega\mu(\mathbf{H_t} \times \hat{\mathbf{z}}) \tag{2.5}$$

$$\frac{\partial \mathbf{H_t}}{\partial z} = \nabla_t H_z - \iota\omega\varepsilon(\hat{\mathbf{z}} \times \mathbf{E_t}) \tag{2.6}$$

$$E_z = \frac{1}{\iota\omega\varepsilon}\nabla_t \cdot (\mathbf{H_t} \times \hat{\mathbf{z}}) \tag{2.7}$$

$$H_z = \frac{1}{\iota\omega\mu}\nabla_t \cdot (\hat{\mathbf{z}} \times \mathbf{E_t}) \tag{2.8}$$

Under the assumption of slow cross-sectional changes, the field can be expressed with an infinite set of TE and TM modes that locally match the modes of an equivalent uniform waveguide. Modal expansions are as follows

$$\begin{aligned} \mathbf{E_t} &= \sum_p V_p(z)\mathbf{e_t}_p(\xi_1, \xi_2, z) \\ \mathbf{H_t} &= \sum_p I_p(z)\mathbf{h_t}_p(\xi_1, \xi_2, z) \\ E_z &= \sum_p v_p(z)e_{zp}(\xi_1, \xi_2, z) \\ H_z &= \sum_p i_p(z)h_{zp}(\xi_1, \xi_2, z) \end{aligned} \tag{2.9}$$

where ξ_1 and ξ_2 are the curvilinear transversal coordinates and V_p, I_p, v_p and i_p are the amplitudes of the field components.

The eigenfunctions have a weak dependence on the longitudinal coordinate; the following definitions are adopted throughout this chapter:

	TE modes	TM modes
$\mathbf{e_t}_p =$	$\nabla_t \Phi_p^{\mathrm{TE}} \times \hat{\mathbf{z}}$	$\nabla_t \Phi_p^{\mathrm{TM}}$
$e_{zp} =$	0	$\dfrac{k_{tp}^2}{\gamma_p}\Phi_p^{\mathrm{TM}}$
$\mathbf{h_t}_p =$	$\nabla_t \Phi_p^{\mathrm{TE}}$	$\hat{\mathbf{z}} \times \nabla_t \Phi_p^{\mathrm{TM}}$
$h_{zp} =$	$\dfrac{k_{tp}^2}{\gamma_p}\Phi_p^{\mathrm{TE}}$	0

(2.10)

The functions Φ_p^{TE} and Φ_p^{TM} are the scalar potential for TE and TM modes given by the following homogeneous, scalar, linear, differential equation of the second order

$$\nabla_t^2 \Phi = k_t^2 \Phi$$

with boundary conditions

$$\frac{\partial \Phi^{\mathrm{TE}}}{\partial n} = 0 \qquad \text{and} \qquad \Phi^{\mathrm{TM}} = 0 \qquad \text{on } \partial S \tag{2.11}$$

being n the coordinate normal to the cross-section contour. The quantities k_{tp} and γ_p are the eigenvalue of the corresponding eigenfunction and the propagation constant. They are related to the free-space wavenumber defined as $k_0 = -\omega^2 \mu\varepsilon$ according to the following formula:

$$k_0^2 = k_{t_p}^2 + \gamma_p^2 \tag{2.12}$$

so that $k_{t_p}^2$ is a real negative quantity and γ_p is real for evanescent modes. The eigenfunctions are normalized so that their orthogonality relation is unitary:

$$\iint_S \nabla_t \Phi_p \cdot \nabla_t \Phi_q dS = \iint_S \mathbf{e}_{\mathbf{t}p} \cdot \mathbf{e}_{\mathbf{t}q} dS = \iint_S \mathbf{h}_{\mathbf{t}p} \cdot \mathbf{h}_{\mathbf{t}q} dS = \delta_{pq} \tag{2.13}$$

where δ_{pq} ($= 1$ for $p = q$, 0 for $p \neq q$) is the Kronecker delta. This position sets up an equivalence between modes and transmission lines. The field amplitudes can be written

$$\begin{cases} V_p(z) = \sqrt{Z_p}\left[A_p^+(z) + A_p^-(z)\right] \\ I_p(z) = \sqrt{Y_p}\left[A_p^+(z) - A_p^-(z)\right] \end{cases} \tag{2.14}$$

where Z_p and Y_p are respectively the wave impedance and the wave admittance of the mode, given by

$$Z_p = \frac{1}{Y_p} = \begin{cases} \dfrac{\iota\omega\mu}{\gamma_p} & \text{for TE modes} \\ \dfrac{\gamma_p}{\iota\omega\varepsilon} & \text{for TM modes} \end{cases} \tag{2.15}$$

Owing to the orthogonality relation (2.13) the power carried by the mode is

$$P_p = \frac{1}{2} V_p I_p^* = \frac{1}{2}(|A_p^+|^2 - |A_p^-|^2)$$

so A_p^+ and A_p^- represent the amplitudes of forward and backward waves, respectively. Some useful formulas relating field components are

TE modes	TM modes	
$\mathbf{h}_{\mathbf{t}p} = \dfrac{\gamma_p}{k_{t_p}^2} \nabla_t h_{zp}$	$\mathbf{e}_{\mathbf{t}p} = \dfrac{\gamma_p}{k_{t_p}^2} \nabla_t e_{zp}$	(2.16)
$\nabla_t \cdot \mathbf{h}_{\mathbf{t}p} = \gamma_p h_{zp}$	$\nabla_t \cdot \mathbf{e}_{\mathbf{t}p} = \gamma_p e_{zp}$	(2.17)
$\nabla_t \nabla_t \cdot \mathbf{h}_{\mathbf{t}p} = k_{t_p}^2 \mathbf{h}_{\mathbf{t}p}$	$\nabla_t \nabla_t \cdot \mathbf{e}_{\mathbf{t}p} = k_{t_p}^2 \mathbf{e}_{\mathbf{t}p}$	(2.18)

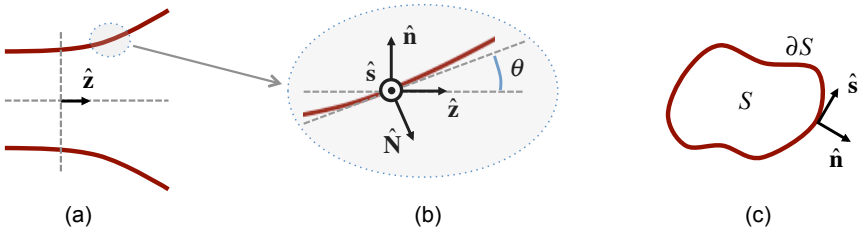

Figure 2.1: Waveguide with varying cross-section: general view (a), enlargement (b) and cross-sectional view (c).

and for both types of modes

$$\mathbf{e}_{\mathbf{t}p} = \mathbf{h}_{\mathbf{t}p} \times \hat{\mathbf{z}} \qquad \text{and} \qquad \mathbf{h}_{\mathbf{t}p} = \hat{\mathbf{z}} \times \mathbf{e}_{\mathbf{t}p} \tag{2.19}$$

At any z, the eigenfunctions correspond to the modes of a waveguide with a constant cross-section identical to the local contour of the waveguide with varying cross-section. This explains why boundary conditions (2.11) implies

$$\frac{\partial h_z}{\partial n} = 0 \quad \text{on } \partial S \qquad \text{for TE modes} \tag{2.20}$$

$$e_z = 0 \quad \text{on } \partial S \qquad \text{for TM modes} \tag{2.21}$$

Nevertheless the total field has to satisfy the boundary conditions dictated by the actual, perturbed cross-section, which is sketched in Fig. 2.1. This implies that

$$\mathbf{E} \times \hat{\mathbf{N}} = 0 \quad \text{on } \partial S \tag{2.22}$$

$$\mathbf{H} \cdot \hat{\mathbf{N}} = 0 \quad \text{on } \partial S \tag{2.23}$$

with

$$\hat{\mathbf{N}} = -\hat{\mathbf{n}} \cos\theta + \hat{\mathbf{z}} \sin\theta$$

The (2.22) gives

$$\begin{aligned} \mathbf{E} \times \hat{\mathbf{N}} &= (E_n \hat{\mathbf{n}} + E_s \hat{\mathbf{s}} + E_z \hat{\mathbf{z}}) \times (-\hat{\mathbf{n}} \cos\theta + \hat{\mathbf{z}} \sin\theta) = \\ &= -\hat{\mathbf{s}}(E_n \sin\theta + E_z \cos\theta) + \hat{\mathbf{z}} E_s \cos\theta \end{aligned}$$

which leads to

$$\mathbf{E}_{\mathbf{t}} \cdot \hat{\mathbf{s}} = 0 \quad \text{on } \partial S \tag{2.24}$$

$$\mathbf{E}_{\mathbf{t}} \cdot \hat{\mathbf{n}} \tan\theta + E_z = 0 \quad \text{on } \partial S \tag{2.25}$$

The (2.23) gives instead

$$\begin{aligned} \mathbf{E} \cdot \hat{\mathbf{N}} &= (H_n \hat{\mathbf{n}} + H_s \hat{\mathbf{s}} + H_z \hat{\mathbf{z}}) \cdot (-\hat{\mathbf{n}} \cos\theta + \hat{\mathbf{z}} \sin\theta) = \\ &= -H_n \cos\theta + H_z \sin\theta \end{aligned}$$

which leads to

$$\mathbf{H_t} \cdot \hat{\mathbf{n}} - H_z \tan\theta = 0 \quad \text{on } \partial S \tag{2.26}$$

The quantity $\tan\theta$ represents the local slope of the varying cross-section $a(z)$, namely

$$\frac{da}{dz} = \tan\theta \tag{2.27}$$

As pointed out in [64], the different boundary conditions between field and mode components can coexist owing to the different convergence rate of the series in (2.9).

Some formulas that are useful for next demonstrations and worth reporting here are the two-dimensional Green theorem and the integration of varying surfaces. The former states that, given a scalar function f and a vector field $\mathbf{F}$ defined and continuously differentiable on a surface S,

$$\iint_S (\nabla_t f \cdot \mathbf{F} + f \nabla_t \cdot \mathbf{F}) dS = \oint_{\partial S} f \mathbf{F} \cdot \hat{\mathbf{n}} ds \tag{2.28}$$

The latter states that, given a scalar function f and a varying surface S,

$$\frac{d}{dz}\left[\iint_S f dS\right] = \iint_S \frac{df}{dz} dS + \oint_{\partial S} f \tan\theta ds \tag{2.29}$$

being $\tan\theta$ the change rate of the varying surface, i.e. da/dz.

At this point, the (2.5) and (2.6) can be easily projected on the modes to derive the generalized telegraphist's equations as well as the expressions for the ratios of the transformers coupling the equivalent transmission lines. The procedure consists in scalar multiplying (2.5) and (2.6) by the transversal component of a given modes and integrating over the waveguide cross-section.

2.1.1 Projection on TM modes

We scalar multiply the (2.5) by the transversal electric component of the i-th TM mode and integrate over the cross-section:

$$\iint_S \frac{\partial \mathbf{E_t}}{\partial z} \cdot \mathbf{e_{t}}_i dS = \iint_S \nabla_t E_z \cdot \mathbf{e_{t}}_i dS - \iota\omega\mu \iint_S \mathbf{H_t} \times \hat{\mathbf{z}} \cdot \mathbf{e_{t}}_i dS \tag{2.30}$$

The first integral of (2.30) can be simplified using (2.29), (2.24), (2.25) and (2.13):

$$\begin{aligned}
&\iint_S \frac{\partial \mathbf{E_t}}{\partial z} \cdot \mathbf{e_{t}}_i dS = \\
&= \frac{d}{dz}\left(\iint_S \mathbf{E_t} \cdot \mathbf{e_{t}}_i dS\right) - \iint_S \mathbf{E_t} \cdot \frac{\partial \mathbf{e_{t}}_i}{\partial z} dS - \oint_{\partial S} \mathbf{E_t} \cdot \mathbf{e_{t}}_i \tan\theta ds = \\
&= \frac{d}{dz}\left(\sum_p V_p \iint_S \mathbf{e_{t}}_p \cdot \mathbf{e_{t}}_i dS\right) - \sum_p V_p \iint_S \mathbf{e_{t}}_p \cdot \frac{\partial \mathbf{e_{t}}_i}{\partial z} dS + \\
&\quad - \oint_{\partial S} E_n \tan\theta e_{ni} ds = \\
&= \frac{dV_i}{dz} - \sum_p V_p T_{pi} + \oint_{\partial S} E_z e_{ni} ds
\end{aligned}$$

with

$$T_{pi} = \iint_S \mathbf{e_{t}}_p \cdot \frac{\partial \mathbf{e_{t}}_i}{\partial z} dS \tag{2.31}$$

The second integral of (2.30) can be simplified using (2.28), (2.21), (2.16), (2.18), (2.19), (2.13) and (2.7) as follows

$$\begin{aligned}
\iint_S \nabla_t E_z \cdot \mathbf{e_{t}}_i dS &= \oint_{\partial S} E_z \mathbf{e_{t}}_i \cdot \hat{\mathbf{n}} ds - \iint_S E_z \nabla_t \cdot \mathbf{e_{t}}_i dS = \\
&= \oint_{\partial S} E_z e_{ni} ds - \frac{1}{\iota\omega\varepsilon} \iint_S \nabla_t \cdot (\mathbf{H_t} \times \hat{\mathbf{z}}) \nabla_t \cdot \mathbf{e_{t}}_i dS = \\
&= \oint_{\partial S} E_z e_{ni} ds - \frac{1}{\iota\omega\varepsilon} \oint_{\partial S} \nabla_t \cdot \mathbf{e_{t}}_i (\mathbf{H_t} \times \hat{\mathbf{z}}) \cdot \hat{\mathbf{n}} ds + \\
&\qquad + \frac{1}{\iota\omega\varepsilon} \iint_S (\mathbf{H_t} \times \hat{\mathbf{z}}) \cdot \nabla_t \nabla_t \cdot \mathbf{e_{t}}_i dS = \\
&= \oint_{\partial S} E_z e_{ni} ds - \frac{\gamma_p}{\iota\omega\varepsilon} \cancel{\oint_{\partial S} e_{zi} (\mathbf{H_t} \times \hat{\mathbf{z}}) \cdot \hat{\mathbf{n}} ds} + \\
&\qquad + \frac{k_{ti}^2}{\iota\omega\varepsilon} \sum_p I_p \iint_S (\mathbf{h_{t}}_p \times \hat{\mathbf{z}}) \cdot \mathbf{e_{t}}_i dS = \\
&= \oint_{\partial S} E_z e_{ni} ds + \frac{k_{ti}^2}{\iota\omega\varepsilon} I_i
\end{aligned}$$

The last integral of (2.30) can be simplified using (2.19) and (2.13):

$$-\iota\omega\mu \iint_S \mathbf{H_t} \times \hat{\mathbf{z}} \cdot \mathbf{e_{t}}_i dS = -\iota\omega\mu \sum_p I_p \iint_S \mathbf{h_{t}}_p \times \hat{\mathbf{z}} \cdot \mathbf{e_{t}}_i dS = -\iota\omega\mu I_i$$

By combining all terms, the (2.30) becomes

$$\frac{dV_i}{dz} - \sum_p V_p T_{pi} + \cancel{\oint_{\partial S} E_z e_{ni} ds} = \cancel{\oint_{\partial S} E_z e_{ni} ds} + \frac{k_{ti}^2}{\iota\omega\varepsilon} I_i - \iota\omega\mu I_i$$

which, considering that

$$\frac{k_{ti}^2}{\iota\omega\varepsilon} - \iota\omega\mu = \frac{k_{ti}^2 + \omega^2\mu\varepsilon}{\iota\omega\varepsilon} = \frac{k_{ti}^2 - k_0^2}{\iota\omega\varepsilon} = -\frac{\gamma_i^2}{\iota\omega\varepsilon} = -\gamma_i Z_i$$

yields

$$\frac{dV_i}{dz} = -\gamma_i Z_i I_i + \sum_p T_{pi} V_p \tag{2.32}$$

A similar procedure is followed for the (2.5), but the scalar product with the transversal magnetic component of the i-th TM mode is taken:

$$\iint_S \frac{\partial \mathbf{H_t}}{\partial z} \cdot \mathbf{h_{t}}_i dS = \iint_S \nabla_t H_z \cdot \mathbf{h_{t}}_i dS - \iota\omega\varepsilon \iint_S \hat{\mathbf{z}} \times \mathbf{E_t} \cdot \mathbf{h_{t}}_i dS \tag{2.33}$$

The first term of (2.33) is simplified using (2.13), (2.19) and twice (2.29):

$$\begin{aligned}
&\iint_S \frac{\partial \mathbf{H_t}}{\partial z} \cdot \mathbf{h_{t}}_i dS = \\
&= \frac{d}{dz}\left(\iint_S \mathbf{H_t} \cdot \mathbf{h_{t}}_i dS\right) - \iint_S \mathbf{H_t} \cdot \frac{\partial \mathbf{h_{t}}_i}{\partial z} dS - \oint_{\partial S} \mathbf{H_t} \cdot \mathbf{h_{t}}_i \tan\theta ds = \\
&= \frac{dI_i}{dz} - \sum_p I_p \left(\iint_S \mathbf{h_{t}}_p \cdot \frac{\partial \mathbf{h_{t}}_i}{\partial z} dS + \oint_{\partial S} \mathbf{h_{t}}_p \cdot \mathbf{h_{t}}_i \tan\theta ds\right) = \\
&= \frac{dI_i}{dz} - \sum_p I_p \left[\frac{d}{dz}\left(\iint_S \mathbf{h_{t}}_p \cdot \mathbf{h_{t}}_i dS\right) - \iint_S \frac{\partial \mathbf{h_{t}}_p}{\partial z} \cdot \mathbf{h_{t}}_i dS\right] = \\
&= \frac{dI_i}{dz} - \sum_p I_p \left[\cancel{\frac{d\delta_{pi}}{dz}} - \iint_S \left(\frac{\partial \mathbf{e_{t}}_p}{\partial z} \times \hat{\mathbf{z}}\right) \cdot \left(\mathbf{e_{t}}_i \times \hat{\mathbf{z}}\right) dS\right] = \\
&= \frac{dI_i}{dz} + \sum_p I_p T_{ip}
\end{aligned}$$

The second term of (2.33) vanishes

$$\iint_S \nabla_t H_z \cdot \mathbf{h_{t}}_i dS = \oint_{\partial S} H_z \mathbf{h_{t}}_i \cdot \hat{\mathbf{n}} ds - \iint_S H_z \nabla_t \cdot \mathbf{h_{t}}_i dS = 0$$

because $h_{ni} = 0$ on ∂S and $\nabla \cdot \mathbf{B} = 0$, that for TM modes becomes $\nabla_t \cdot \mathbf{h_{t}}_p = 0$. The last term of (2.33) is simplified using (2.19) and (2.13):

$$-\iota\omega\varepsilon \iint_S \hat{\mathbf{z}} \times \mathbf{E_t} \cdot \mathbf{h_{t}}_i dS = -\iota\omega\varepsilon \sum_p V_p \iint_S \mathbf{h_{t}}_p \cdot \mathbf{h_{t}}_i dS = -\iota\omega\varepsilon V_i$$

By combining all terms, the (2.33) becomes

$$\frac{dI_i}{dz} = -\gamma_i Y_i V_i - \sum_p T_{ip} I_p \tag{2.34}$$

being $\iota\omega\varepsilon = \gamma_i Y_i$.

The (2.32) and (2.34) are the generalized telegraphist's equations. The use of the two-dimensional Green theorem, the integration by part and the formula for integrals of varying surfaces is mandatory to remove the derivative operation from the total field. As explained in [64], when using the modal expansion in place of the total field, derivation and summation operators cannot be interchanged because term-by-term differentiation of the infinite series requires stronger convergence. The main aim of previous passages thus consists in moving the derivation from the total field to the eigenfunction of the i-th mode.

2.1.2 Projection on TE modes

We scalar multiply the (2.5) by the transversal electric component of the i-th TE mode and integrate over the cross-section. The same simplifications performed for (2.30) can be done except for the second integrals that becomes:

$$\iint_S \nabla_t E_z \cdot \mathbf{e_t}_i dS = \oint_{\partial S} E_z \mathbf{e_t}_i \cdot \hat{\mathbf{n}} ds - \iint_S E_z \nabla_t \cdot \mathbf{e_t}_i dS = \\ = \oint_{\partial S} E_z e_{ni} ds$$

because $\nabla \cdot \mathbf{D} = 0$ gives for TE modes $\nabla_t \cdot \mathbf{e_t}_p = 0$. By combining again all terms, the same equation as (2.32) is obtained, i.e.

$$\frac{dV_i}{dz} - \sum_p V_p T_{pi} + \cancel{\oint_{\partial S} E_z e_{ni} ds} = \cancel{\oint_{\partial S} E_z e_{ni} ds} + -\iota\omega\mu I_i$$

$$\frac{dV_i}{dz} = \sum_p V_p T_{pi} - \gamma_i Z_i I_i$$

In case of (2.5), the second integral again undergoes a different simplification using (2.28), (2.24), (2.18), (2.19), (2.13) and (2.8):

$$\begin{aligned}
&\iint_S \nabla_t H_z \cdot \mathbf{h_t}_i dS = \oint_{\partial S} H_z \mathbf{h_t}_i \cdot \hat{\mathbf{n}} ds - \iint_S H_z \nabla_t \cdot \mathbf{h_t}_i dS = \\
&= \cancel{\oint_{\partial S} H_z h_{ni} ds} - \frac{1}{\iota\omega\mu} \iint_S \nabla_t \cdot (\hat{\mathbf{z}} \times \mathbf{E_t}) \nabla_t \cdot \mathbf{h_t}_i dS = \\
&= -\frac{1}{\iota\omega\mu} \oint_{\partial S} \hat{\mathbf{z}} \times \mathbf{E_t} \cdot \hat{\mathbf{n}} \nabla_t \cdot \mathbf{h_t}_i ds + \frac{1}{\iota\omega\mu} \iint_S \hat{\mathbf{z}} \times \mathbf{E_t} \cdot \nabla_t \nabla_t \cdot \mathbf{h_t}_i dS = \\
&= \cancel{\frac{1}{\iota\omega\mu} \oint_{\partial S} \nabla_t \cdot \mathbf{h_t}_i \mathbf{E_t} \cdot \hat{\mathbf{s}} ds} + \frac{k_{ti}^2}{\iota\omega\mu} \iint_S \hat{\mathbf{z}} \times \mathbf{E_t} \cdot \mathbf{h_t}_i dS = \\
&= \frac{k_{ti}^2}{\iota\omega\mu} \sum_p V_p \iint_S \hat{\mathbf{z}} \times \mathbf{e_t}_p \cdot \mathbf{h_t}_i dS = \frac{k_{ti}^2}{\iota\omega\mu} V_i
\end{aligned}$$

where the first closed loop integral vanishes because $h_{ni} = 0$ on ∂S. By combining all terms, the (2.33) becomes

$$\frac{dI_i}{dz} + \sum_p T_{ip} I_p = \frac{k_{ti}^2}{\iota\omega\mu} V_i - \iota\omega\varepsilon V_i$$

and considering that

$$\frac{k_{ti}^2}{\iota\omega\mu} - \iota\omega\varepsilon = \frac{k_{ti}^2 + \omega^2\mu\varepsilon}{\iota\omega\mu} = \frac{k_{ti}^2 - k_0^2}{\iota\omega\mu} = -\frac{\gamma_i^2}{\iota\omega\mu} = -\gamma_i Y_i$$

the same equation as (2.34) is obtained.

2.1.3 Transfer coefficients

The expression of the transfer coefficients (2.31) is calculated more easily if rewritten as a function of the scalar potential. We follow the approach by Solymar [65], deriving the new expression for the interaction between modes of the same types and same index and use (2.29):

$$\begin{aligned} T_{pp} &= \iint_S \mathbf{e}_{\mathbf{t}p} \cdot \frac{\partial \mathbf{e}_{\mathbf{t}p}}{\partial z} dS = \\ &= \frac{d}{dz}\left(\iint_S \|\mathbf{e}_{\mathbf{t}p}\|^2 dS\right) - \iint_S \frac{\partial \mathbf{e}_{\mathbf{t}p}}{\partial z} \cdot \mathbf{e}_{\mathbf{t}p} dS - \oint_{\partial S} \|\mathbf{e}_{\mathbf{t}p}\|^2 \tan\theta ds = \\ &= \cancel{\frac{d}{dz}}(1) - T_{pp} - \oint_{\partial S} e_{np}^2 \tan\theta ds \end{aligned}$$

The symbol $\|\cdot\|$ denotes the norm of the vector, $\tan\theta$ is the change rate of the varying surface (see Fig. 2.1) and the last term reduces to the normal component because at the boundary $\mathbf{e}_{\mathbf{t}p} \cdot \hat{\mathbf{s}} = 0$. Using the notation by Schelkunoff and the modal expressions (2.10), the transfer coefficients become

$$T_{[p][p]} = -\frac{1}{2} \oint_{\partial S} \left(\frac{\partial \Phi_p^{\mathrm{TE}}}{\partial s}\right)^2 \tan\theta ds$$

and

$$T_{(p)(p)} = -\frac{1}{2} \oint_{\partial S} \left(\frac{\partial \Phi_p^{\mathrm{TM}}}{\partial n}\right)^2 \tan\theta ds$$

In case of different indices, we always have that

$$\Phi = f\left[\frac{n}{a(z)}\right] g(s)$$

and

$$\left.\frac{\partial \Phi}{\partial z}\right|_{n=a(z)} = \left.-\frac{n a'(z)}{a^2(z)} f' g\right|_{n=a(z)} = \left.-a'(z)\frac{f' g}{a(z)}\right|_{n=a(z)} = -\tan\theta \left.\frac{\partial \Phi}{\partial n}\right|_{n=a(z)}$$

so the following identities apply on the cross-section contour

$$\frac{\partial \Phi^{\mathrm{TM}}}{\partial z} = -\frac{\partial \Phi^{\mathrm{TM}}}{\partial n}\tan\theta$$
$$\frac{\partial}{\partial z}\frac{\partial \Phi^{\mathrm{TE}}}{\partial n} = -\frac{\partial^2 \Phi^{\mathrm{TE}}}{\partial n^2}\tan\theta$$

The expression for TE-TE interaction is developed as follows

$$T_{[p][i]} = \iint_S \mathbf{e}_{\mathbf{t}p}\cdot\frac{\partial \mathbf{e}_{\mathbf{t}}i}{\partial z}dS = \iint_S \left(\nabla_t \Phi_p^{\mathrm{TE}}\times\hat{\mathbf{z}}\right)\cdot\left(\frac{\partial}{\partial z}\nabla_t\Phi_i^{\mathrm{TE}}\times\hat{\mathbf{z}}\right)dS =$$
$$= \iint_S \left(\nabla_t \Phi_p^{\mathrm{TE}}\times\hat{\mathbf{z}}\right)\cdot\left(\frac{\partial \nabla_t\Phi_i^{\mathrm{TE}}}{\partial z}\times\hat{\mathbf{z}}\right)dS = -\iint_S \nabla_t\Phi_p^{\mathrm{TE}}\cdot\frac{\partial\nabla_t\Phi_i^{\mathrm{TE}}}{\partial z}dS$$

Now the two-dimensional Green theorem is firstly applied to remove the derivation from the p-th function

$$T_{[p][i]} = \oint_{\partial S}\Phi_p^{\mathrm{TE}}\left(\frac{\partial\nabla_t\Phi_i^{\mathrm{TE}}}{\partial z}\right)\cdot\hat{\mathbf{n}}ds - \iint_S \Phi_p^{\mathrm{TE}}\frac{\partial\nabla_t^2\Phi_i^{\mathrm{TE}}}{\partial z}dS =$$
$$= -\oint_{\partial S}\Phi_p^{\mathrm{TE}}\frac{\partial^2\Phi_i^{\mathrm{TE}}}{\partial n^2}\tan\theta ds - k_{ti}^2\iint_S\Phi_p^{\mathrm{TE}}\frac{\partial\Phi_i^{\mathrm{TE}}}{\partial z}dS$$

and then from the i-th function

$$T_{[p][i]} = \oint_{\partial S}\left(\nabla_t\Phi_p^{\mathrm{TE}}\cdot\hat{\mathbf{n}}\right)\frac{\partial\Phi_i^{\mathrm{TE}}}{\partial z}ds - \iint_S\nabla_t^2\Phi_p^{\mathrm{TE}}\frac{\partial\Phi_i^{\mathrm{TE}}}{\partial z}dS =$$
$$= \oint_{\partial S}\frac{\partial\Phi_p^{\mathrm{TE}}}{\partial n}\frac{\partial\Phi_i^{\mathrm{TE}}}{\partial z}ds - k_{tp}^2\iint_S\Phi_p^{\mathrm{TE}}\frac{\partial\Phi_i^{\mathrm{TE}}}{\partial z}dS = -k_{tp}^2\iint_S\Phi_p^{\mathrm{TE}}\frac{\partial\Phi_i^{\mathrm{TE}}}{\partial z}dS$$

where the (2.11) has been used. By combining the last two expressions

$$T_{[p][i]} = -\oint_{\partial S}\Phi_p^{\mathrm{TE}}\frac{\partial^2\Phi_i^{\mathrm{TE}}}{\partial n^2}\tan\theta ds - k_{ti}^2\iint_S\Phi_p^{\mathrm{TE}}\frac{\partial\Phi_i^{\mathrm{TE}}}{\partial z}dS =$$
$$= -\oint_{\partial S}\Phi_p^{\mathrm{TE}}\frac{\partial^2\Phi_i^{\mathrm{TE}}}{\partial n^2}\tan\theta ds + \frac{k_{ti}^2}{k_{tp}^2}T_{[p][i]}$$

the transfer coefficient for TE-TE interaction is

$$T_{[p][i]} = \frac{k_{tp}^2}{k_{ti}^2 - k_{tp}^2}\oint_{\partial S}\Phi_p^{\mathrm{TE}}\frac{\partial^2\Phi_i^{\mathrm{TE}}}{\partial n^2}\tan\theta ds \qquad \text{with } p\neq i$$

The TM-TM interaction is similarly developed by applying the two-dimensional Green theorem to remove the derivation from the p-th function

$$T_{(p)(i)} = \iint_S\nabla_t\Phi_p^{\mathrm{TM}}\cdot\frac{\partial\nabla_t\Phi_i^{\mathrm{TM}}}{\partial z}dS =$$
$$= \oint_{\partial S}\Phi_p^{\mathrm{TM}}\left(\frac{\partial\nabla_t\Phi_i^{\mathrm{TM}}}{\partial z}\right)\cdot\hat{\mathbf{n}}ds - \iint_S\Phi_p^{\mathrm{TM}}\frac{\partial\nabla_t^2\Phi_i^{\mathrm{TM}}}{\partial z}dS =$$
$$= -k_{ti}^2\iint_S\Phi_p^{\mathrm{TM}}\frac{\partial\Phi_i^{\mathrm{TM}}}{\partial z}dS$$

where the (2.11) has been used, and then from the i-th function

$$\begin{aligned} T_{(p)(i)} &= \iint_S \nabla_t \Phi_p^{\mathrm{TM}} \cdot \frac{\partial \nabla_t \Phi_i^{\mathrm{TM}}}{\partial z} dS = \\ &= \oint_{\partial S} \left(\nabla_t \Phi_p^{\mathrm{TM}} \cdot \hat{\mathbf{n}}\right) \frac{\partial \Phi_i^{\mathrm{TM}}}{\partial z} ds - \iint_S \nabla_t^2 \Phi_p^{\mathrm{TM}} \frac{\partial \Phi_i^{\mathrm{TM}}}{\partial z} dS = \\ &= \oint_{\partial S} \frac{\partial \Phi_p^{\mathrm{TM}}}{\partial n} \frac{\partial \Phi_i^{\mathrm{TM}}}{\partial z} ds - k_{tp}^2 \iint_S \Phi_p^{\mathrm{TM}} \frac{\partial \Phi_i^{\mathrm{TM}}}{\partial z} dS = \\ &= -\oint_{\partial S} \frac{\partial \Phi_p^{\mathrm{TM}}}{\partial n} \frac{\partial \Phi_i^{\mathrm{TM}}}{\partial n} \tan\theta ds - k_{tp}^2 \iint_S \Phi_p^{\mathrm{TM}} \frac{\partial \Phi_i^{\mathrm{TM}}}{\partial z} dS \end{aligned}$$

By combining the last two expressions

$$\begin{aligned} T_{(p)(i)} &= -\oint_{\partial S} \frac{\partial \Phi_p^{\mathrm{TM}}}{\partial n} \frac{\partial \Phi_i^{\mathrm{TM}}}{\partial n} \tan\theta ds - k_{tp}^2 \iint_S \Phi_p^{\mathrm{TM}} \frac{\partial \Phi_i^{\mathrm{TM}}}{\partial z} dS = \\ &= -\oint_{\partial S} \frac{\partial \Phi_p^{\mathrm{TM}}}{\partial n} \frac{\partial \Phi_i^{\mathrm{TM}}}{\partial n} \tan\theta ds + \frac{k_{tp}^2}{k_{ti}^2} T_{(p)(i)} \end{aligned}$$

the transfer coefficient for TM-TM interaction is

$$T_{(p)(i)} = \frac{k_{ti}^2}{k_{tp}^2 - k_{ti}^2} \oint_{\partial S} \frac{\partial \Phi_p^{\mathrm{TM}}}{\partial n} \frac{\partial \Phi_i^{\mathrm{TM}}}{\partial n} \tan\theta ds \qquad \text{with } p \neq i$$

The derivation of the transfer coefficient for the TE-TM interaction makes use of the vector identities $\nabla \cdot (\mathbf{F} \times \mathbf{G}) = \mathbf{G} \cdot \nabla \times \mathbf{F} - \mathbf{F} \cdot \nabla \times \mathbf{G}$ and $\nabla \times \nabla f = 0$, giving

$$\begin{aligned} T_{[p](i)} &= \iint_S \mathbf{e}_{\mathbf{t}p} \cdot \frac{\partial \mathbf{e}_{\mathbf{t}i}}{\partial z} dS = \iint_S \left(\nabla_t \Phi_p^{\mathrm{TE}} \times \hat{\mathbf{z}}\right) \cdot \frac{\partial \nabla_t \Phi_i^{\mathrm{TM}}}{\partial z} dS = \\ &= \oint_{\partial S} \left(\nabla_t \Phi_p^{\mathrm{TE}} \times \hat{\mathbf{z}} \cdot \hat{\mathbf{n}}\right) \frac{\partial \Phi_i^{\mathrm{TM}}}{\partial z} ds - \iint_S \nabla_t \cdot \left(\nabla_t \Phi_p^{\mathrm{TE}} \times \hat{\mathbf{z}}\right) \frac{\partial \Phi_i^{\mathrm{TM}}}{\partial z} dS = \\ &= \oint_{\partial S} \left(\nabla_t \Phi_p^{\mathrm{TE}} \cdot \hat{\mathbf{s}}\right) \frac{\partial \Phi_i^{\mathrm{TM}}}{\partial z} ds + \\ &\quad - \iint_S \left(\hat{\mathbf{z}} \cdot \nabla_t \times \nabla_t \Phi_p^{\mathrm{TE}} - \nabla_t \Phi_p^{\mathrm{TE}} \cdot \nabla_t \times \hat{\mathbf{z}}\right) \frac{\partial \Phi_i^{\mathrm{TM}}}{\partial z} dS = \\ &= -\oint_{\partial S} \frac{\partial \Phi_p^{\mathrm{TE}}}{\partial s} \frac{\partial \Phi_i^{\mathrm{TM}}}{\partial n} \tan\theta ds \end{aligned}$$

so that

$$T_{[p](i)} = -\oint_{\partial S} \frac{\partial \Phi_p^{\mathrm{TE}}}{\partial s} \frac{\partial \Phi_i^{\mathrm{TM}}}{\partial n} \tan\theta ds$$

Finally for the TM-TE interaction

$$\begin{aligned}T_{(p)[i]} &= \iint_S \mathbf{e}_{\mathbf{t}p} \cdot \frac{\partial \mathbf{e}_{\mathbf{t}i}}{\partial z} dS = \iint_S \nabla_t \Phi_p^{\mathrm{TM}} \cdot \frac{\partial \nabla_t \Phi_i^{\mathrm{TE}} \times \hat{\mathbf{z}}}{\partial z} dS = \\ &= \oint_{\partial S} \Phi_p^{\mathrm{TM}} \frac{\partial}{\partial z} \left(\nabla_t \Phi_i^{\mathrm{TE}} \times \hat{\mathbf{z}} \cdot \hat{\mathbf{n}}\right) ds - \iint_S \Phi_p^{\mathrm{TM}} \frac{\partial}{\partial z} \left(\nabla_t \cdot \nabla_t \Phi_i^{\mathrm{TE}} \times \hat{\mathbf{z}}\right) dS = \\ &= \oint_{\partial S} \Phi_p^{\mathrm{TM}} \frac{\partial}{\partial z} \left(\nabla_t \Phi_i^{\mathrm{TE}} \cdot \hat{\mathbf{s}}\right) ds - \iint_S \Phi_p^{\mathrm{TM}} \frac{\partial}{\partial z} \left(\hat{\mathbf{z}} \cdot \nabla_t \times \nabla_t \Phi_i^{\mathrm{TE}}\right) dS\end{aligned}$$

that, using previous vector identities and (2.11), gives

$$T_{(p)[i]} = 0$$

Here is a summary of previous expressions

$$T_{[p][p]} = -\frac{1}{2} \oint_{\partial S} \left(\frac{\partial \Phi_p^{\mathrm{TE}}}{\partial s}\right)^2 \tan\theta ds \tag{2.35}$$

$$T_{(p)(p)} = -\frac{1}{2} \oint_{\partial S} \left(\frac{\partial \Phi_p^{\mathrm{TM}}}{\partial n}\right)^2 \tan\theta ds \tag{2.36}$$

$$T_{[p][i]} = \frac{k_{tp}^2}{k_{ti}^2 - k_{tp}^2} \oint_{\partial S} \Phi_p^{\mathrm{TE}} \frac{\partial^2 \Phi_i^{\mathrm{TE}}}{\partial n^2} \tan\theta ds, \quad p \neq i \tag{2.37}$$

$$T_{(p)(i)} = \frac{k_{ti}^2}{k_{tp}^2 - k_{ti}^2} \oint_{\partial S} \frac{\partial \Phi_p^{\mathrm{TM}}}{\partial n} \frac{\partial \Phi_i^{\mathrm{TM}}}{\partial n} \tan\theta ds, \quad p \neq i \tag{2.38}$$

$$T_{[p](i)} = -\oint_{\partial S} \frac{\partial \Phi_p^{\mathrm{TE}}}{\partial s} \frac{\partial \Phi_i^{\mathrm{TM}}}{\partial n} \tan\theta ds \tag{2.39}$$

$$T_{(p)[i]} = 0 \tag{2.40}$$

2.1.4 T-parameters in circular waveguide

The transfer coefficients can be expressed in closed form in waveguides with circular cross-section of radius $a(z)$. Normal and tangential coordinate (n, s) correspond to $(r, a(z)\phi)$. The transversal wavenumber is

$$k_{ti}^2 = k_{t\ell m}^2 = \begin{cases} -\dfrac{u'^2_{\ell m}}{a^2(z)} & \text{for TE modes} \\ -\dfrac{u^2_{\ell m}}{a^2(z)} & \text{for TM modes} \end{cases} \tag{2.41}$$

being $u'_{\ell m}$ the m-th zeros of J'_ℓ, i.e. the first derivative of the ℓ-th order Bessel function of the first kind and $u_{\ell m}$ the m-th zeros of J_ℓ. The normalized scalar

potentials are

$$\Phi_i = \Phi_{\ell m} = \\ = \sqrt{N_{\ell m}} \cdot \begin{cases} J_\ell\left(\dfrac{u'_{\ell m}}{a(z)} r\right) \sin(\ell\phi + \phi_1) & \text{for TE modes} \\ & (\phi_1 = \frac{\pi}{2} \text{ if } \ell = 0) \\ J_\ell\left(\dfrac{u_{\ell m}}{a(z)} r\right) \sin(\ell\phi + \phi_2) & \text{for TM modes} \\ & (\phi_2 = \frac{\pi}{2} \text{ if } \ell = 0) \end{cases} \tag{2.42}$$

The terms ϕ_1 and ϕ_2 are arbitrary initial phasings indicating the polarization of the field; for circular modes (TE_{0m} and TM_{0m}), no polarization can be defined and $\phi_{1,2} = \pi/2$. The normalization factors $N_{\ell m}$ are

$$N_{\ell m} = \begin{cases} \left[\dfrac{\epsilon_{0\ell}\pi}{2} J_\ell^2(u'_{\ell m})(u'^2_{\ell m} - \ell^2)\right]^{-1} & \text{for TE modes} \\ \left[\dfrac{\epsilon_{0\ell}\pi}{2} J'^2_\ell(u_{\ell m}) u^2_{\ell m}\right]^{-1} & \text{for TM modes} \end{cases}$$

where the symbol $\epsilon_{0\ell}$ is 2 for $\ell = 0$ and 1 for $\ell \neq 0$. Previous choices assure the fulfilment of (2.13).

The transfer coefficients consist of closed loop integrals along the cross-section contour. Involved functions are reported here:

$$\Phi^{\mathrm{TE}}_{\ell m}|_{r=a(z)} = \sqrt{\frac{2}{\epsilon_{0\ell}\pi}} \frac{\sin(\ell\phi + \phi_1)}{\sqrt{u'^2_{\ell m} - \ell^2}}$$

$$\left.\frac{\partial \Phi^{\mathrm{TE}}_{\ell m}}{\partial s}\right|_{r=a(z)} = \left.\frac{\partial \Phi^{\mathrm{TE}}_{\ell m}}{a(z)\partial \phi}\right|_{r=a(z)} = \sqrt{\frac{2}{\epsilon_{0\ell}\pi}} \frac{\ell}{a(z)} \frac{\cos(\ell\phi + \phi_1)}{\sqrt{u'^2_{\ell m} - \ell^2}}$$

$$\left.\frac{\partial^2 \Phi^{\mathrm{TE}}_{\ell m}}{\partial n^2}\right|_{r=a(z)} = \left.\frac{\partial^2 \Phi^{\mathrm{TE}}_{\ell m}}{\partial r^2}\right|_{r=a(z)} = \sqrt{\frac{2}{\epsilon_{0\ell}\pi}} \frac{u'^2_{\ell m}}{a^2(z)} \frac{J''_\ell(u'_{\ell m})}{J_\ell(u'_{\ell m})} \frac{\sin(\ell\phi + \phi_1)}{\sqrt{u'^2_{\ell m} - \ell^2}}$$

$$\left.\frac{\partial \Phi^{\mathrm{TM}}_{\ell m}}{\partial n}\right|_{r=a(z)} = \left.\frac{\partial \Phi^{\mathrm{TM}}_{\ell m}}{\partial r}\right|_{r=a(z)} = \sqrt{\frac{2}{\epsilon_{0\ell}\pi}} \frac{1}{a(z)} \sin(\ell\phi + \phi_2)$$

The third expression can be further simplified using the equation of Bessel functions, i.e.

$$J''_\ell(x) + \frac{1}{x} J'_\ell(x) + \left(1 - \frac{\ell^2}{x^2}\right) J_\ell(x) = 0$$

that for $x = u'_{\ell m}$ becomes

$$J''_\ell(u'_{\ell m}) = -\frac{u'^2_{\ell m} - \ell^2}{u'^2_{\ell m}} J_\ell(u'_{\ell m})$$

to get

$$\left.\frac{\partial^2 \Phi^{\mathrm{TE}}_{\ell m}}{\partial r^2}\right|_{r=a(z)} = -\sqrt{\frac{2}{\epsilon_{0\ell}\pi}} \frac{\sqrt{u'^2_{\ell m} - \ell^2}}{a^2(z)} \sin(\ell\phi + \phi_1)$$

Useful integrals to be evaluated are

$$\int_0^{2\pi} \cos(q\phi+\phi_1)\cos(\ell\phi+\phi_1)d\phi = \begin{cases} \pi\delta_{\ell q}, & \ell\neq 0,\ \forall\phi_1 \\ 0, & \ell=0,\ \phi_1=\frac{\pi}{2} \end{cases} \tag{2.43}$$

$$\begin{aligned} &\int_0^{2\pi} \sin(q\phi+\phi_1)\sin(\ell\phi+\phi_1)d\phi = \\ &= \int_0^{2\pi} \sin(q\phi+\phi_2)\sin(\ell\phi+\phi_2)d\phi = \\ &\qquad = \pi\delta_{\ell q}\epsilon_{0\ell} \quad \begin{cases} \forall\phi_{1,2} \text{ if } \ell\neq 0 \\ \phi_{1,2}=\frac{\pi}{2} \text{ if } \ell=0 \end{cases} \end{aligned} \tag{2.44}$$

and

$$\begin{aligned} &\int_0^{2\pi} \cos(\ell\phi+\phi_1)\sin(q\phi+\phi_2)d\phi = \\ &\qquad = \pi\delta_{\ell q}\sin(\phi_2-\phi_1) \quad \begin{cases} \forall\phi_{1,2} \text{ if } \ell\neq 0 \\ \phi_{1,2}=\frac{\pi}{2} \text{ if } \ell=0 \end{cases} \end{aligned} \tag{2.45}$$

The (2.43) and (2.44) refer to TE-TE and TM-TM interactions, which are maximized between modes with equal polarization. The (2.45) corresponds to the interaction TE-TM, which maximally occurs between orthogonally polarized modes. Apart from circular modes, all other fields present two degenerate orthogonal configurations with in-quadrature polarization; we can limit our analysis to one of them provided that, if the one is chosen for TE modes, the other is taken for TM modes. A reference system aligned with these directions can be always fixed; we opt for TE modes aligned with the x-axis ($\phi_1=0$) and TM modes aligned with the y-axis ($\phi_2=\pi/2$).

We now solve the closed loop integrals in the definition of the transfer coefficients. The (2.35) gives

$$\begin{aligned} T_{[\ell m][\ell m]} &= -\frac{1}{2}\tan\theta\frac{2}{\pi}\frac{\ell^2}{a^2(z)}\frac{1}{u'^2_{\ell m}-\ell^2}\int_0^{2\pi}\cos^2(\ell\phi+\phi_1)a(z)d\phi = \\ &= -\frac{1}{2}\tan\theta\frac{2}{\pi}\frac{\ell^2}{a^2(z)}\frac{1}{u'^2_{\ell m}-\ell^2}a(z)\pi = \\ &= -\frac{\tan\theta}{a(z)}\frac{\ell^2}{(u'^2_{\ell m}-\ell^2)} \end{aligned}$$

The (2.36) becomes

$$\begin{aligned} T_{(\ell m)(\ell m)} &= -\frac{1}{2}\tan\theta\frac{2}{\epsilon_{0\ell}\pi}\frac{1}{a^2(z)}\int_0^{2\pi}\sin^2(\ell\phi+\phi_2)a(z)d\phi = \\ &= -\frac{1}{2}\tan\theta\frac{2}{\epsilon_{0\ell}\pi}\frac{1}{a^2(z)}a(z)\epsilon_{0\ell}\pi = \\ &= -\frac{\tan\theta}{a(z)} \end{aligned}$$

The (2.37) leads to

$$T_{[\ell m][qp]} = -\frac{u'^2_{\ell m}}{u'^2_{qp} - u'^2_{\ell m}} \tan\theta \frac{2}{\sqrt{\epsilon_{0\ell}}\sqrt{\epsilon_{0q}}\pi} \frac{1}{a^2(z)} \frac{\sqrt{u'^2_{qp} - q^2}}{\sqrt{u'^2_{\ell m} - \ell^2}} \cdot \cdot \int_0^{2\pi} \sin(\ell\phi + \phi_1)\sin(q\phi + \phi_1)a(z)d\phi =$$

$$= -\frac{u'^2_{\ell m}}{u'^2_{qp} - u'^2_{\ell m}} \tan\theta \frac{2}{\sqrt{\epsilon_{0\ell}}\sqrt{\epsilon_{0q}}\pi} \frac{1}{a^2(z)} \frac{\sqrt{u'^2_{qp} - q^2}}{\sqrt{u'^2_{\ell m} - \ell^2}} \cdot a(z)\epsilon_{0\ell}\pi\delta_{\ell q} =$$

$$= -\frac{\tan\theta}{a(z)} \frac{2u'^2_{\ell m}}{u'^2_{qp} - u'^2_{\ell m}} \frac{\sqrt{u'^2_{qp} - q^2}}{\sqrt{u'^2_{\ell m} - \ell^2}} \delta_{\ell q} \qquad \text{with } p \neq m$$

The (2.38) becomes

$$T_{(\ell m)(qp)} = \frac{u^2_{qp}}{u^2_{\ell m} - u^2_{qp}} \tan\theta \frac{2}{\sqrt{\epsilon_{0\ell}}\sqrt{\epsilon_{0q}}\pi} \frac{1}{a^2(z)} \cdot \cdot \int_0^{2\pi} \sin(\ell\phi + \phi_2)\sin(q\phi + \phi_2)a(z)d\phi =$$

$$= \frac{u^2_{qp}}{u^2_{\ell m} - u^2_{qp}} \tan\theta \frac{2}{\sqrt{\epsilon_{0\ell}}\sqrt{\epsilon_{0q}}\pi} \frac{1}{a^2(z)} \cdot a(z)\epsilon_{0\ell}\pi\delta_{\ell q} =$$

$$= \frac{\tan\theta}{a(z)} \frac{2u^2_{qp}}{u^2_{\ell m} - u^2_{qp}} \delta_{\ell q}$$

The (2.39) gives

$$T_{[\ell m](qp)} = -\tan\theta \frac{2}{\sqrt{\epsilon_{0\ell}}\sqrt{\epsilon_{0q}}\pi} \frac{\ell}{a^2(z)} \frac{1}{\sqrt{u'^2_{\ell m} - \ell^2}} \cdot \cdot \int_0^{2\pi} \cos(\ell\phi + \phi_1)\sin(q\phi + \phi_2)a(z)d\phi =$$

$$= -\tan\theta \frac{2}{\sqrt{\epsilon_{0\ell}}\sqrt{\epsilon_{0q}}\pi} \frac{\ell}{a^2(z)} \frac{1}{\sqrt{u'^2_{\ell m} - \ell^2}} \cdot a(z)\epsilon_{0\ell}\pi\delta_{\ell q} =$$

$$= -\frac{\tan\theta}{a(z)} \frac{2\ell}{\sqrt{u'^2_{\ell m} - \ell^2}} \delta_{\ell q}$$

and $T_{(\ell m)[qp]} = 0$.

Here is a summary of previous expressions

$$T_{[\ell m][\ell m]} = -\frac{\tan\theta}{a(z)}\frac{\ell^2}{(u'^2_{\ell m}-\ell^2)} \tag{2.46}$$

$$T_{(\ell m)(\ell m)} = -\frac{\tan\theta}{a(z)} \tag{2.47}$$

$$T_{[\ell m][pq]} = -\frac{\tan\theta}{a(z)}\frac{2u'^2_{\ell m}}{u'^2_{qp}-u'^2_{\ell m}}\frac{\sqrt{u'^2_{qp}-q^2}}{\sqrt{u'^2_{\ell m}-\ell^2}}\delta_{\ell q}, \quad m \neq p \tag{2.48}$$

$$T_{(\ell m)(pq)} = -\frac{\tan\theta}{a(z)}\frac{2u^2_{qp}}{u^2_{qp}-u^2_{\ell m}}\delta_{\ell q}, \quad m \neq p \tag{2.49}$$

$$T_{[\ell m](pq)} = -\frac{\tan\theta}{a(z)}\frac{2\ell}{\sqrt{u'^2_{\ell m}-\ell^2}}\delta_{\ell q} \tag{2.50}$$

$$T_{(\ell m)[pq]} = 0 \tag{2.51}$$

2.2 Coupling Coefficients

We replace (2.14) inside (2.32) and (2.34) to derive similar coupled equations relating forward and backward waves:

$$\begin{cases} \dfrac{d}{dz}\left[\sqrt{Z_i}\left(A_i^+ + A_i^-\right)\right] = -\gamma_i Z_i \sqrt{Y_p}\left(A_i^+ - A_i^-\right) + \displaystyle\sum_p T_{pi}\sqrt{Z_p}\left(A_p^+ + A_p^-\right) \\ \dfrac{d}{dz}\left[\sqrt{Y_i}\left(A_i^+ - A_i^-\right)\right] = -\gamma_i Y_i \sqrt{Z_i}\left(A_i^+ + A_i^-\right) - \displaystyle\sum_p T_{ip}\sqrt{Y_p}\left(A_p^+ - A_p^-\right) \end{cases}$$

The lhs of both equations is

$$\begin{cases} \sqrt{Z_i}\left(\dfrac{dA_i^+}{dz} + \dfrac{dA_i^-}{dz}\right) + \dfrac{1}{2\sqrt{Z_i}}\dfrac{dZ_i}{dz}\left(A_i^+ + A_i^-\right) = \dots \\ \sqrt{Y_i}\left(\dfrac{dA_i^+}{dz} - \dfrac{dA_i^-}{dz}\right) + \dfrac{1}{2\sqrt{Y_i}}\dfrac{dY_i}{dz}\left(A_i^+ - A_i^-\right) = \dots \end{cases}$$

where

$$\frac{1}{2\sqrt{Y_i}}\frac{dY_i}{dz} = \frac{\sqrt{Z_i}}{2}\frac{d}{dz}\left(\frac{1}{Z_i}\right) = -\frac{1}{2\sqrt{Z_i}}\frac{dZ_i}{dz}$$

The first equation is now divided by $\sqrt{Z_i}$, whereas the second one by $\sqrt{Y_i}$:

$$\begin{cases} \dfrac{dA_i^+}{dz} + \dfrac{dA_i^-}{dz} = -\dfrac{1}{2Z_i}\dfrac{dZ_i}{dz}\left(A_i^+ + A_i^-\right) - \gamma_i\left(A_i^+ - A_i^-\right) + \\ \qquad\qquad + \displaystyle\sum_p \sqrt{\frac{Z_p}{Z_i}} T_{pi}\left(A_p^+ + A_p^-\right) \\ \dfrac{dA_i^+}{dz} - \dfrac{dA_i^-}{dz} = +\dfrac{1}{2Z_i}\dfrac{dZ_i}{dz}\left(A_i^+ - A_i^-\right) - \gamma_i\left(A_i^+ + A_i^-\right) + \\ \qquad\qquad - \displaystyle\sum_p \sqrt{\frac{Z_i}{Z_p}} T_{ip}\left(A_p^+ - A_p^-\right) \end{cases}$$

After summing and subtracting previous equations, the system can be rearranged as follows

$$\begin{cases} \dfrac{dA_i^+}{dz} = -\dfrac{1}{2Z_i}\dfrac{dZ_i}{dz}A_i^- - \gamma_i A_i^+ + \displaystyle\sum_p \frac{1}{2}\left[\left(\sqrt{\frac{Z_p}{Z_i}}T_{pi} - \sqrt{\frac{Z_i}{Z_p}}T_{ip}\right)A_p^+ + \right. \\ \qquad\qquad \left. + \left(\sqrt{\frac{Z_p}{Z_i}}T_{pi} + \sqrt{\frac{Z_i}{Z_p}}T_{ip}\right)A_p^-\right] \\ \dfrac{dA_i^-}{dz} = -\dfrac{1}{2Z_i}\dfrac{dZ_i}{dz}A_i^+ + \gamma_i A_i^- + \displaystyle\sum_p \frac{1}{2}\left[\left(\sqrt{\frac{Z_p}{Z_i}}T_{pi} + \sqrt{\frac{Z_i}{Z_p}}T_{ip}\right)A_p^+ + \right. \\ \qquad\qquad \left. + \left(\sqrt{\frac{Z_p}{Z_i}}T_{pi} - \sqrt{\frac{Z_i}{Z_p}}T_{ip}\right)A_p^-\right] \end{cases}$$

We define the coupling coefficients as

$$S_{ip}^{\pm} = \frac{1}{2}\left(\sqrt{\frac{Z_p}{Z_i}}T_{pi} \mp \sqrt{\frac{Z_i}{Z_p}}T_{ip}\right) \tag{2.52}$$

and the coupled equations between forward and backward waves assume the following form

$$\begin{cases} \dfrac{dA_i^+}{dz} = -\dfrac{1}{2Z_i}\dfrac{dZ_i}{dz}A_i^- - \gamma_i A_i^+ + \displaystyle\sum_p \left(S_{ip}^+ A_p^+ + S_{ip}^- A_p^-\right) \\ \dfrac{dA_i^-}{dz} = -\dfrac{1}{2Z_i}\dfrac{dZ_i}{dz}A_i^+ + \gamma_i A_i^- + \displaystyle\sum_p \left(S_{ip}^- A_p^+ + S_{ip}^+ A_p^-\right) \end{cases} \tag{2.53}$$

The derivative of the wave impedance can be calculated, leading to the same expression for TE and TM modes:

$$\frac{1}{Z_i}\frac{dZ_i}{dz} = \begin{cases} \dfrac{\iota\omega\varepsilon}{\gamma_i}\dfrac{d}{dz}\left(\dfrac{\gamma_i}{\iota\omega\varepsilon}\right) = \dfrac{1}{\gamma_i}\dfrac{d\gamma_i}{dz} & \text{TM modes} \\ -\dfrac{1}{Y_i}\dfrac{dY_i}{dz} = -\dfrac{\iota\omega\mu}{\gamma_i}\dfrac{d}{dz}\left(\dfrac{\gamma_i}{\iota\omega\mu}\right) = -\dfrac{1}{\gamma_i}\dfrac{d\gamma_i}{dz} & \text{TE modes} \end{cases}$$

The latter expression can be further developed as follows

$$\begin{aligned} \frac{1}{\gamma_i}\frac{d\gamma_i}{dz} &= \frac{1}{\sqrt{k_0^2 - k_{ti}^2(z)}}\frac{d\sqrt{k_0^2 - k_{ti}^2(z)}}{dz} = \frac{1}{2[k_0^2 - k_{ti}^2(z)]}\frac{d[-k_{ti}^2(z)]}{dz} = \\ &= -\frac{1}{2\gamma_i^2}\frac{dk_{ti}^2(z)}{dz} \end{aligned} \tag{2.54}$$

For circular waveguides with varying radius $a(z)$, the (2.54) becomes

$$\begin{aligned} \frac{1}{Z_{\ell m}}\frac{dZ_{\ell m}}{dz} &= \frac{1}{2\gamma_{\ell m}^2}\frac{d}{dz}\left[\frac{u_{\ell m}^2}{a^2(z)}\right] = -\frac{2u_{\ell m}^2}{2\gamma_{\ell m}^2 a^3(z)}\frac{da(z)}{dz} = \\ &= -\frac{u_{\ell m}^2}{\gamma_{\ell m}^2 a^3(z)}\tan\theta \end{aligned} \tag{2.55}$$

and similarly for TE modes

$$\frac{1}{Z_{\ell m}}\frac{dZ_{\ell m}}{dz} = \frac{u'^2_{\ell m}}{\gamma_{\ell m}^2 a^3(z)}\tan\theta \tag{2.56}$$

2.2.1 Bragg condition

Both the coupling coefficients and the expression of the derivative of Z_i are proportional to $\tan\theta$. We take this term out and rewrite the coupled equations in the following compact form

$$\begin{cases} \dfrac{dA_i^+}{dz} = -\gamma_i A_i^+ + \tan\theta \displaystyle\sum_p \left(c_{ip}^+ A_p^+ + c_{ip}^- A_p^- \right) \\ \dfrac{dA_i^-}{dz} = +\gamma_i A_i^- + \tan\theta \displaystyle\sum_p \left(c_{ip}^- A_p^+ + c_{ip}^+ A_p^- \right) \end{cases}$$

with

$$c_{ip}^+ = \frac{1}{\tan\theta} S_{ip}^+ \qquad \text{and} \qquad c_{ip}^- = \frac{1}{\tan\theta} \left(S_{ip}^- - \frac{1}{2Z_i} \frac{dZ_i}{dz} \delta_{ip} \right)$$

We now consider propagating waves with $A_i^\pm = f_i^\pm \mathrm{e}^{\mp\gamma_i z} = f_i^\pm \mathrm{e}^{\mp\iota\beta_i z}$, so that

$$\begin{cases} \dfrac{df_i^+}{dz}\mathrm{e}^{-\iota\beta_i z} - \cancel{\iota\beta_i f_i^+ \mathrm{e}^{-\iota\beta_i z}} = & -\cancel{\iota\beta_i f_i^+ \mathrm{e}^{-\iota\beta_i z}} + \\ & + \tan\theta \displaystyle\sum_p \left(c_{ip}^+ f_p^+ \mathrm{e}^{-\iota\beta_p z} + c_{ip}^- f_p^- \mathrm{e}^{\iota\beta_p z} \right) \\ \dfrac{df_i^-}{dz}\mathrm{e}^{\iota\beta_i z} + \cancel{\iota\beta_i f_i^- \mathrm{e}^{\iota\beta_i z}} = & \cancel{\iota\beta_i f_i^- \mathrm{e}^{\iota\beta_i z}} + \\ & + \tan\theta \displaystyle\sum_p \left(c_{ip}^- f_p^+ \mathrm{e}^{-\iota\beta_p z} + c_{ip}^+ f_p^- \mathrm{e}^{\iota\beta_p z} \right) \end{cases}$$

$$\begin{cases} \dfrac{df_i^+}{dz} = \tan\theta \displaystyle\sum_p \left(c_{ip}^+ f_p^+ \mathrm{e}^{-\iota(\beta_p - \beta_i) z} + c_{ip}^- f_p^- \mathrm{e}^{\iota(\beta_p + \beta_i) z} \right) \\ \dfrac{df_i^-}{dz} = \tan\theta \displaystyle\sum_p \left(c_{ip}^- f_p^+ \mathrm{e}^{-\iota(\beta_p + \beta_i) z} + c_{ip}^+ f_p^- \mathrm{e}^{\iota(\beta_p - \beta_i) z} \right) \end{cases}$$

Bragg reflectors consist of waveguides with a periodically varying radius; we choose the following sinusoidal profile with period Λ:

$$a(z) = a_0 + b_0 \cos(k_b z) \qquad \text{with} \quad k_b = \frac{2\pi}{\Lambda} \tag{2.57}$$

From (2.57) we derive

$$\tan\theta = \frac{da(z)}{dz} = -b_0 k_b \sin(k_b z) = \frac{\iota b_0 k_b}{2} (\mathrm{e}^{\iota k_b z} - \mathrm{e}^{-\iota k_b z})$$

and the system of differential equations becomes

$$\begin{cases} \dfrac{df_i^+}{dz} = \displaystyle\sum_p \left\{ \left(\frac{\iota b_0 k_b}{2} c_{ip}^+ \right) f_p^+ \left[\mathrm{e}^{-\iota(\beta_p - \beta_i - k_b)z} - \mathrm{e}^{-\iota(\beta_p - \beta_i + k_b)z} \right] + \right. \\ \qquad \left. + \left(\frac{\iota b_0 k_b}{2} c_{ip}^- \right) f_p^- \left[\mathrm{e}^{\iota(\beta_p + \beta_i + k_b)z} - \mathrm{e}^{\iota(\beta_p + \beta_i - k_b)z} \right] \right\} \\ \dfrac{df_i^-}{dz} = \displaystyle\sum_p \left\{ \left(\frac{\iota b_0 k_b}{2} c_{ip}^- \right) f_p^+ \left[\mathrm{e}^{-\iota(\beta_p + \beta_i - k_b)z} - \mathrm{e}^{-\iota(\beta_p + \beta_i + k_b)z} \right] + \right. \\ \qquad \left. + \left(\frac{\iota b_0 k_b}{2} c_{ip}^+ \right) f_p^- \left[\mathrm{e}^{\iota(\beta_p - \beta_i + k_b)z} - \mathrm{e}^{\iota(\beta_p - \beta_i - k_b)z} \right] \right\} \end{cases}$$

The waves that satisfy the Bragg condition $\beta_i + \beta_p = k_b$ give a significant contribution in the summation because they constructively interfere, whereas the other modes can be neglected. Keeping only the terms fulfilling this condition leads to

$$\begin{cases} \dfrac{df_i^+}{dz} = -\displaystyle\sum_p \left(\frac{\iota b_0 k_b}{2} c_{ip}^- \right) f_p^- \mathrm{e}^{\iota \Delta_{ip} z} \\ \dfrac{df_i^-}{dz} = \displaystyle\sum_p \left(\frac{\iota b_0 k_b}{2} c_{ip}^- \right) f_p^+ \mathrm{e}^{-\iota \Delta_{ip} z} \end{cases} \tag{2.58}$$

where we have introduced the mismatch parameter

$$\Delta_{ip} = \beta_p + \beta_i - k_b \tag{2.59}$$

The (2.58) often appear in two different forms. The former is

$$\begin{cases} \dfrac{df_i^+}{dz} = \displaystyle\sum_p \kappa_{ip}^* f_p^- \mathrm{e}^{\iota \Delta_{ip} z} \\ \dfrac{df_i^-}{dz} = \displaystyle\sum_p \kappa_{ip} f_p^+ \mathrm{e}^{-\iota \Delta_{ip} z} \end{cases} \tag{2.60}$$

which uses the coupling constants

$$\kappa_{ip} = \frac{\iota b_0 k_b}{2} c_{ip}^-$$

and is mostly used by Yariv [66] and others. The latter uses the coupling constants

$$G_{ip} = \frac{b_0 k_b}{2} c_{ip}^-$$

and performs the following additional simplification

$$f_i^\pm = B_i^\pm \mathrm{e}^{\pm \iota \frac{\Delta_{ii}}{2} z}$$

This implies

$$\begin{cases} \dfrac{dB_i^+}{dz}\mathrm{e}^{\iota\frac{\Delta_{ii}}{2}z} + \iota\dfrac{\Delta_{ii}}{2}B_i^+\mathrm{e}^{\iota\frac{\Delta_{ii}}{2}z} = -\iota\displaystyle\sum_p G_{ip}B_p^-\mathrm{e}^{-\iota\frac{\Delta_{pp}}{2}z}\mathrm{e}^{\iota\Delta_{ip}z} \\ \dfrac{dB_i^-}{dz}\mathrm{e}^{-\iota\frac{\Delta_{ii}}{2}z} - \iota\dfrac{\Delta_{ii}}{2}B_i^-\mathrm{e}^{-\iota\frac{\Delta_{ii}}{2}z} = \iota\displaystyle\sum_p G_{ip}B_p^+\mathrm{e}^{\iota\frac{\Delta_{pp}}{2}z}\mathrm{e}^{-\iota\Delta_{ip}z} \end{cases}$$

$$\begin{cases} \dfrac{dB_i^+}{dz} = -\iota\dfrac{\Delta_{ii}}{2}B_i^+ - \iota\displaystyle\sum_p G_{ip}B_p^-\mathrm{e}^{\iota(\Delta_{ip}-\frac{\Delta_{pp}}{2}-\frac{\Delta_{ii}}{2})z} \\ \dfrac{dB_i^-}{dz} = \iota\dfrac{\Delta_{ii}}{2}B_i^- + \iota\displaystyle\sum_p G_{ip}B_p^+\mathrm{e}^{-\iota(\Delta_{ip}-\frac{\Delta_{pp}}{2}-\frac{\Delta_{ii}}{2})z} \end{cases}$$

$$\begin{cases} \dfrac{dB_i^+}{dz} = -\iota\dfrac{\Delta_{ii}}{2}B_i^+ - \iota\displaystyle\sum_p G_{ip}B_p^- \\ \dfrac{dB_i^-}{dz} = \iota\dfrac{\Delta_{ii}}{2}B_i^- + \iota\displaystyle\sum_p G_{ip}B_p^+ \end{cases} \tag{2.61}$$

since

$$\Delta_{ip} - \frac{\Delta_{pp}}{2} - \frac{\Delta_{ii}}{2} = \beta_p + \beta_i - k_b - \beta_p + \frac{k_b}{2} - \beta_i + \frac{k_b}{2} = 0$$

The system (2.61) is mostly used by Bratman [67] and others.

2.2.2 Lossy metals

The ohmic losses due to real metals can be included introducing a complex propagation constant, where an imaginary term α_i represents the attenuation constant per unit length of the i-th mode. In the case of small corrugation depths and small losses, the perturbative method can be adopted and the attenuation constants are computed with the standard expressions of smooth-wall circular waveguides as follows:

$$\alpha_i = \begin{cases} \alpha_{[\ell m]} = \sqrt{\dfrac{\omega\mu}{2\sigma}}\dfrac{\omega/c}{Z_0 a\beta_{\ell m}}\left(\dfrac{k_{t\ell m}^2}{k_0^2} + \dfrac{\ell^2}{u'^2_{\ell m}-\ell^2}\right), & \text{TE modes} \\ \alpha_{(\ell m)} = \sqrt{\dfrac{\omega\mu}{2\sigma}}\dfrac{\omega/c}{aZ_0\beta_{\ell m}}, & \text{TM modes} \end{cases} \tag{2.62}$$

where σ [S/m] is the metal conductivity and $Z_0 = 120\pi$ is the vacuum impedance.

The systems of equations for lossy structures are derived starting from the position $A_i^\pm = f_i^\pm \mathrm{e}^{\mp\iota\overline{\gamma}_i z}$, with $\overline{\gamma}_i = \beta_i - \iota\alpha_i$. They are formally the same as the ideal case, but the following complex $\overline{\Delta}_{ip}$ is obtained:

$$\overline{\Delta}_{ip} = \Delta_{ip} - \iota(\alpha_i + \alpha_p)$$

and the formulations (2.60) and (2.61) respectively become

$$\begin{cases} \dfrac{df_i^+}{dz} = \displaystyle\sum_p \kappa_{ip}^* f_p^- \mathrm{e}^{\iota\Delta_{ip}z}\mathrm{e}^{(\alpha_i+\alpha_p)z} \\ \dfrac{df_i^-}{dz} = \displaystyle\sum_p \kappa_{ip} f_p^+ \mathrm{e}^{-\iota\Delta_{ip}z}\mathrm{e}^{-(\alpha_i+\alpha_p)z} \end{cases}$$

and

$$\begin{cases} \dfrac{dB_i^+}{dz} = -\left(\iota\dfrac{\Delta_{ii}}{2} + \alpha_i\right) B_i^+ - \iota\displaystyle\sum_p G_{ip} B_p^- \\ \dfrac{dB_i^-}{dz} = \left(\iota\dfrac{\Delta_{ii}}{2} + \alpha_i\right) B_i^- + \iota\displaystyle\sum_p G_{ip} B_p^+ \end{cases}$$

The reflectivity R and transmissivity T are defined as

$$R = \left|\frac{A_p^-(0)}{A_i^+(0)}\right|^2 = \left|A_p^-(0)\right|^2 \qquad \text{and} \qquad T = \left|\frac{A_p^+(L)}{A_i^+(0)}\right|^2 = \left|A_p^+(L)\right|^2$$

where L is the total length of the reflector and an excitation A_i^+ with unitary amplitude entering the structure from $z = 0$ is assumed. In Yariv's formulation, these parameters are expressed as follows

$$\begin{aligned} R &= \left|A_p^-(0)\right|^2 = \left|f_p^-(0)\mathrm{e}^{\iota\overline{\gamma}_p\cdot 0}\right|^2 &&= \left|f_p^-(0)\right|^2 \\ T &= \left|A_p^+(L)\right|^2 = \left|f_p^+(L)\mathrm{e}^{-\iota\overline{\gamma}_p L}\right|^2 &&= \left|f_p^+(L)\right|^2 \mathrm{e}^{-2\alpha_p L} \end{aligned}$$

In Bratman's formulation, they are

$$\begin{aligned} R &= \left|A_p^-(0)\right|^2 = \left|f_p^-(0)\right|^2 = \left|B_p^-(0)\mathrm{e}^{-\iota\frac{\overline{\Delta}_{pp}}{2}\cdot 0}\right|^2 &&= \left|B_p^-(0)\right|^2 \\ T &= \left|A_p^+(L)\right|^2 = \left|B_p^+(L)\mathrm{e}^{\iota\frac{\overline{\Delta}_{pp}}{2}\cdot L}\mathrm{e}^{-2\alpha_p L}\right|^2 &&= \left|B_p^+(L)\right|^2 \end{aligned}$$

2.2.3 Expressions in circular waveguide

Closed-form expressions for the coupling coefficients G_{ip} in circular waveguides can be derived from

$$G_{ip} = \frac{b_0 k_b}{2}\frac{1}{\tan\theta}\left(S_{ip}^- - \frac{1}{2Z_i}\frac{dZ_i}{dz}\delta_{ip}\right)$$

using (2.52) and the expressions of the transfer coefficients given in section 2.1.4. We consider propagating waves, so $\gamma_i = \iota\beta_i$ and, assuming that $b_0 \ll a_0$, the radius $a(z)$ is approximated with a_0.

The coupling between TE modes with the same indices is

$$\begin{aligned} G_{[\ell m][\ell m]} &= \frac{b_0 k_b}{2}\frac{1}{\tan\theta}\left(T_{[\ell m][\ell m]} - \frac{1}{2Z_{\ell m}}\frac{dZ_{\ell m}}{dz}\right) = \\ &= \frac{b_0 k_b}{2}\frac{1}{\tan\theta}\left[-\frac{\tan\theta}{a_0}\frac{\ell^2}{(u'^2_{\ell m}-\ell^2)} + \frac{1}{2}\frac{u'^2_{\ell m}}{\beta^2_{\ell m}a_0^3}\tan\theta\right] = \\ &= \frac{k_b b_0}{2a_0}\left[\frac{1}{2}\frac{u'^2_{\ell m}}{\beta^2_{\ell m}a_0^2} - \frac{\ell^2}{(u'^2_{\ell m}-\ell^2)}\right] \end{aligned}$$

that can be rewritten as

$$\begin{aligned} &\frac{k_b b_0}{2a_0}\frac{u'^2_{\ell m}(u'^2_{\ell m}-\ell^2) - 2\beta^2_{\ell m}a_0^2\ell^2}{2\beta^2_{\ell m}a_0^2(u'^2_{\ell m}-\ell^2)} = \frac{k_b b_0}{2a_0}\frac{u'^4_{\ell m} - u'^2_{\ell m}\ell^2 - 2\beta^2_{\ell m}a_0^2\ell^2}{2\beta^2_{\ell m}a_0^2(u'^2_{\ell m}-\ell^2)} = \\ =&\frac{k_b b_0}{2a_0}\frac{u'^4_{\ell m} - (\omega/c)^2a_0^2\ell^2 + \beta^2_{\ell m}a_0^2\ell^2 - 2\beta^2_{\ell m}a_0^2\ell^2}{2\beta^2_{\ell m}a_0^2(u'^2_{\ell m}-\ell^2)} = \\ =&\frac{k_b b_0}{2a_0}\frac{u'^4_{\ell m} - a_0^2\ell^2[(\omega/c)^2 + \beta^2_{\ell m}]}{2\beta^2_{\ell m}a_0^2(u'^2_{\ell m}-\ell^2)} \end{aligned}$$

and for TM modes with the same indices

$$\begin{aligned} G_{(\ell m)(\ell m)} &= \frac{b_0 k_b}{2}\frac{1}{\tan\theta}\left(T_{(\ell m)(\ell m)} - \frac{1}{2Z_{\ell m}}\frac{dZ_{\ell m}}{dz}\right) = \\ &= \frac{b_0 k_b}{2}\frac{1}{\tan\theta}\left[-\frac{\tan\theta}{a_0} - \frac{1}{2}\frac{u^2_{\ell m}}{\beta^2_{\ell m}a_0^3}\tan\theta\right] = \\ &= -\frac{k_b b_0}{2a_0}\left[1 + \frac{1}{2}\frac{u^2_{\ell m}}{\beta^2_{\ell m}a_0^2}\right] = -\frac{k_b b_0}{2a_0}\left[\frac{2\beta^2_{\ell m} + u^2_{\ell m}/a_0^2}{2}\right] = \\ &= \frac{k_b b_0}{2a_0}\left[\frac{k_0^2 - \beta^2_{\ell m}}{2\beta^2_{\ell m}}\right] \end{aligned}$$

For different indices, TE-TE coupling yields

$$\begin{aligned} G_{[\ell m][qp]} &= \frac{b_0 k_b}{2}\frac{1}{2\tan\theta}\left(\sqrt{\frac{\omega\mu}{\beta_{\ell m}}\frac{\beta_{qp}}{\omega\mu}}T_{[\ell m][qp]} + \sqrt{\frac{\omega\mu}{\beta_{qp}}\frac{\beta_{\ell m}}{\omega\mu}}T_{[qp][\ell m]}\right) = \\ &= \frac{k_b b_0}{2a_0}\frac{1}{u'^2_{\ell m} - u'^2_{qp}}\cdot \\ &\cdot\left(u'^2_{\ell m}\sqrt{\frac{\beta_{qp}(u'^2_{qp}-q^2)}{\beta_{\ell m}(u'^2_{\ell m}-\ell^2)}} - u'^2_{qp}\sqrt{\frac{\beta_{\ell m}(u'^2_{\ell m}-\ell^2)}{\beta_{qp}(u'^2_{qp}-q^2)}}\right)\delta_{\ell q} \end{aligned}$$

TM-TM coupling gives

$$G_{(\ell m)(qp)} = \frac{b_0 k_b}{2} \frac{1}{2\tan\theta} \left(\sqrt{\frac{\beta_{\ell m}}{\omega\varepsilon} \frac{\omega\varepsilon}{\beta_{qp}}} T_{(\ell m)(qp)} + \sqrt{\frac{\beta_{qp}}{\omega\varepsilon} \frac{\omega\varepsilon}{\beta_{\ell m}}} T_{(qp)(\ell m)} \right) =$$
$$= \frac{k_b b_0}{2a_0} \frac{u_{qp}^2 \beta_{\ell m} - u_{\ell m}^2 \beta_{qp}}{(u_{\ell m}^2 - u_{qp}^2)\sqrt{\beta_{\ell m}\beta_{qp}}} \delta_{\ell q}$$

and TE-TM coupling is

$$G_{[\ell m](qp)} = \frac{b_0 k_b}{2} \frac{1}{2\tan\theta} \left(\sqrt{\frac{\omega\mu}{\beta_{\ell m}} \frac{\omega\varepsilon}{\beta_{qp}}} T_{[\ell m](qp)} \right) =$$
$$= -\frac{k_b b_0}{2a_0} \frac{\ell(\omega/c)}{\sqrt{\beta_{\ell m}\beta_{qp}}\sqrt{u'^2_{\ell m} - \ell^2}} \delta_{\ell q}$$

where c is the speed of light.

Provided that $m \neq p$, we summarize the coupling coefficients as follows

$$\frac{k_b b_0}{2a_0} \cdot \begin{cases} \dfrac{u'^4_{\ell m} - a_0^2 \ell^2 [(\omega/c)^2 + \beta_{\ell m}^2]}{2\beta_{\ell m}^2 a_0^2 (u'^2_{\ell m} - \ell^2)} & \text{TE}_{\ell m}\text{-TE}_{\ell m} \\ -\dfrac{(\omega/c)^2 + \beta_{\ell m}^2}{2\beta_{\ell m}^2} & \text{TM}_{\ell m}\text{-TM}_{\ell m} \\ \dfrac{u'^2_{\ell m}\sqrt{\frac{\beta_{qp}(u'^2_{qp} - q^2)}{\beta_{\ell m}(u'^2_{\ell m} - \ell^2)}} - u'^2_{qp}\sqrt{\frac{\beta_{\ell m}(u'^2_{\ell m} - \ell^2)}{\beta_{qp}(u'^2_{qp} - q^2)}}}{u'^2_{\ell m} - u'^2_{qp}} \delta_{\ell q} & \text{TE}_{\ell m}\text{-TE}_{qp} \\ \dfrac{u_{qp}^2 \beta_{\ell m} - u_{\ell m}^2 \beta_{qp}}{(u_{\ell m}^2 - u_{qp}^2)\sqrt{\beta_{\ell m}\beta_{qp}}} \delta_{\ell q} & \text{TM}_{\ell m}\text{-TM}_{qp} \\ -\dfrac{\ell(\omega/c)}{\sqrt{\beta_{\ell m}\beta_{qp}}\sqrt{u'^2_{\ell m} - \ell^2}} \delta_{\ell q} & \text{TE}_{\ell m}\text{-TM}_{qp} \end{cases} \tag{2.63}$$

2.2.4 Different corrugation profiles

So far we have used corrugations with a cosine profile given by (2.57), but the theoretical model can be generalized to support any periodic function $a(z)$. The latter can be always expressed through a Fourier series as follows:

$$a(z) = \sum_n b_n \mathrm{e}^{\iota \frac{2\pi n}{\Lambda} z} \qquad \text{with} \qquad b_n = \frac{1}{\Lambda} \int_{-\Lambda/2}^{\Lambda/2} a(z) \mathrm{e}^{-\iota \frac{2\pi n}{\Lambda} z} dz \tag{2.64}$$

where Λ is the spatial period, as shown in Fig. 2.2. According to the properties of Fourier series,

$$\frac{da(z)}{dz} = \sum_n g_n \mathrm{e}^{\iota \frac{2\pi n}{\Lambda} z} \qquad \text{with} \qquad g_n = \iota n k_b b_n$$

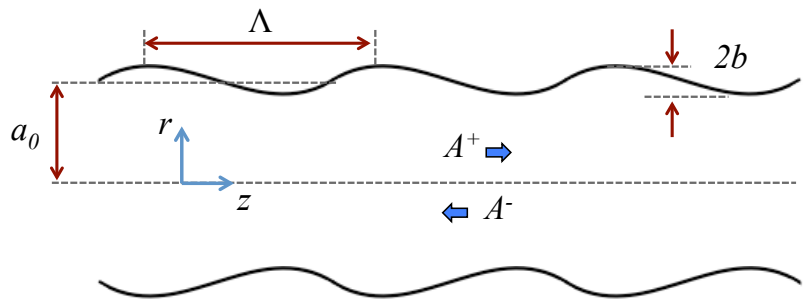

Figure 2.2: Parameters of the rippled wall.

and the coupled equations become

$$\begin{cases} \dfrac{df_i^+}{dz} = \displaystyle\sum_n g_n \sum_p \left[c_{ip}^+ f_p^+ \mathrm{e}^{-\iota(\beta_p - \beta_i - nk_b)z} + c_{ip}^- f_p^- \mathrm{e}^{\iota(\beta_p + \beta_i + nk_b)z} \right] \\ \dfrac{df_i^-}{dz} = \displaystyle\sum_n g_n \sum_p \left[c_{ip}^- f_p^+ \mathrm{e}^{-\iota(\beta_p + \beta_i - nk_b)z} + c_{ip}^+ f_p^- \mathrm{e}^{\iota(\beta_p - \beta_i + nk_b)z} \right] \end{cases} \tag{2.65}$$

Owing to the Bragg condition, the two terms on the left side of (2.65) can be influenced only by terms on the right hand side that possess the same phase dependence, that is, are *phase matched*, whereas the contribution of terms with no phase matching averages to zero over a few phase beat lengths. It follows that only the harmonics $n = -1$ and $n = 1$ contribute in the first and the second equations of (2.65), respectively. The system reduces to

$$\begin{cases} \dfrac{df_i^+}{dz} = \displaystyle\sum_p g_{-1} c_{ip}^- f_p^- \mathrm{e}^{\iota(\beta_p + \beta_i - k_b)z} \\ \dfrac{df_i^-}{dz} = \displaystyle\sum_p g_1 c_{ip}^- f_p^+ \mathrm{e}^{-\iota(\beta_p + \beta_i - k_b)z} \end{cases}$$

The Fourier coefficients of real functions satisfy the condition $g_{-n} = g_n^*$, i.e. $g_{-1} = -\iota k_b b_1^*$. With these positions and including losses, the systems of coupled equations in Yariv's and Bratman's form respectively become

$$\begin{cases} \dfrac{df_i^+}{dz} = \displaystyle\sum_p \kappa_{ip}^* f_p^- \mathrm{e}^{\iota\Delta_{ip} z} \mathrm{e}^{(\alpha_i + \alpha_p)z} \\ \dfrac{df_i^-}{dz} = \displaystyle\sum_p \kappa_{ip} f_p^+ \mathrm{e}^{-\iota\Delta_{ip} z} \mathrm{e}^{-(\alpha_i + \alpha_p)z} \end{cases} \quad \text{with} \quad \kappa_{ip} = (\iota k_b b_1) c_{ip}^-$$

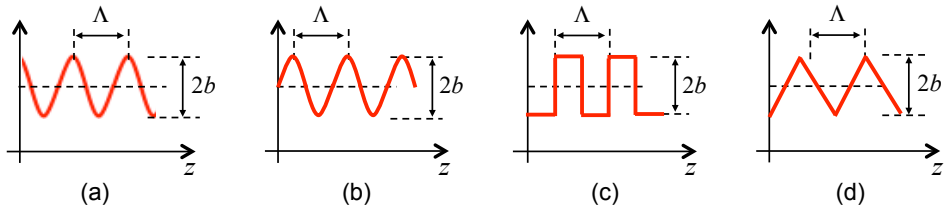

Figure 2.3: Cosine (a), sine (b), square (c) and triangle (d) profiles.

and

$$\begin{cases} \dfrac{dB_i^+}{dz} = -\left(\iota\dfrac{\Delta_{ii}}{2} + \alpha_i\right) B_i^+ - \iota \displaystyle\sum_p G_{ip}^* B_p^- \\ \dfrac{dB_i^-}{dz} = \left(\iota\dfrac{\Delta_{ii}}{2} + \alpha_i\right) B_i^- + \iota \displaystyle\sum_p G_{ip} B_p^+ \end{cases} \quad \text{with} \quad G_{ip} = (k_b b_1) c_{ip}^-$$

In the expressions of G_{ip} given by (2.63), the $b_0/2$ must be thus replaced with the first coefficient of the Fourier series of $a(z)$. The expressions of b_1 for common corrugations are

profiles	Fig.	$a(z)$	b_1
cosine	2.3(a)	$a_0 + b\cos\left(\frac{2\pi}{\Lambda}z\right)$	$\frac{b}{2}$
sine	2.3(b)	$a_0 + b\sin\left(\frac{2\pi}{\Lambda}z\right)$	$-\frac{\iota b}{2}$
square	2.3(c)	$a_0 + b\left[2\sum_n \mathrm{rect}\left(\frac{z}{\Lambda} - n\right) - 1\right]$	$\frac{\iota 2b}{\pi}$
triangle	2.3(d)	$a_0 + b\left[4\sum_n \mathrm{tri}\left(\frac{z}{\Lambda} - n\right) - 1\right]$	$\frac{4b}{\pi^2}$

where the functions rect and tri are defined as follows

$$\mathrm{rect}(x) = \begin{cases} 0, & 0 < x < \frac{1}{2} \\ \frac{1}{2}, & x = \frac{1}{2} \\ 1, & \frac{1}{2} < x < 1 \end{cases}; \qquad \mathrm{tri}(x) = \begin{cases} \mathrm{mod}(x, 1), & 0 < x \leq \frac{1}{2} \\ \mathrm{mod}(1 - x, 1), & \frac{1}{2} \leq x < 1 \end{cases}$$

2.3 Benchmarks

2.3.1 Comparison with other formulas

The coupling constants given in [68] are

$$\begin{cases} \dfrac{b_0}{2}\dfrac{u'^4_{\ell m}-\ell^2 a_0^2[(\omega/c)^2+\beta^2_{\ell m}]}{a_0^3\beta_{\ell m}(u'^2_{\ell m}-\ell^2)} & \text{TE}_{\ell m}\text{-TE}_{\ell m} \\ \dfrac{b_0}{2a_0}\dfrac{(\omega/c)^2+\beta^2_{\ell m}}{\beta_{\ell m}} & \text{TM}_{\ell m}\text{-TM}_{\ell m} \\ \dfrac{k_b b_0}{2a_0}\dfrac{u'^2_{qp}(u'^2_{\ell m}-\ell^2)\sqrt{\frac{\beta_{\ell m}}{\beta_{qp}}}-u'^2_{\ell m}(u'^2_{qp}-q^2)\sqrt{\frac{\beta_{qp}}{\beta_{\ell m}}}}{(u'^2_{\ell m}-u'^2_{qp})\sqrt{u'^2_{qp}-q^2}\sqrt{u'^2_{\ell m}-\ell^2}} & \text{TE}_{\ell m}\text{-TE}_{qp} \\ \dfrac{k_b b_0}{2a_0}\dfrac{u^2_{qp}\beta_{\ell m}-u^2_{\ell m}\beta_{qp}}{(u^2_{qp}-u^2_{\ell m})\sqrt{\beta_{\ell m}\beta_{qp}}} & \text{TM}_{\ell m}\text{-TM}_{qp} \\ \dfrac{k_b b_0}{2a_0}\dfrac{\ell(\omega/c)}{\sqrt{\beta_{\ell m}\beta_{qp}}\sqrt{u'^2_{\ell m}-\ell^2}} & \text{TE}_{\ell m}\text{-TM}_{qp} \end{cases} \tag{2.66}$$

where in the first two expression k_b has been replaced with $2\beta_{\ell m}$. By dividing the expressions in (2.63) with these coupling constants and neglecting the missing $\delta_{\ell q}$, we find

$$\frac{G^{(2.63)}_{pi}}{G^{(2.66)}_{pi}} = \begin{cases} 1 & \text{TE}_{\ell m}\text{-TE}_{\ell m} \\ -1 & \text{TM}_{\ell m}\text{-TM}_{\ell m} \\ -1 & \text{TE}_{\ell m}\text{-TE}_{qp} \\ -1 & \text{TM}_{\ell m}\text{-TM}_{qp} \\ -1 & \text{TE}_{\ell m}\text{-TM}_{qp} \end{cases}$$

The coupling constants given in [67] and [69] are

$$\begin{cases} \dfrac{b_0}{2a_0^3}\dfrac{-u'^2_{\ell m}u'^2_{qp}+\ell q a_0^2(\omega^2/c^2+\beta_{\ell m}\beta_{qp})}{\sqrt{\beta_{\ell m}\beta_{qp}}\sqrt{(u'^2_{\ell m}-\ell^2)(u'^2_{qp}-q^2)}} & \text{TE}_{\ell m}\text{-TE}_{qp} \\ \dfrac{b_0}{2a_0}\dfrac{\omega^2/c^2+\beta_{\ell m}\beta_{qp}}{\sqrt{\beta_{\ell m}\beta_{qp}}} & \text{TM}_{\ell m}\text{-TM}_{qp} \\ \dfrac{b_0}{2a_0}\dfrac{\ell(\omega/c)(\beta_{\ell m}+\beta_{qp})}{\sqrt{\beta_{\ell m}\beta_{qp}}\sqrt{u'^2_{\ell m}-\ell^2}} & \text{TE}_{\ell m}\text{-TM}_{qp} \end{cases} \tag{2.67}$$

where the approximation $k_b = \beta_{\ell m} + \beta_{qp}$ was employed. This position removes the singularity in the coupling coefficients between modes with different indices so that the same expressions can be used for both $(\ell m) = (qp)$

and $(\ell m) \neq (qp)$. We introduce the same approximation in (2.63); for $\mathrm{TE}_{\ell m}$-$\mathrm{TE}_{\ell m}$ and $\mathrm{TM}_{\ell m}$-$\mathrm{TM}_{\ell m}$ interaction, this yields

$$\begin{aligned} G_{[\ell m][\ell m]} &= \frac{2\beta_{\ell m} b_0}{2a_0^3} \frac{u'^4_{\ell m} - a_0^2 \ell^2 [(\omega/c)^2 + \beta^2_{\ell m}]}{2\beta^2_{\ell m}(u'^2_{\ell m} - \ell^2)} = \\ &= -\frac{b_0}{2a_0^3} \frac{-u'^4_{\ell m} + a_0^2 \ell^2 [(\omega/c)^2 + \beta^2_{\ell m}]}{\beta_{\ell m}(u'^2_{\ell m} - \ell^2)} \\ G_{(\ell m),(\ell m)} &= -\frac{b_0}{2a_0} \frac{\omega^2/c^2 + \beta^2_{\ell m}}{\beta_{\ell m}} \end{aligned}$$

In case of $\mathrm{TE}_{\ell m}$-TE_{qp}, neglecting $\delta_{\ell q}$,

$$G_{[\ell m][qp]} = \frac{(\beta_{\ell m} + \beta_{qp}) b_0}{2a_0} \frac{u'^2_{\ell m} \sqrt{\frac{\beta_{qp}(u'^2_{qp} - q^2)}{\beta_{\ell m}(u'^2_{\ell m} - \ell^2)}} - u'^2_{qp} \sqrt{\frac{\beta_{\ell m}(u'^2_{\ell m} - \ell^2)}{\beta_{qp}(u'^2_{qp} - q^2)}}}{u'^2_{\ell m} - u'^2_{qp}} =$$

$$= -\frac{b_0}{2a_0} \frac{(\beta_{\ell m} + \beta_{qp})[u'^2_{qp}(u'^2_{\ell m} - \ell^2)\beta_{\ell m} - u'^2_{\ell m}(u'^2_{qp} - q^2)\beta_{qp}]}{(u'^2_{\ell m} - u'^2_{qp})\sqrt{(u'^2_{qp} - q^2)}\sqrt{u'^2_{\ell m} - \ell^2}\sqrt{\beta_{\ell m}\beta_{qp}}}$$

and, remembering that $\ell = q$, the denominator is expanded

$$\begin{aligned} &(\beta_{\ell m} + \beta_{qp})(u'^2_{qp}\beta_{\ell m}u'^2_{\ell m} - u'^2_{qp}\beta_{\ell m}\ell^2 - u'^2_{\ell m}\beta_{qp}u'^2_{qp} + u'^2_{\ell m}\beta_{qp}q^2) = \\ =&\beta^2_{\ell m}u'^2_{qp}u'^2_{\ell m} - \beta^2_{\ell m}u'^2_{qp}\ell^2 - \cancel{\beta_{\ell m}\beta_{qp}u'^2_{\ell m}u'^2_{qp}} + \beta_{\ell m}\beta_{qp}u'^2_{\ell m}q^2 + \\ &+ \cancel{\beta_{\ell m}\beta_{qp}u'^2_{qp}u'^2_{\ell m}} - \beta_{\ell m}\beta_{qp}u'^2_{qp}\ell^2 - \beta^2_{qp}u'^2_{\ell m}u'^2_{qp} + \beta^2_{qp}u'^2_{\ell m}q^2 = \\ =&\left(\frac{\omega^2}{c^2} - \frac{u'^2_{\ell m}}{a_0^2}\right)u'^2_{qp}u'^2_{\ell m} - \left(\frac{\omega^2}{c^2} - \frac{u'^2_{\ell m}}{a_0^2}\right)u'^2_{qp}\ell^2 + \\ &- \left(\frac{\omega^2}{c^2} - \frac{u'^2_{qp}}{a_0^2}\right)u'^2_{\ell m}u'^2_{qp} + \left(\frac{\omega^2}{c^2} - \frac{u'^2_{qp}}{a_0^2}\right)u'^2_{\ell m}q^2 + \\ &+ (u'^2_{\ell m} - u'^2_{qp})\beta_{\ell m}\beta_{qp}q\ell = \\ =&\cancel{\frac{\omega^2}{c^2}u'^2_{qp}u'^2_{\ell m}} - \frac{u'^2_{\ell m}}{a_0^2}u'^2_{qp}u'^2_{\ell m} - \frac{\omega^2}{c^2}u'^2_{qp}\ell^2 + \cancel{\frac{u'^2_{\ell m}}{a_0^2}u'^2_{qp}\ell^2} + \\ &- \cancel{\frac{\omega^2}{c^2}u'^2_{\ell m}u'^2_{qp}} + \frac{u'^2_{qp}}{a_0^2}u'^2_{\ell m}u'^2_{qp} + \frac{\omega^2}{c^2}u'^2_{\ell m}q^2 - \cancel{\frac{u'^2_{qp}}{a_0^2}u'^2_{\ell m}q^2} + \\ &+ (u'^2_{\ell m} - u'^2_{qp})\beta_{\ell m}\beta_{qp}q\ell = \\ =&(u'^2_{\ell m} - u'^2_{qp})(\ell q\frac{\omega^2}{c^2} - \frac{u'^2_{\ell m}u'^2_{qp}}{a_0^2}) + (u'^2_{\ell m} - u'^2_{qp})\beta_{\ell m}\beta_{qp}q\ell = \\ =&(u'^2_{\ell m} - u'^2_{qp})\frac{1}{a_0^2}[\ell q a_0^2(\omega^2/c^2 + \beta_{\ell m}\beta_{qp}) - u'^2_{\ell m}u'^2_{qp}] \end{aligned}$$

The coupling coefficient becomes

$$G_{[\ell m][qp]} = -\frac{b_0}{2a_0}\frac{\cancel{(u'^2_{\ell m} - u'^2_{qp})}[\ell q a_0^2(\omega^2/c^2 + \beta_{\ell m}\beta_{qp}) - u'^2_{\ell m}u'^2_{qp}]}{a_0^2\cancel{(u'^2_{\ell m} - u'^2_{qp})}\sqrt{(u'^2_{qp} - q^2)}\sqrt{u'^2_{\ell m} - \ell^2}\sqrt{\beta_{\ell m}\beta_{qp}}} =$$
$$= -\frac{b_0}{2a_0^3}\frac{-u'^2_{\ell m}u'^2_{qp} + \ell q a_0^2(\omega^2/c^2 + \beta_{\ell m}\beta_{qp})}{\sqrt{(u'^2_{qp} - q^2)}\sqrt{u'^2_{\ell m} - \ell^2}\sqrt{\beta_{\ell m}\beta_{qp}}}$$

In case of $\mathrm{TM}_{\ell m}$-TM_{qp}

$$G_{(\ell m)(qp)} = \frac{(\beta_{\ell m} + \beta_{qp})b_0}{2a_0}\frac{u_{qp}^2\beta_{\ell m} - u_{\ell m}^2\beta_{qp}}{(u_{\ell m}^2 - u_{qp}^2)\sqrt{\beta_{\ell m}\beta_{qp}}} =$$
$$= \frac{b_0}{2a_0}\frac{\beta_{\ell m}^2u_{qp}^2 + \beta_{\ell m}\beta_{qp}u_{qp}^2 - \beta_{\ell m}\beta_{qp}u_{\ell m}^2 - \beta_{qp}^2u_{\ell m}^2}{(u_{\ell m}^2 - u_{qp}^2)\sqrt{\beta_{\ell m}\beta_{qp}}} =$$
$$= \frac{b_0}{2a_0}\frac{\frac{\omega^2}{c^2}u_{qp}^2 + \cancel{\frac{u_{\ell m}^2}{a_0^2}u_{qp}^2} + \beta_{\ell m}\beta_{qp}(u_{qp}^2 - u_{\ell m}^2) - \frac{\omega^2}{c^2}u_{\ell m}^2 - \cancel{\frac{u_{qp}^2}{a_0^2}u_{\ell m}^2}}{(u_{\ell m}^2 - u_{qp}^2)\sqrt{\beta_{\ell m}\beta_{qp}}} =$$
$$= -\frac{b_0}{2a_0}\frac{\cancel{(u_{\ell m}^2 - u_{qp}^2)}(\frac{\omega^2}{c^2} + \beta_{\ell m}\beta_{qp})}{\cancel{(u_{qp}^2 - u_{\ell m}^2)}\sqrt{\beta_{\ell m}\beta_{qp}}} = -\frac{b_0}{2a_0}\frac{\frac{\omega^2}{c^2} + \beta_{\ell m}\beta_{qp}}{\sqrt{\beta_{\ell m}\beta_{qp}}}$$

and for $\mathrm{TE}_{\ell m}$-TM_{qp} interaction

$$G_{[\ell m](qp)} = -\frac{b_0}{2a_0}\frac{\ell(\omega/c)(\beta_{\ell m} + \beta_{qp})}{\sqrt{\beta_{\ell m}\beta_{qp}}\sqrt{u'^2_{\ell m} - \ell^2}}$$

We now divide these new expressions by (2.67):

$$\frac{G_{pi}^{(2.63)}}{G_{pi}^{(2.67)}} = \begin{cases} -1 & \mathrm{TE}_{\ell m}\text{-}\mathrm{TE}_{\ell m} \\ -1 & \mathrm{TM}_{\ell m}\text{-}\mathrm{TM}_{\ell m} \\ -1 & \mathrm{TE}_{\ell m}\text{-}\mathrm{TE}_{qp} \\ -1 & \mathrm{TM}_{\ell m}\text{-}\mathrm{TM}_{qp} \\ -1 & \mathrm{TE}_{\ell m}\text{-}\mathrm{TM}_{qp} \end{cases} \tag{2.68}$$

Almost all comparisons show that calculated coupling constants match the coefficients of other papers apart from a sign. The only exception is the $G_{[\ell m][\ell m]}$ in (2.66), but it is probably due to a mistake in McCowan's paper because many other equations in that paper present doubtful signs.

2.3.2 Comparison with results from literature

We start this comparison from a technical report by McCowan et al. [68], where two examples are described, but in the first one the design parameters

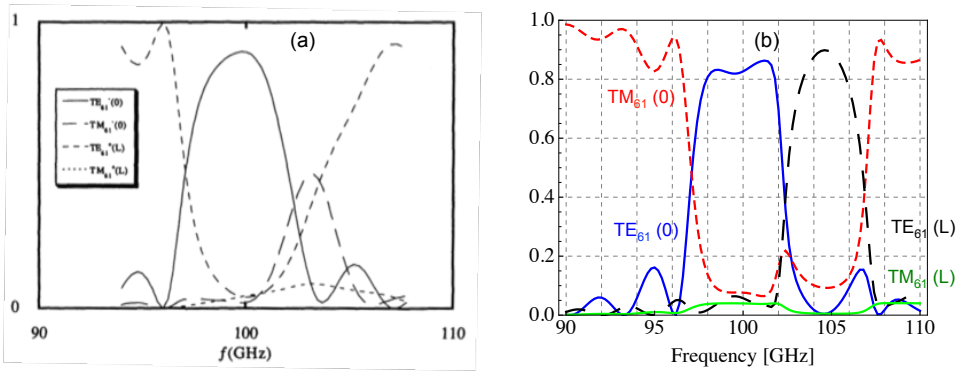

Figure 2.4: Reflection and transmission of the TE_{61} and TM_{61} modes versus frequency in a cylindrical, TE_{61}-excited, Bragg reflector with parameters Λ=1.7 mm, a_0=7.5 mm (estimated), L=40 mm and b_0=0.12 mm. (a) is taken from [68]; (b) is calculated according to our model.

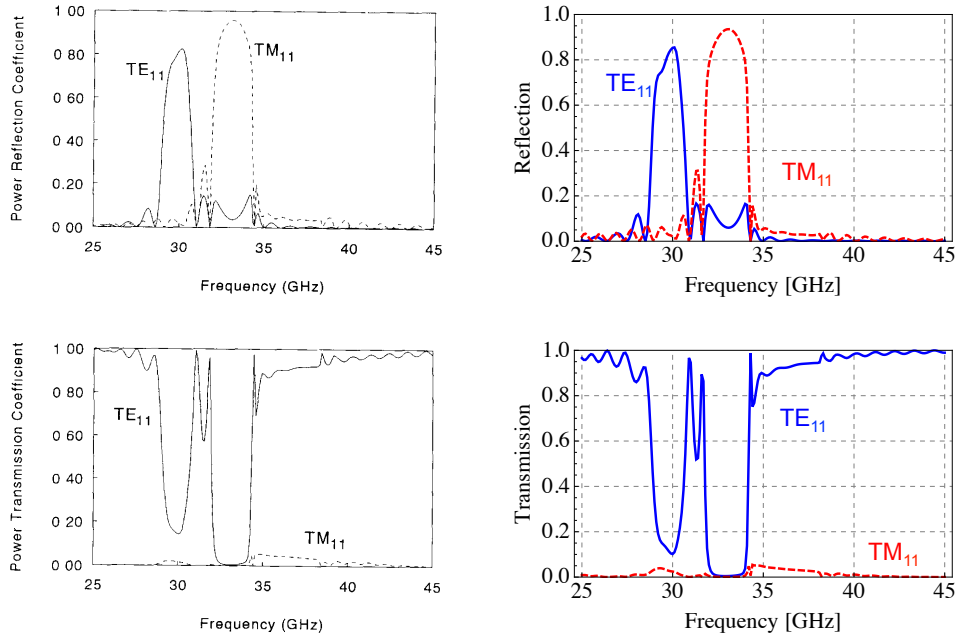

Figure 2.5: Reflection and transmission of the TE_{11} and TM_{11} modes versus frequency in a cylindrical, TE_{11}-excited, Bragg reflector with parameters Λ=5.37 mm, a_0=8 mm (estimated), L=120 mm and b_0=0.5 mm. Left plots are taken from [70], whereas right ones are calculated according to our expressions.

are contradictory probably owing to some cut and paste errors. Hence the second example has been only used. The radius of the unperturbed waveguide is not given in the text and has been derived to fulfil Bragg condition.

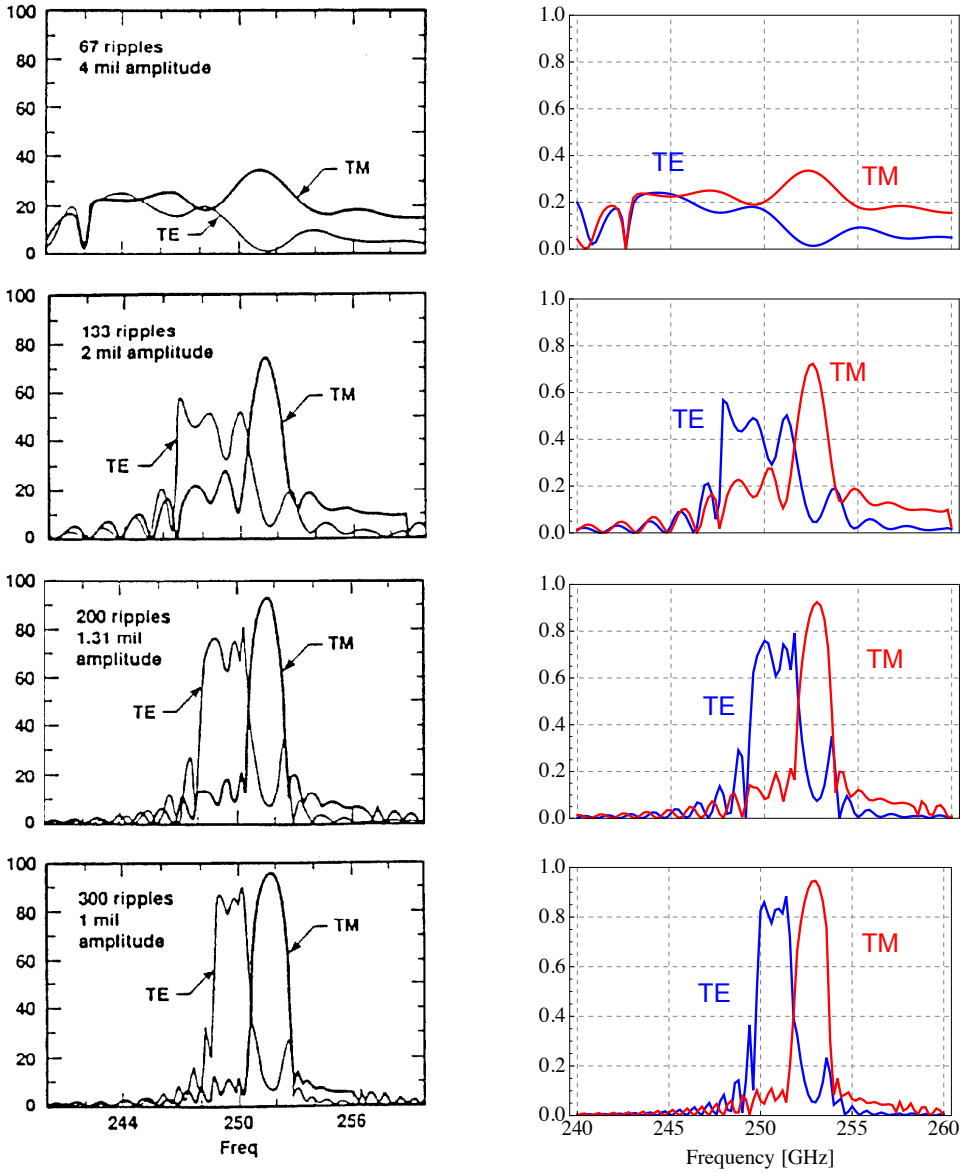

Figure 2.6: Reflectivities of the TE_{11} and TM_{11} modes versus frequency in cylindrical, TE_{11}-excited, Bragg reflectors taken from [71] (left) and calculated with our formulation (right). Design parameters are Λ=0.6 mm, a_0=3.5 mm, whereas (b_0, L) are, from top to bottom, (101.6 μm, 40.2 mm), (50.8 μm, 79.8 mm), (33.27 μm, 120 mm) and (25.4 μm, 180 mm).

The agreement, reported in Fig. 2.4 is good, but not perfect; L is the length of the rippled section. Nevertheless a different plot from [68] is obtained also if McCowan's coupling constants are used.

A very good match is shown in Fig. 2.5 and refers to a paper from

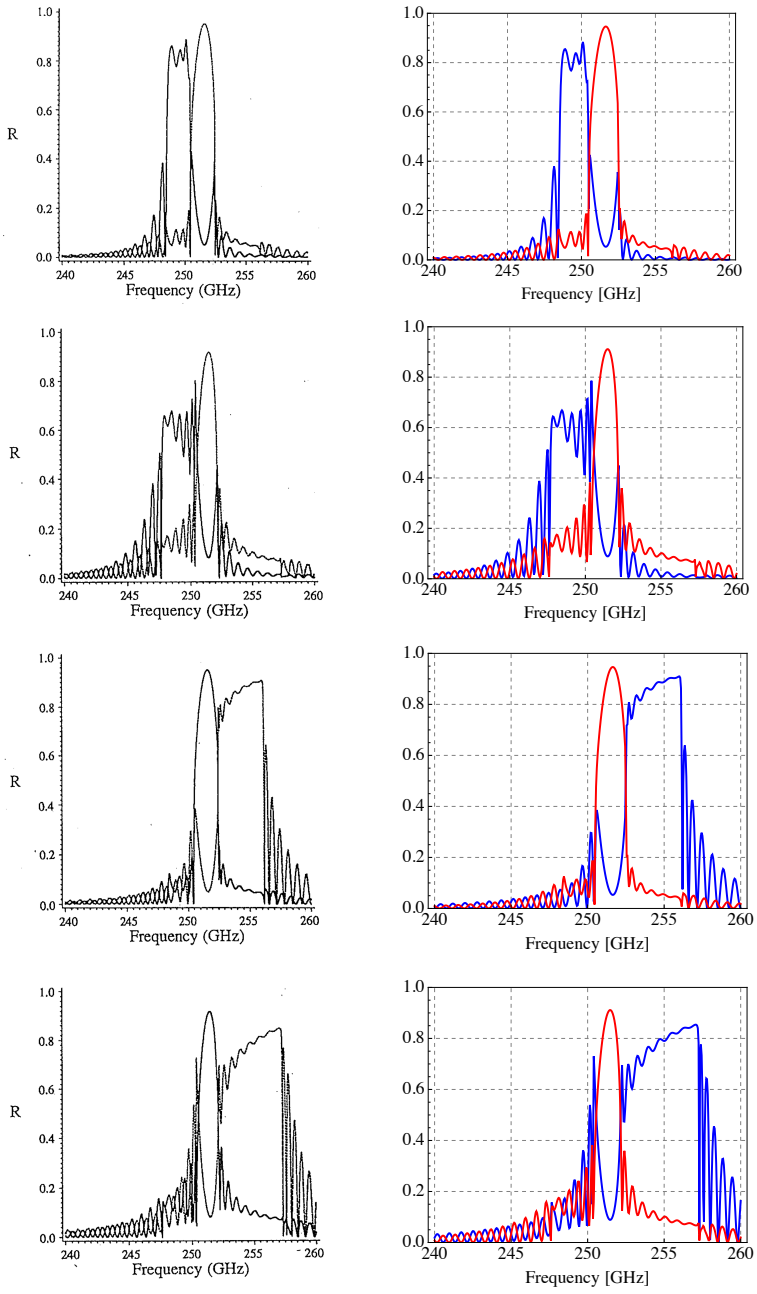

Figure 2.7: Reflection of the TE_{11} and TM_{11} modes versus frequency in cylindrical, Bragg reflectors taken from [69] (left) and calculated with our formulation (right). Design parameters are Λ=603 μm, a_0=3.525 mm, L=180.9 mm and b_0 is 26 μm (a) and 39 μm (b), with TE_{11} as input mode, and 26 μm (c) and 39 μm (d), with TM_{11} as input mode.

Zambon et al. [70]. Also in this case the radius of the unperturbed waveguide has been estimating enforcing the Bragg condition because its value was not reported in the paper.

Another paper relying on the coupled-mode theory is a work from Kulke et al. [71] for a 250 GHz cyclotron auto-resonance maser mostly meant for nuclear fusion. Four calculations are given for Bragg-reflector with different lengths and ripple depths. The comparison is shown in Fig. 2.6, resulting in a perfect agreement.

The last benchmark, shown in Fig. 2.7, refers again to a 250 GHz cyclotron auto-resonance maser working with low-order modes. There is a perfect match between our calculations and the plots taken from this paper by Chong et al. [69].

2.3.3 Comparison with CST MWS

A further comparison of the model has been carried out using the transient solver of CST MICROWAVE STUDIO (MWS), the time-domain proprietary method based on the finite integration technique [32]. The transient solver is a general-purpose 3D electromagnetic simulator, also suitable for waveguide problems provided that the electrical size of the domain is not much larger than the minimum wavelength in vacuum.

A Bragg reflector with $a_0 = 1.5$ mm, $\Lambda = 617$ μm, $L = 50\Lambda$, and $b_0 = 20$ μm has been studied in the range 245÷265 GHz; it is designed to reflect the TE_{11} mode at 250 GHz. The dimensions are acceptable for CST MWS, where electric and magnetic planes of symmetry were also inserted to reduce the simulation domain. The structure that was built in the software CAD is shown in Fig. 2.8 together with the symmetry planes. At the central frequency of the bandwidth under investigation, there are 18 modes above cutoff which become 32 if degenerate modes with orthogonal polarization,

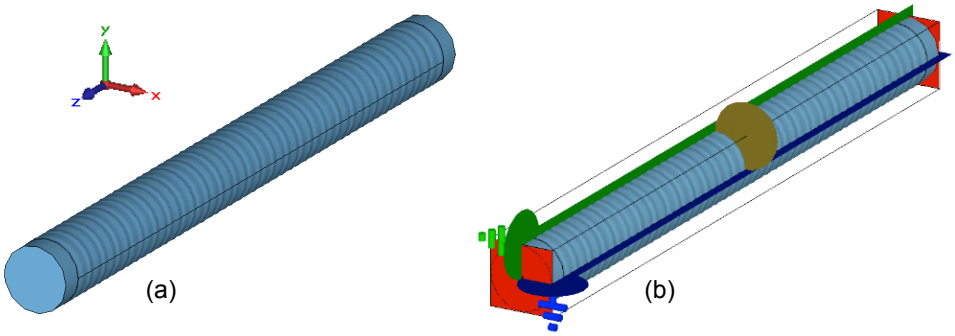

Figure 2.8: Bragg reflector with a_0=1.5 mm, Λ=617 μm, L=50Λ, and b_0=20 μm: structure built in CST MWS (a) and electric (green) and magnetic (blue) symmetry planes (b).

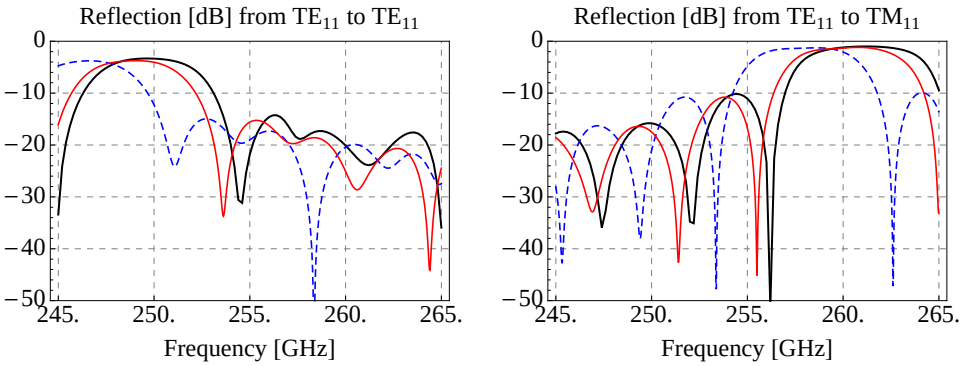

Figure 2.9: Reflection predicted by the coupled-mode theory (black) and by CST MWS with 10 (blue dashed) and 20 (red) lines per wavelength for the Bragg reflector of Fig. 2.8.

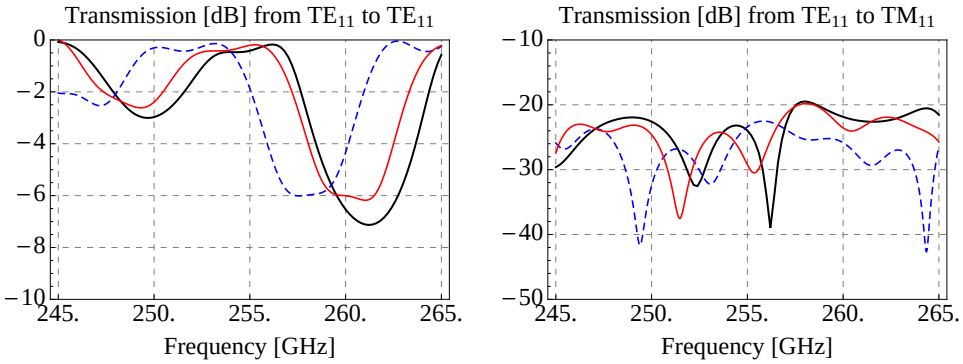

Figure 2.10: Transmission predicted by the coupled-mode theory (black) and by CST MWS with 10 (blue dashed) and 20 (red) lines per wavelength for the Bragg reflector of Fig. 2.8.

i.e. TE_{nm} and TM_{nm} modes with n>0, are considered. All these modes should be included in the simulation with CST MWS to get reliable results, nevertheless the symmetry planes cancel degenerate modes as well as all TE_{nm} and TM_{nm} with n even and the computations can be run with only 8 modes. This simplification is justified by the fact that, according to the coupled-mode theory, the coupling coefficients between modes with different azimuthal index vanish.

The standard meshing global parameters in CST MWS are set to 10 lines per wavelength with a lower mesh limit of 10. These values give rather inaccurate results because they cause a shift of the resonances towards lower frequencies; by setting both parameters to at least 20, the outcomes become more reliable and the agreement with the coupled-mode equations significantly improves. This can be appreciated by comparing the scattering parameters of the modes that mostly interact, namely the TE_{11}, which

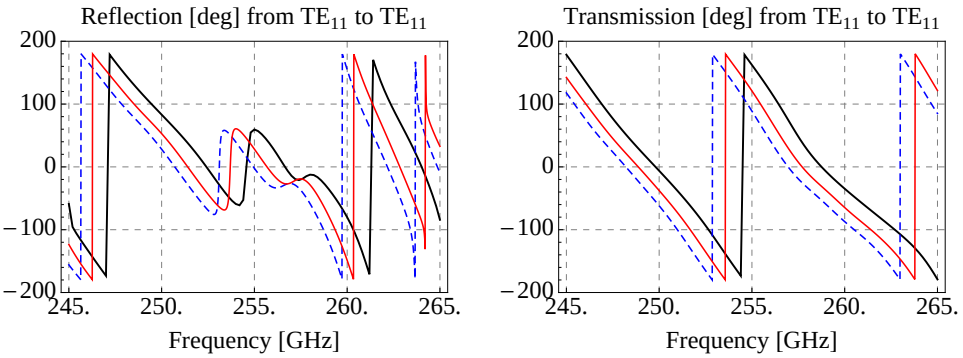

Figure 2.11: Phase of the reflection and transmission coefficients predicted by the coupled-mode theory (black) and by CST MWS with 15 (blue dashed) and 20 (red) lines per wavelength for the reflector of Fig. 2.8.

excites the reflector, and the TM_{11}. Fig. 2.9 reports the reflection coefficients relevant to these modes calculated with the coupled-mode theory and with CST MWS using different meshing settings. The outcomes of the same simulations are similarly overlapped in Fig. 2.10 in terms of transmission coefficients.

If the discretization in CST MWS is fine enough, a good agreement is obtained with the coupled-mode theory with reference to the amplitude of the scattering parameters. As far as the phase is concerned, the predictions of the two methods are shown in Fig. 2.11 for the reflection and transmission coefficients of the fundamental mode. A difference of 180 deg was found in (2.68) when comparing the coupling constants derived here with the ones given in [67] and [69]. Nevertheless the match with CST MWS in Fig. 2.11 is good, demonstrating the full correctness of the coupling constants derived in this document. In CST MWS input and output waveguides are needed to avoid issues generated by evanescent modes; these smooth-wall waveguides have been set with a radius of $a_0 + b_0$ because the comparison is carried out with reference to a reflector with a cosine ripple profile. Built-in de-embedding operations in CST MWS enable to remove the contribution due to the input and output sections, which are 1 mm in length, in the phase of the scattering parameters. Similar comparisons using sinusoidal corrugations also returned a good agreement.

2.4 Analysis of a Resonant Cavity

A resonant cavity can be created by placing a section of straight, smooth-wall waveguide between two Bragg reflectors and used for microwave amplification by stimulated emission of radiation (MASER). The operational waveguide mode, which takes energy at the expenses of an electron beam passing through the structure, is ideally trapped between the Bragg reflectors and grows after each round trip. Similarly to RLC circuits, the energy in the cavity reaches stationary conditions owing to losses arising from the wave leakage at the mirrors and attenuation by imperfect conductors.

As depicted in Fig. 2.12, the mirror on the gun-side, i.e. facing the origin of the beam, is called upstream reflector; the one on the opposite position, i.e. the window-side, is named downstream reflector. The former has to provide high confinement (reflectivity ≈99%), whereas the latter is partially transmitting (reflectivity ≈90%) to permit the wave to escape and reach the vacuum window.

The main characteristics of a resonator are its eigenfrequencies and quality factors. The former are obtained requiring that the phase change of a mode in one round trip of the resonator is an integer multiple of 2π. For a cavity having a smooth-wall section of length d and ideal reflectors with negligible length, the eigenfrequencies can be found from the condition:

$$\phi_u(\omega) + \phi_d(\omega) + 2\beta_i d = 2m\pi, \qquad m = 0, \pm 1, \pm 2, \ldots$$

where ϕ_u and ϕ_d are the phases of the reflection coefficients of the upstream and downstream mirrors, respectively. Real resonators employ reflectors with finite length and feature additional eigenfrequencies which can be found with a deeper, self-consistent analysis. Similar considerations apply to the Q-factor, which is defined as the ratio between the energy stored in the resonator to the average power loss in a cycle:

$$Q = \omega_r \frac{W_{\text{stored}}}{P_{\text{loss}}} \tag{2.69}$$

where ω_r is the resonance frequency. Under some approximations, we can give the Q-factor a simple, closed-form expression, but an accurate calculation has to adopt the more complicated formalism that is described in the following.

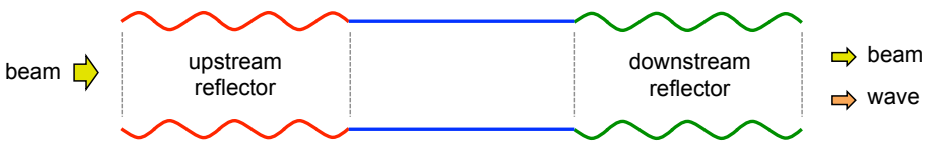

Figure 2.12: Schematic layout of a cavity based on Bragg reflectors.

2.4.1 Eigenvalue/eigenvector method

In section 2.2.4, we derived the following system of differential equations for lossy Bragg reflectors with a generic ripple profile and Bratman's formalism:

$$\begin{cases} \dfrac{dB_i^+}{dz} = -\left(\iota\dfrac{\Delta_{ii}}{2} + \alpha_i\right) B_i^+ - \iota \displaystyle\sum_p G_{ip}^* B_p^- \\ \dfrac{dB_i^-}{dz} = \left(\iota\dfrac{\Delta_{ii}}{2} + \alpha_i\right) B_i^- + \iota \displaystyle\sum_p G_{ip} B_p^+ \end{cases}$$

where $B^{\pm}$ are the amplitudes of forward and backward waves, Δ_{ii} the mismatch parameter defined in (2.59), α_i the attenuation constants given in (2.62) and G_{ip} the coupling constants summarized in (2.63) for sinusoidal corrugations. By considering the interaction between N modes in the lossless case, the previous system can be written in matrix form as follows:

$$\frac{d}{dz}\begin{bmatrix} B_1^+ \\ B_1^- \\ \vdots \\ B_N^+ \\ B_N^- \end{bmatrix} = \begin{bmatrix} -\iota\frac{\Delta_{11}}{2} & -\iota G_{11}^* & \cdots & 0 & -\iota G_{1N}^* \\ \iota G_{11} & \iota\frac{\Delta_{11}}{2} & \cdots & \iota G_{1N} & 0 \\ \vdots & \vdots & \ddots & \vdots & \vdots \\ 0 & -\iota G_{N1}^* & \cdots & -\iota\frac{\Delta_{NN}}{2} & -\iota G_{NN}^* \\ \iota G_{N1} & 0 & \cdots & \iota G_{NN} & \iota\frac{\Delta_{NN}}{2} \end{bmatrix} \cdot \begin{bmatrix} B_1^+ \\ B_1^- \\ \vdots \\ B_N^+ \\ B_N^- \end{bmatrix}$$

namely as

$$\frac{d}{dz}(\mathbf{B}) = \underline{\mathbf{M}} \cdot \mathbf{B} \tag{2.70}$$

where, in presence of losses, the coupling matrix $\underline{\mathbf{M}}$ becomes

$$\underline{\mathbf{M}} = \begin{bmatrix} -\iota\frac{\Delta_{11}}{2} - \alpha_1 & -\iota G_{11}^* & \cdots & 0 & -\iota G_{1N}^* \\ \iota G_{11} & \iota\frac{\Delta_{11}}{2} + \alpha_1 & \cdots & \iota G_{1N} & 0 \\ \vdots & \vdots & \ddots & \vdots & \vdots \\ 0 & -\iota G_{N1}^* & \cdots & -\iota\frac{\Delta_{NN}}{2} - \alpha_N & -\iota G_{NN}^* \\ \iota G_{N1} & 0 & \cdots & \iota G_{NN} & \iota\frac{\Delta_{NN}}{2} + \alpha_N \end{bmatrix}$$

Such a linear system can be solved letting the wave amplitudes satisfy $B \propto \mathrm{e}^{kz}$, where k is a complex constant. This position converts the (2.70) into

$$(\underline{\mathbf{M}} - k\underline{\mathbf{I}}) \cdot \mathbf{v} = \mathbf{0} \tag{2.71}$$

being $\underline{\mathbf{I}}$ the identity matrix; the (2.71) is a classical problem with eigenvalues k_i and eigenvectors $\mathbf{v}_i$. Once obtained k_i and $\mathbf{v}_i$ with the standard techniques of matrix algebra, the amplitude vector can be expressed at any position of the reflector as a linear combination of eigenvectors with coefficients w_i

$$\begin{bmatrix} B_1^+ \\ B_1^- \\ \vdots \\ B_N^- \end{bmatrix} = \begin{bmatrix} v_{1,1} \\ v_{2,1} \\ \vdots \\ v_{2N,1} \end{bmatrix} w_1 \mathrm{e}^{k_1 z} + \begin{bmatrix} v_{1,2} \\ v_{2,2} \\ \vdots \\ v_{2N,2} \end{bmatrix} w_2 \mathrm{e}^{k_2 z} + \ldots + \begin{bmatrix} v_{1,2N} \\ v_{2,2N} \\ \vdots \\ v_{2N,2N} \end{bmatrix} w_{2N} \mathrm{e}^{k_{2N} z}$$

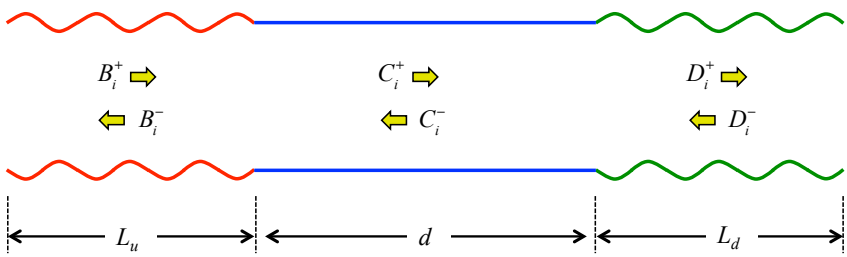

Figure 2.13: Forward and backward waves propagating in the resonator.

namely

$$\mathbf{B} = \sum_{i=1}^{2N} w_i \mathbf{v}_i \mathrm{e}^{k_i z}$$

The constants w_i are determined by the boundary conditions on $B_i^{\pm}(z)$ that, if the first mode excites the reflector, are

$$B_i^+(0) = B_i^-(L) = 0 \qquad \forall i \quad \text{except for} \quad B_1^+(0) = 1$$

In the straight section of a smooth-wall waveguide, modes are uncoupled and the interaction matrix $\underline{\mathbf{G}}_c$, ruling the longitudinal variation of the wave amplitudes, is diagonal, i.e. the eigenvalues are the diagonal matrix terms. If the same N modes of the Bragg reflector are considered, we have

$$\underline{\mathbf{G}}_c = \begin{bmatrix} -\iota\beta_1 - \alpha_1 & 0 & \cdots & 0 & 0 \\ 0 & \iota\beta_1 + \alpha_1 & \cdots & 0 & 0 \\ \vdots & \vdots & \ddots & \vdots & \vdots \\ 0 & 0 & \cdots & -\iota\beta_N - \alpha_N & 0 \\ 0 & 0 & \cdots & 0 & \iota\beta_N + \alpha_N \end{bmatrix}$$

By combining the coupling matrices of smooth- and rippled-wall waveguides, we can build a system of differential equations that characterizes a resonator and self-consistently relates its wave amplitudes. If we refer to Fig. 2.13, the equations of the resonator are

$$\frac{d}{dz}\begin{bmatrix}\mathbf{B}\\ \mathbf{C}\\ \mathbf{D}\end{bmatrix} = \begin{bmatrix}\underline{\mathbf{G}}_u & 0 & 0\\ 0 & \underline{\mathbf{G}}_c & 0\\ 0 & 0 & \underline{\mathbf{G}}_d\end{bmatrix} \cdot \begin{bmatrix}\mathbf{B}\\ \mathbf{C}\\ \mathbf{D}\end{bmatrix} \tag{2.72}$$

where $\underline{\mathbf{G}}_u$, $\underline{\mathbf{G}}_c$ and $\underline{\mathbf{G}}_d$ indicate the coupling matrices of upstream reflector, smooth-wall section and downstream reflector, respectively. For N modes, the (2.72) is a system of $3\times2\times N$ differential equations and the same number of unknown wave amplitudes; it can be recast in compact form as

$$\frac{d}{dz}(\mathbf{P}) = \underline{\mathbf{M}} \cdot \mathbf{P}$$

with

$$\mathbf{P} = \begin{bmatrix} B_1^+ & B_1^- & B_2^+ & \cdots & B_N^- & C_1^+ & \cdots & C_N^- & D_1^+ & \cdots & D_N^+ & D_N^- \end{bmatrix}^T = \\ = \begin{bmatrix} P_1^+ & P_1^- & P_2^+ & \cdots & P_N^- & P_{N+1}^+ & \cdots & P_{2N}^- & P_{2N+1}^+ & \cdots & P_{3N}^+ & P_{3N}^- \end{bmatrix}^T$$

After reducing it to a linear system and calculating eigenvalues $\mathbf{k}$ and eigenvectors $\underline{\mathbf{v}}$, $6N$ boundary conditions are required to derive the coefficients w_i so that

$$\mathbf{P}(z) = \sum_{i=1}^{6N} w_i \mathbf{v}_i \mathrm{e}^{k_i z}$$

If the reference system is centred in the middle of the resonator with z ranging from $-(d/2 + L_u)$ to $(d/2 + L_d)$ and we excite with the first mode entering from the gun side, the boundary conditions are

- $P_1^+(-d/2 - L_u) = 1$, it gives the condition on the excitation mode;
- $P_n^+(-d/2 - L_u) = 0$ for $n = 2, 3, \ldots, N$, they consist on $N-1$ equations at the left end of the upstream reflector;
- $P_n^{\pm}(-d/2) = P_{N+n}^{\pm}(-d/2)$ for $n = 1, 2, \ldots, N$, they enforce the continuity of forward and backward waves at the interface between the upstream reflector and the smooth-wall section ($2N$ equations);
- $P_{N+n}^{\pm}(d/2) = P_{2N+n}^{\pm}(d/2)$ for $n = 1, 2, \ldots, N$, they give $2N$ conditions for the continuity of forward and backward waves at the interface between the smooth-wall waveguide and the downstream reflector;
- $P_{2N+n}^{-}(d/2 + L_d) = 0$ for $n = 1, 2, \ldots, N$, they give the last N equations due to the absence of waves entering from the downstream reflector.

2.4.2 Energy, losses and quality factor

The calculation of the quality factor according to the definition (2.69) implies the total knowledge of the electromagnetic field in a resonator made of perfect electric conductors; actually the magnetic field is enough to compute both the energy close to the resonance and the ohmic losses according to the perturbation method. The modal expansion of the fields given in (2.9) are here rewritten in a cylindrical coordinate system using N modes:

$$\mathbf{E_t} = \sum_{n=1}^{3N} V_n(z) \mathbf{e_t}_n(r, \phi) \qquad E_z = \sum_{n=1}^{3N} v_n(z) e_{zn}(r, \phi)$$

$$\mathbf{H_t} = \sum_{n=1}^{3N} I_n(z) \mathbf{h_t}_n(r, \phi) \qquad H_z = \sum_{n=1}^{3N} i_n(z) h_{zn}(r, \phi)$$

The unperturbed eigenmodes repeat after N, e.g. $\mathbf{e_t}_n = \mathbf{e_t}_{N+n} = \mathbf{e_t}_{2N+n}$, whereas the amplitudes vanish everywhere except in their relevant longitudinal section, i.e. $V_n = I_n = v_n = i_n = 0$ outside the following intervals

$$\begin{aligned} -L_u - d/2 < z < -d/2, &\quad \text{for } n = 1, 2, \ldots, N \\ -d/2 < z < d/2, &\quad \text{for } n = N+1, N+2, \ldots, 2N \\ d/2 < z < d/2 + L_d, &\quad \text{for } n = 2N+1, 2N+2, \ldots, 3N \end{aligned}$$

The normalized transverse components $\mathbf{e_t}_n$ and $\mathbf{h_t}_n$ satisfy the orthogonality relation (2.13), whereas for the longitudinal eigenfunctions the following relation applies:

$$\iint_S e_{zn} e_{zq} dS = \iint_S h_{zn} h_{zq} dS = \frac{k_{tn}^2}{\gamma_n} \frac{k_{tq}^2}{\gamma_q} \iint_S \Phi_n \Phi_q dS = \frac{k_{tn}^2}{\gamma_n^2} \delta_{nq} \tag{2.73}$$

The amplitudes of the transversal field components V_n and I_n can be expressed according to (2.14) and the Bratman's formalism as

$$\begin{cases} V_n(z) = \sqrt{Z_n} \left[P_n^+(z) \mathrm{e}^{-\iota \pi z / \Lambda_n} + P_n^-(z) \mathrm{e}^{\iota \pi z / \Lambda_n} \right] \\ I_n(z) = \sqrt{Y_n} \left[P_n^+(z) \mathrm{e}^{-\iota \pi z / \Lambda_n} - P_n^-(z) \mathrm{e}^{\iota \pi z / \Lambda_n} \right] \end{cases} \tag{2.74}$$

with

$$\Lambda_n = \begin{cases} \Lambda_u, & \text{for } n = 1, 2, \ldots, N \\ \infty, & \text{for } n = N+1, N+2, \ldots, 2N \\ \Lambda_d, & \text{for } n = 2N+1, 2N+2, \ldots, 3N \end{cases}$$

being Λ_u and Λ_d the ripple periods of the upstream and downstream reflector respectively. The amplitudes of the longitudinal field components v_n and i_n can be derived from the ones of the transversal fields by using the equations (2.7) and (2.8). We respectively multiply them by e_{zq} and h_{zq} and integrate over the waveguide cross-section as follows:

$$\iota \omega \varepsilon \iint_S E_z e_{zq} dS = \iint_S \nabla_t \cdot (\mathbf{H_t} \times \hat{\mathbf{z}}) e_{zq} dS \tag{2.75}$$

$$\iota \omega \mu \iint_S H_z h_{zq} dS = \iint_S \nabla_t \cdot (\hat{\mathbf{z}} \times \mathbf{E_t}) h_{zq} dS \tag{2.76}$$

The (2.75) is simplified using (2.28), (2.21), (2.16), (2.19), (2.13) and (2.73):

$$\iota\omega\varepsilon \iint_S E_z e_{zq} dS = \iint_S \nabla_t \cdot (\mathbf{H_t} \times \hat{\mathbf{z}}) e_{zq} dS$$

$$\iota\omega\varepsilon \iint_S E_z e_{zq} dS = \cancel{\oint_{\partial S} e_{zq} (\mathbf{H_t} \times \hat{\mathbf{z}} \cdot \hat{\mathbf{n}}) ds} - \iint_S (\mathbf{H_t} \times \hat{\mathbf{z}}) \cdot \nabla_t e_{zq} dS$$

$$\iota\omega\varepsilon \sum_{n=1}^{3N} v_n \iint_S e_{zn} e_{zq} dS = -\sum_{n=1}^{3N} I_n \iint_S (\mathbf{h_t}_n \times \hat{\mathbf{z}}) \cdot \nabla_t e_{zq} dS$$

$$\iota\omega\varepsilon \sum_{n=1}^{3N} v_n \frac{k_{tn}^2}{\gamma_n^2} \delta_{nq} = -\frac{k_{tp}^2}{\gamma_p} \sum_{n=1}^{3N} I_n \iint_S \mathbf{e_t}_n \cdot \mathbf{e_t}_q dS$$

$$\iota\omega\varepsilon \frac{k_{tp}^2}{\gamma_p^2} v_p = -\frac{k_{tp}^2}{\gamma_p} I_p$$

The (2.76) is simplified using (2.28), (2.24), (2.16), (2.19), (2.13) and (2.73):

$$\iota\omega\mu \iint_S H_z h_{zq} dS = \iint_S \nabla_t \cdot (\hat{\mathbf{z}} \times \mathbf{E_t}) h_{zq} dS$$

$$\iota\omega\mu \iint_S H_z h_{zq} dS = \oint_{\partial S} h_{zq} (\hat{\mathbf{z}} \times \mathbf{E_t} \cdot \hat{\mathbf{n}}) ds - \iint_S (\hat{\mathbf{z}} \times \mathbf{E_t}) \cdot \nabla_t h_{zq} dS$$

$$\iota\omega\mu \iint_S H_z h_{zq} dS = \cancel{\oint_{\partial S} h_{zq} (-\hat{\mathbf{s}} \cdot \mathbf{E_t}) ds} - \iint_S (\hat{\mathbf{z}} \times \mathbf{E_t}) \cdot \nabla_t h_{zq} dS$$

$$\iota\omega\mu \sum_{n=1}^{3N} i_n \iint_S h_{zn} h_{zq} dS = -\frac{k_{tp}^2}{\gamma_p} \sum_{n=1}^{3N} V_n \iint_S (\hat{\mathbf{z}} \times \mathbf{e_t}_n) \cdot \mathbf{h_t}_q dS$$

$$\iota\omega\mu \frac{k_{tp}^2}{\gamma_p^2} i_p = -\frac{k_{tp}^2}{\gamma_p} V_p$$

Using (2.15), the previous relations can be summarized as follows

$$v_p = -Z_n I_p \qquad \text{and} \qquad i_p = -Y_n V_p \tag{2.77}$$

With (2.74) and (2.77), the total electromagnetic field is determined in any position of the resonator.

The energy stored in the cavity with volume τ is the sum of the electric and magnetic energy, which are respectively defined as

$$W_E = \frac{\varepsilon}{4} \iiint_\tau \mathbf{E} \cdot \mathbf{E}^* d\tau \tag{2.78}$$

and

$$W_H = \frac{\mu}{4} \iiint_\tau \mathbf{H} \cdot \mathbf{H}^* d\tau \tag{2.79}$$

Both expressions can be simplified using the modal expansions and the orthogonality relations; the (2.78) becomes

$$\begin{aligned}
W_E &= \frac{\varepsilon}{4}\iiint_\tau \left(\sum_{n=1}^{3N} V_n \mathbf{e}_{\mathbf{t}n} + v_n \mathbf{e}_{\mathbf{z}n}\right)\left(\sum_{q=1}^{3N} V_q \mathbf{e}_{\mathbf{t}q} + v_q \mathbf{e}_{\mathbf{z}q}\right)^* d\tau \\
&= \frac{\varepsilon}{4}\sum_{n=1}^{3N}\sum_{q=1}^{3N}\iiint_\tau \left(V_n \mathbf{e}_{\mathbf{t}n} + v_n \mathbf{e}_{\mathbf{z}n}\right)\left(V_q \mathbf{e}_{\mathbf{t}q} + v_q \mathbf{e}_{\mathbf{z}q}\right)^* d\tau \\
&= \frac{\varepsilon}{4}\sum_{n=1}^{3N}\sum_{q=1}^{3N}\iiint_\tau \left(V_n V_q^* \mathbf{e}_{\mathbf{t}n}\cdot\mathbf{e}_{\mathbf{t}q}^* + v_n v_q^* \mathbf{e}_{\mathbf{z}n}\cdot\mathbf{e}_{\mathbf{z}q}^*\right) d\tau \\
&= \frac{\varepsilon}{4}\sum_{n=1}^{3N}\sum_{q=1}^{3N}\left[\left(\int_{-L_u-d/2}^{d/2+L_d} V_n V_q^* dz\right)\left(\iint_S \mathbf{e}_{\mathbf{t}n}\cdot\mathbf{e}_{\mathbf{t}q}^* dS\right) + \right. \\
&\qquad \left. + \left(\int_{-L_u-d/2}^{d/2+L_d} v_n v_q^* dz\right)\left(\iint_S \mathbf{e}_{\mathbf{z}n}\cdot\mathbf{e}_{\mathbf{z}q}^* dS\right)\right] \\
&= \frac{\varepsilon}{4}\sum_{n=1}^{3N}\left(\int_{-L_u-d/2}^{d/2+L_d} |V_n|^2 dz + \left|\frac{k_{tn}}{\gamma_n}\right|^2 \int_{-L_u-d/2}^{d/2+L_d} |v_n|^2 dz\right)
\end{aligned}$$

and using (2.77), we get

$$W_E = \frac{\varepsilon}{4}\sum_{n=1}^{3N}\int_{-L_u-d/2}^{d/2+L_d}\left(|V_n|^2 + \left|\frac{k_{tn}}{\omega\varepsilon} I_n\right|^2\right) dz$$

Following a similar procedure, the (2.79) can be written as

$$W_H = \frac{\mu}{4}\sum_{n=1}^{3N}\int_{-L_u-d/2}^{d/2+L_d}\left(|I_n|^2 + \left|\frac{k_{tn}}{\omega\mu} V_n\right|^2\right) dz$$

At the resonance, $W_E = W_H$ as in the case of a resonant LC circuit.

The sources of loss in the resonator are two: the power leakages from the reflectors and the ohmic losses. The former are the real part of the flux of the Poynting vector that leaves the structure along the z axis:

$$P_{\text{leak}} = \frac{1}{2}\sum_{i=1}^{N}\left(\left|B_i^-(z=-L_u-d/2)\right|^2 + \left|D_i^+(z=d/2+L_d)\right|^2\right) \tag{2.80}$$

The latter are the real part of the flux of the Poynting vector across the conductors:

$$P_{\text{ohmic}} = \frac{1}{2}\mathcal{R}\!e\left\{\int_{z=-L_u-d/2}^{d/2+L_u}\int_{\phi=0}^{2\pi} \mathbf{E}\times\mathbf{H}^*\cdot\hat{\mathbf{r}}\, a\, d\phi\, dz\right\} \tag{2.81}$$

Usually $P_{\text{leak}} \gg P_{\text{ohmic}}$. The (2.81) can be simplified using the Leontovich's condition for good conductors and the modal expansions:

$$\begin{aligned}
&\frac{1}{2}\mathcal{R}e\left\{\sqrt{\frac{\mu}{\varepsilon+\frac{\sigma}{\iota\omega}}}\int_{z=-L_u-d/2}^{d/2+L_u}\int_{\phi=0}^{2\pi}(\mathbf{H}^*\times\hat{\mathbf{r}})\cdot(\mathbf{H}\times\hat{\mathbf{r}})\Big|_{r=a} ad\phi dz\right\} = \\
=&\frac{1}{2}\mathcal{R}e\left\{\frac{1+\iota}{\sqrt{2}}\sqrt{\frac{\mu\omega}{\sigma}}\right\}\int_{z=-L_u-d/2}^{d/2+L_u}\int_{\phi=0}^{2\pi}|\mathbf{H}\times\hat{\mathbf{r}}|^2_{r=a}\, ad\phi dz = \\
=&\frac{R_S}{2}\int_{z=-L_u-d/2}^{d/2+L_u}\int_{\phi=0}^{2\pi}\left|\sum_{n=1}^{3N}\left(I_n\mathbf{h}_{\phi_n}+i_n\mathbf{h}_{\mathbf{z}n}\right)\right|^2_{r=a} ad\phi dz
\end{aligned}$$

where

$$R_s=\sqrt{\frac{\mu\omega}{2\sigma}}$$

is the surface resistance with σ [S/m] = electrical conductivity. The expression of P_{ohmic} can be further developed as follows

$$\begin{aligned}
&\sum_{n=1}^{3N}\sum_{q=1}^{3N}\int_{z=-L_u-d/2}^{d/2+L_u}\int_{\phi=0}^{2\pi}\left(I_nI_q^*h_{\phi_n}h_{\phi_q}^*+i_ni_q^*h_{zn}h_{zq}^*\right)\Big|_{r=a} ad\phi dz = \\
=&\sum_{n=1}^{3N}\sum_{q=1}^{3N}\left(\int_{-L_u-d/2}^{d/2+L_u}I_nI_q^*dz\cdot\int_0^{2\pi}h_{\phi_n}h_{\phi_q}^*\Big|_{r=a} ad\phi+\right. \\
&\left.+\int_{-L_u-d/2}^{d/2+L_u}i_ni_q^*dz\cdot\int_0^{2\pi}h_{zn}h_{zq}^*\Big|_{r=a} ad\phi\right)
\end{aligned}$$

According to (2.42) and (2.10), the eigenfunctions for $r=a$ are

	TE modes	TM modes
$h_{\phi_n}=h_{\phi\ell m}=$	$\frac{\ell}{a}\frac{\sqrt{2}\sin(\ell\phi+\phi_1)}{\sqrt{\epsilon_0\ell\pi}\sqrt{u'^2_{\ell m}-\ell^2}}$	$\frac{1}{a}\frac{\sqrt{2}\sin(\ell\phi+\phi_2)}{\sqrt{\epsilon_0\ell\pi}}$
$h_{zn}=h_{z\ell m}=$	$-\frac{u'^2_{\ell m}}{\iota\beta_{\ell m}a^2}\frac{\sqrt{2}\sin(\ell\phi+\phi_1)}{\sqrt{\epsilon_0\ell\pi}\sqrt{u'^2_{\ell m}-\ell^2}}$	0

and the integrals along the azimuthal coordinate give

$$\Upsilon_{nq}^{(\phi)}=\int_0^{2\pi}h_{\phi_n}h_{\phi_q}^*\Big|_{r=a} ad\phi=\begin{cases}\frac{2}{a}\delta_{\ell q}\frac{\ell q}{\sqrt{u'^2_{\ell m}-\ell^2}\sqrt{u'^2_{qp}-q^2}} & \text{TE-TE}\\ \frac{2}{a}\delta_{\ell q} & \text{TM-TM}\\ \frac{2}{a}\delta_{\ell q}\frac{\ell}{\sqrt{u'^2_{\ell m}-\ell^2}} & \text{TE-TM}\end{cases}$$

and

$$\Upsilon_{nq}^{(z)} = \int_0^{2\pi} h_{zn} h_{zq}^* \Big|_{r=a} a d\phi = \begin{cases} \dfrac{2\delta_{\ell q}}{\beta_{\ell m}\beta_{qp}} \dfrac{u'^2_{\ell m} u'^2_{qp}/a^3}{\sqrt{u'^2_{\ell m} - \ell^2}\sqrt{u'^2_{qp} - q^2}} & \text{TE-TE} \\ 0 & \text{TM-TM} \\ 0 & \text{TE-TM} \end{cases}$$

The final expression for losses due to imperfect conductors is

$$P_{\text{ohmic}} = \frac{R_s}{2} \sum_{n=1}^{3N} \sum_{q=1}^{3N} \int_{-L_u - d/2}^{d/2 + L_u} \left(I_n I_q^* \Upsilon_{nq}^{(\phi)} + i_n i_q^* \Upsilon_{nq}^{(z)} \right) dz \tag{2.82}$$

The computation of the previous integral can be heavy from the numerical viewpoint and a different approach is usually preferable. The alternative method consists in re-calculating the wave amplitudes in the case of lossy conductors; the average power loss in a cycle is then obtained as

$$P_{\text{ohmic}} = \frac{1}{2} \left[1 - \sum_{n=1}^{N} \left(\left| B_n^-(-L_u - d/2) \right|^2 + \left| D_n^+(d/2 + L_d) \right|^2 \right) \right] \tag{2.83}$$

Leakage and ohmic losses give the following quality factors:

$$Q_{\text{leak}} = \omega \frac{W_E + W_H}{P_{\text{leak}}} \qquad \text{and} \qquad Q_{\text{ohmic}} = \omega \frac{W_E + W_H}{P_{\text{ohmic}}}$$

The total quality factor is derived with the following rule:

$$Q_{\text{tot}} = \left(\frac{1}{Q_{\text{leak}}} + \frac{1}{Q_{\text{ohmic}}} + \frac{1}{Q_{\text{ext}}} \right)^{-1}$$

where the external Q-factor due to a possible load has been included too.

A simple, approximate formula of the quality factor at the resonance can be derived neglecting ohmic losses since usually $Q_{\text{leak}} \ll Q_{\text{ohmic}}$. We consider a single TE mode and assume almost ideal mirrors such that

$$\begin{aligned} G_u L_u &\gg 1, & R_u &\approx 1 \\ G_d L_d &\gg 1, & R_d &\approx 1 \end{aligned}$$

where G_u and G_d are the coupling constants in the upstream and downstream reflectors respectively. With these positions, the electromagnetic field rapidly decays in the resonators and is mostly concentrated in the smooth-wall section. The amplitude of the electric field is

$$V_2(z) = \sqrt{Z_1} \left[C_1^+(z) + C_1^-(z) \right] = \sqrt{Z_1} \left[\overline{C}_1^+ \mathrm{e}^{-\iota\beta_1 z} + \overline{C}_1^- \mathrm{e}^{\iota\beta_1 z} \right]$$

where the horizontal bars over the C indicate the phasors independent of z. Owing to the boundary conditions $V_2(-d/2) \approx V_2(d/2) \approx 0$, a stationary wave sets up with $\beta_z = m\pi/d$ ($m = 1, 2, \ldots$). The electric energy becomes

$$\begin{aligned} W_E &= \frac{\varepsilon}{4} \iiint_\tau |\mathbf{E}|^2 \, d\tau \approx \frac{\varepsilon}{4} \int_{-d/2}^{d/2} |V_2|^2 \, dz = \\ &= \frac{\varepsilon}{4} |Z_1| \int_{-d/2}^{d/2} \left|\overline{C}_1^+\right|^2 4 \sin^2\left(\frac{m\pi z}{d}\right) dz = \frac{\varepsilon}{4} \frac{\omega\mu}{\beta_1} \left|\overline{C}_1^+\right|^2 4 \frac{d}{2} = \\ &= \frac{\omega/c^2}{2\beta_1} d \left|\overline{C}_1^+\right|^2 \end{aligned}$$

If T_u and T_d are the transmissivities of the upstream and downstream reflectors respectively, the expression (2.80) for leakage losses can be written

$$\begin{aligned} P_{\text{leak}} &= \frac{1}{2} \left(\left|B_1^-(-L_u - d/2)\right|^2 + \left|D_1^+(d/2 + L_d)\right|^2 \right) \approx \\ &\approx \frac{1}{2} \left(\left|T_u C_1^-(-d/2)\right|^2 + \left|T_d D_1^+(d/2)\right|^2 \right) = \\ &= \frac{1}{2} \left((1 - R_u) \left|C_1^-(-d/2)\right|^2 + (1 - R_d) \left|C_1^+(d/2)\right|^2 \right) = \\ &= \left|\overline{C}_1^+\right|^2 \frac{1 - R_u + 1 - R_d}{2} = \left|\overline{C}_1^+\right|^2 \left(1 - \frac{R_u + R_d}{2}\right) \approx \\ &\approx \left|\overline{C}_1^+\right|^2 \left(1 - \sqrt{R_u R_d}\right) \end{aligned}$$

Taking into account that at the resonance the total energy is twice the electric energy, the quality factor is

$$Q = \omega \frac{2\cancel{\left|\overline{C}_1^+\right|^2} \frac{\omega/c^2}{2\beta_1} d}{\cancel{\left|\overline{C}_1^+\right|^2} \left(1 - \sqrt{R_u R_d}\right)} = \frac{(\omega/c)^2}{\beta_1} \frac{d}{1 - \sqrt{R_u R_d}} \tag{2.84}$$

which is the expression given in [67] and [69]. Other authors [72] introduces an effective length

$$d_{\text{eff}} = d + \frac{1 - \mathrm{e}^{-G_u L_u}}{G_u} + \frac{1 - \mathrm{e}^{-G_d L_d}}{G_d}$$

to consider the field that exponentially decays in the resonator. The approximate formula of the quality factor is thus

$$Q = \frac{(\omega/c)^2}{\beta_1} \frac{d_{\text{eff}}}{1 - \sqrt{R_u R_d}} \tag{2.85}$$

2.4.3 Model validation against CST MWS

The model of the cavity has been benchmarked with CST MWS in the case of a small resonator with parameters reported in Table 2.1. It has two identical Bragg reflectors with sinusoidal profile; the CST model is depicted in Fig. 2.14. There are 7 propagating modes in a circular waveguide with $a_0 = 1$ mm at 250 GHz, but only the TM_{11} can interact with the TE_{11} in presence of circular corrugations. Both E- and H-plane symmetries have been used in CST MWS, where 30 lines per wavelength and an accuracy of -35 dB have been set among the hexahedral mesh properties and the transient solver parameters, respectively.

A comparison between the main scattering parameters is shown in Fig. 2.15. The resonator fed at one edge behaves like an electromagnetic band-gap material with a defect: it obstructs the propagation of the excitation mode within a frequency band centred at $\lambda_g = 2\Lambda$, but a transmission peak

Mode	TE_{11}
Frequency	250 GHz
Mean wall radius	1 mm
Center section length (d)	4 mm
Reflectors	
ripple depth (b_0)	25 μm
ripple period (Λ)	640.4 μm
length (L)	23 mm
reflectivity	58%

Table 2.1: Cavity parameters.

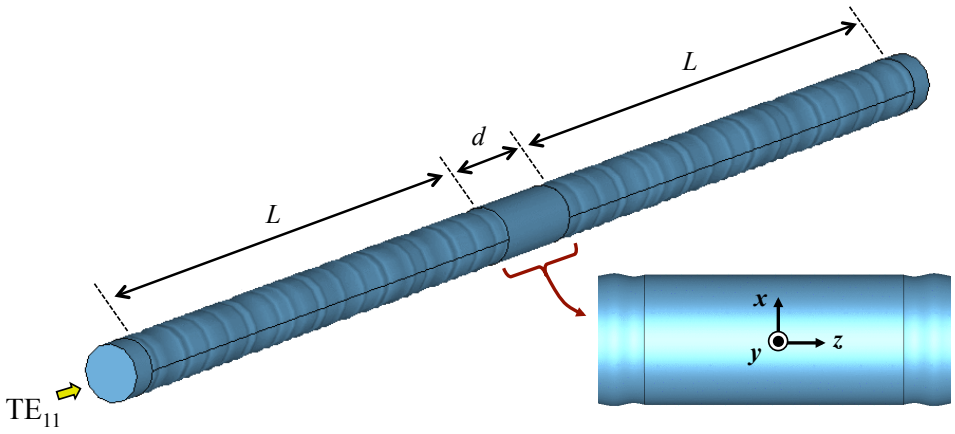

Figure 2.14: Cavity model in CST MWS with enlargement of the corrugation phases in the central section.

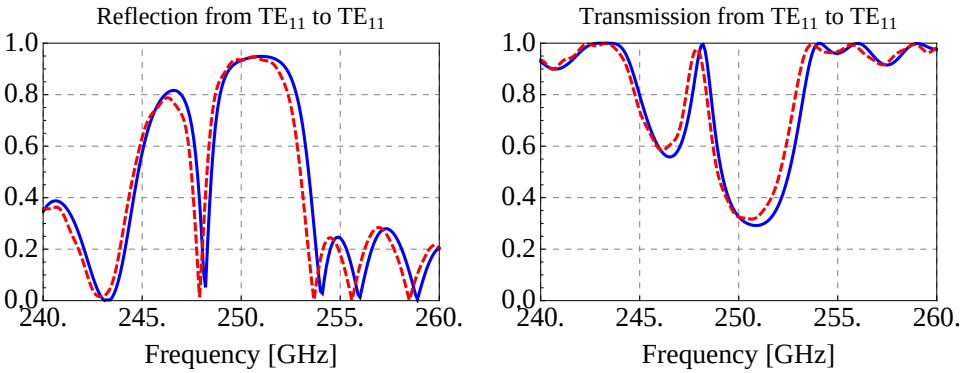

Figure 2.15: Reflection and transmission coefficients of the TE_{11} mode predicted by the coupled-mode theory (blue) and by CST MWS (red dashed) for the resonator of Table. 2.1.

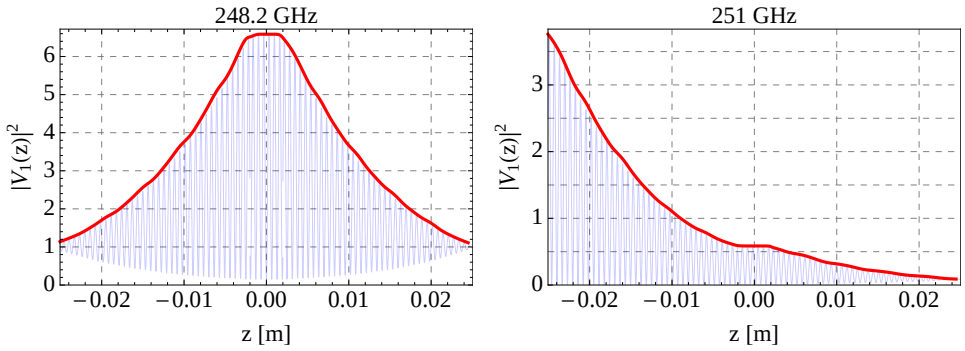

Figure 2.16: E-field squared amplitude $|V_1(z)|^2$ and its envelope along the resonator of Table. 2.1 at 248.2 GHz and 251 GHz.

emerges due to the interruption of periodicity caused by the smooth-wall section. In correspondence of the transmission peak, the E-field amplitude undergoes an amplification in the central part of the cavity because forward and backward waves sum in phase and accumulate energy inside the structure; on the contrary, when the reflection is very high, the field exponentially decays in the mirrors. This behaviour is elucidated in Fig. 2.16, where the envelope of $|V_1(z)|^2$ is depicted at two frequencies.

The electric and magnetic energies in CST MWS can be calculated using a set of monitors at different frequencies for each energy density, which is integrated over the volume as a postoprocessing operation in the software itself. The results are the peak energies which must be halved to derived the average stored energy in a cycle according to the harmonic time dependence. Electric and magnetic energies are identical in CST MWS and the agreement with the coupled-mode theory is rather good as shown in Fig. 2.17. Alternatively the total energy can be obtained, according to the perturba-

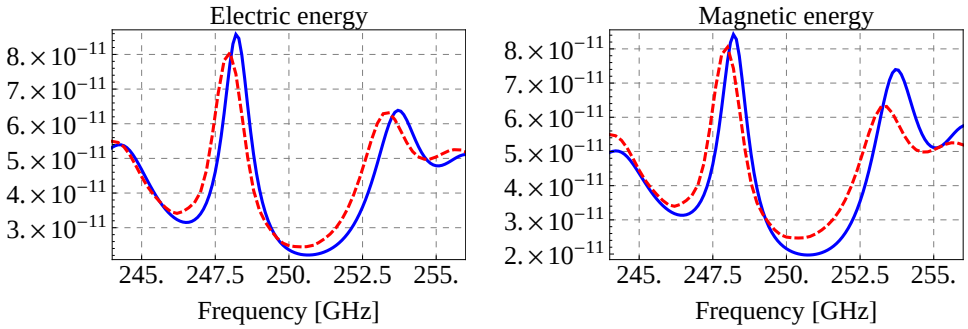

Figure 2.17: Total electric and magnetic energies [J] stored in a cycle predicted by the coupled-mode theory (blue) and by CST MWS (red dashed) for the resonator of Table. 2.1.

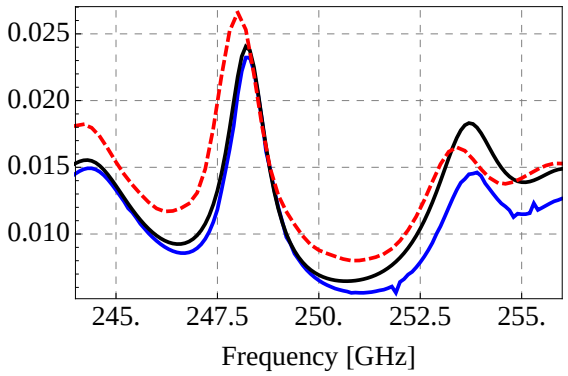

Figure 2.18: Average ohmic loss [W] in a cycle predicted by the coupled-mode theory according to (2.82) (blue) and (2.83) (black) and by CST MWS (red dashed) for the resonator of Table. 2.1.

tion method, by employing H-field monitors; no division by 2 is required in this case. The same approach allows the calculation of ohmic losses and Q_{ohmic}; the former are compared in Fig. 2.18 with the curves obtained by both (2.82) and (2.83). The matching between the two approaches is good at the resonance and gets worse at higher frequencies; the curves from CST MWS are also comparable: the absolute values are approximately similar but resonances are shifted.

We finally report the plot of the quality factor versus frequency, despite what is only important is the maximum value at the resonance. In Fig. 2.19 the quality factors due to leakage and conductor losses are depicted; as for the former, the results obtained with both integration and output waves are given. Owing to the very low performance of the Bragg reflectors in this cavity, there are orders of magnitude of difference between the diffractive and ohmic Q-factors. The leakage mostly determines the total quality factor which is plotted in Fig. 2.20. The approximate formulas (2.84) and (2.85)

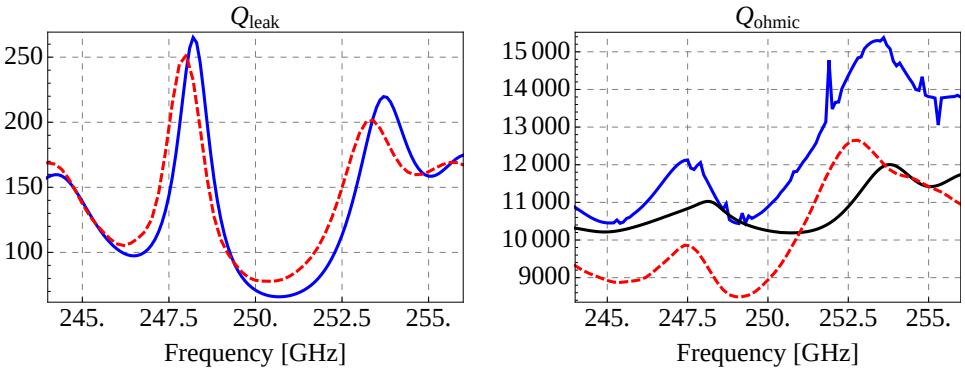

Figure 2.19: Q_{leak} and Q_{ohmic} calculated with the coupled-mode theory integrating the fields (blue) and with CST MWS (red dashed) for the resonator of Table. 2.1; in the case of Q_{ohmic} the result using (2.83) (black) is also shown.

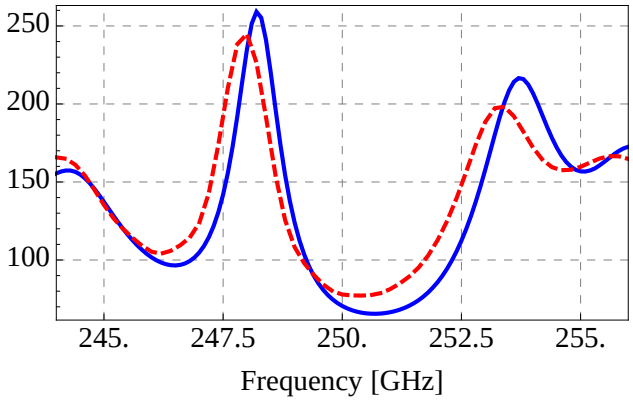

Figure 2.20: Q-factor predicted by the coupled-mode theory and by CST MWS (red dashed) for the resonator of Table. 2.1.

would instead give quality factors of 54 and 447 with a resonant frequency of 250 GHz. The quality factor could be also derived from the total energy as

$$Q_{\text{leak}} = \frac{f_r}{\Delta f} \approx \frac{248.22\text{GHz}}{0.93\text{GHz}} = 266.9$$

where Δf is the half-power bandwidth. Because of the low performance of the reflectors, in this case Δf has been taken at the half height between the maximum ($\approx 2 \times 8.5 \times 10^{-11}$) and the closest minimum ($\approx 2 \times 3 \times 10^{-11}$) of the quality factor.

2.4.4 Validation with a square ripple profile

Further comparison with other calculation methods has been performed using Bragg reflectors with square ripple profile. The latter is developed as a Fourier series where only the first term is retained, neglecting higher-order harmonics which are supposed to give no contribution. The reliability of this approximation is checked here by comparison with CST MWS and a mode-matching code for the cavity depicted in Fig. 2.21. It is worth noticing that the unperturbed radius along the mirrors is the radius of the smooth-wall section a_0 plus b_0.

Fig. 2.22 shows two transmissivity plots of the cavity. The one on the left compares the outputs of the coupled-mode theory, coded in MATHEMATICA [73], when the mean radius in the distributed reflectors is either a_0 or a_0+b_0; the latter case is also computed with a MATLAB implementation and shown in both plots of the figure. In the plot on the right, the calculations done with CST MWS and with a mode-matching code are also overlapped. All results are very similar apart from minor shifts of the transmission peak.

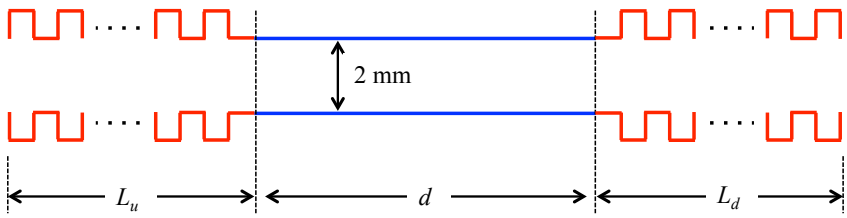

Figure 2.21: Cavity based on reflectors with square ripple profile: $d = 3.9$ mm, $L_u = L_d = 23.04$ mm (36 ripples with $\Lambda = 640$ μm, $b_0 = 25$ μm).

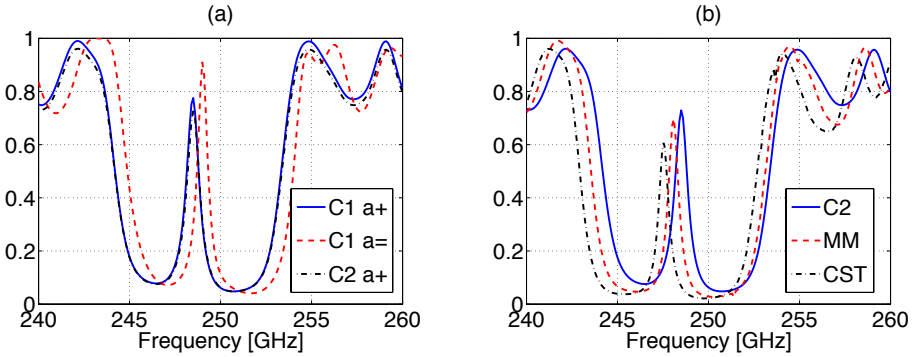

Figure 2.22: Transmissivity of the cavity of Fig. 2.21: a) computations with the coupled-mode theory coded in MATHEMATICA (C1) or MATLAB (C2) setting the mean radius in the mirrors to 1 (a=) or 1.025 (a+) mm; b) curves of the last case and outputs from CST MWS and the mode-matching method (MM).

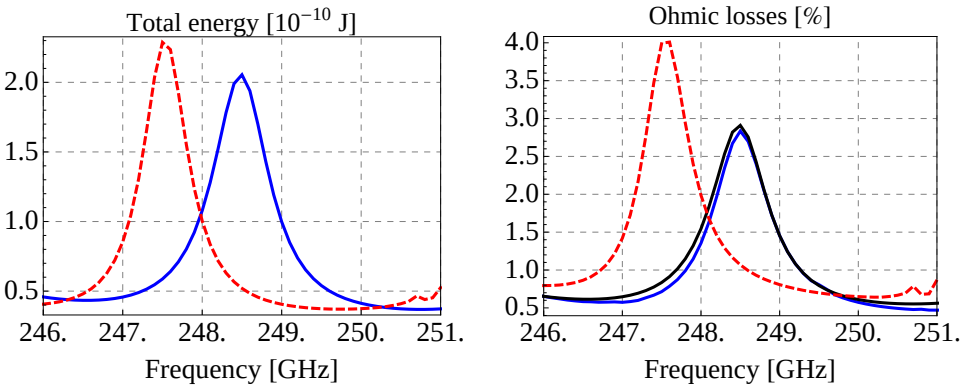

Figure 2.23: Comparison between CST MWS (red dashed) and the calculations by coupled-mode theory for energy and ohmic losses computed by integration (solid blue) and power balance (solid black) for the cavity of Fig. 2.21.

The computations with more realistic mean radius in the mirrors ($= a_0 + b_0$) give closer results to full-wave approaches; therefore the precise unperturbed radii have to be always set in order to improve the accuracy.

The total energy stored inside the cavity in a period and the ohmic losses on the cavity walls have been finally computed and compared to CST MWS; Fig. 2.23 reports this benchmark. As regards the total energy, the peak values are rather similar despite their positions are about 1 GHz apart; the higher reliability of a method over the other cannot be asserted, moreover the mode-matching method gave a transmission peak in between the predictions by CST MWS and the coupled-mode theory. Concerning the ohmic losses, both the computation with the flux of the Poynting vector across the metallic walls and the power balance with the standard attenuation constants provide very similar results. With reference to CST MWS, higher dissipation on the metallic walls is predicted.

2.5 Mode Converters by Coupled Forward Waves

We consider a circular waveguide the radius of which is a function of both z and ϕ; the dependence is in a form that allows the separation of variables:

$$a(\phi, z) = a_0 + b_0\, h(\phi)\, g(z) \tag{2.86}$$

The functions h and g vary in the range $[-1 \div 1]$ and the perturbation amplitude b_0 is negligible with respect to the unperturbed radius ($b_0 \ll a_0$). We can therefore approximate $a(\phi, z)$ with a_0 and deal with the modes of the unperturbed waveguide.

2.5.1 Transfer coefficients

The new transfer coefficients are derived following the procedure of section 2.1.4 and taking into account that $\tan\theta$ now depends on ϕ:

$$\tan\theta = \frac{da}{dz} = b_0\, \frac{dg}{dz}\, h = (\tan\theta)_z\, h$$

The function h has to be also integrated in equations from (2.35) to (2.39). We firstly consider the following dependence

$$h(\phi) = \cos(n_c\phi + \phi_3)$$

which reduces to the case $a = a(z)$ for $n_c = 0$ and $\phi_3 = 0$. The reference system can be always rotated in order to have $\phi_3 = 0$; this phasing is thus omitted in the following.

By using the normalized scalar potentials given by (2.42), the closed loop integral of (2.35) becomes for $\ell \neq 0$

$$\int_0^{2\pi} \cos^2(\ell\phi + \phi_1)\cos(n_c\phi)\, d\phi = \begin{cases} \pi, & n_c = 0 \\ \frac{\pi}{2}\cos(2\phi_1)\delta_{2\ell,n_c}, & n_c \neq 0 \end{cases} \tag{2.87}$$

The result of (2.87) reaches its peak values for two TE modes, orthogonally polarized, i.e. with either $\phi_1 = 0$ or $\phi_1 = \pi/2$. Since $T_{[p][p]} \propto \ell^2$, the case $\ell = 0$ is not worth being studied.

The integral of (2.36) becomes instead

$$\int_0^{2\pi} \sin^2(\ell\phi + \phi_2)\cos(n_c\phi)\, d\phi = \begin{cases} \pi\epsilon_{0,\ell}, & n_c = 0 \\ -\frac{\pi}{2}\cos(2\phi_2)\delta_{2\ell,n_c}, & n_c \neq 0 \end{cases} \tag{2.88}$$

If $\ell = 0$, the result is $2\pi\sin^2(\phi_2)\delta_{0,n_c}$ and it is included under the case $n_c = 0$ because circular modes have $\phi_{1,2} = \pi/2$. With reference to noncircular modes, the ones with $\phi_2 = 0$ and $\phi_2 = \pi/2$ lead to peak values of (2.88).

The cross integrals of (2.37) and (2.38) are similar and equal to

$$\int_0^{2\pi} \sin(\ell\phi+\phi_{1,2})\sin(q\phi+\phi'_{1,2})\cos(n_c\phi)\,d\phi = \\ = \begin{cases} \pi\epsilon_{0,\ell}, & n_c=0,\ \ell=q \\ \pi\sin(\phi'_{1,2}), & n_c\neq 0,\ \ell=0,\ q=n_c \\ \pi\sin(\phi_{1,2}), & n_c\neq 0,\ q=0,\ \ell=n_c \\ -\frac{\pi}{2}\cos(\phi_{1,2}+\phi'_{1,2}), & n_c\neq 0,\ \ell+q=n_c \\ \frac{\pi}{2}\cos(\phi_{1,2}-\phi'_{1,2}), & n_c\neq 0,\ |\ell-q|=n_c \\ 0, & \text{otherwise} \end{cases} \tag{2.89}$$

The solutions of (2.89) shows that only a single polarization of the TE (TM) modes gives the highest transfer coefficient from or to circular TE (TM) modes. If the x-axis is aligned to have $\phi_3 = 0$, the modes polarized along y only exchange energy with the circular modes of the same type.

Finally the integral (2.39) becomes

$$\int_0^{2\pi} \cos(\ell\phi+\phi_1)\sin(q\phi+\phi_2)\cos(n_c\phi)\,d\phi = \\ = \begin{cases} \pi\sin(\phi_2-\phi_1), & n_c=0,\ \ell=q \\ \pi\cos(\phi_1), & n_c\neq 0,\ q=0,\ \ell=n_c \\ \frac{\pi}{2}\sin(\phi_2+\phi_1), & n_c\neq 0,\ \ell+q=n_c \\ \frac{\pi}{2}\sin(\phi_2-\phi_1), & n_c\neq 0,\ |\ell-q|=n_c \\ 0, & \text{otherwise} \end{cases} \tag{2.90}$$

where the case $q = 0$ is not listed because $T_{[p](i)} \propto \ell$, i.e. TM modes with $q = n_c$ cannot transfer energy to $\mathrm{TE}_{0\mathrm{m}}$. On the contrary, there is coupling between TE modes with $\ell = n_c$ and polarization along x and $\mathrm{TM}_{0\mathrm{p}}$.

In section 2.1.4, the study was restricted to TM modes with $\phi_2 = \pi/2$ and TE modes with $\phi_1 = 0$ (except for circular TE modes that featured $\phi_1 = \pi/2$) because the use of the corresponding degenerate modes gives the same results. In the present case the same considerations apply only if circular electric modes are not involved; otherwise degenerate modes with different polarization must be considered. On one hand, TE and TM modes maximally interact when aligned on orthogonal axes; on the other hand circular electric and magnetic modes exhibit the peak values in the transfer coefficients when $|\phi_{1,2} - \phi_3| = \pi/2$. For the latter modes, the polarization angle is in-quadrature with respect to the initial phasing of the ripple.

Rather than their exact value, the main outcome of the previous integrals consists in the orthogonality properties of periodic functions. The transfer coefficients always vanish between modes that do not satisfy

$$|\ell \pm q| = n_c \tag{2.91}$$

This consideration can be also applied to different ripple profiles, because the function $h(\phi)$ must be periodic over 2π and is always characterized by a

number of azimuthal ripples n_c. Therefore the (2.91) provides a first design formula to choose n_c when the modes to couple are known.

In order to express the transfer coefficients in a circular waveguide with varying cross-section given by the (2.86), the following definitions are introduced:

$$\begin{aligned}
\text{hint}_c &= \frac{1}{\pi\epsilon_{0,\ell}} \int_0^{2\pi} \cos^2(\ell\phi + \phi_{\ell m}) h(\phi)\, d\phi \\
\text{hint}_s &= \frac{1}{\pi\epsilon_{0,\ell}} \int_0^{2\pi} \sin^2(\ell\phi + \phi_{\ell m}) h(\phi)\, d\phi \\
\text{hint}_{ss} &= \frac{1}{\pi\sqrt{\epsilon_{0,\ell}\ \epsilon_{0,q}}} \int_0^{2\pi} \sin(\ell\phi + \phi_{\ell m}) \sin(q\phi + \phi_{qp}) h(\phi)\, d\phi \\
\text{hint}_{cs} &= \frac{1}{\pi\sqrt{\epsilon_{0,\ell}\ \epsilon_{0,q}}} \int_0^{2\pi} \cos(\ell\phi + \phi_{\ell m}) \sin(q\phi + \phi_{qp}) h(\phi)\, d\phi
\end{aligned} \tag{2.92}$$

Under the assumption of small ripple amplitude and for $m \neq p$, we get

$$\begin{aligned}
T_{[\ell m][\ell m]} &= -\frac{(\tan\theta)_z}{a_0} \frac{\ell^2}{(u'^2_{\ell m} - \ell^2)} \text{hint}_c \\
T_{(\ell m)(\ell m)} &= -\frac{(\tan\theta)_z}{a_0} \text{hint}_s \\
T_{[\ell m][pq]} &= -\frac{(\tan\theta)_z}{a_0} \frac{2u'^2_{\ell m}}{u'^2_{qp} - u'^2_{\ell m}} \frac{\sqrt{u'^2_{qp} - q^2}}{\sqrt{u'^2_{\ell m} - \ell^2}} \text{hint}_{ss} \\
T_{(\ell m)(pq)} &= -\frac{(\tan\theta)_z}{a_0} \frac{2u^2_{qp}}{u^2_{qp} - u^2_{\ell m}} \text{hint}_{ss} \\
T_{[\ell m](pq)} &= -\frac{(\tan\theta)_z}{a_0} \frac{2\ell}{\sqrt{u'^2_{\ell m} - \ell^2}} \text{hint}_{cs} \\
T_{(\ell m)[pq]} &= 0
\end{aligned}$$

2.5.2 Coupling coefficients

We define the coefficients for contra-directional coupling as follows

$$c^-_{ip} = \frac{1}{2(\tan\theta)_z} \left(\sqrt{\frac{Z_p}{Z_i}} T_{pi} + \sqrt{\frac{Z_i}{Z_p}} T_{ip} - \frac{1}{Z_i} \frac{dZ_i}{dz} \delta_{ip} \right)$$

Apart from small changes, expressions similar to (2.63) are obtained; provided that $m \neq p$, the coefficients are

$$\begin{aligned}
c^{-}_{[\ell m][\ell m]} =& -\frac{1}{a_0}\left[\frac{\mathrm{hint}_c\,\ell^2}{(u'^2_{\ell m}-\ell^2)} - \frac{u'^2_{\ell m}}{2\beta^2_{\ell m}a_0^2}\right] \\
c^{-}_{(\ell m)(\ell m)} =& -\frac{1}{a_0}\left(\mathrm{hint}_s + \frac{u^2_{\ell m}}{2\beta^2_{\ell m}a_0^2}\right) \\
c^{-}_{[\ell m][pq]} =& \frac{\mathrm{hint}_{ss}}{a_0}\frac{u'^2_{\ell m}\sqrt{\frac{\beta_{qp}(u'^2_{qp}-q^2)}{\beta_{\ell m}(u'^2_{\ell m}-\ell^2)}} - u'^2_{qp}\sqrt{\frac{\beta_{\ell m}(u'^2_{\ell m}-\ell^2)}{\beta_{qp}(u'^2_{qp}-q^2)}}}{u'^2_{\ell m}-u'^2_{qp}} \\
c^{-}_{(\ell m)(pq)} =& \frac{\mathrm{hint}_{ss}}{a_0}\frac{u^2_{qp}\beta_{\ell m}-u^2_{\ell m}\beta_{qp}}{(u^2_{\ell m}-u^2_{qp})\sqrt{\beta_{\ell m}\beta_{qp}}} \\
c^{-}_{[\ell m](pq)} =& -\frac{\mathrm{hint}_{cs}}{a_0}\frac{\ell(\omega/c)}{\sqrt{\beta_{\ell m}\beta_{qp}}\sqrt{u'^2_{\ell m}-\ell^2}} \\
c^{-}_{(\ell m)[pq]} =& -\frac{\mathrm{hint}_{cs}}{a_0}\frac{\ell(\omega/c)}{\sqrt{\beta_{\ell m}\beta_{qp}}\sqrt{u'^2_{\ell m}-\ell^2}}
\end{aligned} \tag{2.93}$$

With reference to co-directional coupling, we define the coefficients as

$$c^{+}_{ip} = \frac{1}{2(\tan\theta)_z}\left(\sqrt{\frac{Z_p}{Z_i}}T_{pi} - \sqrt{\frac{Z_i}{Z_p}}T_{ip}\right)$$

which, after some manipulations, gives

$$\begin{aligned}
c^{+}_{[\ell m][\ell m]} =& 0 \\
c^{+}_{(\ell m)(\ell m)} =& 0 \\
c^{+}_{[\ell m][pq]} =& \frac{\mathrm{hint}_{ss}}{a_0}\frac{u'^2_{\ell m}\sqrt{\frac{\beta_{qp}(u'^2_{qp}-q^2)}{\beta_{\ell m}(u'^2_{\ell m}-\ell^2)}} + u'^2_{qp}\sqrt{\frac{\beta_{\ell m}(u'^2_{\ell m}-\ell^2)}{\beta_{qp}(u'^2_{qp}-q^2)}}}{u'^2_{\ell m}-u'^2_{qp}} \\
c^{+}_{(\ell m)(pq)} =& \frac{\mathrm{hint}_{ss}}{a_0}\frac{u^2_{qp}\beta_{\ell m}+u^2_{\ell m}\beta_{qp}}{(u^2_{\ell m}-u^2_{qp})\sqrt{\beta_{\ell m}\beta_{qp}}} \\
c^{+}_{[\ell m](pq)} =& \frac{\mathrm{hint}_{cs}}{a_0}\frac{\ell(\omega/c)}{\sqrt{\beta_{\ell m}\beta_{qp}}\sqrt{u'^2_{\ell m}-\ell^2}} \\
c^{+}_{(\ell m)[pq]} =& -\frac{\mathrm{hint}_{cs}}{a_0}\frac{\ell(\omega/c)}{\sqrt{\beta_{\ell m}\beta_{qp}}\sqrt{u'^2_{\ell m}-\ell^2}}
\end{aligned} \tag{2.94}$$

A preliminary check of the previous expressions can be done in terms of power conservation. We refer to the coupled-mode formalism in the simplest case of power exchange between two modes expressed through their

unperturbed eigenvectors and the complex amplitudes depending on z [74]. They obey relations of the type

$$\frac{dP_1}{dz} = c_{12}P_2\mathrm{e}^{-\iota\Delta z}$$
$$\frac{dP_2}{dz} = c_{21}P_1\mathrm{e}^{\iota\Delta z}$$

where the phase-mismatch constant Δ depends on the propagation constants as well as on the spatial variation of the coupling perturbation. The complex amplitudes are defined in such a way that $|P_1(z)|^2$ and $|P_2(z)|^2$ correspond to the power carried by each mode. The coupling coefficients c_{12} and c_{21} are determined by the physical situation under consideration, but they must adhere some general rules.

In case of co-directional coupling, i.e. both modes carry power in the same direction, the conservation of total power is expressed as

$$\frac{d}{dz}\left(|P_1(z)|^2 + |P_2(z)|^2\right) = 0$$

which implies

$$c_{12} = -c_{21}^* \tag{2.95}$$

As far as contra-directional coupling is concerned, the conservation of total power requires instead that

$$\frac{d}{dz}\left(|P_1(z)|^2 - |P_2(z)|^2\right) = 0$$

which implies

$$c_{12} = c_{21}^* \tag{2.96}$$

The expressions in (2.94) and (2.93) fulfil the (2.95) and (2.96), respectively.

Another useful general rule can be derived solving the system of differential equations for the co-directional coupling. The power is found to cyclically transfer between the two modes in a length of

$$L_p = \frac{\pi}{c_{12}^+}$$

2.5.3 Coupled-mode equations

We refer to the following coupled-mode equations

$$\begin{cases} \dfrac{df_i^+}{dz} = b_0\dfrac{dg}{dz}\displaystyle\sum_p \left[c_{ip}^+ f_p^+ \mathrm{e}^{-\iota(\beta_p-\beta_i)z} + c_{ip}^- f_p^- \mathrm{e}^{\iota(\beta_p+\beta_i)z}\right] \\ \dfrac{df_i^-}{dz} = b_0\dfrac{dg}{dz}\displaystyle\sum_p \left[c_{ip}^- f_p^+ \mathrm{e}^{-\iota(\beta_p+\beta_i)z} + c_{ip}^+ f_p^- \mathrm{e}^{\iota(\beta_p-\beta_i)z}\right] \end{cases} \tag{2.97}$$

which can be given in different forms according to the ripple profile along z and to the adopted approximations. The power transfer between two forward waves with nonzero coupling coefficient is maximum at the frequency that satisfies the in-phase matching condition

$$|\beta_i - \beta_p| = k_b = \frac{2\pi}{\Lambda} \tag{2.98}$$

where Λ is the spatial periodicity along z.

We rewrite here the (2.65), which is obtained from (2.97) after expanding the ripple profile along z as a Fourier series:

$$\begin{cases} \dfrac{df_i^+}{dz} = \displaystyle\sum_n g_n \sum_p \left[c_{ip}^+ f_p^+ \mathrm{e}^{-\iota(\beta_p - \beta_i - nk_b)z} + c_{ip}^- f_p^- \mathrm{e}^{\iota(\beta_p + \beta_i + nk_b)z} \right] \\ \dfrac{df_i^-}{dz} = \displaystyle\sum_n g_n \sum_p \left[c_{ip}^- f_p^+ \mathrm{e}^{-\iota(\beta_p + \beta_i - nk_b)z} + c_{ip}^+ f_p^- \mathrm{e}^{\iota(\beta_p - \beta_i + nk_b)z} \right] \end{cases}$$

with

$$g_n = \iota n k_b b_n \qquad \text{and} \qquad b_n = \frac{1}{\Lambda} \int_{-\Lambda/2}^{\Lambda/2} b_0 g(z) \mathrm{e}^{-\iota \frac{2\pi n}{\Lambda} z} dz$$

In very long rippled sections, all waves far from the condition (2.98) give a negligible contribution in the summation of (2.65) and can be ignored. Hence only the terms ± 1 of the Fourier series play a role and two separate systems of differential equations are obtained from (2.65). With reference to forward waves, the system is

$$\frac{df_i^+}{dz} = \sum_p \left(\iota k_b b_{\pm 1} c_{ip}^+ \right) f_p^+ \mathrm{e}^{\iota(\beta_i - \beta_p \pm k_b)z}$$

where the sign $\pm$ depends on whether $\beta_p > \beta_i$ or $\beta_p < \beta_i$. To improve the accuracy and simplify the numerical implementation, the terms ± 1 of the Fourier series can be both included to have

$$\frac{df_i^+}{dz} = \iota \left(b_1 \mathrm{e}^{\iota k_b z} - b_{-1} \mathrm{e}^{-\iota k_b z} \right) \sum_p \left(k_b c_{ip}^+ \right) f_p^+ \mathrm{e}^{-\iota(\beta_p - \beta_i)z}$$

Being $g(z)$ a real function, $b_1 = b_{-1}^*$; furthermore if $g(z)$ is an even or odd function (like in Fig. 2.3), b_1 is purely real or imaginary, respectively. We can focus on the former case since, being $g(z)$ periodic, we can make it even from odd by translating the reference system along z. We can thus write

$$\iota \left(b_1 \mathrm{e}^{\iota k_b z} - b_{-1} \mathrm{e}^{-\iota k_b z} \right) = -2 b_1 \sin(k_b z)$$

and the approximate system of different equations for even $g(z)$ becomes

$$\frac{df_i^+}{dz} = \sin(k_b z) \sum_p \kappa_{ip}^+ f_p^+ \mathrm{e}^{-\iota(\beta_p - \beta_i)z} \qquad \text{with} \quad \kappa_{ip}^+ = -2 b_1 k_b c_{ip}^+$$

For example, a sinusoidal profile $g(z) = \cos(k_b z)$ has $\kappa_{ip}^{+} = -b_0 k_b c_{ip}^{+}$.

In the frame of previous limitations and approximations, i.e. even profiles and matching condition ruling out Fourier coefficients other than $\pm$ 1, reflected waves can be included too. The new, more general system is

$$\begin{cases} \dfrac{df_i^{+}}{dz} = -2b_1 k_b \sin(k_b z) \displaystyle\sum_p \left[c_{ip}^{+} f_p^{+} \mathrm{e}^{-\iota(\beta_p - \beta_i)z} + c_{ip}^{-} f_p^{-} \mathrm{e}^{\iota(\beta_p + \beta_i)z} \right] \\ \dfrac{df_i^{-}}{dz} = -2b_1 k_b \sin(k_b z) \displaystyle\sum_p \left[c_{ip}^{-} f_p^{+} \mathrm{e}^{-\iota(\beta_p + \beta_i)z} + c_{ip}^{+} f_p^{-} \mathrm{e}^{\iota(\beta_p - \beta_i)z} \right] \end{cases}$$

In the particular case of a sinusoidal profile, the Fourier series is utterly considered since $b_{n \neq \pm 1} = 0$.

Chapter 3

Mode-Matching Method

The standard mode matching method is applied to study both step discontinuity and continuous variation of waveguides with circular cross-section, concentric along the longitudinal axis. The method is then enhanced, by using the resonator technique, to study rectangular waveguides provided with junctions. A CAD tool is finally developed for the analysis and design of mode filters in rectangular waveguide.

3.1 Classical Theoretical Model

3.1.1 Field matching at a waveguide discontinuity

We consider two concentric, homogeneous circular waveguides with different cross-section connected in the direction of their longitudinal axis z as depicted in Fig. 3.1: region I on the left is supposed to be larger than region II on the right. The procedure detailed hereafter allows the derivation of the generalized scattering matrix (GSM) of the discontinuity. It holds true in the case of different waveguides, provided that the modes in each region are known in advance either analytically or numerically.

The electromagnetic field in each region is expressed as a modal expansion with unknown amplitudes $A_{i,j}$ and $B_{i,j}$ for respectively incoming and outcoming waves. At the discontinuity plane $z = 0$, their expressions are

$$\begin{aligned}
\mathbf{E}^{\mathrm{I}} &= \sum_i \left(A_i^{\mathrm{I}} + B_i^{\mathrm{I}}\right) \mathbf{e}_{t_i}^{\mathrm{I}} &&+ \left(A_i^{\mathrm{I}} - B_i^{\mathrm{I}}\right) \mathbf{e}_{z_i}^{\mathrm{I}} \\
\mathbf{H}^{\mathrm{I}} &= \sum_i \left(A_i^{\mathrm{I}} - B_i^{\mathrm{I}}\right) \mathbf{h}_{t_i}^{\mathrm{I}} &&+ \left(A_i^{\mathrm{I}} + B_i^{\mathrm{I}}\right) \mathbf{h}_{z_i}^{\mathrm{I}} \\
\mathbf{E}^{\mathrm{II}} &= \sum_j \left(A_j^{\mathrm{II}} + B_j^{\mathrm{II}}\right) \mathbf{e}_{t_j}^{\mathrm{II}} &&+ \left(B_j^{\mathrm{II}} - A_j^{\mathrm{II}}\right) \mathbf{e}_{z_j}^{\mathrm{II}} \\
\mathbf{H}^{\mathrm{II}} &= \sum_j \left(B_j^{\mathrm{II}} - A_j^{\mathrm{II}}\right) \mathbf{h}_{t_j}^{\mathrm{II}} &&+ \left(A_j^{\mathrm{II}} + B_j^{\mathrm{II}}\right) \mathbf{h}_{z_j}^{\mathrm{II}}
\end{aligned}$$

Evanescent modes with very high order give a negligible contribution to the calculation of the GSM, so in practical applications, the series are truncated to make the problem computationally feasible. In particular we take $i = 1, 2, \ldots, N$ and $j = 1, 2, \ldots, M$. The best choice of the truncation orders in the mode-matching techniques has been deeply studied mostly with reference to the relative convergence problem. The convergence depends not only on

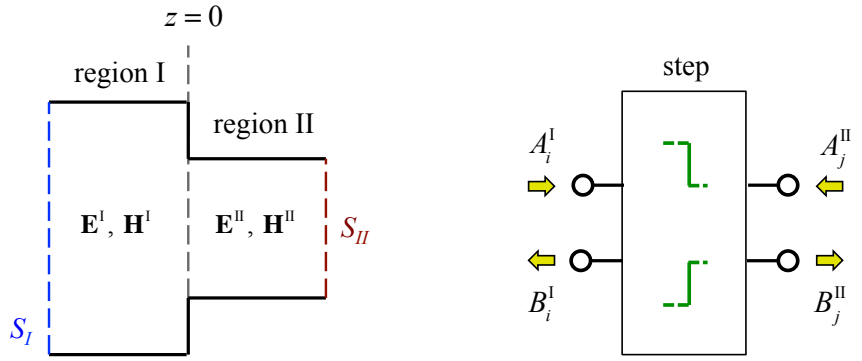

Figure 3.1: Layout of a step discontinuity in circular waveguide (left) and equivalent microwave building block (right).

the truncation criterion of a single series, but also in the relation between the numbers used in the different expansions. When increasing the truncation order until the changes in the GSM are negligible, a usual criterion consists in setting the ratio N/M approximately equal to S_I/S_{II} so as to adopt the same spatial resolution in the two regions [75].

The boundary conditions dictate the matching of the transversal field components at $z = 0$. The mode orthogonality (*Galerkin* method) is then applied to convert the boundary conditions on the electric and magnetic field into two finite sets of equations. More precisely, the condition on the electric field is cross-multiplied by the transversal magnetic components of the ℓ-th eigenmode of region I and integrated over S_I after taking the dot product by z. The condition on the magnetic field is instead cross-multiplied by $\mathbf{e}^{\mathrm{II}}_{t_\ell}$ and integrated over S_{II}, being that eigenfunction null outside S_{II}. In mathematical terms

$$\begin{aligned}
\mathbf{E}^{\mathrm{I}}_t &= \mathbf{E}^{\mathrm{II}}_t \\
\iint_{S_{\mathrm{I}}} \mathbf{E}^{\mathrm{I}}_t \times \mathbf{h}^{\mathrm{I}}_{t_\ell} \cdot \hat{\mathbf{z}} dS &= \iint_{S_{\mathrm{I}}} \mathbf{E}^{\mathrm{II}}_t \times \mathbf{h}^{\mathrm{I}}_{t_\ell} \cdot \hat{\mathbf{z}} dS \\
\iint_{S_{\mathrm{I}}} \sum_i \left(A^{\mathrm{I}}_i + B^{\mathrm{I}}_i\right) \mathbf{e}^{\mathrm{I}}_{t_i} \times \mathbf{h}^{\mathrm{I}}_{t_\ell} \cdot \hat{\mathbf{z}} dS &= \iint_{S_{\mathrm{I}}} \sum_j \left(A^{\mathrm{II}}_j + B^{\mathrm{II}}_j\right) \mathbf{e}^{\mathrm{II}}_{t_j} \times \mathbf{h}^{\mathrm{I}}_{t_\ell} \cdot \hat{\mathbf{z}} dS \\
\sum_i \left(A^{\mathrm{I}}_i + B^{\mathrm{I}}_i\right) \iint_{S_{\mathrm{I}}} \mathbf{e}^{\mathrm{I}}_{t_i} \times \mathbf{h}^{\mathrm{I}}_{t_\ell} \cdot \hat{\mathbf{z}} dS &= \sum_j \left(A^{\mathrm{II}}_j + B^{\mathrm{II}}_j\right) \iint_{S_{\mathrm{II}}} \mathbf{e}^{\mathrm{II}}_{t_j} \times \mathbf{h}^{\mathrm{I}}_{t_\ell} \cdot \hat{\mathbf{z}} dS
\end{aligned}$$

for the electric field boundary condition (EFBC), with $\ell = 1, 2, \ldots, N$, and

$$\begin{aligned}
\mathbf{H}^{\mathrm{I}}_t &= \mathbf{H}^{\mathrm{II}}_t \\
\iint_{S_{\mathrm{II}}} \mathbf{e}^{\mathrm{II}}_{t_\ell} \times \mathbf{H}^{\mathrm{I}}_t \cdot \hat{\mathbf{z}} dS &= \iint_{S_{\mathrm{II}}} \mathbf{e}^{\mathrm{II}}_{t_\ell} \times \mathbf{H}^{\mathrm{II}}_t \cdot \hat{\mathbf{z}} dS \\
\sum_i \left(A^{\mathrm{I}}_i - B^{\mathrm{I}}_i\right) \iint_{S_{\mathrm{II}}} \mathbf{e}^{\mathrm{II}}_{t_\ell} \times \mathbf{h}^{\mathrm{I}}_{t_i} \cdot \hat{\mathbf{z}} dS &= \sum_j \left(B^{\mathrm{II}}_j - A^{\mathrm{II}}_j\right) \iint_{S_{\mathrm{II}}} \mathbf{e}^{\mathrm{II}}_{t_\ell} \times \mathbf{h}^{\mathrm{II}}_{t_j} \cdot \hat{\mathbf{z}} dS
\end{aligned}$$

for the magnetic field boundary condition (MFBC), with $\ell = 1, 2, \ldots, M$.

The definition of transversal fields adopted here is slightly different from (2.10), where the normalization led to the orthogonality relation (2.13). In the mode-matching method, the following definitions are preferred:

$$\begin{array}{lcc}
 & \text{TE modes} & \text{TM modes} \\
\mathbf{e}_{t_\ell} = & \sqrt{Q_\ell}\sqrt{Z_\ell}\nabla_t \Phi^{\mathrm{TE}}_\ell \times \hat{\mathbf{z}} & \sqrt{Q_\ell}\sqrt{Z_\ell}\nabla_t \Phi^{\mathrm{TM}}_\ell \\
\mathbf{h}_{t_\ell} = & \sqrt{Q_\ell}\sqrt{Y_\ell}\nabla_t \Phi^{\mathrm{TE}}_\ell & \sqrt{Q_\ell}\sqrt{Y_\ell}\,\hat{\mathbf{z}} \times \nabla_t \Phi^{\mathrm{TM}}_\ell
\end{array} \tag{3.1}$$

and the orthogonality relation becomes

$$\iint_S \mathbf{e}_{t_i} \times \mathbf{h}_{t_\ell} \cdot \hat{\mathbf{z}} dS = Q_\ell \delta_{i\ell} \tag{3.2}$$

being S the cross-section of the region where those eigenfunctions are used. The latter do not depend on the waveguide dielectric and can be written as frequency independent functions that take real values. The terms Q_ℓ are complex normalization factors that can be arbitrarily chosen. Another important relation, mostly useful with reference to power flow, is

$$\iint_S \mathbf{e}_{t_i} \times \mathbf{h}^*_{t_\ell} \cdot \hat{\mathbf{z}} dS = P_\ell \delta_{i\ell}$$

which is related to (3.2) by

$$P_\ell = \frac{\sqrt{Z_\ell}}{(\sqrt{Z_\ell})^*}|Q_\ell| = \begin{cases} |Q_\ell| & \text{for propagating modes} \\ +\iota|Q_\ell| & \text{for evanescent TE modes} \\ -\iota|Q_\ell| & \text{for evanescent TM modes} \end{cases}$$

where the last equality is true if the medium filling the waveguide is lossless, namely $\varepsilon'' = \mu'' = 0$.

The boundary conditions can be written in matrix form by arranging the modal amplitudes in column vectors

$$\mathbf{A}^{\mathrm{I}}_{N\times 1} = \begin{bmatrix} A^{\mathrm{I}}_1 \\ \vdots \\ A^{\mathrm{I}}_i \\ \vdots \\ A^{\mathrm{I}}_N \end{bmatrix}, \quad \mathbf{B}^{\mathrm{I}}_{N\times 1} = \begin{bmatrix} B^{\mathrm{I}}_1 \\ \vdots \\ B^{\mathrm{I}}_i \\ \vdots \\ B^{\mathrm{I}}_N \end{bmatrix}, \quad \mathbf{A}^{\mathrm{II}}_{M\times 1} = \begin{bmatrix} A^{\mathrm{II}}_1 \\ \vdots \\ A^{\mathrm{II}}_j \\ \vdots \\ A^{\mathrm{II}}_M \end{bmatrix}, \quad \mathbf{B}^{\mathrm{II}}_{M\times 1} = \begin{bmatrix} B^{\mathrm{II}}_1 \\ \vdots \\ B^{\mathrm{II}}_j \\ \vdots \\ B^{\mathrm{II}}_M \end{bmatrix}$$

and introducing the diagonal matrices

$$\underline{\mathbf{Q}}_N = \begin{bmatrix} Q^{\mathrm{I}}_1 & 0 & \dots & 0 \\ 0 & Q^{\mathrm{I}}_2 & \dots & 0 \\ \vdots & \vdots & \ddots & \vdots \\ 0 & 0 & \dots & Q^{\mathrm{I}}_N \end{bmatrix}, \qquad \underline{\mathbf{Q}}_M = \begin{bmatrix} Q^{\mathrm{II}}_1 & 0 & \dots & 0 \\ 0 & Q^{\mathrm{II}}_2 & \dots & 0 \\ \vdots & \vdots & \ddots & \vdots \\ 0 & 0 & \dots & Q^{\mathrm{II}}_M \end{bmatrix}$$

It is common to set $Q^{\mathrm{I}}_i = Q^{\mathrm{II}}_j = 1$ as assured by the normalized eigenfunctions used in previous chapters (see section 2.1.4). With these positions the matrices $\underline{\mathbf{Q}}$ are unitary and the (3.2) becomes an orthonormality relation. The (3.2) expresses the lhs of the EFBC and the rhs of the MFBC, whereas the inner products between modes of different regions are indicated with an interaction matrix $\underline{\mathbf{X}}^{(h)}_{M\times N}$, the elements of which are

$$X_{ji} = \iint_{S_{\mathrm{II}}} \mathbf{e}^{\mathrm{II}}_{t_j} \times \mathbf{h}^{\mathrm{I}}_{t_i} \cdot \hat{\mathbf{z}} dS \tag{3.3}$$

With these definitions, the linear system obtained from the boundary conditions is expressed as

$$\begin{cases} \text{EFBC} & \underline{\mathbf{Q}}_N \left(\mathbf{A}^{\mathrm{I}} + \mathbf{B}^{\mathrm{I}}\right) = \underline{\mathbf{X}}^T \left(\mathbf{A}^{\mathrm{II}} + \mathbf{B}^{\mathrm{II}}\right) & N \text{ eqns.} \\ \text{MFBC} & \underline{\mathbf{X}} \left(\mathbf{A}^{\mathrm{I}} - \mathbf{B}^{\mathrm{I}}\right) = \underline{\mathbf{Q}}_M \left(\mathbf{B}^{\mathrm{II}} - \mathbf{A}^{\mathrm{II}}\right) & M \text{ eqns.} \end{cases} \tag{3.4}$$

The GSM of the following microwave network

$$\begin{bmatrix} \mathbf{B}^{\mathrm{I}} \\ \mathbf{B}^{\mathrm{II}} \end{bmatrix} = \underline{\mathbf{S}}_{(N+M)\times(N+M)} \cdot \begin{bmatrix} \mathbf{A}^{\mathrm{I}} \\ \mathbf{A}^{\mathrm{II}} \end{bmatrix}$$

is derived after some matrix algebra manipulations

$$\underline{\mathbf{S}} = \begin{bmatrix} \underline{\mathbf{Q}}_N^{-1} \cdot \underline{\mathbf{X}}^T \cdot \underline{\mathbf{F}} \cdot \underline{\mathbf{X}} - \underline{\mathbf{I}}_N & \underline{\mathbf{Q}}_N^{-1} \cdot \underline{\mathbf{X}}^T \cdot \underline{\mathbf{F}} \cdot \underline{\mathbf{Q}}_M \\ \underline{\mathbf{F}} \cdot \underline{\mathbf{X}} & \underline{\mathbf{F}} \cdot \underline{\mathbf{Q}}_M - \underline{\mathbf{I}}_M \end{bmatrix} \tag{3.5}$$

with

$$\underline{\mathbf{F}} = 2\left(\underline{\mathbf{Q}}_M + \underline{\mathbf{X}} \cdot \underline{\mathbf{Q}}_N^{-1} \cdot \underline{\mathbf{X}}^T\right)^{-1}$$

being $\underline{\mathbf{I}}_N$ and $\underline{\mathbf{I}}_M$ the identity matrices with dimensions $N \times N$ and $M \times M$, respectively.

3.1.2 Normalized inner cross products

The inner products can be expressed in terms of eigenfunctions by considering the possible combinations of interaction between TE and TM modes according to the (3.1). We have for TE-TE interaction

$$\begin{aligned} X_{[j][i]} &= \iint_{S_{\mathrm{II}}} \mathbf{e}_{t_j}^{\mathrm{II(TE)}} \times \mathbf{h}_{t_i}^{\mathrm{I(TE)}} \cdot \hat{\mathbf{z}} dS = \\ &= \sqrt{Q_j^{\mathrm{II}}}\sqrt{Z_j^{\mathrm{II}}}\sqrt{Q_i^{\mathrm{I}}}\sqrt{Y_i^{\mathrm{I}}} \iint_{S_{\mathrm{II}}} (\nabla_t \Phi_j^{\mathrm{II}} \times \hat{\mathbf{z}}) \times \nabla_t \Phi_i^{\mathrm{I}} \cdot \hat{\mathbf{z}} dS = \\ &= \sqrt{Q_j^{\mathrm{II}}}\sqrt{Z_j^{\mathrm{II}}}\sqrt{Q_i^{\mathrm{I}}}\sqrt{Y_i^{\mathrm{I}}} \iint_{S_{\mathrm{II}}} (\nabla_t \Phi_i^{\mathrm{I}} \times \hat{\mathbf{z}}) \cdot (\nabla_t \Phi_j^{\mathrm{II}} \times \hat{\mathbf{z}}) dS = \\ &= \sqrt{Q_j^{\mathrm{II}}}\sqrt{Z_j^{\mathrm{II}}}\sqrt{Q_i^{\mathrm{I}}}\sqrt{Y_i^{\mathrm{I}}} \iint_{S_{\mathrm{II}}} \nabla_t \Phi_i^{\mathrm{I}} \cdot \nabla_t \Phi_j^{\mathrm{II}} dS \end{aligned}$$

while for TM-TM interaction

$$\begin{aligned} X_{(j)(i)}^{\mathrm{TM-TM}} &= \iint_{S_{\mathrm{II}}} \mathbf{e}_{t_j}^{\mathrm{II(TM)}} \times \mathbf{h}_{t_i}^{\mathrm{I(TM)}} \cdot \hat{\mathbf{z}} dS = \\ &= \sqrt{Q_j^{\mathrm{II}}}\sqrt{Z_j^{\mathrm{II}}}\sqrt{Q_i^{\mathrm{I}}}\sqrt{Y_i^{\mathrm{I}}} \iint_{S_{\mathrm{II}}} \nabla_t \Phi_j^{\mathrm{II}} \times (\hat{\mathbf{z}} \times \nabla_t \Phi_i^{\mathrm{I}}) \cdot \hat{\mathbf{z}} dS = \\ &= \sqrt{Q_j^{\mathrm{II}}}\sqrt{Z_j^{\mathrm{II}}}\sqrt{Q_i^{\mathrm{I}}}\sqrt{Y_i^{\mathrm{I}}} \iint_{S_{\mathrm{II}}} (\hat{\mathbf{z}} \times \nabla_t \Phi_j^{\mathrm{II}}) \cdot (\hat{\mathbf{z}} \times \nabla_t \Phi_i^{\mathrm{I}}) dS = \\ &= \sqrt{Q_j^{\mathrm{II}}}\sqrt{Z_j^{\mathrm{II}}}\sqrt{Q_i^{\mathrm{I}}}\sqrt{Y_i^{\mathrm{I}}} \iint_{S_{\mathrm{II}}} \nabla_t \Phi_j^{\mathrm{II}} \cdot \nabla_t \Phi_i^{\mathrm{I}} dS \end{aligned}$$

If we first write the mode type in region I and then the one in region II, for TE-TM interaction we find

$$\begin{aligned} X_{(j)[i]} &= \iint_{S_{\mathrm{II}}} \mathbf{e}_{t_j}^{\mathrm{II(TM)}} \times \mathbf{h}_{t_i}^{\mathrm{I(TE)}} \cdot \hat{\mathbf{z}} dS = \\ &= \sqrt{Q_j^{\mathrm{II}}}\sqrt{Z_j^{\mathrm{II}}}\sqrt{Q_i^{\mathrm{I}}}\sqrt{Y_i^{\mathrm{I}}} \iint_{S_{\mathrm{II}}} \nabla_t \Phi_j^{\mathrm{II}} \times \nabla_t \Phi_i^{\mathrm{I}} \cdot \hat{\mathbf{z}} dS \end{aligned}$$

where the integrand can be developed as follows

$$\nabla_t \Phi_j^{\mathrm{II}} \times \nabla_t \Phi_i^{\mathrm{I}} \cdot \hat{\mathbf{z}} = \begin{vmatrix} \hat{\mathbf{q}}_1 & \hat{\mathbf{q}}_1 & \hat{\mathbf{z}} \\ \nabla_{q_1} \Phi_j^{\mathrm{II}} & \nabla_{q_2} \Phi_j^{\mathrm{II}} & 0 \\ \nabla_{q_1} \Phi_i^{\mathrm{I}} & \nabla_{q_2} \Phi_i^{\mathrm{I}} & 0 \end{vmatrix} \cdot \hat{\mathbf{z}} = \\ = \nabla_{q_1} \Phi_j^{\mathrm{II}} \nabla_{q_2} \Phi_i^{\mathrm{I}} - \nabla_{q_2} \Phi_j^{\mathrm{II}} \nabla_{q_1} \Phi_i^{\mathrm{I}}$$

being $\mathbf{q}_1$ and $\mathbf{q}_2$ the unit vectors of the curvilinear cylindrical coordinate systems, which respectively correspond to $\hat{\mathbf{n}}$ and $\hat{\mathbf{s}}$ of the previous chapters. We thus have

$$X_{[j](i)} = \sqrt{Q_j^{\mathrm{II}}} \sqrt{Z_j^{\mathrm{II}}} \sqrt{Q_i^{\mathrm{I}}} \sqrt{Y_i^{\mathrm{I}}} \iint_{S_{\mathrm{II}}} \left(\frac{\partial \Phi_j^{\mathrm{II}}}{\partial n} \frac{\partial \Phi_i^{\mathrm{I}}}{\partial s} - \frac{\partial \Phi_j^{\mathrm{II}}}{\partial s} \frac{\partial \Phi_i^{\mathrm{I}}}{\partial n} \right) dS$$

and for TM-TE interaction

$$\begin{aligned} X_{[j](i)} &= \iint_{S_{\mathrm{II}}} \mathbf{e}_{t_j}^{\mathrm{II(TE)}} \times \mathbf{h}_{t_i}^{\mathrm{I(TM)}} \cdot \hat{\mathbf{z}} dS = \\ &= \sqrt{Q_j^{\mathrm{II}}} \sqrt{Z_j^{\mathrm{II}}} \sqrt{Q_i^{\mathrm{I}}} \sqrt{Y_i^{\mathrm{I}}} \iint_{S_{\mathrm{II}}} (\nabla_t \Phi_j^{\mathrm{II}} \times \hat{\mathbf{z}}) \times (\hat{\mathbf{z}} \times \nabla_t \Phi_i^{\mathrm{I}}) \cdot \hat{\mathbf{z}} dS = \\ &= -\sqrt{Q_j^{\mathrm{II}}} \sqrt{Z_j^{\mathrm{II}}} \sqrt{Q_i^{\mathrm{I}}} \sqrt{Y_i^{\mathrm{I}}} \iint_{S_{\mathrm{II}}} (\hat{\mathbf{z}} \times \nabla_t \Phi_j^{\mathrm{II}}) \times (\hat{\mathbf{z}} \times \nabla_t \Phi_i^{\mathrm{I}}) \cdot \hat{\mathbf{z}} dS = \\ &= -\sqrt{Q_j^{\mathrm{II}}} \sqrt{Z_j^{\mathrm{II}}} \sqrt{Q_i^{\mathrm{I}}} \sqrt{Y_i^{\mathrm{I}}} \iint_{S_{\mathrm{II}}} \nabla_t \Phi_j^{\mathrm{II}} \times \nabla_t \Phi_i^{\mathrm{I}} \cdot \hat{\mathbf{z}} dS = \\ &= -\sqrt{Q_j^{\mathrm{II}}} \sqrt{Z_j^{\mathrm{II}}} \sqrt{Q_i^{\mathrm{I}}} \sqrt{Y_i^{\mathrm{I}}} \iint_{S_{\mathrm{II}}} \left(\frac{\partial \Phi_j^{\mathrm{II}}}{\partial n} \frac{\partial \Phi_i^{\mathrm{I}}}{\partial s} - \frac{\partial \Phi_j^{\mathrm{II}}}{\partial s} \frac{\partial \Phi_i^{\mathrm{I}}}{\partial n} \right) dS \end{aligned}$$

The integrals only depend on the geometry of the discontinuity because the eigenfunctions are supposed to be written as frequency independent functions. We can thus introduce a matrix with terms

$$\widehat{X}_{ji} = \begin{cases} \iint_{S_{\mathrm{II}}} \nabla_t \Phi_i^{\mathrm{I}} \cdot \nabla_t \Phi_j^{\mathrm{II}} dS & i(\mathrm{TE})\text{-}j(\mathrm{TE}) \\ \iint_{S_{\mathrm{II}}} \nabla_t \Phi_i^{\mathrm{I}} \cdot \nabla_t \Phi_j^{\mathrm{II}} dS & i(\mathrm{TM})\text{-}j(\mathrm{TM}) \\ \iint_{S_{\mathrm{II}}} \left(\frac{\partial \Phi_j^{\mathrm{II}}}{\partial n} \frac{\partial \Phi_i^{\mathrm{I}}}{\partial s} - \frac{\partial \Phi_j^{\mathrm{II}}}{\partial s} \frac{\partial \Phi_i^{\mathrm{I}}}{\partial n} \right) dS & i(\mathrm{TE})\text{-}j(\mathrm{TM}) \\ \iint_{S_{\mathrm{II}}} \left(\frac{\partial \Phi_i^{\mathrm{I}}}{\partial n} \frac{\partial \Phi_j^{\mathrm{II}}}{\partial s} - \frac{\partial \Phi_i^{\mathrm{I}}}{\partial s} \frac{\partial \Phi_j^{\mathrm{II}}}{\partial n} \right) dS & i(\mathrm{TM})\text{-}j(\mathrm{TE}) \end{cases} \tag{3.6}$$

which can be considered normalized inner cross products or projection integrals returning the cross-correlation between different modes. The (3.6) is computed only once in a frequency sweep and is then multiplied by diagonal

matrices to include the frequency dependence and the waveguide medium information. The interaction matrix $\underline{\mathbf{X}}$ with the inner cross products is obtained at each frequency sample with the following factorization rule

$$\underline{\mathbf{X}} = \underline{\mathbf{Q}}_M^{0.5} \cdot \underline{\mathbf{Z}}_M^{0.5} \cdot \underline{\widehat{\mathbf{X}}} \cdot \underline{\mathbf{Y}}_N^{0.5} \cdot \underline{\mathbf{Q}}_N^{0.5}$$

being $\underline{\mathbf{Z}}_M$ and $\underline{\mathbf{Y}}_N$ the diagonal matrices with the wave impedances in region II and with the wave admittances in region I, respectively.

3.1.3 Cascade and discretization

The overall characterization of a structure made up of a number of step discontinuities is obtained by cascading the individual GSMs using matrix operations. For example a corrugated circular waveguide, like a Bragg reflector with square ripple profile, can be represented through the block scheme of Fig. 3.2 and analysed with cascading operations.

We consider two consecutive blocks (X) and (Y) characterized by their own generalized scattering matrix

$$\mathbf{B}^{(X)} = \underline{\mathbf{S}}^{(X)} \cdot \mathbf{A}^{(X)} \qquad \text{and} \qquad \mathbf{B}^{(Y)} = \underline{\mathbf{S}}^{(Y)} \cdot \mathbf{A}^{(Y)}$$

and connected by a waveguide with length d, where N_Z modes are considered. If, in each building block, we identify the set of ports on the left of the cascade with the subscript 1 (input ports) and the set on the right with the subscript 2 (output ports), $N_Z = N_2^{(X)} = N_1^{(Y)}$. The boundary conditions on the modal amplitudes in the region (Z) connecting the two blocks are

$$\mathbf{A}_1^{(Y)} = \underline{\mathbf{G}} \cdot \mathbf{B}_2^{(X)} \qquad \text{and} \qquad \mathbf{A}_2^{(X)} = \underline{\mathbf{G}} \cdot \mathbf{B}_1^{(Y)}$$

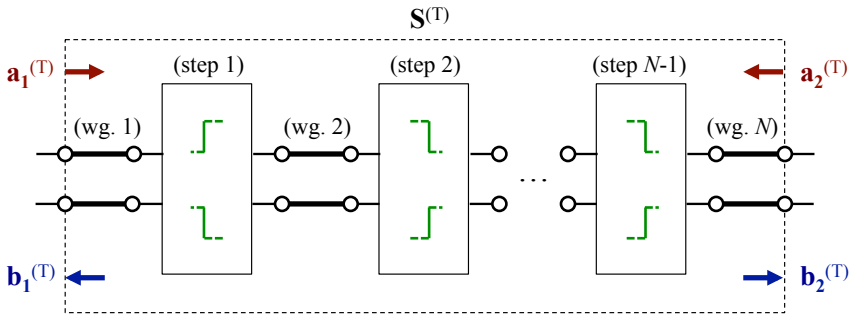

Figure 3.2: Cascading of GSMs; each building block represents a step discontinuity connected to the next one by a straight waveguide.

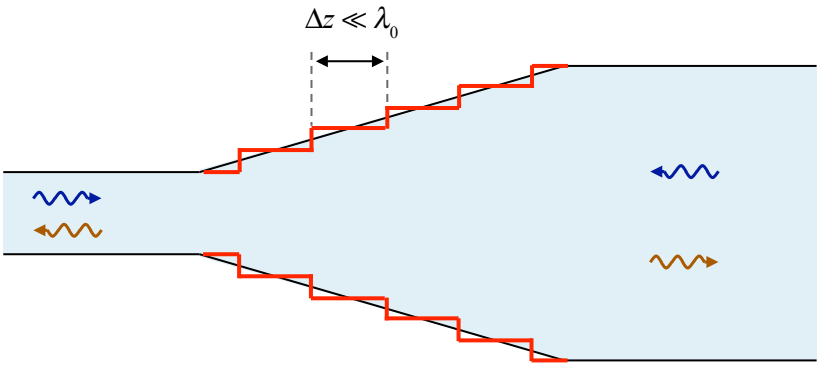

Figure 3.3: Discretization of a linear taper in circular waveguide.

with

$$\underline{\mathbf{G}} = \begin{bmatrix} \mathrm{e}^{-\iota\gamma_1^{(Z)}d} & 0 & \dots & 0 \\ 0 & \mathrm{e}^{-\iota\gamma_2^{(Z)}d} & \dots & 0 \\ \vdots & \vdots & \ddots & \vdots \\ 0 & 0 & \dots & \mathrm{e}^{-\iota\gamma_{N_Z}^{(Z)}d} \end{bmatrix}$$

After a few algebraic manipulations, the new GSM

$$\mathbf{B}^{(C)} = \underline{\mathbf{S}}^{(C)} \cdot \mathbf{A}^{(C)}$$

representing the composite block is given by

$$\underline{\mathbf{S}}^{(C)} = \begin{bmatrix} \underline{\mathbf{S}}_{11}^{(A)} + \underline{\mathbf{S}}_{12}^{(A)} \cdot \underline{\mathbf{G}} \cdot \underline{\mathbf{F}} \cdot \underline{\mathbf{S}}_{11}^{(B)} \cdot \underline{\mathbf{G}} \cdot \underline{\mathbf{S}}_{21}^{(A)} & \underline{\mathbf{S}}_{12}^{(A)} \cdot \underline{\mathbf{G}} \cdot \underline{\mathbf{F}} \cdot \underline{\mathbf{S}}_{12}^{(B)} \\ \underline{\mathbf{S}}_{21}^{(B)} \cdot \underline{\mathbf{G}} \cdot [\underline{\mathbf{I}}_Z + \underline{\mathbf{S}}_{22}^{(A)} \cdot \underline{\mathbf{G}} \cdot \underline{\mathbf{F}} \cdot \underline{\mathbf{S}}_{11}^{(B)} \cdot \underline{\mathbf{G}} \cdot \underline{\mathbf{S}}_{21}^{(A)}] & \underline{\mathbf{S}}_{22}^{(B)} + \underline{\mathbf{S}}_{21}^{(B)} \cdot \underline{\mathbf{G}} \cdot \underline{\mathbf{S}}_{22}^{(A)} \cdot \underline{\mathbf{G}} \cdot \underline{\mathbf{F}} \cdot \underline{\mathbf{S}}_{12}^{(B)} \end{bmatrix}$$

being $\underline{\mathbf{I}}_Z$ an identity matrix with dimensions $N_z \times N_z$ and

$$\underline{\mathbf{F}} = \left[\underline{\mathbf{I}}_Z - \underline{\mathbf{S}}_{11}^{(B)} \cdot \underline{\mathbf{G}} \cdot \underline{\mathbf{S}}_{22}^{(A)} \cdot \underline{\mathbf{G}}\right]^{-1}$$

This process can be repeated iteratively till the overall GSM representing the total structure is obtained. For the scheme of Fig. 3.2, an equivalent building block comprising 2^i discontinuities could be derived at the i-th iteration and its cascade would significantly speed up the computation.

The method can be extended to waveguides with a continuous variation of the cross-section after a discretization along the longitudinal axis into sections much smaller than the vacuum wavelength. The latter is indeed always smaller than or approximately equal to the wavelengths of the waveguide modes; usually ten cells in a wavelength represent a satisfactory meshing criterion. Each segment consists in a waveguide with constant cross-section, therefore the problem is converted into the cascade of step discontinuities. An example of this approach is the linear taper depicted in Fig. 3.3, where λ_0 is the wavelength in vacuum.

3.1.4 Evaluation of losses at the discontinuity wall

The attenuation due to the ohmic losses on the metallic surface of the discontinuity, namely on $S_c = S_{\mathrm{I}} - S_{\mathrm{II}}$ can be taken into account by means of a surface impedance boundary condition (the Leontovich condition). Under a perturbative approximation, the electric field tangential to the metallic surface is derived from the tangential magnetic field as

$$\mathbf{E}_t^{\mathrm{I}} = Z_c \mathbf{H}_t^{\mathrm{I}} \times \hat{\mathbf{z}} \qquad \text{on} \quad S_c = S_{\mathrm{I}} - S_{\mathrm{II}} \tag{3.7}$$

with

$$Z_c = \sqrt{\frac{\mu}{\varepsilon_c}} = \sqrt{\frac{\mu}{\varepsilon_0 \varepsilon_r - \iota\sigma/\omega}} \approx (1+\iota)\sqrt{\frac{\omega\mu}{2\sigma}} = (1+\iota)R_s$$

for a good conductor with conductivity σ.

The previous positions do not change the magnetic field boundary condition, whereas EFBC becomes

$$\iint_{S_{\mathrm{I}}} \mathbf{E}_t^{\mathrm{I}} \times \mathbf{h}_{t_\ell}^{\mathrm{I}} \cdot \hat{\mathbf{z}} dS = \iint_{S_{\mathrm{II}}} \mathbf{E}_t^{\mathrm{II}} \times \mathbf{h}_{t_\ell}^{\mathrm{I}} \cdot \hat{\mathbf{z}} dS + \iint_{S_c} \mathbf{E}_t^{\mathrm{I}} \times \mathbf{h}_{t_\ell}^{\mathrm{I}} \cdot \hat{\mathbf{z}} dS$$

The new term on the rhs can be developed using (3.7) as follows

$$\begin{aligned} Z_c \iint_{S_c} (\mathbf{H}_t^{\mathrm{I}} \times \hat{\mathbf{z}}) \times \mathbf{h}_{t_\ell}^{\mathrm{I}} \cdot \hat{\mathbf{z}} dS &= Z_c \iint_{S_c} \left(\mathbf{h}_{t_\ell}^{\mathrm{I}} \times \hat{\mathbf{z}}\right) \cdot \left(\mathbf{H}_t^{\mathrm{I}} \times \hat{\mathbf{z}}\right) dS = \\ &= Z_c \iint_{S_c} \mathbf{h}_{t_\ell}^{\mathrm{I}} \cdot \mathbf{H}_t^{\mathrm{I}} dS = Z_c \sum_i \left(A_i^{\mathrm{I}} - B_i^{\mathrm{I}}\right) \iint_{S_c} \mathbf{h}_{t_\ell}^{\mathrm{I}} \cdot \mathbf{h}_{t_i}^{\mathrm{I}} dS \end{aligned}$$

By introducing the matrix $\underline{\mathbf{L}}_c$ with elements

$$L_{ji} = \iint_{S_c} \mathbf{h}_{t_j}^{\mathrm{I}} \cdot \mathbf{h}_{t_i}^{\mathrm{I}} dS, \qquad [N \times N] \tag{3.8}$$

the system (3.4) becomes

$$\begin{cases} \text{EFBC} & \underline{\mathbf{Q}}_N \left(\mathbf{A}^{\mathrm{I}} + \mathbf{B}^{\mathrm{I}}\right) = \underline{\mathbf{X}}^T \left(\mathbf{A}^{\mathrm{II}} + \mathbf{B}^{\mathrm{II}}\right) + \underline{\mathbf{L}}_c \left(\mathbf{A}^{\mathrm{I}} - \mathbf{B}^{\mathrm{I}}\right) \\ \text{MFBC} & \underline{\mathbf{X}} \left(\mathbf{A}^{\mathrm{I}} - \mathbf{B}^{\mathrm{I}}\right) = \underline{\mathbf{Q}}_M \left(\mathbf{B}^{\mathrm{II}} - \mathbf{A}^{\mathrm{II}}\right) \end{cases}$$

and the GSM of the lossy discontinuity is calculated as

$$\underline{\mathbf{S}} = \begin{bmatrix} \underline{\mathbf{I}}_N - \underline{\mathbf{F}} \cdot \underline{\mathbf{Q}}_N & \underline{\mathbf{F}} \cdot \underline{\mathbf{X}}^T \\ \underline{\mathbf{Q}}_M^{-1} \cdot \underline{\mathbf{X}} \cdot \underline{\mathbf{F}} \cdot \underline{\mathbf{Q}}_N & \underline{\mathbf{I}}_M - \underline{\mathbf{Q}}_M^{-1} \cdot \underline{\mathbf{X}} \cdot \underline{\mathbf{F}} \cdot \underline{\mathbf{X}}^T \end{bmatrix} \tag{3.9}$$

with

$$\underline{\mathbf{F}} = 2\left(\underline{\mathbf{Q}}_N + \underline{\mathbf{X}}^T \cdot \underline{\mathbf{Q}}_M^{-1} \cdot \underline{\mathbf{X}} + \underline{\mathbf{L}}_c\right)^{-1}$$

The inner products in $\underline{\mathbf{X}}$ remain as in (3.6), while the new matrix $\underline{\mathbf{L}}_c$ is calculated by integrating the modes of the larger waveguide on the conductor

wall. Taking into account that $S_c = S_{\mathrm{I}} - S_{\mathrm{II}}$, the matrix elements L_{ji} can be expressed as

$$\begin{aligned} L_{ji} =& \iint_{S_{\mathrm{I}}} \mathbf{h}^{\mathrm{I}}_{t_j} \cdot \mathbf{h}^{\mathrm{I}}_{t_i} dS - \iint_{S_{\mathrm{II}}} \mathbf{h}^{\mathrm{I}}_{t_j} \cdot \mathbf{h}^{\mathrm{I}}_{t_i} dS = \\ =& Y_j \iint_{S_{\mathrm{I}}} \mathbf{e}^{\mathrm{I}}_{t_j} \times \mathbf{h}^{\mathrm{I}}_{t_i} \cdot \hat{\mathbf{z}} dS - Y_j \iint_{S_{\mathrm{II}}} \mathbf{e}^{\mathrm{I}}_{t_j} \times \mathbf{h}^{\mathrm{I}}_{t_i} \cdot \hat{\mathbf{z}} dS = \\ =& Y_j Q_j \delta_{ij} - Y_j X^{\mathrm{I-I}}_{ji} \end{aligned}$$

being $X^{\mathrm{I-I}}_{ji}$ the inner cross products between modes of region I. By using (3.1), the matrix $\underline{\mathbf{L}}_c$ becomes

$$\underline{\mathbf{L}}_c = Z_c \underline{\mathbf{Q}}_N^{0.5} \cdot \underline{\mathbf{Y}}_N^{0.5} \cdot \underline{\widehat{\mathbf{L}}} \cdot \underline{\mathbf{Y}}_N^{0.5} \cdot \underline{\mathbf{Q}}_N^{0.5}$$

with

$$\widehat{L}_{ji} = \delta_{ji} - \begin{cases} \displaystyle\iint_{S_{\mathrm{II}}} \nabla_t \Phi^{\mathrm{I}}_i \cdot \nabla_t \Phi^{\mathrm{I}}_j dS & i(\mathrm{TE})\text{-}j(\mathrm{TE}) \\ \displaystyle\iint_{S_{\mathrm{II}}} \nabla_t \Phi^{\mathrm{I}}_i \cdot \nabla_t \Phi^{\mathrm{I}}_j dS & i(\mathrm{TM})\text{-}j(\mathrm{TM}) \\ \displaystyle\iint_{S_{\mathrm{II}}} \left(\frac{\partial \Phi^{\mathrm{I}}_j}{\partial n} \frac{\partial \Phi^{\mathrm{I}}_i}{\partial s} - \frac{\partial \Phi^{\mathrm{I}}_j}{\partial s} \frac{\partial \Phi^{\mathrm{I}}_i}{\partial n} \right) dS & i(\mathrm{TE})\text{-}j(\mathrm{TM}) \\ \displaystyle\iint_{S_{\mathrm{II}}} \left(\frac{\partial \Phi^{\mathrm{I}}_i}{\partial n} \frac{\partial \Phi^{\mathrm{I}}_j}{\partial s} - \frac{\partial \Phi^{\mathrm{I}}_i}{\partial s} \frac{\partial \Phi^{\mathrm{I}}_j}{\partial n} \right) dS & i(\mathrm{TM})\text{-}j(\mathrm{TE}) \end{cases} \tag{3.10}$$

3.2 Application to Circular Waveguides

3.2.1 Projection integrals for circular waveguides

The analytical expression of the normalized inner cross products $\widehat{X}_{mn}$ is derived here in the case of a circular waveguide with a step decrease of the radius as in Fig. 3.4. The progressive indices i and j are now replaced by the couples of mode indices (n, m) and (q, p) that describe the transversal dependence of the modes in the circular waveguide. The same definitions of (2.42) are adopted with $a(z < 0) = a$ and $a(z > 0) = b$; the following functions are involved in the calculation:

$$\nabla_{q_1}\Phi_i = \frac{\partial \Phi_{nm}}{\partial \rho}\hat{\rho} = \sqrt{N_{nm}}\alpha J_n'(\alpha\rho)\sin(n\phi + \overline{\phi})\hat{\rho}$$
$$\nabla_{q_2}\Phi_i = \frac{\partial \Phi_{nm}}{\rho\partial \phi}\hat{\phi} = \sqrt{N_{nm}}\frac{n}{\rho}J_n(\alpha\rho)\cos(n\phi + \overline{\phi})\hat{\phi}$$

The transversal wavenumber α and the initial phase $\overline{\phi}$ are

	TE modes	TM modes	
$\alpha =$	u'_{mn}/R	u_{mn}/R	
$\overline{\phi} =$	$\pi/2$	$\pi/2$	for $n = 0$
$\overline{\phi} =$	0	$\pi/2$	for $n \neq 0$

with $R = (a, b)$ in region I and II, respectively and $\overline{\phi}$ chosen according to the considerations drawn from (2.45) in section 2.1.4.

We recall some properties of Bessel functions [37] that will be useful later on. The recurrence relations

$$2J_n'(x) = [J_{n-1}(x) - J_{n+1}(x)] \tag{3.11}$$
$$2\frac{n}{x}J_n(x) = [J_{n-1}(x) + J_{n+1}(x)] \tag{3.12}$$

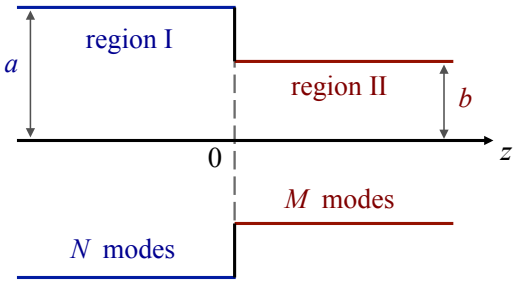

Figure 3.4: Geometry of a step discontinuity in circular waveguide.

allow the development of the products

$$\begin{aligned}
4J_n'(\alpha_1 x)J_n'(\alpha_2 x) &= [J_{n-1}(\alpha_1 x)J_{n-1}(\alpha_2 x) + J_{n+1}(\alpha_1 x)J_{n+1}(\alpha_2 x) + \\
&\quad - J_{n-1}(\alpha_1 x)J_{n+1}(\alpha_2 x) - J_{n+1}(\alpha_1 x)J_{n-1}(\alpha_2 x)] \\
\frac{4n^2}{\alpha_1\alpha_2 x^2}J_n(\alpha_1 x)J_n(\alpha_2 x) &= [J_{n-1}(\alpha_1 x)J_{n-1}(\alpha_2 x) + J_{n+1}(\alpha_1 x)J_{n+1}(\alpha_2 x) + \\
&\quad + J_{n-1}(\alpha_1 x)J_{n+1}(\alpha_2 x) + J_{n+1}(\alpha_1 x)J_{n-1}(\alpha_2 x)] \\
\frac{4n}{\alpha_2 x}J_n'(\alpha_1 x)J_n(\alpha_2 x) &= [J_{n-1}(\alpha_1 x)J_{n-1}(\alpha_2 x) - J_{n+1}(\alpha_1 x)J_{n+1}(\alpha_2 x) + \\
&\quad + J_{n-1}(\alpha_1 x)J_{n+1}(\alpha_2 x) - J_{n+1}(\alpha_1 x)J_{n-1}(\alpha_2 x)] \\
\frac{4n}{\alpha_1 x}J_n(\alpha_1 x)J_n'(\alpha_2 x) &= [J_{n-1}(\alpha_1 x)J_{n-1}(\alpha_2 x) - J_{n+1}(\alpha_1 x)J_{n+1}(\alpha_2 x) + \\
&\quad - J_{n-1}(\alpha_1 x)J_{n+1}(\alpha_2 x) + J_{n+1}(\alpha_1 x)J_{n-1}(\alpha_2 x)]
\end{aligned}$$

which can be linearly combined to give

$$\begin{aligned}
&J_n'(\alpha_1 x)J_n'(\alpha_2 x) + \frac{n^2}{\alpha_1\alpha_2 x^2}J_n(\alpha_1 x)J_n(\alpha_2 x) = \\
&\qquad = \frac{1}{2}\left[J_{n-1}(\alpha_1 x)J_{n-1}(\alpha_2 x) + J_{n+1}(\alpha_1 x)J_{n+1}(\alpha_2 x)\right]
\end{aligned} \tag{3.13}$$

and

$$\begin{aligned}
&\frac{n}{\alpha_2 x}J_n'(\alpha_1 x)J_n(\alpha_2 x) + \frac{n}{\alpha_1 x}J_n(\alpha_1 x)J_n'(\alpha_2 x) = \\
&\qquad = \frac{1}{2}\left[J_{n-1}(\alpha_1 x)J_{n-1}(\alpha_2 x) - J_{n+1}(\alpha_1 x)J_{n+1}(\alpha_2 x)\right]
\end{aligned} \tag{3.14}$$

Owing to the formula $J_{-n}(x) = (-1)^n J_n(x)$, the first recurrence relation leads to

$$J_0'(x) = -J_1(x) \tag{3.15}$$

The following definition is also introduced for the Lommel's integral

$$\begin{aligned}
\mathcal{L}_n(\alpha_1, \alpha_2, R) &= \int_0^R J_n(\alpha_1 x)J_n(\alpha_2 x)x\,dx = \\
&= \frac{R}{\alpha_1^2 - \alpha_2^2}\left[\alpha_1 J_{n+1}(\alpha_1 R)J_n(\alpha_2 R) - \alpha_2 J_n(\alpha_1 R)J_{n+1}(\alpha_2 R)\right]
\end{aligned}$$

For the TE-TE interaction in circular waveguide when either $n \neq 0$ or

$q \neq 0$, the (3.6) becomes with the help of (2.43), (2.44) and (3.13)

$$\begin{aligned}
\widehat{X}_{[j][i]} =& \widehat{X}_{[qp][nm]} = \int_0^{2\pi}\int_0^b \left(\frac{\partial \Phi^{\mathrm{I}}_{nm}}{\partial\rho}\frac{\partial \Phi^{\mathrm{II}}_{qp}}{\partial\rho} + \frac{\partial \Phi^{\mathrm{I}}_{nm}}{\rho\partial\phi}\frac{\partial \Phi^{\mathrm{II}}_{qp}}{\rho\partial\phi}\right)\rho d\rho d\phi = \\
=& \sqrt{N_{nm}}\sqrt{N_{qp}}\cdot \\
& \cdot\left[\int_0^b \frac{u'_{nm}u'_{qp}}{ab} J'_n\!\left(\frac{u'_{nm}}{a}\rho\right) J'_q\!\left(\frac{u'_{qp}}{b}\rho\right)\rho d\rho \int_0^{2\pi}\sin(n\phi)\sin(q\phi)d\phi + \right. \\
& \left. + \int_0^b \frac{nq}{\rho^2} J_n\!\left(\frac{u'_{nm}}{a}\rho\right) J_q\!\left(\frac{u'_{qp}}{b}\rho\right)\rho d\rho \int_0^{2\pi}\cos(n\phi)\cos(q\phi)d\phi\right] = \\
=& \sqrt{N_{nm}N_{qp}}\pi\delta_{nq}\frac{u'_{nm}u'_{np}}{ab}\int_0^b \left[J'_n\left(\frac{u'_{nm}}{a}\rho\right) J'_n\left(\frac{u'_{np}}{b}\rho\right) + \right. \\
& \left. + \frac{ab}{u'_{nm}u'_{np}}\frac{n^2}{\rho^2} J_n\left(\frac{u'_{nm}}{a}\rho\right) J_n\left(\frac{u'_{np}}{b}\rho\right)\right]\rho d\rho = \\
=& \sqrt{N_{nm}N_{qp}}\pi\delta_{nq}\frac{u'_{nm}u'_{np}}{2ab}\int_0^b \left[J_{n-1}\left(\frac{u'_{nm}}{a}\rho\right) J_{n-1}\left(\frac{u'_{np}}{b}\rho\right) + \right. \\
& \left. + J_{n+1}\left(\frac{u'_{nm}}{a}\rho\right) J_{n+1}\left(\frac{u'_{np}}{b}\rho\right)\right]\rho d\rho = \\
=& \sqrt{N_{nm}N_{np}}\pi\delta_{nq}\frac{u'_{nm}u'_{np}}{2ab}\cdot \\
& \cdot\left[\mathcal{L}_{n-1}\left(\frac{u'_{nm}}{a},\frac{u'_{np}}{b},b\right) + \mathcal{L}_{n+1}\left(\frac{u'_{nm}}{a},\frac{u'_{np}}{b},b\right)\right]
\end{aligned}$$

If $n = q = 0$, the (3.15) is used too

$$\begin{aligned}
\widehat{X}_{[0p][0m]} &= \sqrt{N_{0m}N_{0p}}\int_0^b \frac{u'_{0m}u'_{0p}}{ab} J'_0\!\left(\frac{u'_{0m}}{a}\rho\right) J'_0\!\left(\frac{u'_{0p}}{b}\rho\right)\rho d\rho \int_0^{2\pi} d\phi = \\
&= \sqrt{N_{0m}N_{0p}}2\pi\frac{u'_{0m}u'_{0p}}{ab}\int_0^b J'_0\left(\frac{u'_{0m}}{a}\rho\right) J'_0\left(\frac{u'_{0p}}{b}\rho\right)\rho d\rho = \\
&= \sqrt{N_{0m}N_{0p}}2\pi\frac{u'_{0m}u'_{0p}}{ab}\int_0^b J_1\left(\frac{u'_{0m}}{a}\rho\right) J_1\left(\frac{u'_{0p}}{b}\rho\right)\rho d\rho = \\
&= \sqrt{N_{0m}N_{0p}}2\pi\frac{u'_{0m}u'_{0p}}{ab}\mathcal{L}_1\left(\frac{u'_{0m}}{a},\frac{u'_{0p}}{b},b\right)
\end{aligned}$$

Similarly for the TM-TM interaction with $n = q \neq 0$, the (3.6) is developed

using (2.43), (2.44) and (3.13)

$$\begin{aligned}\widehat{X}_{(j)(i)} =&\widehat{X}_{(qp)(nm)} = \int_0^{2\pi}\int_0^b \left(\frac{\partial\Phi^{\mathrm{I}}_{nm}}{\partial\rho}\frac{\partial\Phi^{\mathrm{II}}_{qp}}{\partial\rho} + \frac{\partial\Phi^{\mathrm{I}}_{nm}}{\rho\partial\phi}\frac{\partial\Phi^{\mathrm{II}}_{qp}}{\rho\partial\phi}\right)\rho d\rho d\phi = \\ =&\sqrt{N_{nm}}\sqrt{N_{qp}}\cdot \\ &\cdot\left[\int_0^b \frac{u_{nm}u_{qp}}{ab}J'_n\Big(\frac{u_{nm}}{a}\rho\Big)\,J'_q\Big(\frac{u_{qp}}{b}\rho\Big)\,\rho d\rho\int_0^{2\pi}\cos(n\phi)\cos(q\phi)d\phi + \right. \\ &\left. + \int_0^b \frac{nq}{\rho^2}J_n\Big(\frac{u_{nm}}{a}\rho\Big)\,J_q\Big(\frac{u_{qp}}{b}\rho\Big)\,\rho d\rho\int_0^{2\pi}\sin(n\phi)\sin(q\phi)d\phi\right] = \\ =&\sqrt{N_{nm}N_{np}}\pi\delta_{nq}\frac{u_{nm}u_{np}}{2ab}\cdot \\ &\cdot\left[\mathcal{L}_{n-1}\left(\frac{u_{nm}}{a},\frac{u_{np}}{b},b\right)+\mathcal{L}_{n+1}\left(\frac{u_{nm}}{a},\frac{u_{np}}{b},b\right)\right]\end{aligned}$$

while, for $n = q = 0$,

$$\widehat{X}_{(0p)(0m)} = \sqrt{N_{0m}N_{0p}}2\pi\frac{u_{0m}u_{0p}}{ab}\mathcal{L}_1\left(\frac{u_{0m}}{a},\frac{u_{0p}}{b},b\right)$$

The (3.6) for the TE-TM interaction with $n = q \neq 0$ is manipulated through (2.43), (2.44) and (3.14)

$$\begin{aligned}\widehat{X}_{(j)[i]} =&\widehat{X}_{(qp)[nm]} = \int_0^{2\pi}\int_0^b \left(\frac{\partial\Phi^{\mathrm{II}}_{qp}}{\partial\rho}\frac{\partial\Phi^{\mathrm{I}}_{nm}}{\rho\partial\phi} - \frac{\partial\Phi^{\mathrm{II}}_{qp}}{\rho\partial\phi}\frac{\partial\Phi^{\mathrm{I}}_{nm}}{\partial\rho}\right)\rho d\rho d\phi = \\ =&\sqrt{N_{nm}}\sqrt{N_{qp}}\cdot \\ &\cdot\left\{\int_0^b \frac{u_{qp}}{b}J'_q\Big(\frac{u_{qp}}{b}\rho\Big)\,\frac{n}{\rho}J_n\Big(\frac{u'_{nm}}{a}\rho\Big)\rho d\rho\int_0^{2\pi}\cos(n\phi)\cos(q\phi)d\phi + \right. \\ &\left. -\int_0^b \frac{q}{\rho}J_q\Big(\frac{u_{qp}}{b}\rho\Big)\,\frac{u_{nm}}{a}J'_n\Big(\frac{u'_{nm}}{a}\rho\Big)\rho d\rho\int_0^{2\pi}\sin(n\phi)[-\sin(q\phi)]d\phi\right\} = \\ =&\sqrt{N_{nm}N_{np}}\pi\delta_{nq}\frac{u'_{nm}u_{np}}{ab}\int_0^b\left[\frac{na}{\rho u'_{nm}}J'_n\left(\frac{u_{np}}{b}\rho\right)J_n\left(\frac{u'_{nm}}{a}\rho\right)+\right. \\ &\left.+\frac{nb}{\rho u'_{np}}J_n\left(\frac{u_{np}}{b}\rho\right)\frac{u_{nm}}{a}J'_n\left(\frac{u'_{nm}}{a}\rho\right)\right]\rho d\rho = \\ =&\sqrt{N_{nm}N_{np}}\pi\delta_{nq}\frac{u'_{nm}u_{np}}{2ab}\int_0^b\left[J_{n-1}\left(\frac{u'_{nm}}{a}\rho\right)J_{n-1}\left(\frac{u_{np}}{b}\rho\right)+\right. \\ &\left.-\,J_{n+1}\left(\frac{u'_{nm}}{a}\rho\right)J_{n+1}\left(\frac{u_{np}}{b}\rho\right)\right]\rho d\rho = \\ =&\sqrt{N_{nm}N_{np}}\pi\delta_{nq}\frac{u'_{nm}u_{np}}{2ab}\cdot \\ &\cdot\left[\mathcal{L}_{n-1}\left(\frac{u'_{nm}}{a},\frac{u_{np}}{b},b\right)-\mathcal{L}_{n+1}\left(\frac{u'_{nm}}{a},\frac{u_{np}}{b},b\right)\right]\end{aligned}$$

while $\widehat{X}_{(0p)[0m]} = 0$ because $\nabla_{q_2}\Phi_{0\ell}$ is null for both TE and TM modes. For

TM-TE interaction:

$$\begin{aligned}
\widehat{X}_{[j](i)} =&\widehat{X}_{[qp](nm)} = -\int_0^{2\pi}\int_0^b \left(\frac{\partial\Phi_{qp}^{\mathrm{II}}}{\partial\rho}\frac{\partial\Phi_{nm}^{\mathrm{I}}}{\rho\partial\phi} - \frac{\partial\Phi_{qp}^{\mathrm{II}}}{\rho\partial\phi}\frac{\partial\Phi_{nm}^{\mathrm{I}}}{\partial\rho}\right)\rho d\rho d\phi = \\
&= -\sqrt{N_{nm}}\sqrt{N_{qp}}\cdot \\
&\quad\cdot\left\{\int_0^b \frac{u'_{qp}}{b}J'_q\Big(\frac{u'_{qp}}{b}\rho\Big)\frac{n}{\rho}J_n\Big(\frac{u_{nm}}{a}\rho\Big)\rho d\rho\int_0^{2\pi}[-\sin(n\phi)]\sin(q\phi)d\phi + \right. \\
&\quad\left. -\int_0^b \frac{q}{\rho}J_q\Big(\frac{u'_{qp}}{b}\rho\Big)\frac{u'_{nm}}{a}J'_n\Big(\frac{u_{nm}}{a}\rho\Big)\rho d\rho\int_0^{2\pi}\cos(n\phi)\cos(q\phi)d\phi\right\} = \\
&=\sqrt{N_{nm}N_{np}}\pi\delta_{nq}\frac{u_{nm}u'_{np}}{ab}\int_0^b\left[\frac{na}{\rho u_{nm}}J'_n\left(\frac{u'_{np}}{b}\rho\right)J_n\left(\frac{u_{nm}}{a}\rho\right) + \right. \\
&\quad\left. + \frac{nb}{\rho u_{np}}J_n\left(\frac{u'_{np}}{b}\rho\right)\frac{u'_{nm}}{a}J'_n\left(\frac{u_{nm}}{a}\rho\right)\right]\rho d\rho = \\
&=\sqrt{N_{nm}N_{np}}\pi\delta_{nq}\frac{u_{nm}u'_{np}}{2ab}\cdot \\
&\quad\cdot\left[\mathcal{L}_{n-1}\left(\frac{u_{nm}}{a},\frac{u'_{np}}{b},b\right) - \mathcal{L}_{n+1}\left(\frac{u_{nm}}{a},\frac{u'_{np}}{b},b\right)\right]
\end{aligned}$$

and $\widehat{X}_{[0p](0m)} = 0$.

The closed-form solutions of previous integrals can be rewritten in a more compact form by demonstrating that the expressions of $\widehat{X}_{qp,nm}$ also work for the cases with $n = q = 0$, apart from a factor 2. We consider the Lommel's integrals with subscript ±1 for the interaction with a $\mathrm{TE}_{0\mathrm{p}}$ mode in region II:

$$\begin{aligned}
\mathcal{L}_{-1}\left(\alpha_1,\frac{u'_{0p}}{b},b\right) &= \frac{b}{\alpha_1^2 - \left(\frac{u'_{0p}}{b}\right)^2}\left[\alpha_1 J_0(\alpha_1 b)J_{-1}(u'_{0p}) - \frac{u'_{0p}}{b}J_{-1}(\alpha_1 b)J_0(u'_{0p})\right] \\
\mathcal{L}_1\left(\alpha_1,\frac{u'_{0p}}{b},b\right) &= \frac{b}{\alpha_1^2 - \left(\frac{u'_{0p}}{b}\right)^2}\left[\alpha_1 J_2(\alpha_1 b)J_1(u'_{0p}) - \frac{u'_{0p}}{b}J_1(\alpha_1 b)J_2(u'_{0p})\right]
\end{aligned}$$

According to the (3.15), $J_{-1}(u'_{0p}) = -J_1(u'_{0p}) = -J'_0(u'_{0p}) = 0$, we have

$$\begin{aligned}
\mathcal{L}_{-1}\left(\alpha_1,\frac{u'_{0p}}{b},b\right) &= \frac{u'_{0p}}{\alpha_1^2 - (u'_{0p}/b)^2}J_1(\alpha_1 b)\left[J_0(u'_{0p})\right] \\
\mathcal{L}_1\left(\alpha_1,\frac{u'_{0p}}{b},b\right) &= \frac{u'_{0p}}{\alpha_1^2 - (u'_{0p}/b)^2}J_1(\alpha_1 b)\left[-J_2(u'_{0p})\right]
\end{aligned}$$

where, using the (3.12), $J_0(u'_{qp}) + J_2(u'_{qp}) = 2J_1(u'_{qp})/u'_{qp} = 0$; hence

$$\mathcal{L}_{-1}\left(\alpha_1,\frac{u'_{0p}}{b},b\right) = -\frac{u'_{0p}}{\alpha_1^2 - (u'_{0p}/b)^2}J_1(\alpha_1 b)J_2(u'_{qp}) = \mathcal{L}_1\left(\alpha_1,\frac{u'_{0p}}{b},b\right)$$

and the expression $\widehat{X}_{[qp],nm}$, multiplied by ϵ_{0n}, can be used for all n. The factor 2 when $n = q = 0$ serves for the interaction between modes of the same type, while for the other interactions, the cross integrals correctly vanish. If a $\mathrm{TM_{0p}}$ mode is considered in region II, the relevant Lommel's integrals can be simplified as follows

$$\mathcal{L}_{-1}\left(\alpha_1, \frac{u_{0p}}{b}, b\right) = \frac{b}{\alpha_1^2 - \left(\frac{u_{0p}}{b}\right)^2}\left[-\alpha_1 J_0(\alpha_1 b) J_1(u_{0p})\right]$$

$$\mathcal{L}_{1}\left(\alpha_1, \frac{u_{0p}}{b}, b\right) = \frac{b}{\alpha_1^2 - \left(\frac{u_{0p}}{b}\right)^2}\left[\alpha_1 J_2(\alpha_1 b) J_1(u_{0p}) - \frac{u_{0p}}{b} J_1(\alpha_1 b) J_2(u_{0p})\right]$$

In the second expression, the last term on the rhs can be developed using the (3.12) as

$$\begin{aligned}&\frac{u_{0p}}{b}\left[\frac{\alpha_1 b}{2} J_0(\alpha_1 b) + \frac{\alpha_1 b}{2} J_2(\alpha_1 b)\right]\left[\frac{2}{u_{0p}} J_1(u_{0p}) - \cancel{J_0(u_{0p})}\right] = \\ =&\alpha_1 J_0(\alpha_1 b) J_1(u_{0p}) + \alpha_1 J_2(\alpha_1 b) J_1(u_{0p})\end{aligned}$$

so that

$$\mathcal{L}_{-1}\left(\alpha_1, \frac{u_{0p}}{b}, b\right) = -\frac{b}{\alpha_1^2 - \left(\frac{u_{0p}}{b}\right)^2}\alpha_1 J_0(\alpha_1 b) J_1(u_{0p}) = \mathcal{L}_{1}\left(\alpha_1, \frac{u_{0p}}{b}, b\right)$$

and the same remarks of the TE case hold true.

The analytical expressions of the normalized inner cross products for circular waveguide can be finally summarized as follows

$$\widehat{X}^{II-I}_{qp-nm} = \epsilon_{0n}\delta_{nq}\frac{\pi}{2ab}\sqrt{N_{nm}N_{qp}}\cdot$$

$$\cdot\begin{cases} u'_{nm}u'_{qp}\left[\mathcal{L}_{n-1}\left(\frac{u'_{nm}}{a}, \frac{u'_{qp}}{b}, b\right) + \mathcal{L}_{n+1}\left(\frac{u'_{nm}}{a}, \frac{u'_{qp}}{b}, b\right)\right] & \mathrm{TE^{I}_{nm}\text{-}TE^{II}_{qp}} \\ u_{nm}u_{qp}\left[\mathcal{L}_{n-1}\left(\frac{u_{nm}}{a}, \frac{u_{qp}}{b}, b\right) + \mathcal{L}_{n+1}\left(\frac{u_{nm}}{a}, \frac{u_{qp}}{b}, b\right)\right] & \mathrm{TM^{I}_{nm}\text{-}TM^{II}_{qp}} \\ u'_{nm}u_{qp}\left[\mathcal{L}_{n-1}\left(\frac{u'_{nm}}{a}, \frac{u_{qp}}{b}, b\right) - \mathcal{L}_{n+1}\left(\frac{u'_{nm}}{a}, \frac{u_{qp}}{b}, b\right)\right] & \mathrm{TE^{I}_{nm}\text{-}TM^{II}_{qp}} \\ u_{nm}u'_{qp}\left[\mathcal{L}_{n-1}\left(\frac{u_{nm}}{a}, \frac{u'_{qp}}{b}, b\right) - \mathcal{L}_{n+1}\left(\frac{u_{nm}}{a}, \frac{u'_{qp}}{b}, b\right)\right] & \mathrm{TM^{I}_{nm}\text{-}TE^{II}_{qp}} \end{cases} \quad (3.16)$$

3.2.2 Benchmark with other full-wave methods

The mode-matching method has been implemented in MATLAB and compared with other full-wave tools, using the test geometry given in Fig. 3.5. The latter consists in a circular oversized waveguide provided with 4 corrugations; the geometrical dimensions are $a = 38$ mm, $d_c = w_c = h_c = 10$ mm, while the input/output straight sections with constant radius are 0.1 m long. The structure is studied in the range $[4.9 \div 5.1]$ GHz, where there are 5 modes above the cutoff frequency: $\mathrm{TE_{11}}$, $\mathrm{TM_{01}}$, $\mathrm{TE_{21}}$, $\mathrm{TE_{01}}$ and $\mathrm{TM_{11}}$.

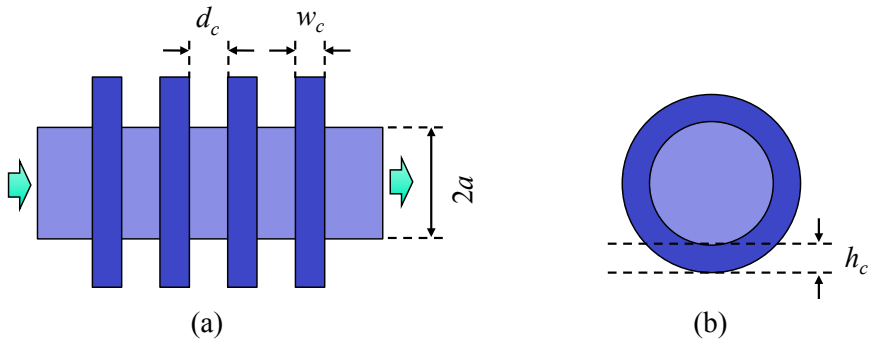

Figure 3.5: Side/top (a) and front (b) views of the test geometry.

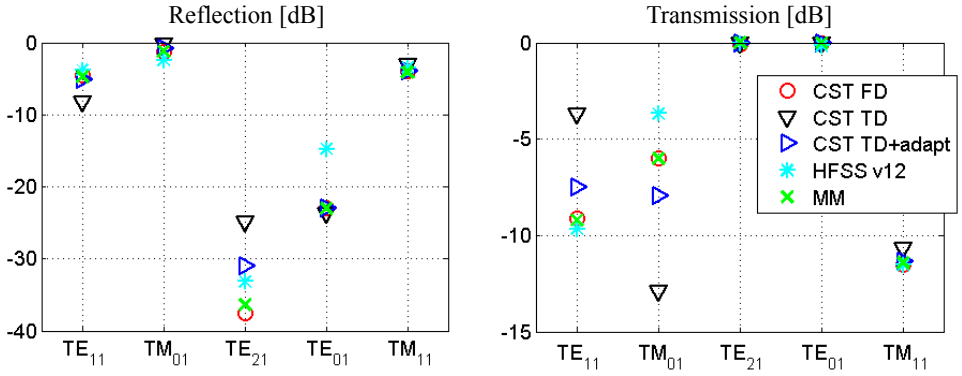

Figure 3.6: Reflection and transmission self-terms of propagating modes at 5 GHz computed with different tools for the test geometry.

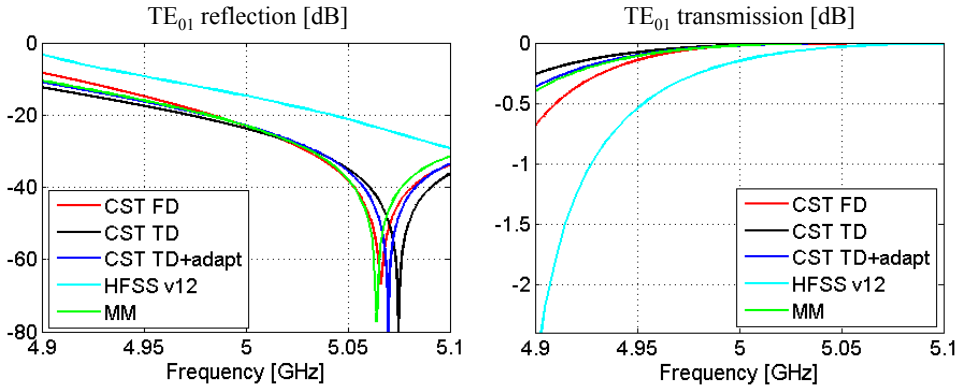

Figure 3.7: Reflection and transmission self-terms of the TE_{01} versus frequency computed with different tools for the test geometry.

Tool	**# cores**	**user time [s]**	**Notes**
CST FD	4	1130	
CST TD (standard)	4	500	
CST TD (adaptive)	4	4756	no convergence after 3 passes
HFSS v.12	1	3751	no convergence
Mode-matching	1	509	

Table 3.1: Solver times [s]

The full-wave methods used for the comparison are the solvers of two commercial softwares: the 12th release of HFSS [76] and both the frequency-domain (FD) and time-domain (TD) solvers of CST MWS. With reference to the latter, two computations were performed: the one was run with the standard mesh settings, while for the other the mesh adaptation was activated. In the mode-matching code, all modes with cutoff frequency lower than 25 GHz were included in the computation; this choice was found to give an accuracy of 0.01 on the magnitude of the scattering parameters as explained in section 3.2.3.

The predictions of the different tools for the scattering matrix of the test geometry are compared in Figs. 3.6 and 3.7: the former provides benchmark at a single frequency, whereas the latter gives a plot versus frequency. In both figures, the results from HFSS often detach from the outcomes of the other tools, while the calculations with the frequency solver of CST MWS agrees very well with those of the mode-matching (MM) method. As far as the time-domain solver is concerned, good agreement is achieved in the plots versus frequency for the TE_{01}, whereas, for the reflection and transmission self-terms of the other propagating modes at 5 GHz, the match improves only when mesh adaptation is activated. The latter fact suggests that the standard mesh adopted by the time-domain solver of CST MWS is inadequate for this structure and needs to be denser similarly to the Bragg resonator studied in section 2.3.3.

All simulations have been performed on a desktop Windows PC with an INTEL® Core™ i7-950 at 3.07 GHz, quad-core, and 12 GB of RAM. The wall-clock times taken by each tool to simulate the test geometry in the frequency range $[4.9 \div 5.1]$ GHz are reported in Table 3.1. The efficiency of the mode-matching method in addressing this kind of structures stands out clearly and becomes even more valuable when considering that the results of both HFSS and the transient solver of CST MWS with standard mesh settings were unreliable in some cases.

3.2.3 Convergence studies

According to the relative convergence issue, the truncation indices of the modal expansions in the two regions at a step discontinuity must be related to the aspect ratio of their cross-sections. This rule allows the derivation of the truncation index in a region when the one in the other region is fixed. In order to choose the first truncation order, a convergence study has to be done, after setting an accuracy criterion, by increasing step-by-step the number of modes included in the computation. In place of increasing N and M, a different approach is preferred here: we increase a frequency value named $\mathrm{fc}_{\max}$ and consider modal expansions comprising all modes with cutoff frequency lower than $\mathrm{fc}_{\max}$. This approach automatically satisfies the convergence relative criterion.

The convergence analysis has been carried out for two test geometries of Fig. 3.5 with $a = 38$ mm, but different electrical size. The one, having $d_c = 10$ mm, $w_c = 5$ mm and $h_c = 10$ mm, works at 5 GHz, while the other, having $d_c = 3$ mm, $w_c = 3$ mm and $h_c = 2$ mm, works at 20 GHz. The ratios a/λ_0 in the two cases are around 0.63 and 2.53, respectively. The value of $\mathrm{fc}_{\max}$ is increased step-by-step starting from the working frequency. At each step the maximum deviation of the magnitude and phase of the scattering parameters from the previous step is calculated and plotted. When the variation of the S-parameters between two consecutive steps is constantly below an accuracy criterion, the convergence has been reached. Good accuracy criteria for the amplitude and phase of the scattering parameters are 0.01 and 1 deg, respectively.

The convergence plots for the two structures are given in Figs. 3.8 and 3.9. In the latter, a dB scale has been used to improve the visualization of the deviation for the S-parameter magnitude. Usually the $\mathrm{fc}_{\max}$ must be taken around a factor 5 higher than the operational frequency to satisfy the accuracy criterion, depicted with red lines in the plots. This rule of thumb implies many evanescent modes to be included in the computation,

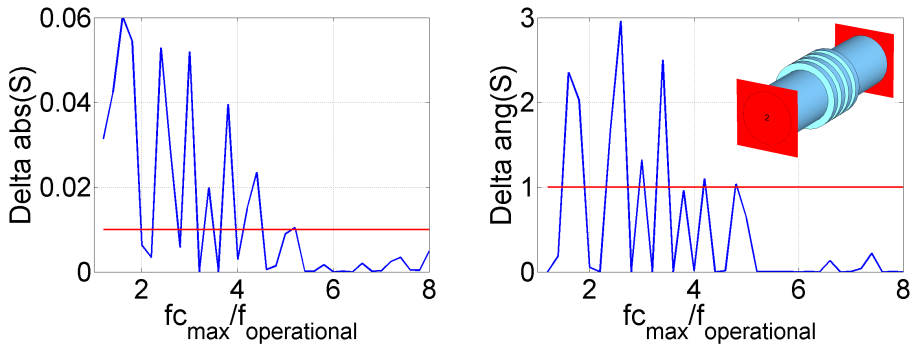

Figure 3.8: Convergence analysis for the test geometry working at 5 GHz.

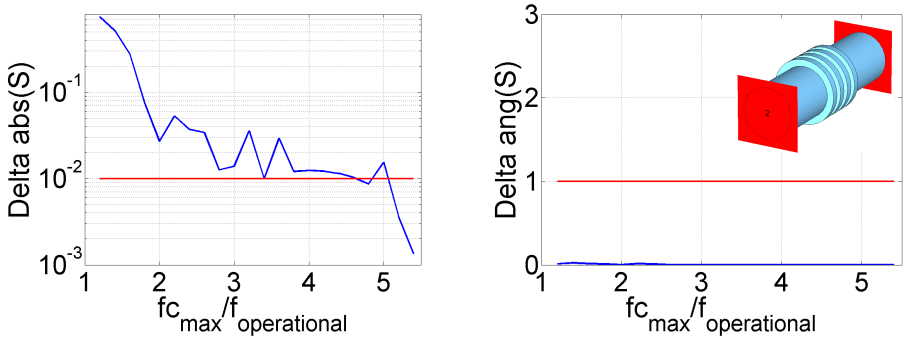

Figure 3.9: Convergence analysis for the test geometry working at 20 GHz.

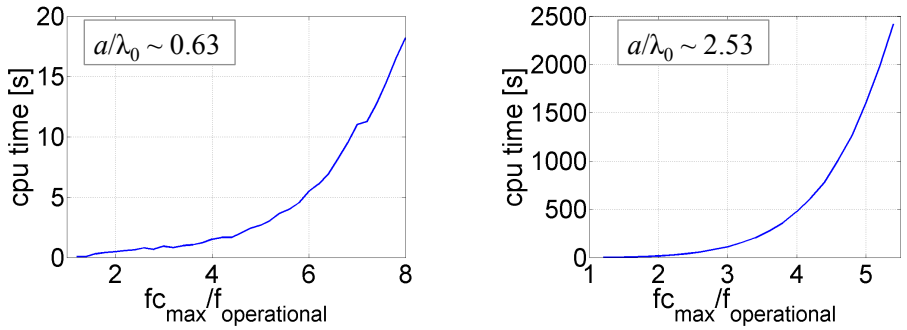

Figure 3.10: Computation times at each step for the convergence analyses of Figs. 3.8 and 3.9.

e.g. around 2200 modes for the 20 GHz structure; their number is as high as the ratio a/λ_0 increases with negative consequences on the duration of the calculation. The computation time taken by the mode-matching code at each convergence step of previous analyses is plotted in Fig. 3.10 as a function of $\mathrm{fc}_{\max}$, showing an exponential growth.

According to previous remarks, the mode-matching method is not suitable to study the CARM cavity of section 2.4 with a/λ_0 of about 8.33, because, apart from the excessive duration of the simulation, the matrices are too big to be handled with standard techniques. Nevertheless the modes to be considered in the calculation can be significantly reduced if only a particular excitation mode has to be studied. The expressions of the normalized inner cross products (3.16) indeed exhibit a δ_{nq}, indicating that only modes with the same azimuthal index interact. Therefore, if the behaviour of a structure with cylindrical symmetry is to be studied under the excitation of the TE_{82}, all modes with $n \neq 8$ can be excluded from the computation without loosing any accuracy. Fig. 3.11 reports an application of this trick to the cavity of Fig. 2.21, designed for the TE_{11} with Bragg reflectors hav-

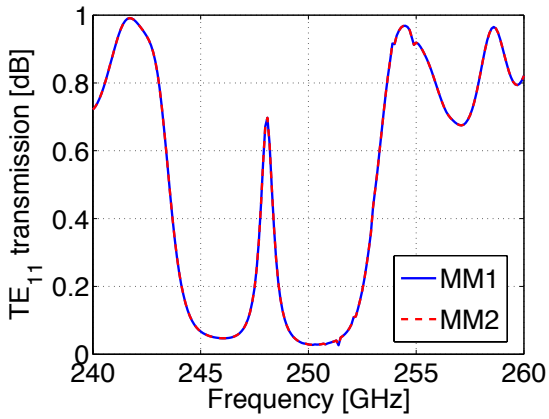

Figure 3.11: Transmission of the TE_{11} mode across the structure of Fig. 2.21, computed using full modal expansions (MM1) and excluding modes with $n \neq 1$ (MM2).

ing rectangular corrugations. The computations with the complete modal expansions and the ones using only the modes with $n = 1$ provide identical transmission coefficients for the TE_{11} mode.

3.2.4 Expression of integrals on the conductive wall

The integrals of the matrix elements $\widehat{L}_{ji}$, giving the contribution of ohmic losses at the discontinuity, have been defined in (3.10). Their expressions are the same as the normalized inner cross products of (3.6) with I in place of II. When $j \neq i$,

$$\widehat{L}_{ji} = \widehat{L}^{I-I}_{qp-nm} = -\epsilon_{0n}\delta_{nq}\frac{\pi}{2a^2}\sqrt{N_{nm}N_{qp}}\cdot$$
$$\cdot\begin{cases} u'_{nm}u'_{qp}\left[\mathcal{L}_{n-1}\left(\frac{u'_{nm}}{a},\frac{u'_{qp}}{a},b\right)+\mathcal{L}_{n+1}\left(\frac{u'_{nm}}{a},\frac{u'_{qp}}{a},b\right)\right] & \text{TE}^{\text{I}}_{nm}\text{-TE}^{\text{I}}_{qp} \\ u_{nm}u_{qp}\left[\mathcal{L}_{n-1}\left(\frac{u_{nm}}{a},\frac{u_{qp}}{a},b\right)+\mathcal{L}_{n+1}\left(\frac{u_{nm}}{a},\frac{u_{qp}}{a},b\right)\right] & \text{TM}^{\text{I}}_{nm}\text{-TM}^{\text{I}}_{qp} \\ u'_{nm}u_{qp}\left[\mathcal{L}_{n-1}\left(\frac{u'_{nm}}{a},\frac{u_{qp}}{a},b\right)-\mathcal{L}_{n+1}\left(\frac{u'_{nm}}{a},\frac{u_{qp}}{a},b\right)\right] & \text{TE}^{\text{I}}_{nm}\text{-TM}^{\text{I}}_{qp} \\ u_{nm}u'_{qp}\left[\mathcal{L}_{n-1}\left(\frac{u_{nm}}{a},\frac{u'_{qp}}{a},b\right)-\mathcal{L}_{n+1}\left(\frac{u_{nm}}{a},\frac{u'_{qp}}{a},b\right)\right] & \text{TM}^{\text{I}}_{nm}\text{-TE}^{\text{I}}_{qp} \end{cases} \quad (3.17)$$

whereas new expressions have to be derived for $j = i$ because this condition causes $\mathcal{L}$ to diverge. To this aim, some integrals of Bessel functions must be recalled from [37]; the one is

$$\int_0^R x\left[J^2_{n-1}(x) - J^2_{n+1}(x)\right]dx = 2nJ^2_n(R) \quad (3.18)$$

another one is defined with the following function

$$\begin{aligned}\mathcal{R}_n(\alpha,b) &= \int_0^b xJ_n(\alpha x)J_n(\alpha x)dx = \\ &= \left[\frac{x^2}{2}\left\{\left(1-\frac{n^2}{\alpha^2x^2}\right)J_n^2(\alpha x)+{J'_n}^2(\alpha x)\right\}\right]_0^b = \\ &= \frac{b^2}{2}\left[\left(1-\frac{n^2}{\alpha^2b^2}\right)J_n^2(\alpha b)+{J'_n}^2(\alpha b)\right]\end{aligned} \tag{3.19}$$

The interaction between the same TE modes thus gives

$$\begin{aligned}\widehat{L}_{[nm][nm]} &= 1-N_{nm}\frac{\pi {u'}^2_{nm}}{2a^2}\int_0^b\left[J_{n-1}^2\left(\frac{u'_{nm}}{a}\rho\right)+J_{n+1}^2\left(\frac{u'_{nm}}{a}\rho\right)\right]\rho d\rho = \\ &= 1-N_{nm}\frac{\pi {u'}^2_{nm}}{2a^2}\left[\mathcal{R}_{n-1}\left(\frac{u'_{nm}}{a},b\right)+\mathcal{R}_{n+1}\left(\frac{u'_{nm}}{a},b\right)\right]\end{aligned}$$

for $n \neq 0$, otherwise

$$\begin{aligned}\widehat{L}_{[0p][0m]} &= 1-N_{0m}\frac{2\pi {u'}^2_{0m}}{a^2}\int_0^b J_1^2\left(\frac{u'_{0m}}{a}\rho\right)\rho d\rho = \\ &= 1-N_{0m}\frac{2\pi {u'}^2_{0m}}{a^2}\mathcal{R}_1\left(\frac{u'_{nm}}{a},b\right) = \\ &= 1-N_{0m}\epsilon_{0m}\frac{\pi {u'}^2_{0m}}{2a^2}\left[\mathcal{R}_{-1}\left(\frac{u'_{0m}}{a},b\right)+\mathcal{R}_1\left(\frac{u'_{0m}}{a},b\right)\right]\end{aligned}$$

The last equality is justified by the fact that $\mathcal{R}_{-1} = \mathcal{R}_1$, as can be easily verified from 3.19. Furthermore the symbol ϵ_{0m} has been introduced in order to derive a single expression for any n. The same expressions can be adopted for the interaction between identical TM modes after replacing the eigenvalue u'_{nm} with u_{nm}. For the integrals between modes of different types but same indices, the expressions (3.17) have to be used. The function $\mathcal{L}$ would diverge for the interaction between $\mathrm{TE}_{0\mathrm{m}}$ and $\mathrm{TM}_{1\mathrm{m}}$ which are degenerate, but such case has $\widehat{L}=0$ because $n \neq q$.

Here follows a summary of the expressions for the $\widehat{L}$ terms for $i = j$:

$$\begin{aligned}&\widehat{L}_{ii} = \widehat{L}^{I-I}_{nm-nm} = 1-\epsilon_{0n}\frac{\pi}{2a^2}N_{nm}\cdot \\ &\cdot\begin{cases} {u'}^2_{nm}\left[\mathcal{R}_{n-1}\left(\frac{u'_{nm}}{a},\,b\right)+\mathcal{R}_{n+1}\left(\frac{u'_{nm}}{a},\,b\right)\right] & \mathrm{TE}^{\mathrm{I}}_{nm}\text{-}\mathrm{TE}^{\mathrm{I}}_{nm} \\ u^2_{nm}\left[\mathcal{R}_{n-1}\left(\frac{u_{nm}}{a},\,b\right)+\mathcal{R}_{n+1}\left(\frac{u_{nm}}{a},\,b\right)\right] & \mathrm{TM}^{\mathrm{I}}_{nm}\text{-}\mathrm{TM}^{\mathrm{I}}_{nm}\end{cases}\end{aligned} \tag{3.20}$$

3.3 Resonator Technique

3.3.1 Right-angle junctions in rectangular waveguide

We initially refer to a waveguide provided with two symmetrical junctions in the middle of the top and bottom wall as shown in Fig. 3.12. This structure can be divided according to Fig. 3.13 into a central cavity (region V) and four homogeneous semi-infinite rectangular waveguides; opposite waveguides have equal cross-sections. Assuming a time dependence $e^{\iota\omega t}$, the electromagnetic field in regions I and II can be expanded as a series of TE

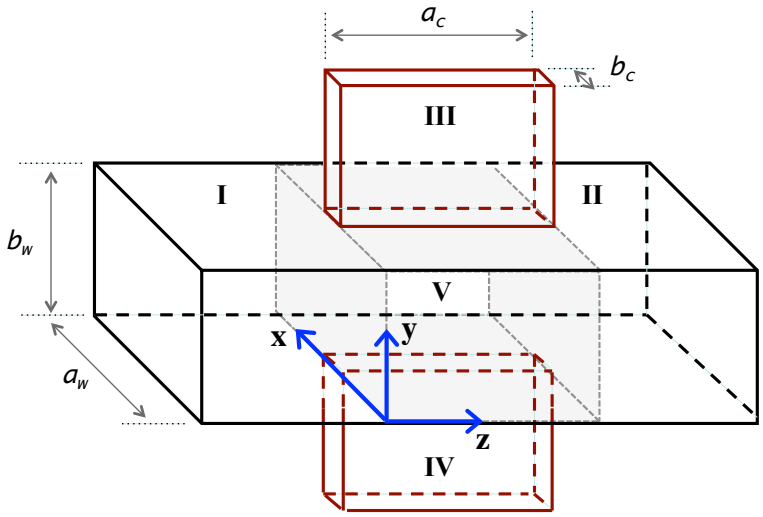

Figure 3.12: Geometry of a waveguide with two rectangular junctions.

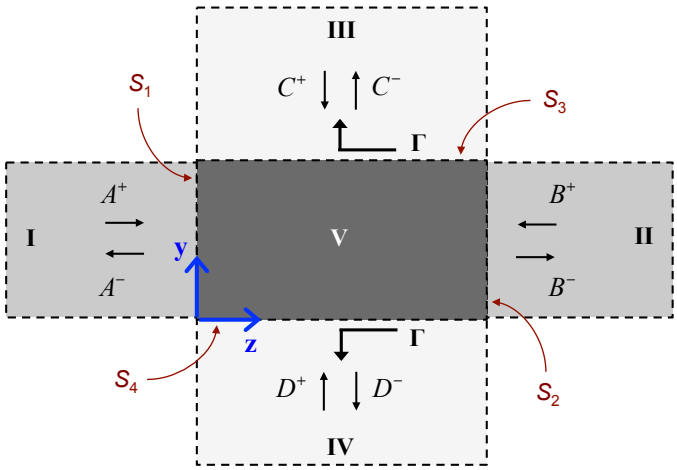

Figure 3.13: Division in five regions with forward and reflected waves.

and TM modes, truncated at an order to be defined, as follows [33]:

$$\begin{aligned}\mathbf{E}^{\mathrm{I,II}} &= \sum_{i=1}^{N_1} \mathrm{f}_i^{\mathrm{I,II}}(z)\,\mathbf{e}_{\mathbf{t}_i}^{\mathrm{I}}(x,y) + \mathrm{g}_i^{\mathrm{I,II}}(z)\,\mathbf{e}_{\mathbf{z}_i}^{\mathrm{I}}(x,y) \\ \mathbf{H}^{\mathrm{I,II}} &= \sum_{i=1}^{N_1} \mathrm{g}_i^{\mathrm{I,II}}(z)\,\mathbf{h}_{\mathbf{t}_i}^{\mathrm{I}}(x,y) + \mathrm{f}_i^{\mathrm{I,II}}(z)\,\mathbf{h}_{\mathbf{z}_i}^{\mathrm{I}}(x,y)\end{aligned} \tag{3.21}$$

with

$$\begin{aligned}\mathrm{f}_i^{\mathrm{I}}(z) &= A_i^{+}\mathrm{e}^{-\gamma_i^{\mathrm{I}} z} &&+ A_i^{-}\mathrm{e}^{\gamma_i^{\mathrm{I}} z} \\ \mathrm{f}_i^{\mathrm{II}}(z) &= B_i^{+}\mathrm{e}^{\gamma_i^{\mathrm{I}}(z-a_c)} &&+ B_i^{-}\mathrm{e}^{-\gamma_i^{\mathrm{I}}(z-a_c)}\end{aligned} \tag{3.22}$$

and

$$\mathrm{g}_i^{\mathrm{I,II}}(z) = -\frac{1}{\gamma_i^{\mathrm{I}}}\frac{d\,\mathrm{f}_i^{\mathrm{I,II}}}{dz} \tag{3.23}$$

The propagation constants γ and the transversal and longitudinal field components $\mathbf{e_t}$ and $\mathbf{e_z}$ are equal in the two regions, whereas the wave amplitudes A and B are taken at different reference planes, respectively corresponding to the surfaces S_1 and S_2 according to Fig. 3.13. The field components are defined as follows [77]

$$\begin{array}{ll} \text{TE modes} & \text{TM modes} \\ \mathbf{e}_{\mathbf{t}_i}^{\mathrm{I}} = \sqrt{Z_i^{\mathrm{I}}}\nabla_t\Phi_i^{\mathrm{I}} \times \hat{\mathbf{z}} & \mathbf{e}_{\mathbf{t}_i}^{\mathrm{I}} = \sqrt{Z_i^{\mathrm{I}}}\nabla_t\Phi_i^{\mathrm{I}} \\ \mathbf{h}_{\mathbf{t}_i}^{\mathrm{I}} = \sqrt{Y_i^{\mathrm{I}}}\nabla_t\Phi_i^{\mathrm{I}} & \mathbf{h}_{\mathbf{t}_i}^{\mathrm{I}} = \sqrt{Y_i^{\mathrm{I}}}\hat{\mathbf{z}} \times \nabla_t\Phi_i^{\mathrm{I}} \\ \mathbf{h}_{\mathbf{z}_i}^{\mathrm{I}} = -\sqrt{Y_i^{\mathrm{I}}}\dfrac{(k_{t_i}^{\mathrm{I}})^2}{\gamma_i^{\mathrm{I}}}\Phi_i^{\mathrm{I}}\hat{\mathbf{z}} & \mathbf{e}_{\mathbf{z}_i}^{\mathrm{I}} = -\sqrt{Z_i^{\mathrm{I}}}\dfrac{(k_{t_i}^{\mathrm{I}})^2}{\gamma_i^{\mathrm{I}}}\Phi_i^{\mathrm{I}}\hat{\mathbf{z}} \\ Z_i^{\mathrm{I}} = \dfrac{1}{Y_i^{\mathrm{I}}} = \dfrac{\iota\omega\mu^{\mathrm{I}}}{\gamma_i^{\mathrm{I}}} & Z_i^{\mathrm{I}} = \dfrac{1}{Y_i^{\mathrm{I}}} = \dfrac{\gamma_i^{\mathrm{I}}}{\iota\omega\varepsilon^{\mathrm{I}}} \end{array} \tag{3.24}$$

with $k_{t_i}^{\mathrm{I}}$ = transversal wavenumber in region I and II, so that

$$\gamma_i^{\mathrm{I}} = \sqrt{(k_{t_i}^{\mathrm{I}})^2 - \omega^2\mu^{\mathrm{I}}\varepsilon^{\mathrm{I}}}$$

The i-th mode is identified by a couple of indices, which will be indicated as (m,n) or (p,q), and defined through the normalized solution of the Helmholtz equation with Neumann and Dirichlet boundary conditions for TE and TM modes respectively:

$$\Phi_i = \Phi_{mn} = \sqrt{N_{mn}}\cdot$$
$$\cdot \begin{cases} \cos\left(\dfrac{m\pi x}{a_w}\right)\cos\left(\dfrac{n\pi y}{b_w}\right) & \begin{array}{l} m = n \neq 0 \\ m,n = 0,1,... \end{array} \quad \text{TE} \\ \sin\left(\dfrac{m\pi x}{a_w}\right)\sin\left(\dfrac{n\pi y}{b_w}\right) & \begin{array}{l} m = 1,2,... \\ n = 1,2,... \end{array} \quad \text{TM} \end{cases}$$

The normalization factors N_{mn} are chosen so that the integration of $\mathbf{e}^{\mathrm{I}}_{\mathbf{t}_i} \times \mathbf{h}^{\mathrm{I}*}_{\mathbf{t}_i}$ over the cross-section of the waveguide yields 1, ι and $-\iota$ [W] for respectively propagating, evanescent TE and evanescent TM modes. The field expansions in region III and IV can be similarly written for modes propagating along y and with (x, z) as transversal coordinates. The longitudinal dependence is

$$\begin{aligned} \mathrm{f}^{\mathrm{III}}_j(y) &= C^+_j \mathrm{e}^{\gamma^{\mathrm{III}}_j (y-b_w)} \quad + C^-_j \mathrm{e}^{-\gamma^{\mathrm{III}}_j (y-b_w)} \\ \mathrm{f}^{\mathrm{IV}}_j(y) &= D^+_j \mathrm{e}^{-\gamma^{\mathrm{IV}}_j y} \quad + D^-_j \mathrm{e}^{\gamma^{\mathrm{IV}}_j y} \end{aligned}$$

with $j = 1, 2, \ldots, N_3$, being the number of modes considered in region III and IV. The functions $\mathrm{g}^{\mathrm{III}}_i(y)$ and $\mathrm{g}^{\mathrm{IV}}_i(y)$ are related to $\mathrm{f}^{\mathrm{III}}_i$ and $\mathrm{f}^{\mathrm{IV}}_i$ through derivative operations similarly to (3.23).

With reference to region V, the resonator technique [78] is applied to the multi-port network, requiring to express the electromagnetic field as a superposition of four sets of standing waves:

$$\begin{aligned} \mathbf{E}^{\mathrm{V}} &= \mathbf{E}^{\mathrm{V}(1)} + \mathbf{E}^{\mathrm{V}(2)} + \mathbf{E}^{\mathrm{V}(3)} + \mathbf{E}^{\mathrm{V}(4)} \\ \mathbf{H}^{\mathrm{V}} &= \mathbf{H}^{\mathrm{V}(1)} + \mathbf{H}^{\mathrm{V}(2)} + \mathbf{H}^{\mathrm{V}(3)} + \mathbf{H}^{\mathrm{V}(4)} \end{aligned} \tag{3.25}$$

The first set ($\mathbf{E}^{\mathrm{V}(1)}$, $\mathbf{H}^{\mathrm{V}(1)}$) is a modal expansion in volume V, derived after replacing all surfaces but S_1 in Fig. 3.13 with perfect electric conductors; S_1 is left open. The second solution ($\mathbf{E}^{\mathrm{V}(2)}$, $\mathbf{H}^{\mathrm{V}(2)}$) is similarly built leaving S_2 open and inserting short circuits at the interfaces with regions I, III and IV, and so on for the last two sets. According to such boundary conditions, the following longitudinal dependences can be derived for each set:

$$\begin{aligned} \mathrm{f}^{\mathrm{V}(1)}_i(z) &= \xi_{A_i} \sinh[\gamma^{\mathrm{I}}_i (z - a_c)] \\ \mathrm{f}^{\mathrm{V}(2)}_i(z) &= \xi_{B_i} \sinh(\gamma^{\mathrm{I}}_i z) \\ \mathrm{f}^{\mathrm{V}(3)}_\ell(y) &= \xi_{C_\ell} \sinh(\gamma^{\mathrm{V}(3)}_\ell y) \\ \mathrm{f}^{\mathrm{V}(4)}_\ell(y) &= \xi_{D_\ell} \sinh[\gamma^{\mathrm{V}(3)}_\ell (y - b_w)] \end{aligned} \tag{3.26}$$

with $\xi_{A,B,C,D}$ = wave amplitudes, $i = 1, 2, \ldots, N_1$ and $\ell = 1, 2, \ldots, N_X$. The corresponding g functions are readily obtained from (3.26), multiplying by -1 and replacing sinh with hyperbolic cosine. It is worth restating that N_1 is the highest i-th mode considered in region I and II as well as in the first two sets of region V; j-th modes in region III and IV are instead taken up to the order N_3, whereas N_X is the truncation order of the modal expansions (index ℓ) in the last two solutions of region V.

At the boundary interfaces S_i, with $i = 1, 2, 3, 4$, the tangential components of the electric and magnetic fields of the first four regions must be matched with the ones of the resonant volume. In the case of S_1, for example, the condition on the electric field reduces to

$$\mathbf{E}^{\mathrm{I}}|_{z=0} = \mathbf{E}^{\mathrm{V}(1)}|_{z=0} \tag{3.27}$$

because the other sets of region V have vanishing tangential components on such surface. Mode orthogonality is then applied through the magnetic field transversal component for the i-th mode of the first set in region V:

$$\sum_k \mathrm{f}_k^{\mathrm{I}}(0) \iint_{S_1} \mathbf{e}_{\mathbf{t}_k}^{\mathrm{I}} \times \mathbf{h}_{\mathbf{t}_i}^{\mathrm{V}(1)} \cdot \hat{\mathbf{z}} dS = \sum_k \mathrm{f}_k^{\mathrm{V}(1)}(0) \iint_{S_1} \mathbf{e}_{\mathbf{t}_k}^{\mathrm{V}(1)} \times \mathbf{h}_{\mathbf{t}_i}^{\mathrm{V}(1)} \cdot \hat{\mathbf{z}} dS \quad (3.28)$$

Both integrals equal 1 for $k = i$ and 0 otherwise, so the (3.28) gives N_1 equations relating $\mathrm{f}_i^{\mathrm{I}}$ to $\mathrm{f}_i^{\mathrm{V}(1)}$. The interface S_2 leads to a similar outcome, whereas, on S_3 and S_4, involved modal expansions differ and the following projection integrals must be defined

$$\mathrm{W}_{\ell j} = \iint_{S_3} \mathbf{e}_{\mathbf{t}_j}^{\mathrm{III}} \times \mathbf{h}_{\mathbf{t}_\ell}^{\mathrm{V}(3)} \cdot \hat{\mathbf{y}} dS = \iint_{S_3} \mathbf{e}_{\mathbf{t}_j}^{\mathrm{IV}} \times \mathbf{h}_{\mathbf{t}_\ell}^{\mathrm{V}(4)} \cdot \hat{\mathbf{y}} dS \quad (3.29)$$

The conditions on the E-field components are therefore

$$\begin{aligned} \mathrm{f}_i^{\mathrm{I}}(0) &= \mathrm{f}_i^{\mathrm{V}(1)}(0) \\ \mathrm{f}_i^{\mathrm{II}}(a_c) &= \mathrm{f}_i^{\mathrm{V}(2)}(a_c) \\ \sum_j \mathrm{W}_{\ell j}\, \mathrm{f}_j^{\mathrm{III}}(b_w) &= \mathrm{f}_\ell^{\mathrm{V}(3)}(b_w) \\ \sum_j \mathrm{W}_{\ell j}\, \mathrm{f}_j^{\mathrm{IV}}(0) &= \mathrm{f}_\ell^{\mathrm{V}(4)}(0) \end{aligned} \quad (3.30)$$

As far as the conditions on the H-field transversal components are concerned, mode orthogonality is applied using the transverse E-field of the modes in the relevant semi-infinite region, e.g. on S_1

$$\sum_k \mathrm{g}_k^{\mathrm{I}}(0) \iint_{S_1} \mathbf{e}_{\mathbf{t}_i}^{\mathrm{I}} \times \mathbf{h}_{\mathbf{t}_k}^{\mathrm{I}} \cdot \hat{\mathbf{z}} dS = \iint_{S_1} \mathbf{e}_{\mathbf{t}_i}^{\mathrm{I}} \times \mathbf{H}^{\mathrm{V}} \Big|_{z=0} \cdot \hat{\mathbf{z}} dS$$

All sets of $\mathbf{H}^{\mathrm{V}}$ contribute and, in the case of V(3) and V(4), the longitudinal components also play a role in allowing for the power transfer between waveguide and corrugation modes. The projection integrals of the latter sets have the same magnitude, but they can differ in phase according to the even or odd symmetry of the modes. The following definitions are introduced to account for this effect

$$\mathrm{U}_{i\ell}^{(rs)} = \mathrm{U}_{mn,pq}^{(rs)} = \frac{(-1)^{rn+sp}}{\xi_{D_\ell}} \iint_{S_1} \mathbf{e}_{\mathbf{t}_{mn}}^{\mathrm{I}} \times \mathbf{H}_{pq}^{\mathrm{V}(4)} \cdot \hat{\mathbf{z}} dS \quad (3.31)$$

$$\mathrm{V}_{ji}^{(rs)} = \mathrm{V}_{mn,pq}^{(rs)} = \frac{(-1)^{rm+sq}}{\xi_{A_i}} \iint_{S_4} \mathbf{e}_{\mathbf{t}_{mn}}^{\mathrm{III}} \times \mathbf{H}_{pq}^{\mathrm{V}(1)} \cdot \hat{\mathbf{y}} dS \quad (3.32)$$

and the conditions on H-field components are

$$\begin{aligned}
\mathrm{g}_i^{\mathrm{I}}(0) =& \mathrm{g}_i^{\mathrm{V}(1)}(0) + \mathrm{g}_i^{\mathrm{V}(2)}(0) + \sum_\ell \mathrm{U}_{i\ell}^{(10)} \xi_{C_\ell} + \sum_\ell \mathrm{U}_{i\ell}^{(00)} \xi_{D_\ell} \\
\mathrm{g}_i^{\mathrm{II}}(a_c) =& \mathrm{g}_i^{\mathrm{V}(1)}(a_c) + \mathrm{g}_i^{\mathrm{V}(2)}(a_c) + \sum_\ell \mathrm{U}_{i\ell}^{(11)} \xi_{C_\ell} + \sum_\ell \mathrm{U}_{i\ell}^{(01)} \xi_{D_\ell} \\
\mathrm{g}_j^{\mathrm{III}}(b_w) =& \sum_i \mathrm{V}_{ji}^{(01)} \xi_{A_i} + \sum_i \mathrm{V}_{ji}^{(11)} \xi_{B_i} + \sum_\ell \mathrm{W}_{\ell j}\, \mathrm{g}_\ell^{\mathrm{V}(3)}(b_w) + \\
& + \sum_\ell \mathrm{W}_{\ell j}\, \mathrm{g}_\ell^{\mathrm{V}(4)}(b_w) \\
\mathrm{g}_j^{\mathrm{IV}}(0) =& \sum_i \mathrm{V}_{ji}^{(00)} \xi_{A_i} + \sum_i \mathrm{V}_{ji}^{(10)} \xi_{B_i} + \sum_\ell \mathrm{W}_{\ell j}\, \mathrm{g}_\ell^{\mathrm{V}(3)}(0) + \\
& + \sum_\ell \mathrm{W}_{\ell j}\, \mathrm{g}_\ell^{\mathrm{V}(4)}(0)
\end{aligned} \tag{3.33}$$

The integrals defined in (3.29), (3.31) and (3.32) can be solved analytically for the geometry under consideration; the solutions are reported in section 3.3.2.

The boundary conditions can be recast in matrix form introducing the diagonal matrices $\underline{\mathbf{L}}_s$, $\underline{\mathbf{L}}_c$, $\underline{\mathbf{M}}_s$ and $\underline{\mathbf{M}}_c$ with the following nonzero elements:

$$\begin{aligned}
L_{s_{ii}} &= -\sinh(\gamma_i^{\mathrm{I}} a_c) & M_{s_{\ell\ell}} &= -\sinh(\gamma_\ell^{\mathrm{V}(3)} b_w) \\
L_{c_{ii}} &= -\cosh(\gamma_i^{\mathrm{I}} a_c) & M_{c_{\ell\ell}} &= -\cosh(\gamma_\ell^{\mathrm{V}(3)} b_w)
\end{aligned} \tag{3.34}$$

By replacing (3.30) into (3.33), the wave amplitudes in the resonant volume can be eliminated and the following linear system is obtained

$$\left(\begin{bmatrix} \mathbf{A}^+ \\ \mathbf{B}^+ \\ \mathbf{C}^+ \\ \mathbf{D}^+ \end{bmatrix} - \begin{bmatrix} \mathbf{A}^- \\ \mathbf{B}^- \\ \mathbf{C}^- \\ \mathbf{D}^- \end{bmatrix} \right) = \underline{\mathbf{Q}} \cdot \left(\begin{bmatrix} \mathbf{A}^+ \\ \mathbf{B}^+ \\ \mathbf{C}^+ \\ \mathbf{D}^+ \end{bmatrix} + \begin{bmatrix} \mathbf{A}^- \\ \mathbf{B}^- \\ \mathbf{C}^- \\ \mathbf{D}^- \end{bmatrix} \right) \tag{3.35}$$

with

$$\underline{\mathbf{Q}} = \begin{bmatrix} \underline{\mathbf{L}}_c \cdot \underline{\mathbf{L}}_s^{-1} & \underline{\mathbf{L}}_s^{-1} & -\underline{\mathbf{U}}^{(10)} \cdot \underline{\mathbf{M}}_s^{-1} \cdot \underline{\mathbf{W}} & \underline{\mathbf{U}}^{(00)} \cdot \underline{\mathbf{M}}_s^{-1} \cdot \underline{\mathbf{W}} \\ \underline{\mathbf{L}}_s^{-1} & \underline{\mathbf{L}}_c \cdot \underline{\mathbf{L}}_s^{-1} & \underline{\mathbf{U}}^{(11)} \cdot \underline{\mathbf{M}}_s^{-1} \cdot \underline{\mathbf{W}} & -\underline{\mathbf{U}}^{(01)} \cdot \underline{\mathbf{M}}_s^{-1} \cdot \underline{\mathbf{W}} \\ -\underline{\mathbf{V}}^{(01)} \cdot \underline{\mathbf{L}}_s^{-1} & \underline{\mathbf{V}}^{(11)} \cdot \underline{\mathbf{L}}_s^{-1} & \underline{\mathbf{W}}^T \cdot \underline{\mathbf{M}}_c \cdot \underline{\mathbf{M}}_s^{-1} \cdot \underline{\mathbf{W}} & \underline{\mathbf{W}}^T \cdot \underline{\mathbf{M}}_s^{-1} \cdot \underline{\mathbf{W}} \\ -\underline{\mathbf{V}}^{(00)} \cdot \underline{\mathbf{L}}_s^{-1} & \underline{\mathbf{V}}^{(10)} \cdot \underline{\mathbf{L}}_s^{-1} & \underline{\mathbf{W}}^T \cdot \underline{\mathbf{M}}_s^{-1} \cdot \underline{\mathbf{W}} & \underline{\mathbf{W}}^T \cdot \underline{\mathbf{M}}_c \cdot \underline{\mathbf{M}}_s^{-1} \cdot \underline{\mathbf{W}} \end{bmatrix}$$

From the latter, the following scattering matrix of a waveguide with two junctions is derived

$$\underline{\mathbf{S}}_{2(N_1+N_3)\times 2(N_1+N_3)}^{\text{junctions}} = 2\left(\underline{\mathbf{I}} + \underline{\mathbf{Q}}\right)^{-1} - \underline{\mathbf{I}} \tag{3.36}$$

being $\underline{\mathbf{I}}$ the identity matrix and $\underline{\mathbf{Q}}$ the matrix of coefficients in (3.35).

3.3.2 Closed-form solutions of projection integrals

Closed-form solutions of the integrals in (3.29), (3.31) and (3.32) can be given for the structure of Fig. 3.12. In this sense the following definitions are useful:

$$\mathcal{R}(k,a,m) = \frac{\sinh(ka)}{k^2 + (m\pi/a)^2}$$

$$\begin{aligned}\mathcal{L}(a,b,m,n) =& \frac{2ab\,(-1)^{\mathrm{floor}(\frac{n}{2})}}{\pi(n^2b^2 - m^2a^2)}\cdot \\ &\cdot \begin{cases} \sin\left[\frac{\pi}{2}\left(\frac{nb}{a} - \mathrm{mod}(m,2)\right)\right], & \text{for } m+n \text{ even} \\ 0, & \text{otherwise} \end{cases}\end{aligned}$$

where $\mathrm{mod}(x,y)$ is the modulus of the ratio x over y, $\mathrm{floor}(x)$ rounds x to the nearest integers less than or equal to x, δ_{xy} is the Kronecker delta and the function ϵ_{xy}, equal to 2 if $x = y$, and 1 if $x \neq y$.

The integral in (3.29) has the following solution

$$\begin{aligned}\mathrm{W}_{\ell j} = \mathrm{W}_{(pq)(mn)} &= \iint_{S_3} \mathbf{e}^{\mathrm{III}}_{\mathbf{t}_{mn}} \times \mathbf{h}^{\mathrm{V}(3)}_{\mathbf{t}_{pq}} \cdot \hat{\mathbf{y}} dS = \\ &= \pi^2 \sqrt{Z^{\mathrm{III}}_{mn} Y^{\mathrm{V}(3)}_{pq}} \sqrt{N^{\mathrm{III}}_{mn} N^{\mathrm{V}(3)}_{pq}} \cdot \\ &\cdot \left(\frac{a_c}{2}\delta_{mp}\epsilon_{0m}\right) \mathcal{L}(a_w, b_c, n, q) \cdot \\ &\cdot \begin{cases} \left(\dfrac{mpqb_c}{a_c a_c} + \dfrac{nqna_w}{b_c a_w}\right), & \text{TE-TE} \\ \left(\dfrac{mpna_w}{a_c a_c} + \dfrac{nqqb_c}{b_c a_w}\right), & \text{TM-TM} \\ \left(\dfrac{npqb_c}{a_c b_c} - \dfrac{mqna_w}{a_c a_w}\right), & \text{TE-TM} \\ \left(\dfrac{mqqb_c}{a_c a_w} - \dfrac{npna_w}{b_c a_c}\right), & \text{TM-TE} \end{cases}\end{aligned} \tag{3.37}$$

except for $n = q = 0$, when the following expression applies

$$\mathrm{W}_{(p0)(m0)} = \sqrt{\frac{b_c Z^{\mathrm{III}}_{m0}}{a_w Z^{\mathrm{V}(3)}_{p0}}}\delta_{mp} \tag{3.38}$$

The integral in (3.31) can be expressed as follows

$$\begin{aligned}
\mathrm{U}_{i\ell}^{(00)} = \mathrm{U}_{(mn)(pq)} &= \frac{1}{\xi_{D_{pq}}} \iint_{S_1} \mathbf{e}^{\mathrm{I}}_{\mathbf{t}_{mn}} \times \mathbf{H}^{\mathrm{V}(4)}_{pq} \cdot \hat{\mathbf{z}} dS = \\
&= \pi^2 \sqrt{Z^{\mathrm{I}}_{mn} Y^{\mathrm{V}(4)}_{pq}} \sqrt{N^{\mathrm{I}}_{mn} N^{\mathrm{V}(4)}_{pq}} \cdot \\
&\cdot \gamma^{\mathrm{V}(4)}_{pq} \left(\frac{a_w}{2} \delta_{mq} \epsilon_{0m} \right) \mathcal{R}(\gamma^{\mathrm{V}(4)}_{pq}, b_w, n) \cdot \\
&\cdot \begin{cases}
\left[-\dfrac{mq}{a_w^2} - \left(\dfrac{n k^{\mathrm{V}(4)}_{t_{pq}}}{b_w \gamma^{\mathrm{V}(4)}_{pq}} \right)^2 \right], & \text{TE-TE} \\
\left(\dfrac{np}{b_w a_c} \right), & \text{TM-TM} \\
\left(\dfrac{mp}{a_w a_c} \right), & \text{TE-TM} \\
\left[-\dfrac{nq}{b_w a_w} + \dfrac{mn}{a_w b_w} \left(\dfrac{k^{\mathrm{V}(4)}_{t_{pq}}}{\gamma^{\mathrm{V}(4)}_{pq}} \right)^2 \right], & \text{TM-TE}
\end{cases}
\end{aligned} \tag{3.39}$$

Finally the integral in (3.32) can be computed as

$$\begin{aligned}
\mathrm{V}_{ji}^{(00)} = \mathrm{V}_{(mn)(pq)} &= \frac{1}{\xi_{A_{pq}}} \iint_{S_4} \mathbf{e}^{\mathrm{III}}_{\mathbf{t}_{mn}} \times \mathbf{H}^{\mathrm{V}(1)}_{pq} \cdot \hat{\mathbf{y}} dS = \\
&= \pi^2 \sqrt{Z^{\mathrm{III}}_{mn} Y^{\mathrm{I}}_{pq}} \sqrt{N^{\mathrm{III}}_{mn} N^{\mathrm{I}}_{pq}} \cdot \\
&\cdot \gamma^{\mathrm{I}}_{pq} \mathcal{L}(a_w, b_c, n, p) \mathcal{R}(\gamma^{\mathrm{I}}_{pq}, a_c, m) \cdot \\
&\cdot \begin{cases}
\left[-\dfrac{npn}{b_c} - p b_c \left(\dfrac{m k^{\mathrm{I}}_{t_{pq}}}{a_c \gamma^{\mathrm{I}}_{pq}} \right)^2 \right], & \text{TE-TE} \\
\left(\dfrac{mqna_w}{b_w a_c} \right), & \text{TM-TM} \\
\left(-\dfrac{nqna_w}{b_c b_w} \right), & \text{TE-TM} \\
\left[\dfrac{mpna_w}{a_w a_c} - \dfrac{nmp}{a_c} \left(\dfrac{k^{\mathrm{I}}_{t_{pq}}}{\gamma^{\mathrm{I}}_{pq}} \right)^2 \right], & \text{TM-TE}
\end{cases}
\end{aligned} \tag{3.40}$$

except for $n = p = 0$, when the following expression applies

$$\mathrm{V}_{(m0)(0q)} = -\pi^2 \sqrt{Z^{\mathrm{III}}_{m0} Y^{\mathrm{I}}_{0q}} \sqrt{N^{\mathrm{III}}_{m0} N^{\mathrm{I}}_{0q}} \cdot \mathcal{R}(\gamma^{\mathrm{I}}_{0q}, a_c, m) \left(\frac{b_c}{\gamma^{\mathrm{I}}_{0q}} \right) \left(\frac{m k^{\mathrm{I}}_{t_{0q}}}{a_c} \right)^2$$

3.3.3 Loaded corrugations

The corrugations of the geometry in Fig. 3.12 can be connected to other microwave networks; we consider single-access structures because such configuration can be used to filter some modes of the main waveguide. In details, we consider that the structure connected to the waveguide slots is a multi-port, single-access, microwave network with N_3 modes. As depicted in Fig. 3.13, it can be characterized with a scattering matrix $\underline{\mathbf{\Gamma}}$, so that

$$\mathbf{C}^+ = \underline{\mathbf{\Gamma}} \cdot \mathbf{C}^- \qquad \text{and} \qquad \mathbf{D}^+ = \underline{\mathbf{\Gamma}} \cdot \mathbf{D}^- \tag{3.41}$$

Several configurations can be conceived and studied; in the present work we restrict the analysis to corrugations with a constant cross-section equal to the waveguide slot.

Three examples are shown in Fig. 3.14; in these configurations $\underline{\mathbf{\Gamma}}$ is diagonal. For the lossless structure of Fig. 3.14a

$$\Gamma_{jj} = -\mathrm{e}^{-2\gamma_j^{\mathrm{III}} h_{cv}}$$

leading to a unitary scattering matrix. To make the corrugations absorb the power extracted from the main waveguide, a lossy dielectric with complex permittivity $\varepsilon_c^{\mathrm{A}}$ can be used. Inside this material the modal expansions are similar to regions III and IV and, if the top corrugation is taken as example, the longitudinal dependence is

$$\begin{aligned} \mathrm{Y}_{\mathrm{e}_j}^{\mathrm{A}} &= Q_j^+ \mathrm{e}^{\gamma_j^{\mathrm{A}}(y-b_w-h_{cv})} + Q_j^- \mathrm{e}^{-\gamma_j^{\mathrm{A}}(y-b_w-h_{cv})} \\ \mathrm{Y}_{\mathrm{h}_j}^{\mathrm{A}} &= -Q_j^+ \mathrm{e}^{\gamma_j^{\mathrm{A}}(y-b_w-h_{cv})} + Q_j^- \mathrm{e}^{-\gamma_j^{\mathrm{A}}(y-b_w-h_{cv})} \end{aligned}$$

where Q and γ_i^{A} are the wave amplitudes and the propagation constant in the absorber (see Fig. 3.15). The boundary conditions to be enforced in the

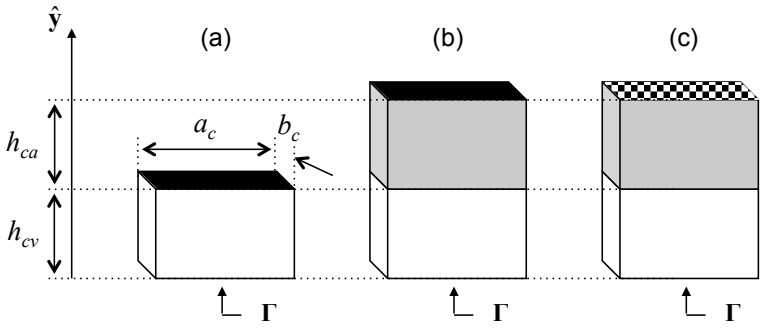

Figure 3.14: Three corrugations with the same cross-section. Grey parts indicate the absorber, black surfaces are perfect electric conductor (PEC) and the chessboard pattern stands for a perfect magnetic conductor (PMC).

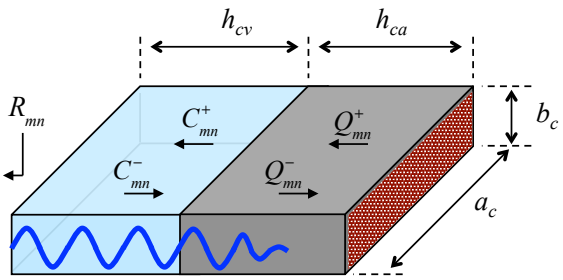

Figure 3.15: Layout of a corrugation with forward and backward waves.

structure of Fig. 3.14b are

$$\begin{aligned}
&\sqrt{Z_j^{\mathrm{III}}}\mathrm{Y}^{\mathrm{III}}_{\mathrm{e}_j}(b_w + h_{cv}) = \sqrt{Z_j^{\mathrm{A}}}\mathrm{Y}^{\mathrm{A}}_{\mathrm{e}_j}(b_w + h_{cv}) \\
&\sqrt{Z_j^{\mathrm{III}}}\mathrm{Y}^{\mathrm{III}}_{\mathrm{h}_j}(b_w + h_{cv}) = \sqrt{Z_j^{\mathrm{A}}}\mathrm{Y}^{\mathrm{A}}_{\mathrm{h}_j}(b_w + h_{cv}) \\
&\mathrm{Y}^{\mathrm{A}}_{\mathrm{e}_j}(b_w + h_{cv} + h_{ca}) = 0
\end{aligned}$$

whereas the last equation has to be replaced with

$$\mathrm{Y}^{\mathrm{A}}_{\mathrm{h}_j}(b_w + h_{cv} + h_{ca}) = 0$$

when the corrugation ends with a PMC as in Fig. 3.14c.

By solving the linear system with respect to the ratio between C_j^+ and C_j^-, the following expression is derived for the S-parameters at the slot:

$$\Gamma_{jj} = \mathrm{e}^{-2\gamma_j^{\mathrm{III}} h_{cv}} \frac{\mathcal{S}(\gamma_j^{\mathrm{A}} h_{ca}) - Z_j^{\mathrm{III}} Y_j^{\mathrm{A}}}{\mathcal{S}(\gamma_j^{\mathrm{A}} h_{ca}) + Z_j^{\mathrm{III}} Y_j^{\mathrm{A}}} \tag{3.42}$$

with

$$\mathcal{S}(t) = \begin{cases} \tanh(t) & \text{for PEC (Fig. 3.14b)} \\ \coth(t) & \text{for PMC (Fig. 3.14c)} \end{cases}$$

Slot size and location determine how corrugations are excited, whereas power absorption is determined by $\underline{\mathbf{\Gamma}}$; with a proper excitation, the lower $\underline{\mathbf{\Gamma}}$, the better filter performance.

The relations (3.41) must be introduced in the formulation of section 3.3.1; they can be directly applied to the boundary conditions in order to express the modal amplitudes $C_j^{\pm}$ and $D_j^{\pm}$ in terms of ξ. In such expressions, there are some recurring matrix operations, which are summarized through the following positions

$$\begin{aligned}
\underline{\mathbf{P}} &= \underline{\mathbf{W}} \cdot (\underline{\mathbf{I}} + \underline{\mathbf{\Gamma}}) \cdot (\underline{\mathbf{I}} - \underline{\mathbf{\Gamma}})^{-1} \\
\underline{\mathbf{F}} &= \underline{\mathbf{P}} \cdot \underline{\mathbf{W}}^T \cdot (\underline{\mathbf{P}} \cdot \underline{\mathbf{W}}^T \cdot \underline{\mathbf{M}}_c + \underline{\mathbf{M}}_s)^{-1} \\
\underline{\mathbf{G}} &= [(\underline{\mathbf{P}} \cdot \underline{\mathbf{W}}^T \cdot \underline{\mathbf{M}}_c + \underline{\mathbf{M}}_s) - \underline{\mathbf{F}} \cdot \underline{\mathbf{P}} \cdot \underline{\mathbf{W}}^T]^{-1}
\end{aligned} \tag{3.43}$$

Using (3.43), the wave amplitudes in region V can be related to each other as follows

$$\begin{bmatrix} \xi_C \\ \xi_D \end{bmatrix} = \begin{bmatrix} \underline{\mathbf{X}}_{ca} & \underline{\mathbf{X}}_{cb} \\ \underline{\mathbf{X}}_{da} & \underline{\mathbf{X}}_{db} \end{bmatrix} \cdot \begin{bmatrix} \xi_A \\ \xi_B \end{bmatrix} \tag{3.44}$$

where

$$\begin{aligned} \underline{\mathbf{X}}_{ca} &= \underline{\mathbf{G}} \cdot (\underline{\mathbf{P}} \cdot \underline{\mathbf{V}}^{(01)} + \underline{\mathbf{F}} \cdot \underline{\mathbf{P}} \cdot \underline{\mathbf{V}}^{(00)}) \\ \underline{\mathbf{X}}_{cb} &= \underline{\mathbf{G}} \cdot (\underline{\mathbf{P}} \cdot \underline{\mathbf{V}}^{(11)} + \underline{\mathbf{F}} \cdot \underline{\mathbf{P}} \cdot \underline{\mathbf{V}}^{(10)}) \\ \underline{\mathbf{X}}_{da} &= \underline{\mathbf{G}} \cdot (\underline{\mathbf{P}} \cdot \underline{\mathbf{V}}^{(00)} + \underline{\mathbf{F}} \cdot \underline{\mathbf{P}} \cdot \underline{\mathbf{V}}^{(01)}) \\ \underline{\mathbf{X}}_{db} &= \underline{\mathbf{G}} \cdot (\underline{\mathbf{P}} \cdot \underline{\mathbf{V}}^{(10)} + \underline{\mathbf{F}} \cdot \underline{\mathbf{P}} \cdot \underline{\mathbf{V}}^{(11)}) \end{aligned} \tag{3.45}$$

A linear system similar to (3.35) for the sole amplitudes $A_i^{\pm}$ and $B_i^{\pm}$ is finally obtained by combining (3.44) with the first two conditions of (3.30) and (3.33). If $\underline{\mathbf{T}}$ is the matrix of coefficients of this system, the generalized scattering matrix of the mode filter is computed as

$$\underline{\mathbf{S}}^{\text{filter}}_{2N_1 \times 2N_1} = 2 \left(\underline{\mathbf{I}} + \begin{bmatrix} \underline{\mathbf{T}}_{11} & \underline{\mathbf{T}}_{12} \\ \underline{\mathbf{T}}_{21} & \underline{\mathbf{T}}_{22} \end{bmatrix} \right)^{-1} - \underline{\mathbf{I}} \tag{3.46}$$

with

$$\begin{aligned} \underline{\mathbf{T}}_{11} &= (\underline{\mathbf{L}}_c - \underline{\mathbf{U}}^{(10)} \cdot \underline{\mathbf{X}}_{ca} - \underline{\mathbf{U}}^{(00)} \cdot \underline{\mathbf{X}}_{da}) \cdot \underline{\mathbf{L}}_s^{-1} \\ \underline{\mathbf{T}}_{12} &= (\underline{\mathbf{I}} + \underline{\mathbf{U}}^{(10)} \cdot \underline{\mathbf{X}}_{cb} + \underline{\mathbf{U}}^{(00)} \cdot \underline{\mathbf{X}}_{db}) \cdot \underline{\mathbf{L}}_s^{-1} \\ \underline{\mathbf{T}}_{21} &= (\underline{\mathbf{I}} + \underline{\mathbf{U}}^{(11)} \cdot \underline{\mathbf{X}}_{ca} + \underline{\mathbf{U}}^{(01)} \cdot \underline{\mathbf{X}}_{da}) \cdot \underline{\mathbf{L}}_s^{-1} \\ \underline{\mathbf{T}}_{22} &= (\underline{\mathbf{L}}_c - \underline{\mathbf{U}}^{(11)} \cdot \underline{\mathbf{X}}_{cb} - \underline{\mathbf{U}}^{(01)} \cdot \underline{\mathbf{X}}_{db}) \cdot \underline{\mathbf{L}}_s^{-1} \end{aligned} \tag{3.47}$$

Despite (3.46) has been derived for geometries with longitudinal slots on the top and bottom wall, it holds validity when $a_w < b_w$ and $a_c < b_c$, i.e. for a mode filter with transversal side corrugations. In this case several consecutive slots are hosted in the device, whose final performance can be calculated by standard cascading techniques of generalized scattering matrices [77]. Once the device is characterized and a combination of injected waves is assigned, the unknown amplitudes of each region can be calculated and inserted in the relevant modal expansions to reconstruct and plot the field distribution in the filter.

The theoretical model has been developed under the assumption of ideal conductors, but losses due to real metals can be introduced according to the perturbation method. To a first approximation, a general complex propagation constant, including the canonical attenuation coefficients in rectangular waveguide, can be used for each mode. This approach requires no modification to the model, which already handles complex γ, e.g. in the absorbing material, and is very accurate for all modes apart from those of the subsets V(3) and V(4). Concerning the latter, the discontinuity on the top and bottom walls introduces additional losses, which can be dealt through a surface impedance boundary condition [79], i.e. the Leontovich condition. Its application to the last two equations of (3.30) represents an improvement of the present model.

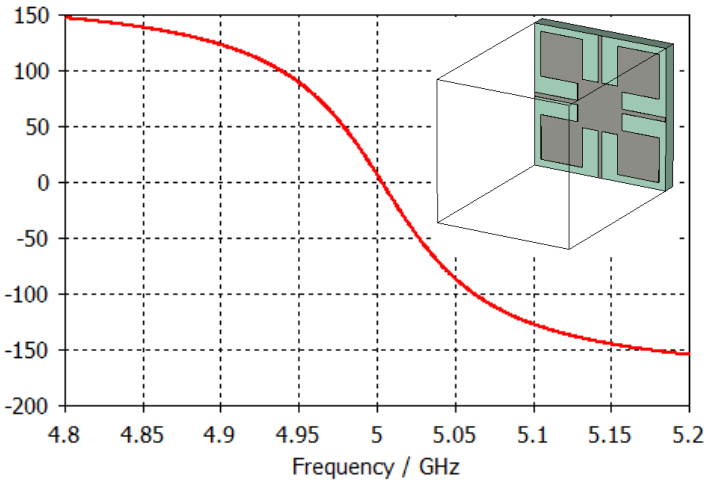

Figure 3.16: Unit cell (a) and phase of the reflected wave (b). The cell consists in a substrate of Rogers RT6010 on a metallic ground plane and a geometric metallization on the top.

Under a practical viewpoint, attenuation by conductors is a minor concern in the considered class of mode filters and will be neglected in the following. Oversized waveguides are meant to reduce ohmic losses that decrease by increasing the ratio between operational and cutoff frequency. The fundamental mode undergoes low dissipation of power on the walls of mode filters (<0.009 dB/m for a copper WR430 at 5 GHz), whereas spurious modes exhibit higher attenuation constants with beneficial effects on the performance of the device.

3.3.4 Practical realization of PMC load

Perfect magnetic conductors were primarily introduced to give an idea about the possibilities of the model. Nevertheless if their practical realization has to be addressed, there are no particular problems apart from a careful assessment of their power handling capability.

In practice, only a few TE modes above cutoff have non-negligible amplitude in the corrugations because, as will be explained later, a dimension of corrugations is always lower than half a vacuum wavelength. This condition is required to avoid the absorption of the fundamental mode in the waveguide and entails that there are no propagating TM modes inside corrugations. In most cases corrugations are even monomodal, so perfect magnetic conductors (PMC) have to be designed for a single mode. Sometimes corrugations could be overmoded, but they rarely support more than two propagating modes.

The particular case of a corrugation with both the TE_{10} and the TE_{20}

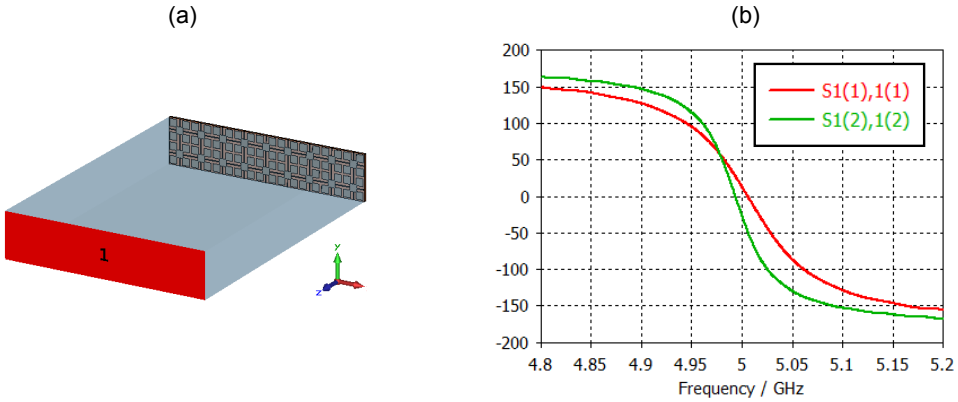

Figure 3.17: Waveguide with PMC load (a) and phase of the reflection coefficients of the TE_{10} and TE_{20} (b).

above cutoff has been studied to clarify the feasibility of a PMC working with different modes at the same frequency. A unit cell achieving PMC behaviour has been initially designed in CST MWS, using one of the manifold patterns proposed in archived literature [80]. The unit cell is depicted in Fig. 3.16 together with the reflection coefficient of a plane wave for normal incidence. The phase of the reflection coefficient, which is 0 deg at 5 GHz, is taken at the surface of the unit cell through de-embedding operations.

Then a lattice of cells was put at the end of a waveguide to assess the effect on two different modes. The waveguide has height of 15.7 mm and width of 71 mm to allow the propagation of both TE_{10} and TE_{20}. Since the behaviour of the lattice in a waveguide with modes slightly differ from the infinite case with a plane wave, the parameters of the unit cell has been reoptimized. The structure and the phase of the reflection coefficients for the two modes are shown in Fig. 3.17. At 5 GHz, the phases of the reflection coefficients, taken at the load plane, are 13 and -26 deg for the TE_{10} and TE_{20}, respectively.

Usually a surface is considered a good perfect magnetic conductor when the phase of the reflected wave is between -90 and 90 deg [81]. Therefore the PMC load of Fig. 3.17 works very well for the TE_{10} and TE_{20} modes at the same time. A dedicated study can lead to enhanced performance and, possibly, to PMC working with more than two propagating modes. However it is worth pointing out that, in overmoded corrugations, the coupled power is not equally distributed between propagating modes. A single mode is always excited to a larger extent, usually $> 80\%$, so the artificial magnetic conductor has to be designed paying particular attention to such mode.

3.4 Mode Filters for Rectangular Waveguide

3.4.1 State of the art

Oversized waveguides and relevant components are of capital importance when very high-power microwave transmissions have to be realized [82, 83]. Several important applications can be considered in this sense such as heating and current drive of plasmas in tokamaks [84], acceleration in high energy linear colliders [85], space propulsion and power beaming [86], directed energy weapons [87] and wireless high-power transmission systems [88].

In plants devoted to this aim, a crucial role is played by mode filters [89], but very few studies are available in literature on this topic. Mode filters based on corrugations are passive microwave components meant to absorb the unwanted propagating modes which are unavoidably excited in oversized transmission lines at discontinuities such as flanges or bends. They are mainly conceived for long-distance high-power transmissions, e.g. for microwave systems in nuclear fusion [90], where oversized rectangular waveguides are preferred to the standard ones due to their higher power-handling capability and lower ohmic losses of the fundamental mode [91]. Since any structure in the waveguide interior (e.g. resistive sheets) increases the risk of RF breakdown, mode filters based on corrugations, partially filled with an absorbing material, are preferred for high-power applications.

The first papers addressing the problem trace back to the 1960s [92, 89] and divided the unwanted modes in rectangular waveguides into two classes. The class A comprises the TE_{mn} and TM_{mn} modes with $n \neq 0$; the class B includes the TE_{m0} modes with $m \neq 1$, which can be further divided depending on whether m is even or odd. The first type of modes can be attenuated with the structure of Fig. 3.18a, whereas the filter of Fig. 3.18b absorbs the second class with m even as well as the TE_{0n}. The study of these components has been abandoned for half a century after optical fibres were preferred to waveguides for long-distance communications. Recently it has

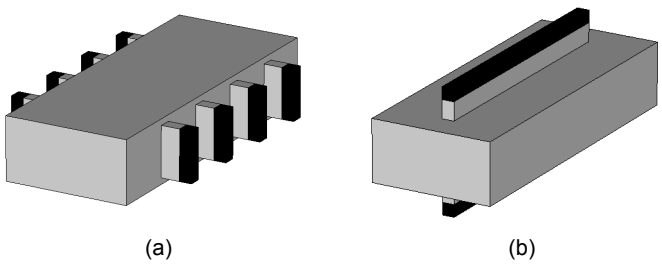

Figure 3.18: Filters with transversal corrugations on the sidewalls (a) and with longitudinal corrugations on the top and bottom walls (b). Light and dark grey parts represent vacuum and absorber, respectively.

received renewed interest, e.g. in nuclear fusion, in connection with systems called to transmit high power rather than a large amount of information.

As pointed out by Neilson [93], discontinuities in overmoded waveguides cannot be accurately modelled with lumped elements and equivalent circuits [94] owing to the excitation of propagating modes other than the fundamental one; hence full-wave techniques must be adopted. Qin and Yang [95] proposed mode filters with deformed cross-sectional shape, but the calculation of the performance is not elucidated. Meschino et al. adopted a finite element method (FEM) [96]; as a drawback volumetric approaches like the latter or like the finite-difference time-domain (FDTD) have large CPU and memory requirements. Moreover they prevent designers from having a clear insight on the underlying physical mechanisms of these components. Recently [97], a simple, approximate formula was used to relate the performance of a single corrugation with its geometrical and electromagnetic parameters.

Here the accurate approach of section 3.3.3, proposed to derive the scattering matrix of mode filters, is assessed. It is a full-wave semi-analytical method relying on the mode matching [98] and the resonator technique [78]. The classical mode-matching method has been successfully used for a large variety of in-line waveguide discontinuities and cavities to design filters, converters, transformers, etc. ([99, 100, 101, 102]) and recently combined with other advanced methods [103, 104]. The resonator technique provides a powerful tool to analyse right-angle waveguide corners as in T-junctions [105], directional couplers [106], diplexers [107], ortho-mode transducers [108], etc.

Mode filters present some differences from the latter devices. The main waveguide always allows multimodal propagation and it is provided with two symmetrical junctions; slots must have very limited impact on the fundamental mode of the waveguide. Corrugations can be considered as finite guiding structures, whose behaviour is expressed through their scattering matrix placing the reference plane at the waveguide wall. This matrix term, which is a fundamental parameter for the analysis and design of mode filters, can be highlighted in the modal approach. Together with some approximate formulas derived under the perturbation method, it provides some insight on the physical behaviour of a corrugation.

The advantage of the proposed method does not rely on physical approximations, but on the effective employment of modal expansions; like any full-wave technique, its application is only constrained by the availability of computational resources. Other full-wave methods, like FDTD or FEM, are still useful to refine a design due to a larger flexibility in drawing geometries, e.g. to model rounded edges, whereas the modal approach has to be preferred during the preliminary optimization phase. This is especially true in the case of multi-dimensional parametric spaces like in mode filters, where a fast evaluation of device performance allows the employment of soft computing techniques.

3.4.2 Convergence and validation

Based on the theoretical model described in section 3.3.3, a computer program has been written in MATLAB [34] to calculate the scattering matrix of mode filters. A critical parameter in the semi-analytical formulation is the number of modes N_1, N_3, N_X to be included in the computation. The approach we adopted is to set a maximum frequency f_c^{max} and to derive the highest indices of the TE_{m0} and TE_{0n} modes having cutoff frequency lower than f_c^{max}. All modes with indices lower than the maximum ones are considered in the calculation as shown in Fig. 3.19.

This choice guarantees that the relative truncations of the series are proportional to the aspect ratios between the different regions [75, 109]. An exception is represented by the resonant region for the case of longitudinal corrugations, where the spatial resolution along x has been doubled. Despite this increase does not follow the canonical rules provided by the relative convergence, it was empirically found to improve the convergence rate. Independently from the series truncation order, the mode-matching formulation always satisfies the power conservation law provided that modes are properly normalized [110]. This property holds true in the present case, where the resonator technique is also used; the convergence is thus studied in terms of S-parameter variation versus f_c^{max}.

As a rule of thumb for usual, realistic configurations, a factor 4 between f_c^{max} and the operational frequency of the filter is generally enough to achieve a convergence threshold of 0.01 on the magnitude of the scattering parameters. This behaviour is clarified by considering mode filters based on five standard waveguides with increasing size from the WR284 to the WR650. The geometrical parameters of their corrugations are defined in Fig. 3.20; all configurations employ silicon carbide ($\varepsilon_r = 13.5$, $\tan\delta = 0.44$) as lossy dielectric. For each case, f_c^{max} is increased from the working frequency of 5 GHz with steps of 1 GHz, and the maximum variation between the S-parameter amplitudes of two consecutive steps is calculated. The outcomes

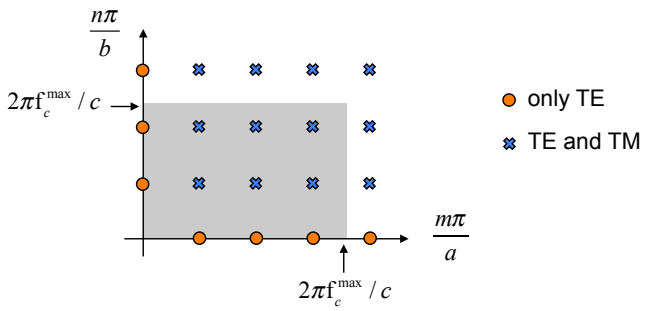

Figure 3.19: Spectrum of modes: a and b represent the dimensions of a specific region. The modes in the shaded area are included in the computation.

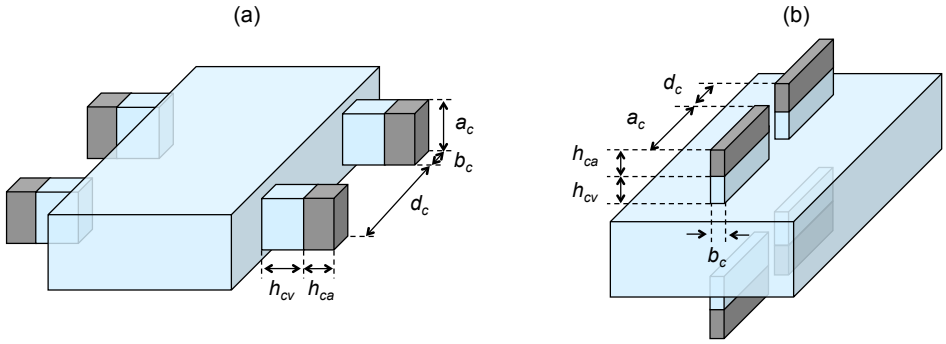

Figure 3.20: Geometrical parameters of mode filters attenuating modes of class A (a) and class B (b).

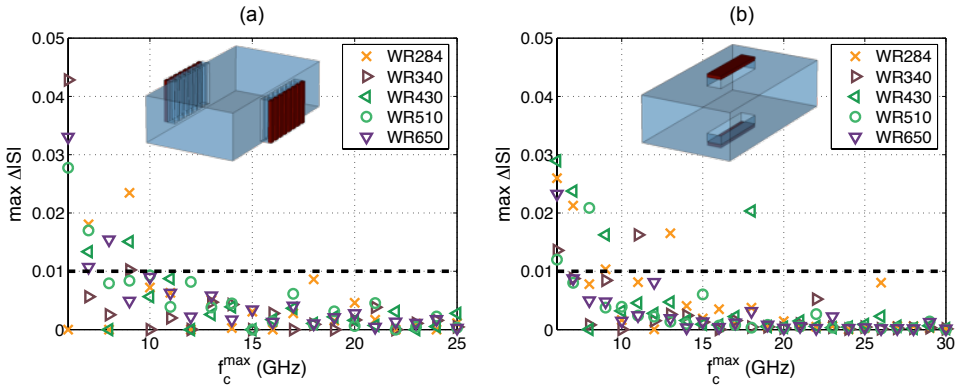

Figure 3.21: Maximum variation of $|S|$ between two consecutive passes versus f_c^{max} for mode filters working at 5 GHz and based on different standard waveguides with either eight corrugations on the sidewalls (a) or single corrugations on the top and bottom walls (b). The former have $a_c = 0.9b_w$, $b_c = 6$ mm, $d_c = 4$ mm, $h_{cv} = 10$ mm, $h_{ca} = 4$ mm; the latter have $a_c = 75$ mm, $b_c = 0.16a_w$, $h_{cv} = 10$ mm, $h_{ca} = 4$ mm.

are plotted in Fig. 3.21. With reference to the case based on the WR430, the convergence curves with standard and double resolution are compared in Fig. 3.22: the one employs f_c^{max} for the sets of modes V(3) and V(4), while the other employs $2f_c^{max}$ along x for such sets and achieves a faster convergence.

The behaviour of $\Delta|S|$ in the previous convergence plots may confuse people used to similar figures in mode-matching application to monomodal waveguides. If Fig. 3.22 is considered for example, the peak at $f_c^{max} = 35$ GHz may be ascribed to the increasing condition numbers of some matrices, which are inverted in the numerical code like the expression in rounded brackets of (3.46) or the matrix $\underline{\mathbf{L}}_s$ in (3.47). Further investigations in this

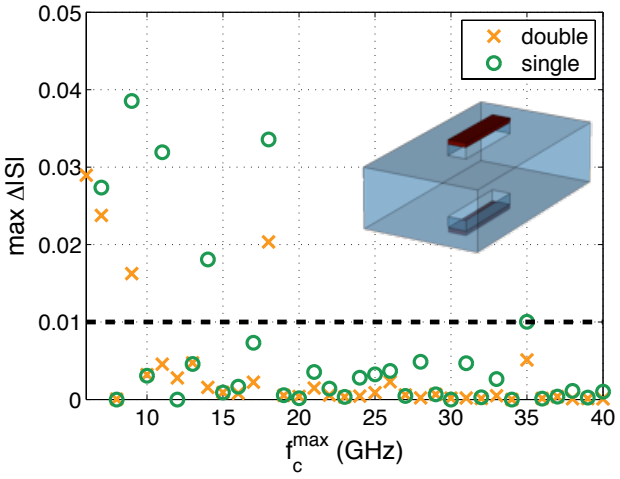

Figure 3.22: Maximum variation of $|S|$ between two consecutive passes versus f_c^{max} for the filter of Fig. 3.21b. Computations with standard (single) and increased (double) spatial resolution along x in the resonant region.

sense do not confirm such hypothesis. On one hand, $\underline{\mathbf{L}}_s$ is a diagonal matrix with terms $\sinh(x)$, which is not inverted because the code directly implements a diagonal matrix with terms $1/\sinh(x)$. As for the term with submatrices $\underline{\mathbf{T}}$, the computations do not provide evidence of either increasing condition numbers or an ill-conditioned matrices. For the example in Fig. 3.22 , the condition numbers of the matrix to be inverted in (3.46), are below 100 and the one at 35 GHz is around 62. On the other hand, the matrix inversion in the last two formulas of (3.43) presents some issues. As f_c^{max} increases, the condition numbers of such matrices increases too, exceeding 10^{20} for $f_c^{max} > 30$ GHz and providing a warning message in MATLAB. Nevertheless this phenomenon is not responsible for the "strange" behaviour of $\Delta|S|$, which also occurs at lower values of f_c^{max} as in the range $[15 \div 20]$ GHz, where all matrices to be inverted are relatively well-conditioned. The variation of scattering parameters is rightly expected to decrease when more and more modes are considered in the computation, but this is true for the single scattering parameter with respect to the higher order modes that give nonzero coupling with it. In Fig. 3.22 the maximum variation in the elements of a scattering matrix, which relates 20 propagating modes, is presented. Some scattering parameters exhibit faster convergence, while the ones related to the modes like the TE_{31} and TM_{31} have to wait that some high-order evanescent modes with nonzero projection integrals are included. Moreover the x-axis of Fig. 3.22 is f_c^{max} rather than the number of modes and, for instance, at $f_c^{max} = 33$ and 34 GHz the number of considered modes is equal ($\Delta|S| = 0$), while it increases at $f_c^{max} = 35$ GHz. A plot versus f_c^{max}

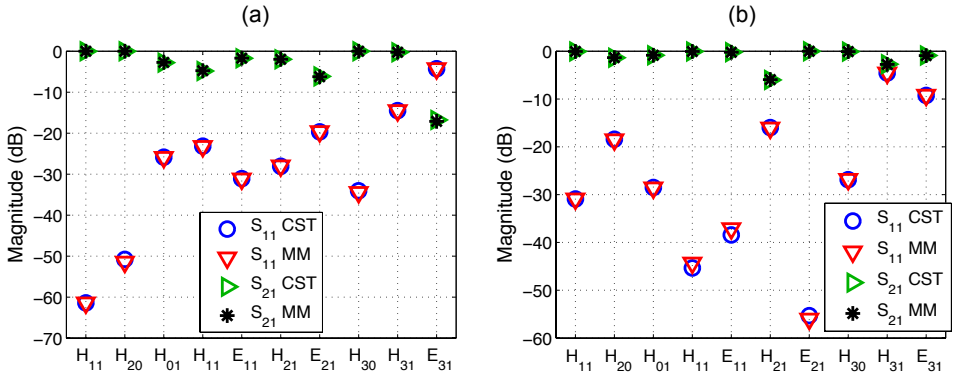

Figure 3.23: Comparison between reflection and transmission self-terms of the scattering matrix calculated by the frequency solver of CST MWS (CST) and the proposed formulation (MM) at 5 GHz for the components of Fig. 3.21a (a) and 3.21a (b), based on the WR430. On the abscissa, the TE (H) and TM (E) modes above cutoff are listed.

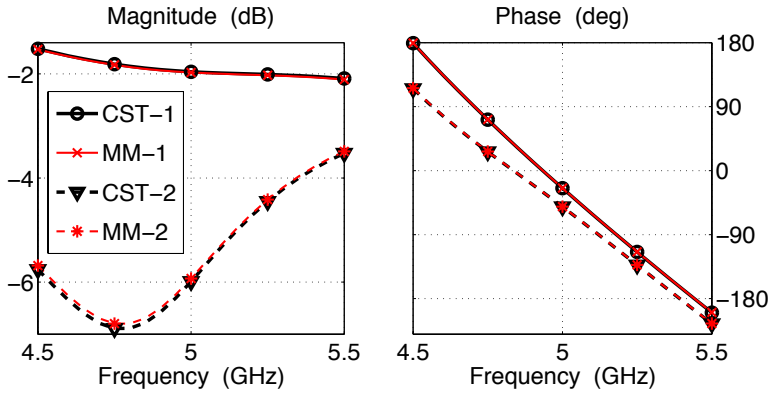

Figure 3.24: Comparison versus frequency between the transmission self-terms of the TE_{21} calculated by the commercial and proposed tools for the components of Fig. 3.21a (CST-1, MM-1) and 3.21b (CST-2, MM-2).

has this drawback, but it has to be preferred to a plot versus the number of modes because the latter depends on the size of the device and is not suitable to derive general rules of thumb for any oversized waveguide.

To validate the mode-matching formulation, two benchmarks were performed using mode filters based on the WR430. This standard waveguide is an intermediate test case among the previous ones; moreover it was proposed for the 5 GHz system of the international tokamak experimental reactor (ITER) [111]. Mode-matching results are compared to those obtained with the frequency solver of CST MWS. Owing to the high number of propagating modes in WR430 at 5 GHz, i.e. 10, only the reflection and transmission

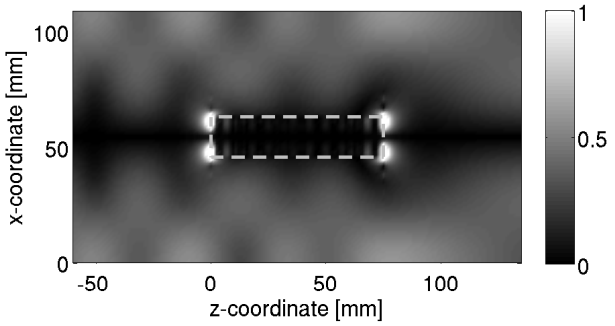

Figure 3.25: Magnitude of a surface current component (J_x) in arbitrary unit on the top wall of the filter of Fig. 3.21b when the TE_{10} is injected.

coefficients between the same modes are reported for demonstration in Figs. 3.23a and 3.23b, which respectively refer to the geometries aimed at absorbing modes of class A (Fig. 3.20a) and B (Fig. 3.20b). The lengths of the input and output smooth-wall waveguides are 60 mm and f_c^{max} is 20 GHz. Very good agreement is achieved with a deviation between the results of the two solvers smaller than the convergence threshold. A deviation of 0.004 is obtained for the structure of Fig. 3.21b based on the WR430, while, without using enhanced spatial resolution, the maximum difference with the S-parameters computed by the commercial software would be 0.023. Further confidence on the proposed method is provided by Fig. 3.24, where a benchmark between the two methods versus frequency is shown. The transmission coefficient of the TE_{21} mode is compared in magnitude and phase since it allows a meaningful visualization of both test cases in the same plot.

Higher f_c^{max} can be used when computing field distributions to improve image resolution. An example of field overlay, computed with $f_c^{max} = 40$ GHz, is given in Fig. 3.25 for the filter with longitudinal corrugations, when the fundamental mode is injected. The plot refers to the x-component of the surface currents on the top wall, which are the main responsible for exciting corrugation modes above cutoff in such device. As can be appreciated, they almost vanish in correspondence of the waveguide slot, thus explaining the minimal absorption of the TE_{10} mode ($< 1\%$) across the device.

The advantage of the mode-matching formulation over a volumetric solver can be clearly appreciated from the figures of execution time reported in Table 3.2. They represent the wall-clock times taken by the two solvers to compute the scattering matrix of the geometries of Fig. 3.21 for 21 frequency samples in the range $4.9 \div 5.1$ GHz. Calculations were run on a desktop computer with a 64-bit INTEL® Core™ i7-950 (3.07 GHz) and 12 GB of RAM. Standards settings were used for the commercial software, which performed a parallel computation up to 4 threads, whereas the MATLAB code was run

	class A		class B	
solver (# threads): WG (# modes)	CST (4)	MM (1)	CST (4)	MM (1)
WR284 (5)	275	5	234	13
WR340 (7)	358	10	300	20
WR430 (10)	735	35	686	46
WR510 (14)	2059	76	1329	74
WR650 (23)	6714	318	3372	207

Table 3.2: Solver times [s].

		N_3		N_X	
	N_1	class A	class B	class A	class B
WR284	115	16	52	115	430
WR340	162	19	52	162	514
WR430	263	22	73	232	640
WR510	351	25	73	314	745
WR650	587	31	94	493	955

Table 3.3: Number of modes.

on a single core. A parallel implementation of the mode-matching formulation can be easily conceived, leading to further improvement of the execution time perceived by the user. From the WR340 on, the wall-clock time of the two approaches exhibits a similar scaling with the electrical length. In Table 3.3 the number of modes considered in the different regions are reported for each waveguide.

3.4.3 Physical mechanisms and design guidelines

The modal approach, in the full-wave form given in section 3.3.3, does not provide much insight into the physical mechanisms ruling the behaviour of mode filters, thus making difficult the derivation of design guidelines. To this aim, approximate formulas are derived here, under the perturbation method, by considering a waveguide with a single corrugation and dividing the problem in two separate sub-tasks: the excitation of the modes in the corrugation and their absorption. The former is a coupling problem of waveguide junctions and depends on slot location, dimensions and exciting modes; the latter reduces to a problem of wave reflection and transmission in a multi-layered geometry.

Excitation

A current source $\mathbf{J}$, located in the volume V of an infinitely long waveguide with cross-section S on xz, excites a set of TE and TM modes. By applying the Lorentz reciprocity formula and according to the adopted normalization, the amplitude of a given forward wave is [33]:

$$C_j^+ = \frac{1}{2}\int_V \mathbf{E}_j^- \cdot \mathbf{J} dxdydz \tag{3.48}$$

being $\mathbf{E}_j^-(x,y,z)$ the E-field of a backward propagating mode. The (3.48) can be applied to a corrugation on the top wall of a waveguide, assuming a small coupling regime: $\mathbf{J}$ symbolizes the surface electric current, given by the magnetic field distribution on the wall of the un-slotted waveguide. The Schelkunoff's field equivalence principle is then applied filling the half-space below the slot with a PMC as shown in Fig. 3.26. The amplitude of the modes excited at the input of the corrugation becomes

$$C_j = \int_{\text{slot}} \mathbf{e}_{\mathbf{t}_j}^{(\text{corr})} \cdot \mathbf{H}^{(\text{wg})} \times \hat{\mathbf{n}} dS \tag{3.49}$$

where, in the present case, $C_j = C_{mn}^-$, $\hat{\mathbf{n}} = \hat{\mathbf{y}}$, $\mathbf{e}_{\mathbf{t}_j}^{(\text{corr})} = \mathbf{e}_{\mathbf{t}_{mn}}^{\text{III}}$ and $\mathbf{H}^{(\text{wg})} = \mathbf{H}^{\text{I}}$. The (3.49) indicates that the surface currents on slotted walls excite the corrugation modes that match the current pattern to the larger extent. The magnitude of the coupling coefficient from the pq-th waveguide mode to the mn-th corrugation mode and is thus

$$\kappa_{pq,mn}^{\text{TOP}} = \frac{1-(-1)^m \mathrm{e}^{-\gamma_{pq}^{\text{I}} a_c}}{\sinh(\gamma_{pq}^{\text{I}} a_c)} \mathrm{V}_{mn,pq}^{(01)} \tag{3.50}$$

which can be expressed analytically using the (3.40). Compared to the (3.40), the (3.49) only differs in the longitudinal dependence of $\mathbf{H}^{\text{I}}$ with respect to $\mathbf{H}^{\text{V}(1)}$: the former is the unperturbed magnetic field in the un-slotted

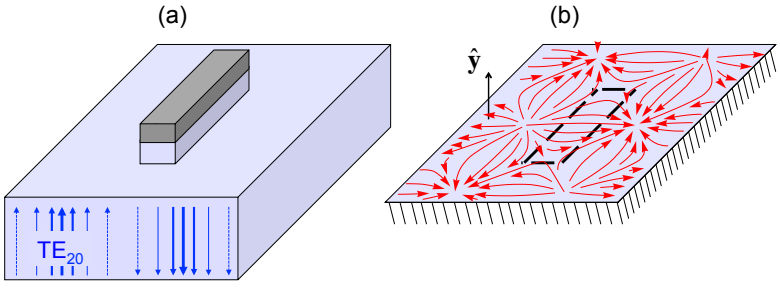

Figure 3.26: (a) E-field of the TE_{20} mode at the input port of the filter of Fig. 3.20b with a single corrugation on the top wall; (b) equivalent surface currents $\mathbf{J}_s = -2\hat{\mathbf{n}} \times \mathbf{H}_{20}^{\text{I}}$ on the slotted wall.

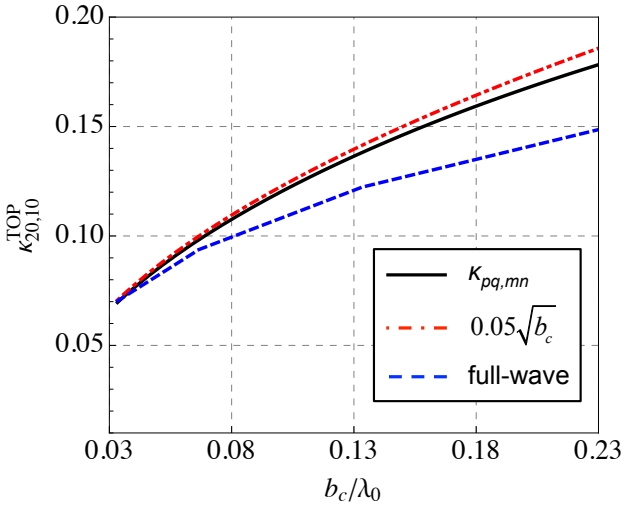

Figure 3.27: Coupling at 5 GHz for a WR430-based filter with $a_c = 45$ mm.

waveguide where no reflected wave is present. This difference results in the correction factor that multiplies $\mathrm{V}^{(01)}_{mn,pq}$ in the (3.50). For a corrugation on the bottom wall, the amplitude of the coupling coefficients is equal to (3.50).

The fundamental mode in the waveguide is the operational mode and it is expected to pass through the filter with minimal insertion losses. Since the function $\mathcal{L}$ in the (3.40) vanishes when $p+n$ is odd, the lowest-order mode excited by the $\mathrm{TE}^{(\mathrm{wg})}_{10}$ in the longitudinal corrugations is the $\mathrm{TE}^{(\mathrm{corr})}_{01}$. For $b_c < \lambda_0/2$, the latter is under its cutoff frequency and the $\mathrm{TE}^{(\mathrm{wg})}_{10}$ only couples to evanescent modes, which exponentially decay in the vacuum section of the corrugation.

A fraction of power from the evanescent modes can reach the lossy dielectric. This fraction is

$$1 - \mathrm{e}^{-\gamma^{\mathrm{III}}_{0n} h_{cv}} \tag{3.51}$$

and can be minimized increasing h_{cv} or $\gamma^{\mathrm{III}}_{0n}$. The former term is constrained by the acceptable size of the device: in the RF systems for nuclear fusion, several waveguides are often closely arranged along the transmission path. The latter term is increased by reducing b_c, which also affects the coupling coefficients of spurious modes. We are interested in the $\mathrm{TE}^{(\mathrm{wg})}_{\mathrm{p0}}$ with p even and in the $\mathrm{TE}^{(\mathrm{corr})}_{\mathrm{m0}}$, being the only modes above cutoff when $b_c < \lambda_0/2$. If the height of the slot is small ($pb_c \ll a_w$), then $\mathcal{L}(a_w, b_c, p, 0) \approx 1$ and

$$\kappa^{\mathrm{TOP}}_{p0,m0} \propto \sqrt{b_c} \tag{3.52}$$

This behaviour is plotted in Fig. 3.27 together with a fitting curve and the prediction of a full-wave commercial software; such comparison confirms that

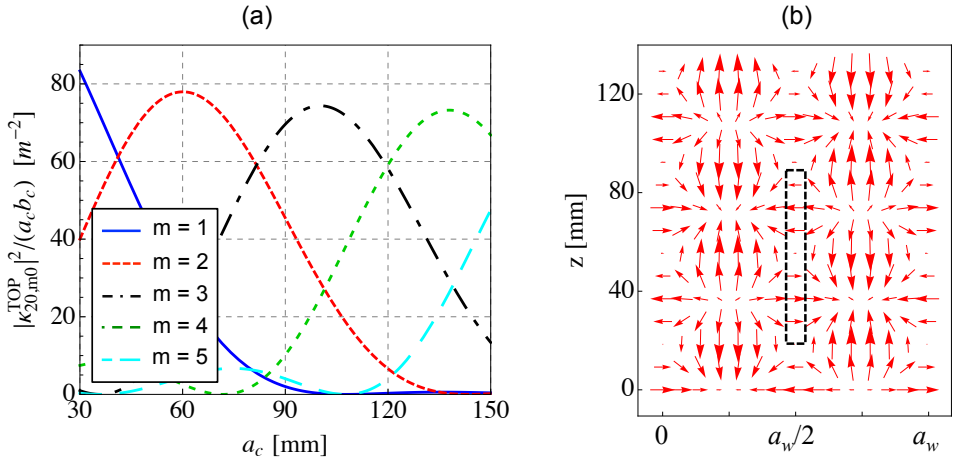

Figure 3.28: (a) Power density, normalized to input power, coupled to the $\mathrm{TE}_{\mathrm{m0}}^{(\mathrm{corr})}$ at 5 GHz for a filter based on the WR430 with $b_c = 5$ mm. (b) Unperturbed surface currents of the $\mathrm{TE}_{20}^{(\mathrm{wg})}$ on the top wall and sketch of a relevant slot with $a_c = 60$ mm.

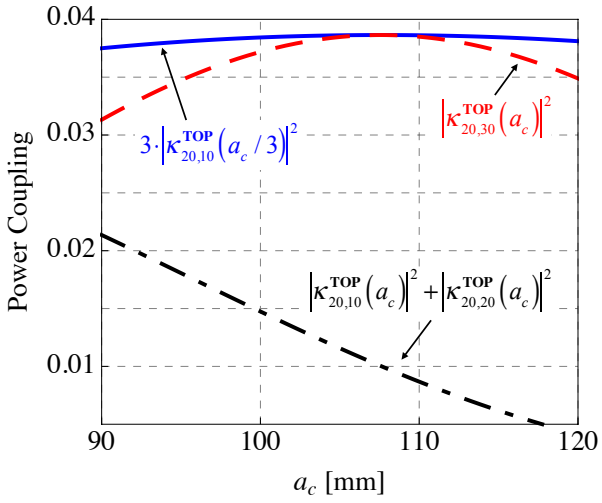

Figure 3.29: Comparison of the power coupling at 5 GHz due to the $\mathrm{TE}_{20}^{(\mathrm{wg})}$ between a long corrugation and three monomodal corrugations for a filter based on the WR430 with $b_c = 5$ mm.

equation (3.50) provides a good approximation in the case of small coupling, detaching from the full-wave result as b_c increases.

The dependence on a_c is instead given in Fig. 3.28 in terms of power coupling coefficients normalized to the slot area for the $\mathrm{TE}_{20}^{(\mathrm{wg})}$; other $\mathrm{TE}_{\mathrm{p0}}^{(\mathrm{wg})}$ modes with p even produce similar curves. The coupling maxima occur in

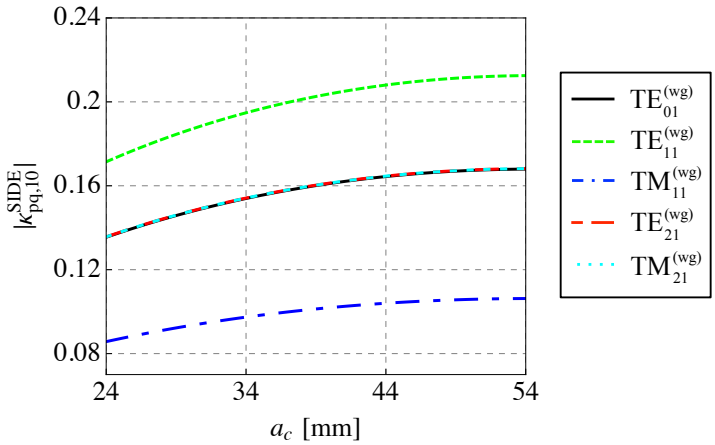

Figure 3.30: Coupling at 5 GHz for a sidewall corrugation with $b_c = 3.1$ mm in a filter based on the WR430.

correspondence of the largest similarity between the patterns of the surface currents and the E-field eigenfunctions of the corrugation. For example Fig. 3.28b shows the sketch of an aperture with $a_c = 60$ mm, where the current lines draw a configuration resembling the $TE^{(corr)}_{20}$. The distance between coupling peaks is indeed close to 36 mm, which is half a wavelength of the $TE^{(wg)}_{20}$ in the example, entailing that an additional half a period of the current pattern enters the wall aperture.

In general, each mode in the corrugation exhibits a range of slot widths where it mainly contributes to the total absorption; far from this region the coupling becomes negligible. In a long corrugation, the dominant mode, i.e. the one with the highest amplitude, extracts from the main waveguide a lower power than several monomodal corrugations with the same total length; an example of this behaviour is reported in Fig. 3.29. The choice between overmoded and monomodal solutions depends on the absorption properties of the corrugation with respect to excited modes; the matter is addressed later on. Anyhow a single TE mode is always excited to a larger extent; this fact simplifies the design of realistic PMC loads.

Similar considerations hold true for corrugations on the sidewalls since, with reference to the dimensions of Fig. 3.20a, the following relation applies:

$$\kappa^{\mathrm{SIDE}}_{pq,mn}(a_w, b_w, a_c, b_c) = \kappa^{\mathrm{TOP}}_{qp,nm}(b_w, a_w, b_c, a_c) \tag{3.53}$$

The choice of b_c is a trade-off between minimizing the insertion losses and maximizing the coupling from unwanted modes; usual values are in the range $0.1\lambda_0 \div 0.5\lambda_0$. As regards a_c, corrugations are often monomodal, e.g. in the Lower Hybrid systems for nuclear fusion, the height of the waveguide is generally shorter than λ_0 and the usual values of a_c are around $0.9b_w$. An example of sidewall coupling is given in Fig. 3.30: being the corrugation

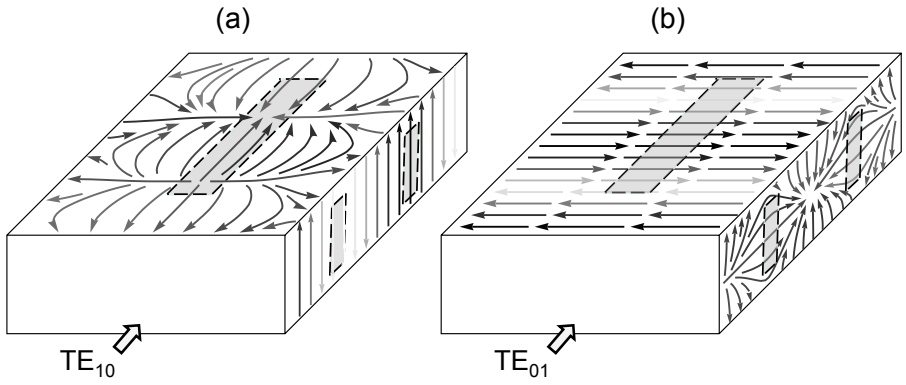

Figure 3.31: Unperturbed electric surface currents on the top and right walls when either the TE_{10} (a) or the TE_{01} (b) mode is injected.

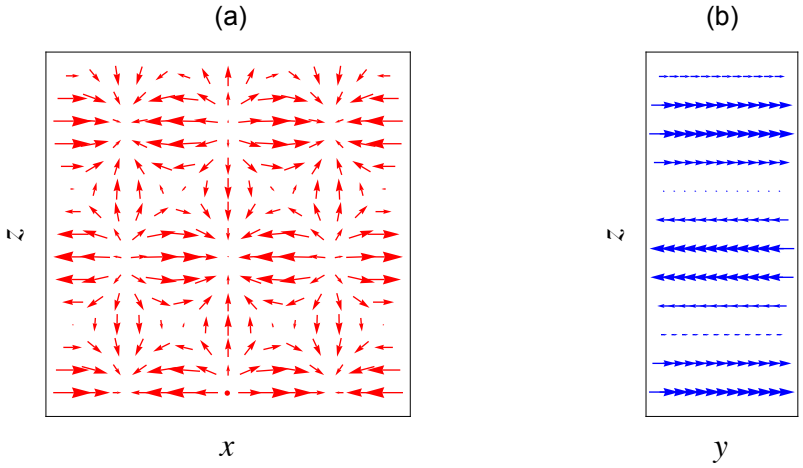

Figure 3.32: $TE_{30}^{(wg)}$ surface currents on the top (a) and right (b) walls.

monomodal, the coupling to the $TE_{10}^{(corr)}$ is depicted considering different waveguide modes.

The reasons of slot positioning in the waveguide can be grasped intuitively by looking at Fig. 3.31. The condition $b_c < \lambda_0/2$ implies that only surface currents perpendicular to the slots excite corrugation modes above cutoff; hence apertures on waveguide walls must be parallel to the surface currents of the $TE_{10}^{(wg)}$ mode (Fig. 3.31a), while crossing the current lines of spurious modes. For example the $TE_{01}^{(wg)}$ excites the slots on both the top and right walls of Fig. 3.31b. This mechanism leads to the main drawback of corrugation-based mode filters: they cannot damp class B modes with odd p, whose surface currents are always parallel to considered slots, as shown for example in Fig. 3.32 for the $TE_{30}^{(wg)}$ mode.

Absorption

Each corrugation can be considered like a waveguide resonator, fed by the main waveguide, according to the scheme of Fig. 3.15. On one side, the waves are totally reflected by a perfect conductor, while, on the other side, they find a discontinuity with reflection coefficient $\mathbf{R}$ corresponding to the slotted wall of the waveguide. To a first approximation, $\mathbf{R}$ can be considered diagonal; such assumption is very close to the real situation in practical cases. At each round trip the j-th mode is attenuated by the factor $|\Gamma_{jj}|^2$, so we can introduce the following figure-of-merit for the corrugation:

$$\mathrm{FoM} = \left| \frac{|\Gamma_{jj}| - R_{jj}\Gamma_{jj}}{1 - R_{jj}\Gamma_{jj}} \right|^2 \tag{3.54}$$

which is the fraction of power that flows back to the main waveguide. The (3.54) is a kind of fitness function, whose minimization corresponds to maximize the absorption of power. R_{jj} is usually fixed because it depends on the slot size and location, therefore the (3.54) is optimized acting on Γ_{jj}, i.e. on h_{cv} and h_{ca}.

A plot of FoM is depicted in Fig. 3.33 for the same structures of Fig. 3.29 and considering optimal values of h_{cv}. The dominant mode in the long corrugation exhibits a higher fitness function in comparison with the fundamental mode in the monomodal corrugation. The other propagating modes achieve higher absorption, but they also have lower amplitude as was seen in Fig. 3.28. The net effect has to be assessed case by case since there

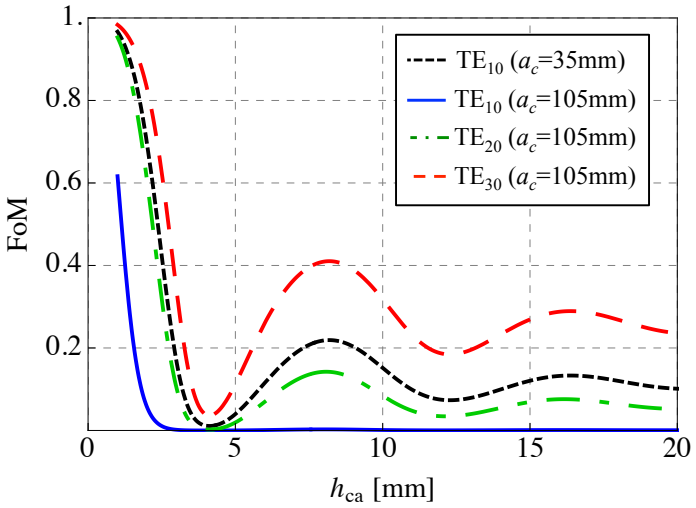

Figure 3.33: FoM at 5 GHz in three corrugations with $a_c = 35$ mm and in a corrugation with $a_c = 105$ mm; the filters are based on the WR430 and have $b_c = 5$ mm, optimal h_{cv} and silicon carbide (SiC) as absorber.

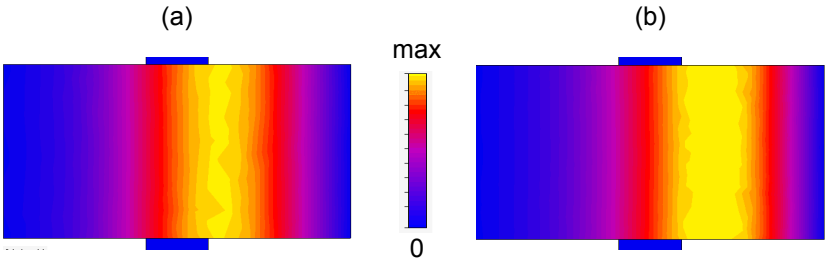

Figure 3.34: E-field amplitude at 5 GHz at the output of WR430-based filters with two corrugations on the top and bottom walls; $a_c = 105$ mm, $b_c = 20$ mm, $h_{cv} = 15$ mm, h_{ca} =3.5 mm (a) and 8.5 mm (b) of SiC.

is no clear indication supporting the use of monomodal corrugations rather than overmoded ones to damp spurious modes of class B.

The connection of Figs. 3.28 and 3.33 with the final behaviour of a component can be better understood by considering a filter with two longitudinal corrugations on the top and bottom walls with the same parameters as in Fig. 3.33 and $h_{cv} = 15$ mm. A mixture of the TE_{10} (70%) and the TE_{20} (30%) is considered at the filter input: the former mode does not excite any propagating mode in the corrugation, whereas the latter one predominantly couples to the $\mathrm{TE}_{30}^{(\mathrm{corr})}$ according to Fig. 3.28. From Fig. 3.33 (red curve), we expect that the best and worst performances of the filter occur close to $h_{ca} = 4$ and 8 mm, respectively, and that their difference is noticeable. Full-wave calculations show that the maximum and minimum absorption of the $\mathrm{TE}_{20}^{(\mathrm{wg})}$ is at $h_{ca} = 3.5$ and 8.5 mm, corresponding to a purity of the fundamental mode at the filter output of 75.2% and 72%, respectively. This difference can be graphically appreciated by increasing the coupling according to (3.52). Fig. 3.34 shows the E-field maps at the output of the previous filters with b_c increased from 5 to 20 mm. The devices with $h_{ca} = 3.5$ and 8.5 mm now achieve a mode purity of 85.5% and 75.3% at the output; the E-field distribution in the former case has a maximum closer to the waveguide centre, thus resembling the pattern of the $\mathrm{TE}_{10}^{(\mathrm{wg})}$ to a larger extent.

Some attention must be paid to the value of h_{cv}, which was supposed in Fig. 3.33 to satisfy the resonance condition of the corrugation. The phase variation due to a round trip in the corrugation has to be an integer multiple of 2π to set up a standing wave with enhanced amplitude and improve the absorption. By referring to Fig. 3.15 and denoting the arguments of R_{jj} and $\Gamma_{jj}(h_{cv} = 0)$ with Φ_w and Φ_a, respectively, the condition of constructive interference gives

$$-2\gamma_j^{\mathrm{III}} h_{cv} + \Phi_w + \Phi_a = 2k\pi \qquad \text{with } k = 0, 1, 2, \ldots$$

The noncompliance with the previous rule determines a small deterioration

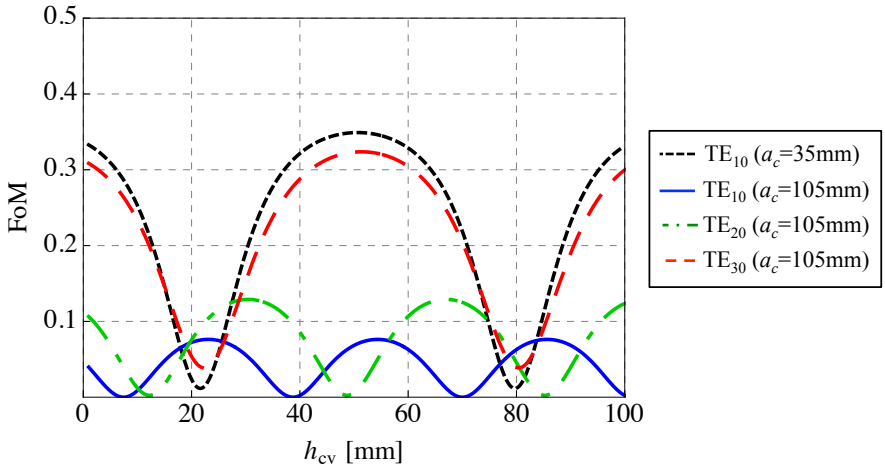

Figure 3.35: FoM versus h_{cv} in the cases of Fig. 3.33 with $h_{ca} = 4$ mm.

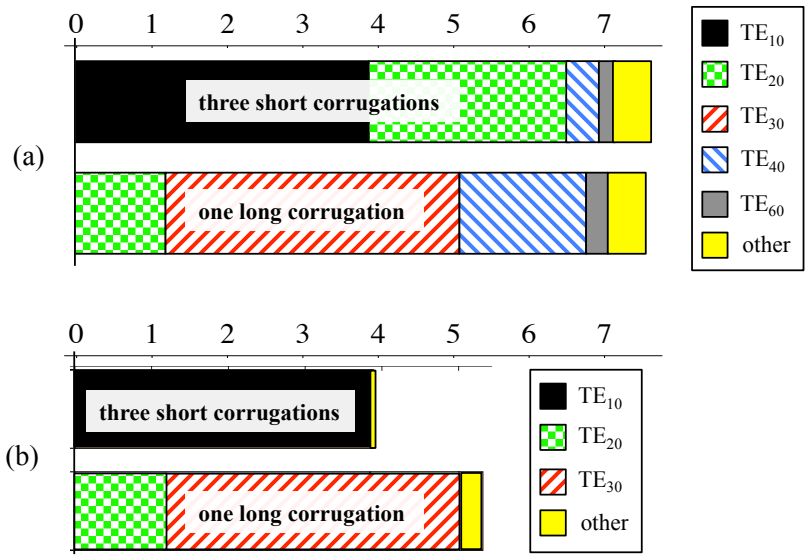

Figure 3.36: Power [%] coupled by the $\mathrm{TE}_{20}^{(\mathrm{wg})}$ for the same structures of Fig. 3.33, present at the slot (a) and after $h_{cv} = 15$ mm (b).

of the FoM, which turns out to be a periodic function of h_{cv} with period equal to half a wavelength of the corrugation mode in the vacuum section. This behaviour can be appreciated in Fig. 3.35: different modes have different optimal values of h_{cv}, so overmoded corrugations can be just optimized for a single propagating mode.

The modal content excited at the corrugation input and the one that reaches the absorber after 15 mm of vacuum are shown in Fig. 3.36: the former reveals a richer spectrum. It follows that the same filters with $h_{cv} = 0$

damp the $\mathrm{TE}_{20}^{(\mathrm{wg})}$ to a greater extent; as a drawback, the evanescent modes excited by the $\mathrm{TE}_{10}^{(\mathrm{wg})}$ would be absorbed too. This phenomenon provides the last design guideline, which concerns the choice of h_{cv}, i.e. of the harmonic k in the resonator-like corrugation. In its vacuum sections, the decay lengths of the evanescent modes that are mostly excited by the fundamental and the unwanted modes of the waveguide are respectively equal to $b_c/(n\pi)$ and $a_c/(m\pi)$. Since $a_c > b_c$, a value of h_{cv} can be generally found so that the power level of the modes excited by the $\mathrm{TE}_{10}^{(\mathrm{wg})}$ is negligible, while other evanescent modes still carry some power. This value is much lower for the corrugations on the sidewalls because the coupling from the $\mathrm{TE}_{10}^{(\mathrm{wg})}$ to modes under cutoff is some order of magnitude lower than the coupling from unwanted modes.

The use of absorbing materials different from silicon carbide does not change previous considerations. Parametric analyses of the FoM show that higher dielectric constants move the minimum of the fitness function towards smaller absorber depth and make the peak steeper. With reference to the variation of the loss tangent, lower and higher values than 0.44 respectively increase and reduce the ripple amplitude of Fig. 3.33.

3.4.4 Numerical examples of optimization

Approximate models provide some insight on the behaviour of mode filters, but they can lead to significant errors, e.g. in long devices, where an accurate prediction of insertion losses is required; a full-wave method is mandatory in such cases. In the following, some examples of design using the Particle Swarm Optimization (PSO) algorithm [112] are presented. The goal to be maximized is the absorption of a given mode, while keeping the insertion loss below 4.4×10^{-3} dB (i.e. about 99.9% of transmitted power in the fundamental mode); soft boundaries have been adopted to delimit the feasible domain. Calculations have been performed as batch jobs in the Computational Research Centre for Complex Systems (CRESCO), a multi-platform high performance computing cluster [113].

The first example of optimization is the design of a filter of class A to damp the TM_{11} by means of lateral corrugations terminated with PECs. The optimization was run with respect to the five geometrical dimensions given in Fig. 3.20a, constraining slot widths and spacings to be greater than 3 mm to ease manufacturability. The number of corrugations is automatically derived, after setting their width and spacing and choosing an approximate total length L, by rounding the ratio $(L + b_c)/(b_c + d_c)$. With $L = 1$ cm, the optimization algorithm returns a structure with 2 corrugations, the performance of which is given in Fig. 3.37a. The absorption of the TM_{11} is correctly peaked at 5 GHz and, at the same frequency, the TE_{11} is optimally filtered too. The latter unwanted mode undergoes higher attenuation

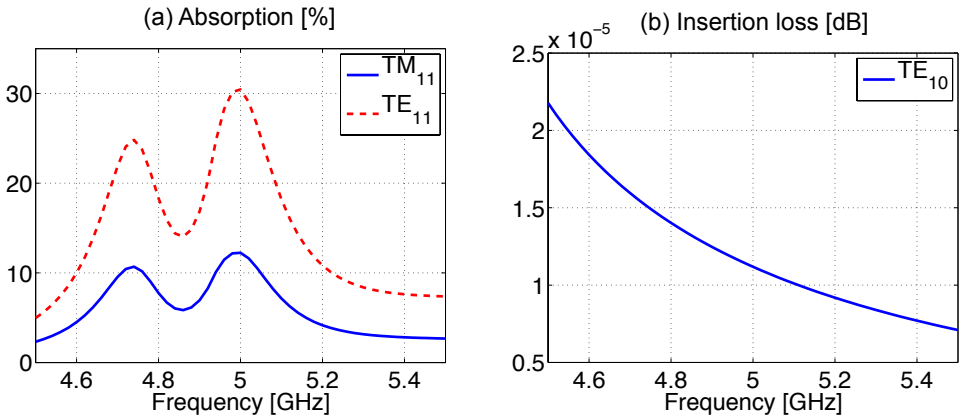

Figure 3.37: Absorption (a) and insertion loss (b) of a filter optimized to absorb the TM_{11} mode at 5 GHz in WR430 with $L = 10$ mm, $a_c = 48.5$ mm, $b_c = 3.1$ mm, $d_c = 8.1$ mm, $h_{cv} = 12.8$ mm, $h_{ca} = 2.1$ mm; corrugations end with a PEC. The absorption of the TE_{11} mode is also shown.

than the TM_{11} because the pattern of its surface currents on the sidewalls of the waveguide excites the corrugations to a larger extent. With reference to the fundamental mode, Fig. 3.37b shows that the insertion loss is lower than 2.5×10^{-5} dB within the whole plotted bandwidth.

The values the optimizer returned are consistent with the suggestions of the approximate model. In particular, $a_c = 54$ mm, which is close to the waveguide height, is a compromise between the coupling maximization of Fig. 3.30 and the amplitude minimization of evanescent corrugation modes and their decay lengths. With reference to h_{cv}, the wavelength of the $TE_{10}^{(\mathrm{corr})}$ mode in vacuum is $\lambda_{10}^{(\mathrm{corr})} = 76.3$ mm, the (3.42) gives $\Phi_a = 151$ deg, while Φ_w is -25 deg in this particular case. For $k = 0$, we obtain

$$h_{cv} = \frac{1}{2}\frac{\lambda_{10}^{(\mathrm{corr})}}{2\pi}(\Phi_a + \Phi_w) = 13.4 \text{ mm}$$

which is very close to 12.8 mm given by the PSO.

Mode absorption can be enhanced increasing the number of corrugations: Fig. 3.38a shows the optimization outcome for a mode filter with a length of approximately half a meter. Compared to the previous device, the absorption presents a smaller variation within the considered bandwidth because, in the present optimization, the cost function is predominantly affected by the constraint on the insertion loss of the fundamental mode as suggested by Fig. 3.38b. This fact causes the corrugations to have both a_c and b_c shorter than $\lambda_0/2$, i.e. to host no propagating modes at 5 GHz. The power that is not delivered to the output port in the form of the TE_{10} mode is reflected back or undergoes co- and contra-directional conversion into the

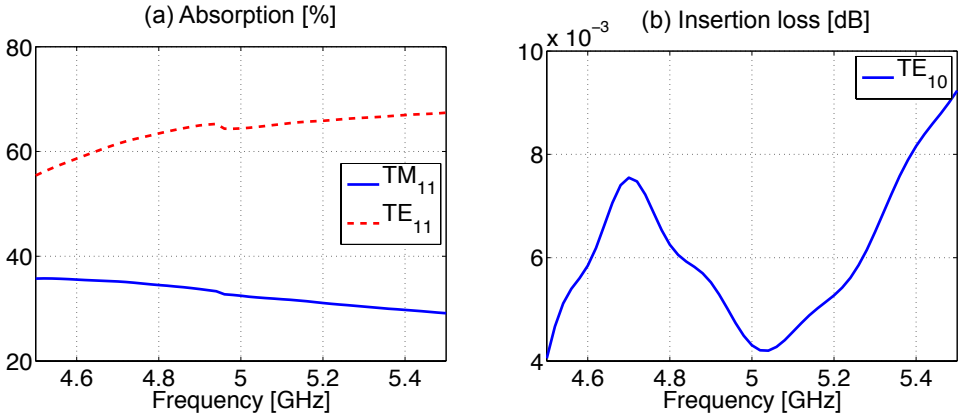

Figure 3.38: Absorption (a) and insertion loss (b) of a filter optimized to absorb the TM_{11} mode at 5 GHz in WR430 with $L = 0.5$ m, $a_c = 27.5$ mm, $b_c = 13.6$ mm, $d_c = 3.0$ mm, $h_{cv} = 12.0$ mm, $h_{ca} = 4.8$ mm; corrugations end with a PEC. The absorption of the TE_{11} mode is also shown.

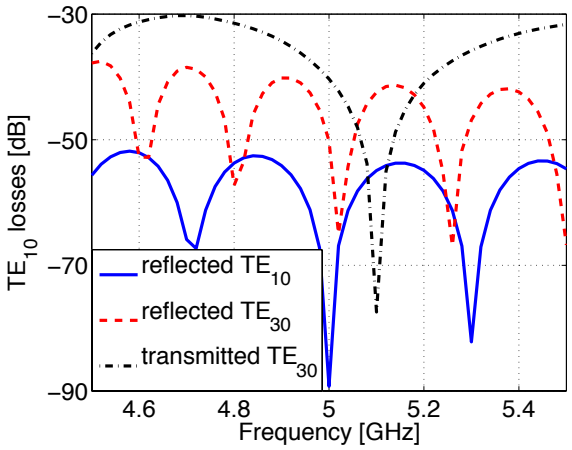

Figure 3.39: Self-reflection and main conversion coefficients of the fundamental mode versus frequency for the mode filter of Fig. 3.38.

TE_{30} mode. This behaviour is described in Fig. 3.39: consistently with the insertion loss of the device, plotted curves take low values. Spurious modes different from the TE_{30} mode do not couple with the fundamental mode and their excitation levels are negligible.

Mode filters are meant to hinder resonances by trapped spurious modes that increase the electric field, within specific sections of the transmission line, and may cause electrical breakdown or, in the case of long-pulse or CW systems, overheating and mechanical deformation of the components. The requirements, a mode filter has to meet, depend on several factors such as

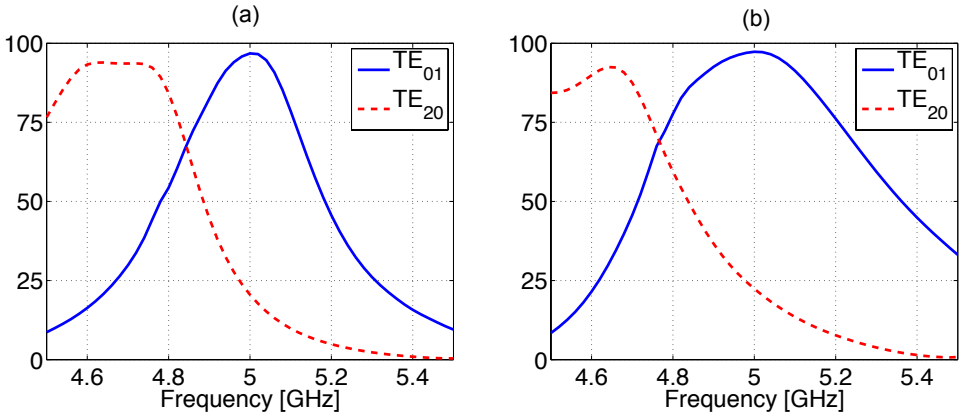

Figure 3.40: Absorption [%] of two filters optimized to absorb the TE_{01} mode at 5 GHz in WR430 with $L = 0.5$ m; the absorption of the TE_{20} mode is also shown. (a) PEC-ended corrugations with $a_c = 41.7$ mm, $b_c = 8.2$ mm, $d_c = 11.8$ mm, $h_{cv} = 19.2$ mm, $h_{ca} = 7.8$ mm; (b) PMC-ended corrugations with $a_c = 40.6$ mm, $b_c = 15.7$ mm, $d_c = 12.6$ mm, $h_{cv} = 19.7$ mm, $h_{ca} = 7.4$ mm.

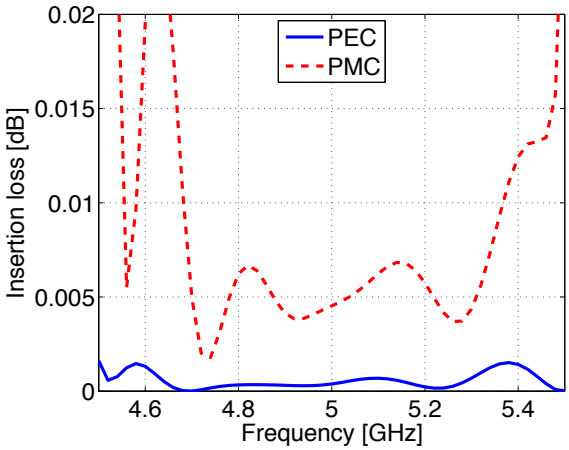

Figure 3.41: Insertion loss of the fundamental mode versus frequency for the mode filters of Fig. 3.40a (PEC) and 3.40b (PMC).

system topology, component performance, conditioning procedure, waveguide pressurization, etc. However, even absorptions that are apparently low, as for the TM_{11} in Fig. 3.38, can reduce the electric field of a trapped mode resonance below the safety limit.

As far as modes of class B are concerned, the optimization has been performed again in a five-dimensional space given by the dimensions of Fig. 3.20b; the number of corrugations is now determined by rounding the ratio

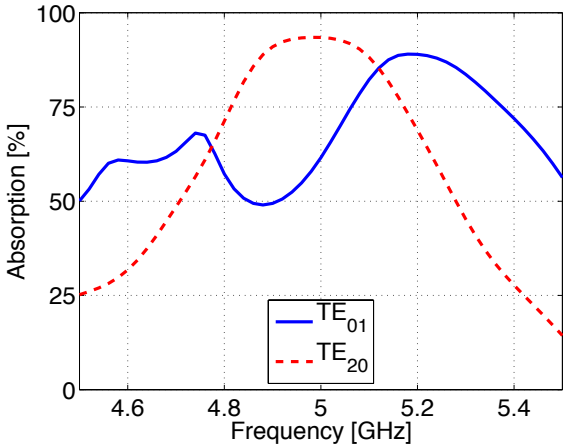

Figure 3.42: Performance of a filter optimized to absorb the TE_{20} mode at 5 GHz in WR430 with $L = 0.5$ m, $a_c = 67.0$ mm, $b_c = 10.7$ mm, $d_c = 23.1$ mm, $h_{cv} = 20.0$ mm, $h_{ca} = 3.6$ mm; corrugations end with a PEC. The absorption of the TE_{01} mode is also shown.

$(L + a_c)/(a_c + d_c)$. Fig. 3.40a presents the performance of a device attaining an almost unitary absorption of the TE_{01} mode using corrugations terminated with a PEC. If PMC are used, the PSO returns a structure with larger slots and the same behaviour at 5 GHz, but the absorption curve has a larger bandwidth, as can be appreciated by Fig. 3.40b. It is worth pointing out that ideal PMC loads have been considered in the model, whereas realistic terminations emulating high impedance surfaces are resonant structures with their own frequency response that further constrains device bandwidth. The latter is not a major concern in current applications, which are usually narrowband, e.g. in systems powered by klystrons. A drawback of the PMC-based solution is represented by higher insertion losses, which are compared to the case with PEC-ended corrugations in Fig. 3.41. They are caused by an increase of conversion losses into the TE_{30} mode, whose excitation level at the 5 GHz changes from -62 to -37 dB at the input and from -42 to -34 dB at the output; self-reflection coefficients are instead similar and below -45 dB.

Finally a mode filter conceived for the TE_{20} mode is presented in Fig. 3.42. It is interesting to notice that overmoded corrugations are more suitable to damp this mode ($a_c = 67$ mm), whereas monomodal corrugations were preferred in the previous case ($a_c = 41.7$ mm). In WR430 the TE_{01} and TE_{20} modes have the same propagation constant, so the different outcome of the optimizer is due to the slightly different pattern of surface currents on the top and bottom walls close to the longitudinal axis.

Chapter 4

Examples of Application Fields in Fusion Reactors

Some areas of fusion engineering, where overmoded components find application, are described paying particular attention to reactor-relevant tokamaks such as DEMO. Sources at mm-waves are initially considered, presenting the design of a cavity for a 250 GHz, 1 MW cyclotron auto-resonance maser. Then lower hybrid frequencies are addressed, discussing the technological maturity of a 5 GHz system to be used in DEMO.

4.1 Design of a 250 GHz CARM Cavity

4.1.1 Sources at mm-waves for fusion reactors

The successful application of mm-waves in fusion devices such as tokamaks and stellarators has experimentally highlighted, during the last decades, the numerous advantages of this frequency range over the others in several areas for heating, current generation and diagnostics purposes [114, 115]. In particular electron cyclotron resonance heating (ECRH) and current drive (ECCD) play a pivotal role in present machines, e.g. for profile control, MHD stabilization, assisted start-up or wall conditioning, by the injection of high-power waves through modest-sized launching structures located far from the plasma. The straightforward coupling together with the high CD and wall-plug efficiencies makes mm-waves greatly effective in current experimental activities as well as particularly suitable and attractive for future magnetic confinement machines.

Next-generation fusion devices are expected to sustain and control burning plasmas, where reactor-grade temperatures, in conjunction with the high toroidal field, require the use of electron cyclotron systems with higher frequency than in present-day and under construction tokamaks. In ITER the ECRH/ECCD system was designed at a frequency of 170 GHz, which represents a downward compromise dictated by the state of the art in gyrotron and window developments [116]. In DEMO [117] there are two models which are currently under assessment: a steady-state design and a pulsed version with main parameters given in Table 4.1. Depending on the density profile configurations (peaked or flat), the central electron temperatures range from 53 keV to 64 keV. The most suitable scheme for both heating and current drive is the low-field side injection of the ordinary mode with absorption primarily at the fundamental resonance. Parasitic absorption at the second harmonic can be reduced by increasing the operational frequency and launching waves from the top. The relativistic wave-particle resonance condition is

$$\gamma - \frac{n\Omega}{\omega} - \mathrm{n}_{||} u_{||} = 0 \tag{4.1}$$

where n is the harmonic number, $\Omega = eB/m_e$ is the electron cyclotron frequency, $\gamma = \sqrt{1+u^2}$ is the relativistic Lorentz factor, u is the normalized

	steady-state	pulsed
Toroidal field B_0 [T]	5.84	7.45
Major radius R_0 [m]	8.5	9.6
Minor radius a [m]	2.83	2.4

Table 4.1: Main parameters of DEMO models

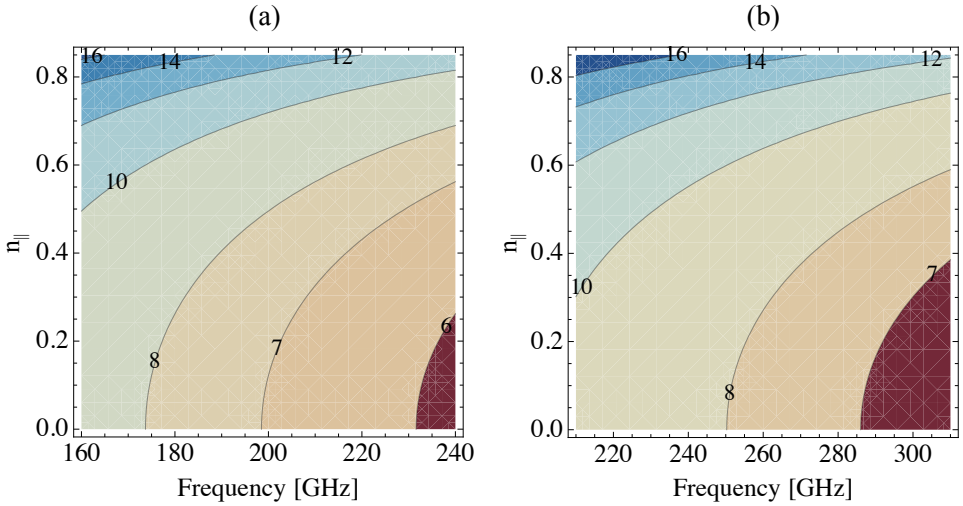

Figure 4.1: Contour plots of major radii [m] at which the first-harmonic absorption becomes possible in the steady-state (a) and pulsed (b) DEMO.

momentum and $n_{||}$ is the parallel refractive index. This condition can be satisfied only for parallel momenta that lie between two roots with collapsing point at the radial position

$$R = \frac{\Omega_0 R_0}{\omega\sqrt{1 - n_{||}^2}} \tag{4.2}$$

where a dependence $\Omega = \Omega_0 R_0 / R$ has been assumed. Such point is the largest radial position at which first harmonic absorption becomes possible. Contour plots versus frequency and $n_{||}$ are provided in Fig. 4.1, showing that the higher the wave frequency, the further the wave travels undamped. Obviously a proper choice of EC system parameters requires careful calculations using beam-tracing codes with fully relativistic absorption models. Hence, previous figures are only intended to give a rough picture of frequency ranges involved in reactor-grade plasmas. Since the optimum CD efficiency is usually found at higher $n_{||}$, the steady-state and pulsed DEMO models are expected to require frequencies around 230 and 280 GHz, respectively, allowing EC waves with higher $n_{||}$ to reach the geometrical axis of the tokamak.

The microwave tubes of current ECRH systems are the gyrotrons, which require substantial R&D to meet EC system requirements in reactor conditions. Moreover, despite the progress on windows and the considerable technological advancement, such type of generator is intrinsically constrained by its operating principles in the attainment of a continuous wave (CW) high-power (> 1 MW), high-frequency (> 200 GHz) source. When increasing frequency and power, the cavity cross-section becomes larger and the order

of the operating mode higher. On one side the increase of its radial index entails serious demands on the electron beam. Since the gyrotron is driven by a high-current low-energy beam, any reduction of the beam radius to couple high-order modes decreases the space charge limited current and deteriorates the beam quality. On the other side, if the azimuthal index is very high, the mode competition becomes critical. Furthermore the higher frequency of operation requires higher static magnetic fields produced by superconducting magnets whose cost can grow out of control. As far as the European 170 GHz coaxial gyrotron for ITER is concerned, the original target of 2 MW is under discussion, in view of essential delays and damages, while the development of 1 MW conventional tubes was started as a fall back [118]. We envisage that CW, 2 MW, 230 GHz sources must be the minimum target in DEMO.

The previous reasons raise well-grounded doubts about the suitability of gyrotrons in fulfilling the future demands of EC systems in the most effective way. Therefore a longer-perspective activity aimed at the parallel development of a different typology of device is suggested. The cyclotron auto-resonance maser (CARM) stands out as the most promising candidate from the theoretical viewpoint [67]. It employs a relativistic electron beam and a different beam-wave interaction than in gyrotrons; the Doppler shift formula allows the working mode to be far from its cutoff frequency and the requirements on the static magnetic field to be significantly relaxed. Nevertheless, from the practical viewpoint, early experiments in the 1990s did not confirm expectations due to several problems. Nowadays some of previous issues have been overcome thanks to the technological advancements in realizing high-quality electron beams, the improvement of both analytical and numerical modelling capability and the availability of unprecedented computational resources. These reasons motivate the development of a new CARM experiment.

The study of a 250 GHz CARM with output power ≥ 0.5 MW was undertaken at ENEA-Frascati within the enabling research of the EUROfusion workprogramme 2014 [119, 120, 121, 122, 123, 124, 125]. The frequency of the CARM project has been set in between the ones required for DEMO at around 250 GHz. Such choice allows a possible employment of the electromagnetic source on FTU [126] to perform second-harmonic EC experiments with toroidal magnetic field of $4 \div 5$ T. In medium size tokamaks, a reliable estimation of the suitable frequency for EC system can be indeed calculated with the practical formula

$$f[\text{GHz}] = 28 n B_0 \tag{4.3}$$

that, for $n = 2$ and $B_0 \approx 4.46$ T, returns 250 GHz.

This section reports the preliminary design of the Bragg resonator for the 250 GHz CARM experiment at ENEA. In this project, the cutoff frequency

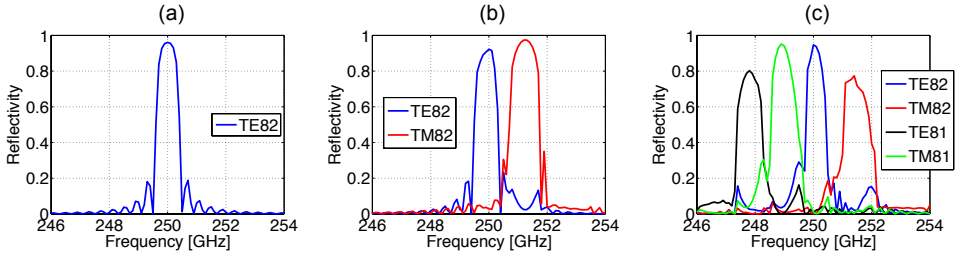

Figure 4.2: Reflectivity curves in a cylindrical, TE_{82}-excited, Bragg reflector with $a_0 = 10$ mm, $\Lambda = 622.6$ μm, $L = 350$ mm and $b_0 = 30$ μm if 1 (a), 2 (b) and 4 (c) modes are included in the computation.

of the working mode has to be in the range 80÷100 GHz to take full advantage of the relativistic wave-particle resonance condition. Moreover modes with radial index $m = 2$ must be preferred because of the radial position of their maximum amplitude. The latter is a compromise between counteracting needs: annular electron beams with higher radius can fulfil more easily the required quality, whereas ohmic losses decrease using $m = 3$ or 4. Taking also into account the high-power requirements and electron beam properties, the use of whispering-gallery TE_{n2} modes, like for example the TE_{82}, and a waveguide diameter in the range 15÷20 mm are suggested. In the following of section 4.1 mode indices will be separated with a comma, e.g. $TE_{8,2}$, to avoid confusion in presence of double-digit indices.

4.1.2 Preliminary calculations

A critical issue is given by the number of modes to be included in the calculation. Fig. 4.2 shows the impact of this value on the reflectivity curves for a waveguide with $a_0 = 10$ mm. Most of modifications occur far from the resonant frequency, i.e. the one that satisfies the Bragg condition for the working mode, but there are also some changes in proximity of such frequency. Despite rather small, these variations represent a major concern and must be assessed.

A study has been carried out for waveguide diameters of 15 mm and 20 mm, which respectively have 397 and 703 modes above cutoff. According to the expressions of the coupling coefficients, each mode only interacts with modes having the same azimuthal index n; the properties of propagating modes with $n = 8$ have been summarized in Table 4.2. We have analysed the convergence rate of the reflectivity of the working mode at 250 GHz including step-by-step a higher number of modes (N) taken from Table 4.2. Outcomes are given in Figs. 4.3 and 4.4 for the waveguides with diameters of 15 mm and 20 mm, respectively. As far as computations including up to 6 modes are concerned, an enlargement of the reflection coefficient ver-

		$a_0 = 10$ mm			$a_0 = 7.5$ mm		
##	Mode	f_c [GHz]	λ_g [mm]	α [dB/m]	f_c [GHz]	λ_g [mm]	α [dB/m]
25	$TE_{8,1}$	46.0	1.22	0.68	61.4	1.24	0.94
41	$TM_{8,1}$	58.3	1.23	0.31	77.8	1.26	0.42
54	$TE_{8,2}$	67.4	1.25	0.17	89.8	1.28	0.26
69	$TM_{8,2}$	76.5	1.26	0.32	102.0	1.31	0.44
83	$TE_{8,3}$	84.8	1.27	0.12	113.1	1.34	0.21
101	$TM_{8,3}$	93.3	1.29	0.32	124.4	1.38	0.46
122	$TE_{8,4}$	101.3	1.31	0.11	135.1	1.43	0.22
139	$TM_{8,4}$	109.5	1.33	0.33	146.0	1.48	0.49
161	$TE_{8,5}$	117.3	1.36	0.12	156.4	1.54	0.26
181	$TM_{8,5}$	125.3	1.39	0.35	167.1	1.61	0.54
204	$TE_{8,6}$	133.1	1.42	0.13	177.4	1.70	0.34
227	$TM_{8,6}$	141.0	1.45	0.36	188.0	1.82	0.61
254	$TE_{8,7}$	148.7	1.49	0.16	198.2	1.97	0.46
278	$TM_{8,7}$	156.5	1.54	0.39	208.6	2.18	0.73
306	$TE_{8,8}$	164.1	1.59	0.19	218.8	2.48	0.68
335	$TM_{8,8}$	171.9	1.65	0.41	229.2	3.00	1.00
364	$TE_{8,9}$	179.5	1.72	0.24	239.3	4.15	1.34
396	$TM_{8,9}$	187.2	1.81	0.45	249.6	22.42	7.50
430	$TE_{8,10}$	194.8	1.91	0.31			
463	$TM_{8,10}$	202.5	2.05	0.51			
497	$TE_{8,11}$	210.1	2.21	0.41			
536	$TM_{8,11}$	217.8	2.44	0.61			
571	$TE_{8,12}$	225.3	2.77	0.58			
610	$TM_{8,12}$	233.0	3.31	0.83			
649	$TE_{8,13}$	240.5	4.39	1.05			
690	$TM_{8,13}$	248.1	9.87	2.48			

Table 4.2: Propagating modes with azimuthal index $n = 8$ for two waveguides with different radius. f_c, λ_g and α respectively stand for cutoff frequency, mode wavelength and attenuation due to copper.

sus frequency close to the Bragg condition has been reported too. Despite variations decrease as N become higher, the performance of the reflectors does not approach a constant value. Furthermore the numerical solver of the differential equations leads to accuracy issues when including higher-order modes. The violation of the tolerance constraint on the mesh occurs in correspondence of the red dashed vertical line of Figs. 4.3a and 4.4b.

The dependence of the reflectivity on the working mode has been analysed to assess the possibility of moving towards lower-order modes. Parametric analyses with respect to the corrugation depth b_0 and the reflector length L have been carried out for the $TE_{6,2}$, $TE_{1,1}$ and $TE_{15,2}$. The former

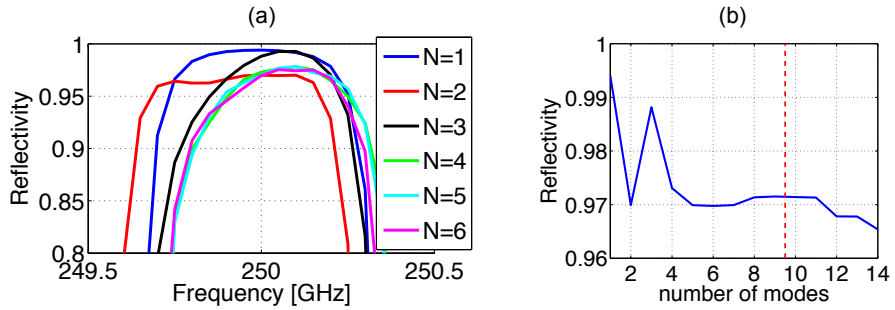

Figure 4.3: Reflectivity computed including a different number of modes (N) for a cylindrical, $TE_{8,2}$-excited, Bragg reflector with a_0 =7.5 mm, $\Lambda = 642.5$ μm, $L = 500$ mm and $b_0 = 25$ μm. Enlargement around the resonant frequency (a) and reflectivity at 250 GHz versus N (b); vertical red line indicate the occurrence of accuracy issues in the numerical solver.

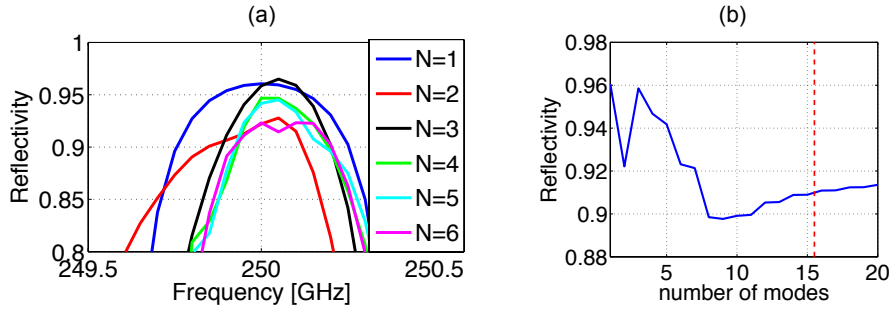

Figure 4.4: Similar plots to Fig. 4.3 but with $a_0 = 10$ mm, $\Lambda = 622.6$ μm, $L = 350$ mm and $b_0 = 30$ μm.

was chosen because some work on the converters for the cold test was done using the $TE_{6,2}$. The $TE_{1,1}$ is the fundamental mode and allows the study of the lowest order. To analyse higher-order modes, the $TE_{15,2}$ was instead used because some converters to this mode are already available at 140 GHz and could be used for an experimental test bench after a proper scaling.

The outcomes of the parametric analyses are shown in Figs. 4.5 and 4.6: modes with cutoff frequency closer to the working frequency give better results. Given a total length of the reflector, its performance can be enhanced by reducing the waveguide radius or using higher-order modes; if the former is fixed too, higher reflectivity can be achieved only using modes with higher azimuthal and radial indices. As a term of reference, a length of 0.5 m can reflect the 97% of the $TE_{8,2}$.

The Bragg reflector with a radius of 7.5 mm, excited by the $TE_{8,2}$, has been studied considering the ripple profiles of Fig. 2.3. Results are given in Fig. 4.7, omitting the sinusoidal ripple that gives the same reflectivity

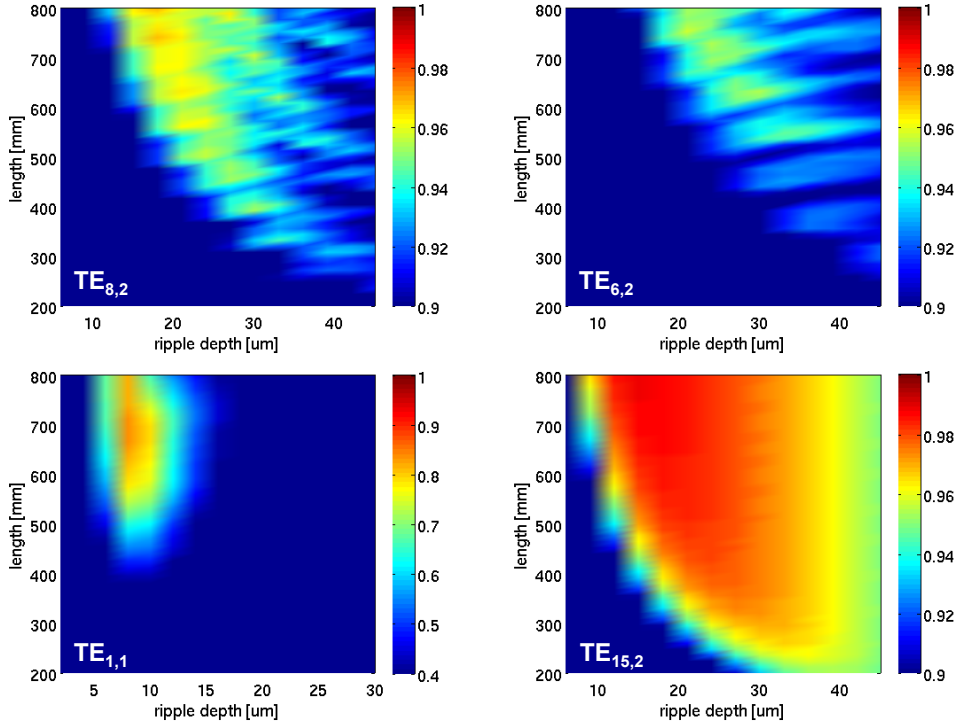

Figure 4.5: Parametric analyses of the reflectivity at 250 GHz of Bragg reflectors with $a_0 = 10$ mm for different excitation modes. Λ has been fixed according to the Bragg condition, while L and b_0 are respectively swept in the ranges 200 to 800 mm (step = 15 mm) and 6 to 45 μm (step = 3 μm).

of the cosine profile (the two cases only differ in the initial phase). The performance is rather similar if the mirror length is fixed, but square and triangle profiles respectively achieve it with shallower and deeper corrugations than the sinusoidal profile. A plot versus frequency of a configuration in the centre of the parametric analysis is reported in Fig. 4.8.

The same configuration in the case of the sinusoidal profile has been studied as regards ohmic losses as shown in Fig. 4.9. There are absorption peaks in correspondence of the steepest changes in the reflectivity curves. They are probably due to numerical errors in the solver of differential equations since the power loss is calculated by subtracting the total power leaving the structure from the one entering the device. The power attenuation at 250 GHz is 1.15% and 1.49% of the input power for the walls made of oxygen-free electronic (OFE) copper and aluminium, respectively. The finite conductivity of the wall implies a degradation of the reflectivity that, at 250 GHz, changes from 97% in absence of losses to 95.6% for aluminium walls. The real amount of ohmic losses is higher at 250 GHz because the roughness of the metallic surface cannot be neglected for such small wavelengths.

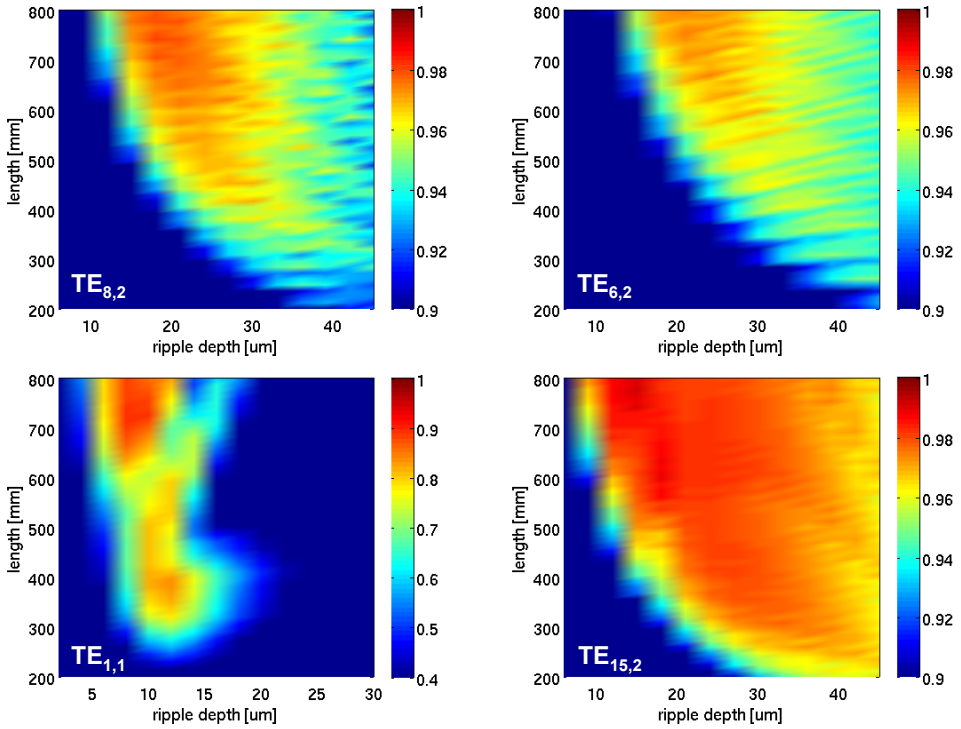

Figure 4.6: Parametric analyses similar to Fig. 4.5, but for Bragg reflectors with $a_0 = 7.5$ mm.

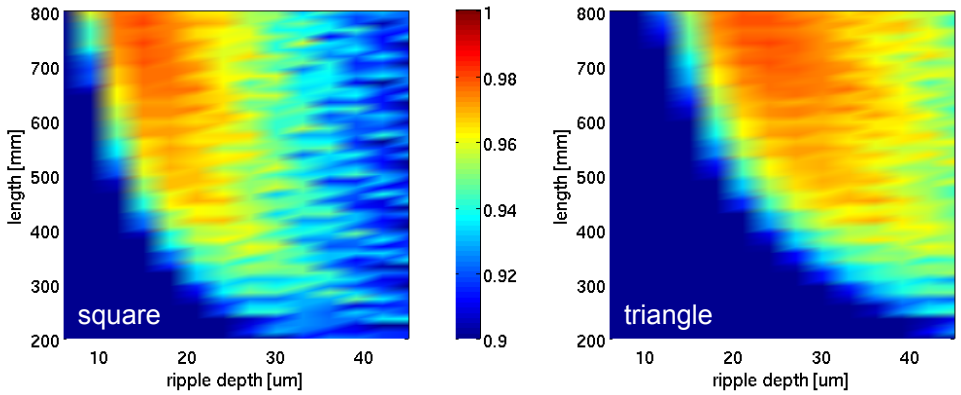

Figure 4.7: Parametric analyses of the reflectivity at 250 GHz of $TE_{8,2}$-excited, Bragg reflectors with $a_0 = 7.5$ mm for corrugations in the shape of squares and triangles.

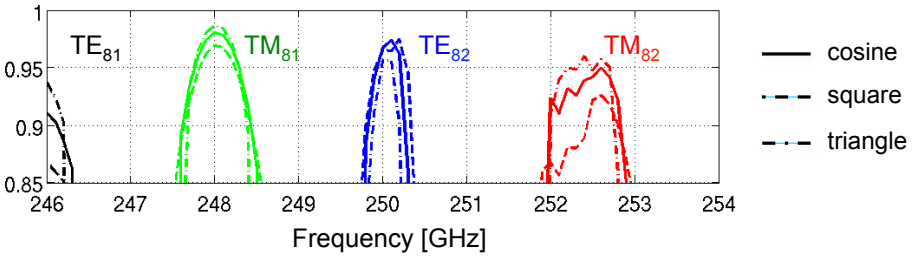

Figure 4.8: Reflectivity in a $TE_{8,2}$-excited, Bragg mirror with $a_0 = 7.5$ mm, $\Lambda = 642.5$ μm, $L = 500$ mm and $b_0 = 23$ μm for different ripple profiles.

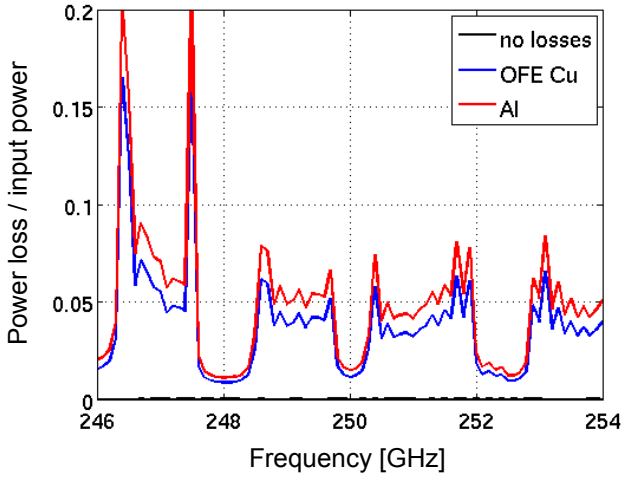

Figure 4.9: Power loss due to the finite conductivity of the walls in the same geometry of Fig. 4.8 using OFE copper ($\sigma = 5.91 \times 10^7$ S/m) or aluminium ($\sigma = 3.5 \times 10^7$ S/m).

4.1.3 Minimization of the upstream mirror length

Reflectivities above 97% can be achieved only with reflector lengths of the order of half a meter, which is a very high value at 250 GHz. Previous results indicated that the decrease of the unperturbed radius and the increase of the mode order have a beneficial impact on the performance of the reflector. Nevertheless the lowest acceptable radius is 7.5 mm and the mode order has to be close to the $TE_{8,2}$ owing to the properties of the electron beam. Further studies have been carried out considering the modes $TE_{9,2}$ and $TE_{10,2}$, the parameters of which are summarized in Table 4.3.

The convergence with the number of modes was studied considering a reflector of 0.5 m with sinusoidal ripple. The outcomes are given in Fig. 4.10: next parametric analyses were performed including 8, 6 and 6 modes when

Mode	f_c [GHz]	β [m^{-1}]	λ_g [mm]	α [dB/m]
$TE_{8,2}$	89.8	4890	1.29	0.33
$TE_{9,2}$	97.3	4827	1.30	0.38
$TE_{10,2}$	106.4	4759	1.32	0.43

Table 4.3: Cutoff frequency (f_c), propagation constant (β), mode wavelength (λ_g) and attenuation due to aluminium (α) for the most suitable operational modes in the CARM under design.

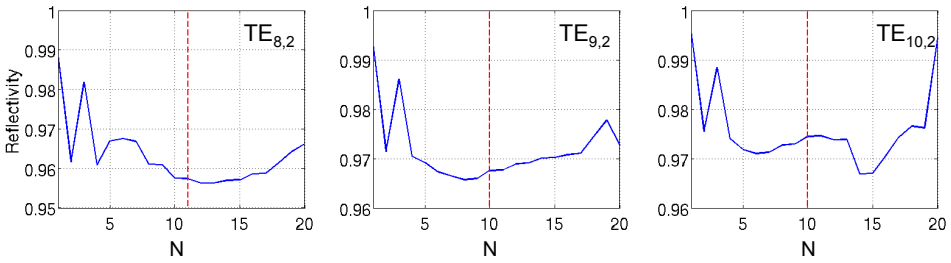

Figure 4.10: Reflectivity computed at 250 GHz increasing the number of modes (N) for Bragg reflectors with $a_0 = 7.5$ mm, $\Lambda = \lambda_g/2$, $L = 500$ mm $b_0 = 25$ μm and different excitations; vertical red line indicate the occurrence of accuracy issues in the numerical solver.

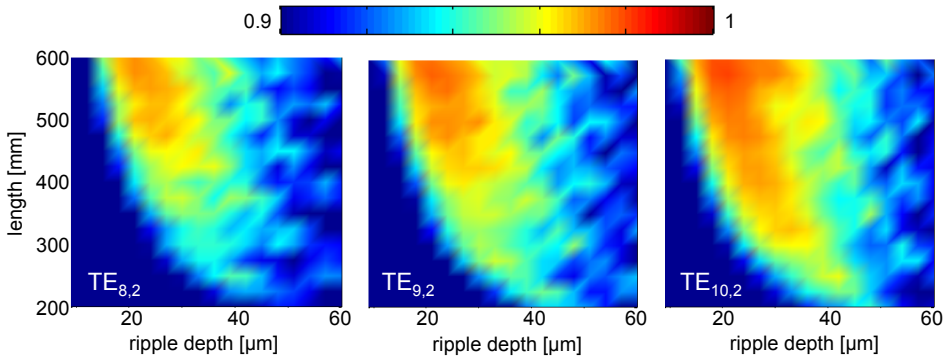

Figure 4.11: Parametric analyses of the reflectivity at 250 GHz of sinusoidal Bragg reflectors with $a_0 = 7.5$ mm for different excitation modes ($\Lambda = \lambda_g/2$).

the reflector is excited by the $TE_{8,2}$, $TE_{9,2}$ and $TE_{10,2}$, respectively. The reflectivities plotted in Fig. 4.11: there is an improvement when increasing the azimuthal index, however reflection coefficients higher than 97% always require long reflectors, i.e. around 0.5 m. A design of such a reflector has been carried out using the $TE_{9,2}$ mode. The frequency behaviour for a length of 0.45 m is shown in Fig. 4.12, giving a full width half power of 0.77 GHz and a reflectivity of 97% at 250 GHz.

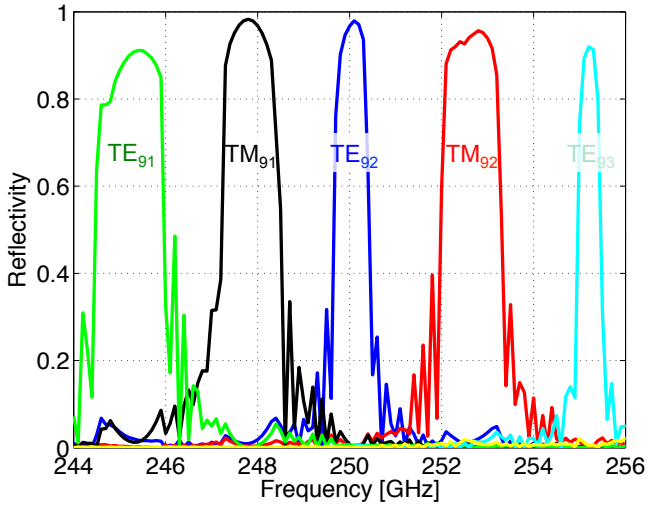

Figure 4.12: Reflectivity versus frequency of a $TE_{9,2}$-excited, sinusoidal Bragg reflector: $a_0 = 7.5$ mm, $\Lambda = 651$ μm, $L = 450$ mm, $b_0 = 25$ μm.

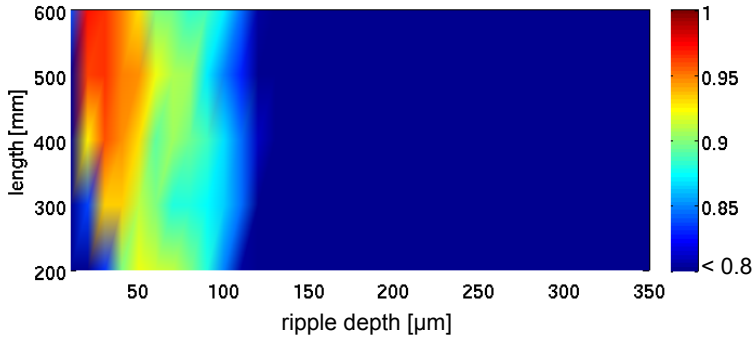

Figure 4.13: Parametric analyses of the reflectivity at 250 GHz in $TE_{8,2}$-excited, sinusoidal Bragg reflectors with $a_0 = 7.5$ mm and $\Lambda = 642.5$ μm.

According to the expressions of the coupling constants, the interaction between modes increases with the ripple depth. This proportionality is beneficial for the reflectivity of the excitation mode provided that the coupling with different modes is negligible. When increasing b_0, the inter-coupling becomes higher and impairs the performance. This behaviour can be appreciated in Fig. 4.13, where the parametric analysis is extended to deeper corrugations. If the computation took into account just one mode, the reflectivity would improve as b_0 increases, giving a wrong result. Calculations with the two closest modes already generate quite reliable outputs because the performance is mostly deteriorated by the inter-coupling with the TM mode that has the same indices of the excitation mode.

The condition for small mode overlap is given in [69] and requires that

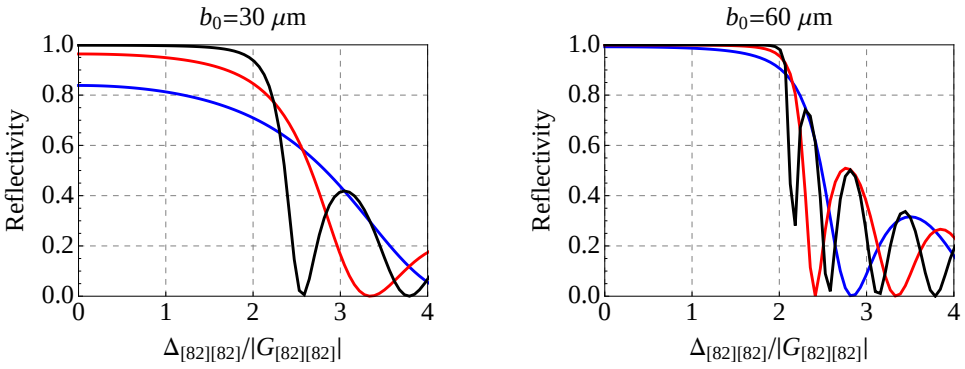

Figure 4.14: Reflectivities at 250 GHz versus the ratio between the mismatch parameter and the coupling constant considering only the $TE_{8,2}$ mode in Bragg reflectors with $a_0 = 7.5$ mm, $\Lambda = 642.5$ and $L = 200$ mm (blue), 300 mm (red) or 500 mm (black).

the resonances of the TE and TM modes with the same indices are separated by at least the sum of their half widths, namely

$$\beta_{(p)}|_{\Delta_{[i](p)}=0} - \beta_{[i]}|_{\Delta_{[i][i]}=0} \geq \frac{1}{2}\left(\mathrm{FWHM}_{[i](p)} + \mathrm{FWHM}_{[i][i]}\right) \tag{4.4}$$

The full width half maximum (FWHM) can be derived from the single mode approach as shown in Fig. 4.14, where the reflectivity calculated considering only the $TE_{8,2}$ mode is plotted for different Bragg reflectors. The half widths occur for $\Delta_{[i][i]} = BW_\Delta \cdot |G_{[i][i]}|$; in the present case, $BW_\Delta \approx 2 \div 3$ and very similar values are obtained for the interaction with the $TM_{8,2}$ as well as for modes with azimuthal index equal to 9 and 10. We can approximate the propagation constants with the vacuum wavenumber, because the working modes are far from their cutoff frequency; by writing the FWHM as a function of the coupling constants, the (4.4) becomes

$$\Delta\omega_{res} = \omega_{[i](p)} - \omega_{[i][i]} \geq c\, BW_\Delta \left(|G_{[i](p)}| + |G_{[i][i]}|\right)$$

where ω_{ip} indicate the resonant frequency satisfying the Bragg condition between the p-th and the i-th mode. Far from the cutoff frequency, the coupling constants for the $TE_{8,2}$ can be approximated as

$$|G_{[\ell m][\ell m]}| \approx 0.47 \frac{b_0}{a_0}\frac{\omega}{c} \qquad \text{and} \qquad |G_{[\ell m](\ell m)}| \approx 0.69 \frac{b_0}{a_0}\frac{\omega}{c}$$

which give the following approximate condition on the ripple depth for small mode overlap:

$$b_0 \leq 1.16 a_0 \frac{\Delta\omega_{res}}{\omega\, BW_\Delta}$$

In the present case, the latter equation returns a maximum b_0 of 27 and 41 μm for $BW_\Delta = 2$ and 3, respectively.

4.1.4 Bragg resonator for the ENEA project

The previous sections have shown that Bragg reflectors in circular waveguides are defined by five geometrical parameters: unperturbed radius a_0, ripple period Λ, ripple depth b_0, number of ripples (i.e. the total length) and ripple type. Frequency, working mode, peak and average power are instead operational parameters, which are externally dictated in most cases.

The mean radius of the rippled-wall waveguide is set according to the maximum allowable peak power in the cavity; in the present case it is 7.5 mm, a value that is expected to bear 1 MW of power, leading to a power density of around 566 kW/cm^2. Once defined the working mode, the ripple period is set according to the Bragg condition $\Lambda = \lambda_g/2$, being $\lambda_g/2$ the wavelength of such mode at the working frequency. Finally the last three parameters can be chosen to meet the required reflectivity, while complying with issues such as manufacture feasibility, acceptable ohmic losses, system integration, etc. In this sense parametric analyses and theoretical studies have taught that:

- The deeper the corrugations, the higher the coupling between modes. When increasing the ripple depth, the reflectivity initially enhances and then deteriorates because the inter-coupling with the closest mode becomes so strong to cause mode overlap. In the present application, suitable ripple depths are in the range $10 \div 50\mu$m.

- The further the cutoff frequency of the working mode is from the operational frequency, the worse the reflectivity for a given mirror length. In other words, given the frequency and the number of ripples, higher order modes work better than lower order modes.

- The longer the device, the smaller the bandwidth.

- The use of different ripple types produces negligible differences.

- The attenuation constants of the $\mathrm{TE_{n,m}}$ modes increase with the azimuthal index n, while, assuming $n \neq 0$, they exhibit a minimum with reference to the radial index m at around 3.

In this frame and taking into account the constraints on the electron beam, the $\mathrm{TE_{8,2}}$, with cutoff frequency of 89.8 GHz, maximum amplitude at a radius of 4.85 mm and attenuation constant of 0.26 dB/m, appears the most suitable choice for the CARM experiment. A cavity has been thus designed with a quality factor around 4000 at the resonant frequency of 258.1 GHz; the latter values have been chosen according to the expected parameters of the electron beam to maximize the efficiency, while keeping acceptable power dissipation at the cavity walls. Copper with standard conductivity ($\sigma = 5.8 \times 10^7$) is assumed as material, nevertheless, at the

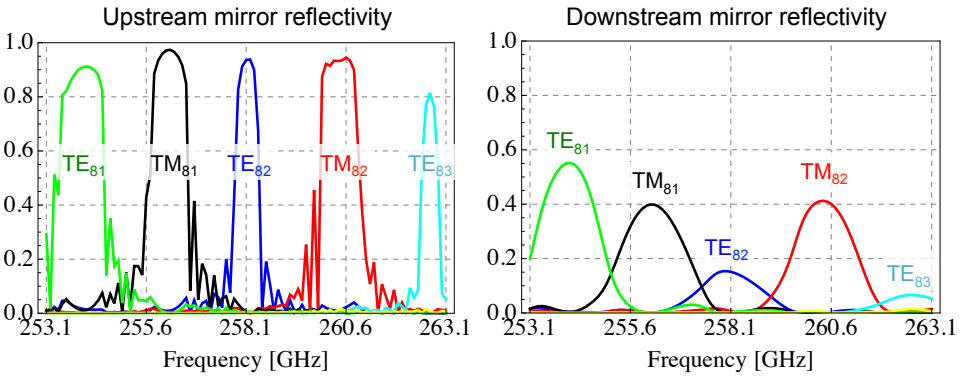

Figure 4.15: Mirror reflectivity versus frequency.

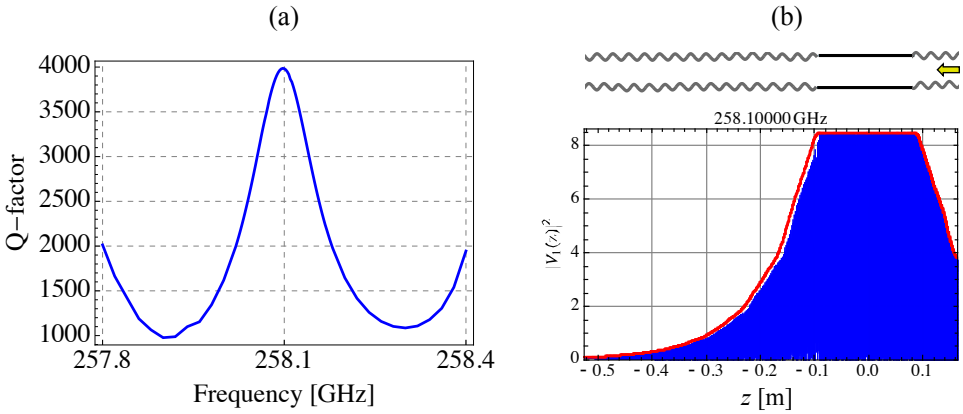

Figure 4.16: Q-factor (a) and E-field squared amplitude at 258.1 GHz (b).

working frequency, the effective electrical resistivity is usually twice higher than the nominal one, so actual losses are expected to be somewhat higher than computed ones.

The reflectors have sinusoidal ripples with period of 619.5 μm and depth of 20 μm. Reflectivity of 93.6% and 15% is respectively achieved with 700 and 120 corrugations for the up- and down-stream mirror, resulting in a total length of 434 and 74 mm; the plots versus frequency are shown in Fig. 4.15. The length of the smooth-wall section has been set to 180.59 mm, a value that provides the desired quality factor and finely tunes the resonance at 258.1 GHz. The behaviour of the resonator is given in Fig. 4.16 for an input signal injected from the downstream mirror. The predicted Q-factor for diffractive losses is 3986 and ohmic losses are 1.4% of the input power.

Different approaches can be followed to calculate the Q-factor. The previous one is based on the exact definition: it provides the most reliable and accurate result, but its measurement is troublesome. The latter is usually

Mode	f_r [GHz]	$Q_{\Delta f}$	Q_W	$Q_{[67]}$	$Q_{[72]}$	P_{ohm} [%]
$TE_{8,2}$	258.1	1 623	3 986	1 672	3 773	1.4
$TE_{8,2}$	96.97	n.a.	1 854	972	1 274	13
$TE_{0,3}$	68.256		1 551	813	962	9
$TE_{1,4}$	74.95		4 791	2 524	2 577	27
$TE_{2,3}$	68.256		1 333	699	879	8
$TE_{3,3}$	72.37		6 540	4 000	4 037	39
$TE_{5,2}$	68.256		2 508	1 315	1 404	19
$TE_{6,2}$	75.17		4 687	2 439	2 495	33
$TE_{8,1}$	68.256		1 126	590	1 925	20
$TE_{9,1}$	68.256		9 032	4 615	4 640	83
$TE_{10,1}$	75.44		4 514	2 357	2 419	65
$TM_{0,4}$	75.59	n.a.	4 467	n.a.	n.a.	25
$TM_{1,3}$	68.256		1 550			10
$TM_{2,3}$	74.32		5 229			29
$TM_{3,2}$	68.256		1 187			8
$TM_{4,2}$	70.44		2 632			33
$TM_{5,2}$	79.88		3 108			18
$TM_{6,1}$	68.256		1 306			8
$TM_{7,1}$	70.59		6 954			53
$TM_{8,1}$	78.96		3 300			19

Table 4.4: Q-factors of TE and TM modes intersecting the beam line.

performed with a pickup inserted in the smooth section, i.e. a RF probe returning a signal proportional to the squared amplitude of the electric field. A frequency sweep provides a bell-shaped form, whose peak position (f_r) and full width half maximum (Δf) give the Q-factor. A calculation according to this approach is done in [69]; in the present case it would give $Q = 1613$. A similar value is obtained by deriving f_r and Δf from Fig. 4.16. Often the use of approximate formulas is preferred for a quick evaluation of the quality factor. In the present case, the one proposed by Bratman et al. [67] would give $Q = 1672$, because it neglects the energy stored inside the reflectors by evanescent fields. The formula by McCowan et al. [72] instead takes into account such contribution and its employment gives $Q = 3773$. Besides the risk of inaccuracy, approaches based on approximate formulas suffer from missing the exact determination of the resonant frequency.

Once designed the cavity, the quality factors of all modes, the dispersion curve of which intersects the beam line in the Brillouin (ω versus β) diagram, have been computed following previous approaches. When the frequency at

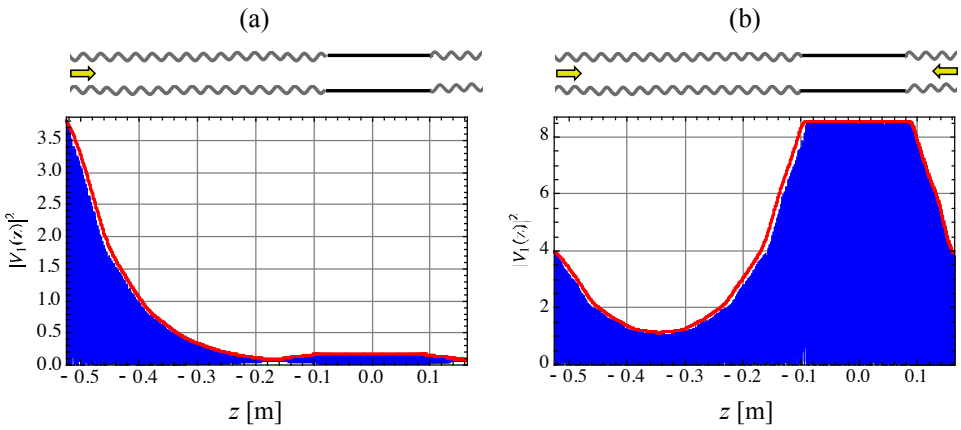

Figure 4.17: E-field squared amplitude at 258.1 GHz in the same resonator of Fig. 4.16, excited from the upstream mirror (a) and from both ends (b).

the intersection is negative, the cyclotron resonance frequency has been used. Results are summarized in Table 4.4, where $Q_{\Delta f} = f_r/\Delta f$, $Q_W = \omega W/P_{\text{leak}}$ is the rigorous calculation and ohmic losses are calculated with the power balance technique. The propagating modes that intersect the beam line very close to their cutoff, exhibit even higher Q-factor than the operational mode, but they are mostly dissipated owing to ohmic attenuation.

Finally it is worth pointing out that the rigorous calculation method has the drawback of being very sensitive to the side the resonator is fed from. The model of section 2.4 does not easily allow the direct excitation of the internal smooth section, but the input signal accesses the resonator from an external side and experiences a different attenuation according to the mirror it has to cross. The excitation side thus affects the field distribution along the structure, stored energy and Q-factor. This mechanism is graphically represented in Fig. 4.17, where two excitations are considered: the one from the down-stream mirror and the one from both reflectors; the corresponding Q-factors are 588 and 4565, respectively. On the contrary the computations according to the other approaches provide almost identical values whichever side of the cavity is fed. A promising solution to this problem could be the development of a mode-matching method, which, compared to the coupled-mode theory, presents the following advantages:

- it is a full-wave method (no physical approximations);
- it easily allows the internal excitation of the cavity;
- it is suitable to study advanced Bragg reflectors.

4.2 A Lower Hybrid and Current Drive System for DEMO

4.2.1 History and outlook of lower hybrid waves

Recent experiments on lower hybrid (LH) penetration at reactor-relevant densities, together with the recent demonstration of the technological viability of the passive active multijunction launcher on long pulses, have removed major concerns about the employment of LH waves on next generation tokamaks, where LH could profitably drive far off-axis plasma current, allowing current profile control and helping in sustaining burning performance. In this frame and with the aim of being prepared for the design phase of next experimental reactors, preliminary investigations on the possibility of using LH on DEMO have been started [127, 128, 129].

Among the three well-proven radio-frequency (RF) heating and current drive (H&CD) systems using electromagnetic waves, namely ion cyclotron resonance frequency (ICRF), electron cyclotron resonance frequency (ECRF) and lower hybrid current drive (LHCD), the latter indeed exhibits the highest experimental current drive efficiency [130, 131]. The latter is comparable only with the high-energy neutral beam H&CD system, which has not been proven to a large extent yet [132].

Primarily conceived as a tool for ion heating, LH waves found a major application in a regime dominated by electron interaction [133]. Here, according to the current drive theory [134], they can transfer parallel momentum to fast tail electrons via Landau damping, as demonstrated at low and high densities with L-mode plasmas on several machines [135, 136, 137]. With high performance plasmas in large-size tokamaks like ITER, where LH deposition takes place in the outer half of the plasma ($r/a = 0.7$) [138], a means of driving off-axis current is essential to achieve advanced regimes [130]. As for the exploitation of LHCD in this sense, most of the open issues were solved in the last decade, indicating LHCD as an effective tool for controlling plasma current profile [139] and saving volt-seconds in the ramp-up phase of the plasma current [138]. Lately, even the serious concerns about LH penetration at reactor-relevant regimes appear well on the way to be solved [140], by using the edge electron temperature like a knob to control the spectral broadening due to parametric instabilities [141].

As far as launcher technology is concerned, remarkable improvements have been performed going from the conventional grill proposed by Lallia [142], through the ELM-resilient full active multijunction (FAM) [143], as far as passive active multijunction (PAM) [144]. The latter concept, whose effectiveness was demonstrated for the first time on FTU at 8 GHz [145], has been recently validated on long pulses on Tore Supra at 3.7 GHz [146], thus dissipating the latest doubts (thermo-mechanical characteristics, heat removal efficiency, etc.) about its employment during steady-state operations

in reactor-relevant machines.

Taking also into account that all present-day superconducting tokamaks have or plan LHCD capability and that LHCD exclusion from ITER's early phase relies more on financial reasons than on scientific issues or technological problems, it follows that such a H&CD system cannot be a priori ruled out of conceivable tools for fusion reactors, but its strengths and weaknesses are worth evaluating. In this scenario, the assessment of H&CD systems for DEMO has been undertaken and a first exploration carried out in the frame of the EFDA workprogramme 2011 and 2012, with the primary aim of defining physics requirements and identifying technological gaps to be filled. Such a step represents the fundamental starting point towards DEMO definition and optimization.

In the following the main outcomes concerning the assessment of the LHCD system for DEMO are reported, focusing on the so-called options 1 and 2 [117]. Namely they are respectively the DEMO pulsed model, where a transformer drives the main current, and the "optimistic" DEMO design pointing at steady-state operations which are at the upper limit of achievable ITER performance. The latter, compared to its "conservative" counterpart (option 1) entails the most demanding challenges which fusion community may expect in LHCD systems during next years.

In order to indicate the better choice for the frequency, power and the launching characteristics of LHCD system, in the option 1 the plasma configuration envisaged today, i.e. the so called L-mode plasma model with peaked density profiles, is assumed. For the option 2 the improved H-mode configuration is considered where the central electron temperature is larger.

LHCD physics has been assessed with the help of two different suites of tools, which allow calculating the sensitivity of LH power deposition and current driven profiles on several parameters. The first code suite relies on the automated system for transport analysis [147], which includes the fast ray-tracing code [148]. The second suite is based on the LHstar code [149]: it is a set of mutually coupled codes (a Grad-Shafranov solver, a ray tracing tool and the quasi-linear Fokker-Planck code), which also models parametric instabilities (PI).

A common starting point for the initial exploration of the H&CD systems in the two DEMO options was agreed at European level in terms of geometry and main plasma zero-dimensional parameters [117]. Some relevant figures are reported in Table 4.5. In compliance with such values and according to different density assumptions and scaling laws, some density and temperature profiles were derived. In details two profiles with peaked and flat density have been conceived for each DEMO option. Fig. 4.18 reports profiles with peaked density, being the most suitable for LH operations. Moreover the presence of a scrape-off layer (SOL) of the order of 20 cm has been also considered. A guess on the density and temperature profiles in the SOL plasma of DEMO has been assumed on the basis of an extrapola-

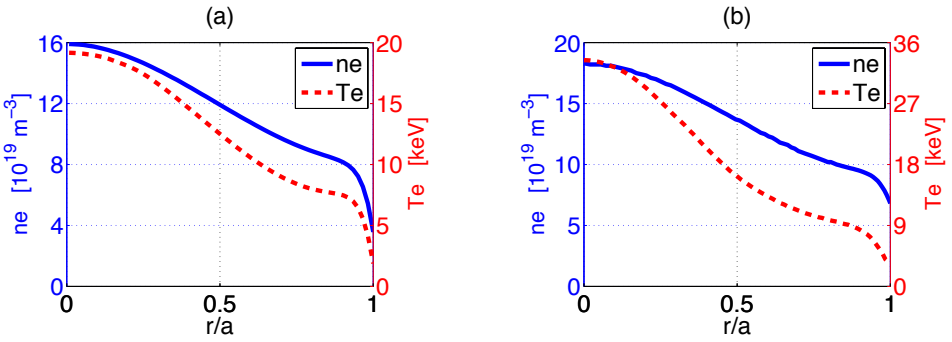

Figure 4.18: Commonly agreed electron density (ne) and electron temperature (Te) profiles ("peaked" case) versus normalized radius for DEMO options 1, i.e. pulsed design (a), and 2, i.e. steady-state design (b).

Parameter	option 1	option 2
Toroidal field	6.8 T	5.74 T
Major radius	9 m	8.5 m
Minor radius	2.25 m	2.83 m
Elongation (95)	1.55	1.66
Triangularity (95)	0.33	0.33
β_N	1.93	2.95
$< n_e > [\times 10^{19}]$	8.5 m^{-3}	9.1 m^{-3}

Table 4.5: Main parameters of DEMO.

tion of the ITER SOL, whose density and temperature profiles have been numerically simulated.

On this basis, trade-off studies have been carried out to investigate the impact of different power spectra, launcher positions and scrape-off layer profiles on LH performances, assuming to inject 5 GHz waves. The reasons for the frequency choice, being the same solution adopted in the LHCD system proposed for ITER, are discussed later on. In order to have LHCD in the plasma region with normalized radius ρ in the range $0.5 \div 1$, i.e. in between the outer half radius and the separatrix, the antenna has to launch a spectrum that is as fast as possible and compatible with

- LH accessibility condition (depending on the local plasma density),
- LH peripheral absorption (depending on the local electron temperature),
- antenna design constraints.

Several launched power spectra have been considered with the peak parallel

refractive index $n_{||}$ assuming values between 1.5 and 2.0 and the half-power width $\Delta n_{||} \approx 0.1$. Reliable spectra have been obtained by running the GRILL3D-U code [150]. Simulation results showed that [151]:

- The sensitivity of LH effects to the launcher poloidal position is very weak: it has been studied with and without SOL, for two different power spectra, considering a power injection at -2, 0 and 2 meters with respect to the equatorial plane.

- A peak $n_{||}$ of 1.8 is a good choice, leading to a deposition always localized inside the separatrix layer $\rho \leq 1$. Lower peak $n_{||}$ move the deposition more internally but give inaccessible waves too. In the peaked density profiles of steady-state and pulsed DEMO designs, LH power deposition is centred at $\rho \approx 0.85$ and 0.6, respectively. More external depositions ($\rho \geq 0.9$) are obtained with the flat density profiles.

- The scrape-off profiles do not influence the absorption of LH waves. Scenarios with and without SOL have been studied, the latter by modeling PI-induced spectral broadenings due to different electron temperature profiles. No variation of current driven density profiles with SOL parameters have been obtained, unless unrealistically low temperatures are assumed in the SOL.

According to previous outcomes, the lower hybrid current drive stands out as a powerful, beneficial tool even for reactor-relevant tokamak machines. Thanks to its high current drive efficiency, at moderate electron temperature, it results remarkably effective in accomplishing two major goals: (i) to drive far off-axis current and (ii) to save the volt-second during the current ramp-up phase. It can actually play a fundamental (even crucial) role in improving confinement time as well as discharge times by acting on the plasma current density profile and by saving magnetic flux. The first issue, i.e. the control of plasma current profile, is essential to sustain steady-state plasmas, representing one of the most important problems for the research on nuclear fusion energy based on the tokamak concept.

Considering the kinetic profiles expected so far in regimes aimed at approaching steady-state operations in DEMO, the most significant contributions to the non-inductive plasma current given by the bootstrap effect would be localised in the outer half of the plasma minor radius, namely near the edge at $r/a = 0.95$ and $r/a = 0.7$. In order to have the necessary flexibility in the current density profile control, tools for actively driving current should be necessarily utilized. In general the deposition of lower hybrid waves was found to be very peripheral except for the peaked density profile of the pulsed design, where the deposition peak is approximately located at a normalized radius of 0.6.

4.2.2 High-power RF generation and transmission

Radio-frequency sources

The choice of LHCD frequency results from a delicate trade-off between manifold counteracting elements: several physics issues demand to increase the frequency, while technological limitations put some upper bounds.

One of the major players in driving the frequency choice is the nonlinear interaction at high harmonic ion cyclotron resonances, causing parasitic damping of LH waves by fusion-born α-particles [152]. This mechanism mostly entails two deleterious effects: the reduction of current drive efficiency and the generation of non-thermal tails on the α-particle distribution function, thus increasing their losses and the risk of damages to plasma facing components. Even if the main wave absorption is close to the plasma edge and α-particles are created in the bulk plasma, their profile may extend up to the periphery, due to their large banana orbits and diffusive effects. Referring to the simulations performed for different ITER scenarios, this absorption was demonstrated to be quite low at 3.7 GHz and negligible at 5 GHz, which would thus provide some margin if the α-particle distribution function was broader than foreseen [153]. Accordingly, albeit no calculations have been carried out for DEMO yet, a LHCD system for this machine can be hardly conceived with a frequency lower than 5 GHz.

Given a certain power to be launched through a port, multipactor also constrains the operational frequency. Although the minimum electric field triggering breakdown can be increased by lowering the secondary electron emission rate γ with several techniques (e.g. high-temperature baking, carbonization, glow discharges, vacuum and plasma conditioning) [154], the threshold scales as ω^2 for the first multipactor order. In other terms, according to the scaling law based on experimental results [145], the higher the frequency, the higher the power-handling capability (33 MW/m^2 at 5 GHz), allowing to couple more power given the same radiating area.

On the other hand, a frequency enhancement also means an increase in the cutoff density, but it does not represent a primary issue even in presence of high-performance plasmas. Remote coupling can be successfully performed using a gas pipe to inject deuterium and control edge density, as demonstrated in JET for an antenna-plasma distance of 15 cm with the 3.7 GHz system [155]. Parametric instabilities, observed since early experiments aimed at heating plasma ions by coupling LH power [156], demand instead higher working frequencies in order to reduce strong PI-produced LH spectral broadening effects on propagation and damping of LH waves.

Coming to technological issues, 5 GHz currently represents the highest frequency that suitable, reliable, high-power, RF sources (i.e. klystrons) are expected to achieve in a reasonable time, unless substantial financial funding was destined to the development of higher frequency sources (i.e.

gyroklystrons) in the next future. Presently the most promising candidate is the 5 GHz, 500 kW klystron (model No. E3762RD0), developed by Toshiba for the LHCD system of the South Korean KSTAR tokamak [157]; some R&D is still needed on it to get a fully CW prototype: during recent laboratory tests, through calorimetric measurements on dummy loads, RF output powers of 500 kW for 2 s and 350 kW for 800 s have been achieved.

Alternatively the 4.6 GHz, 250 kW, klystrons, developed by CPI, represent a backup solution: a pulsed version is presently operating on the LHCD system for Alcator C-Mod, while the CW tubes, namely the prototype VKC-7849A [158], have been installed in EAST. As a drawback, their limited output power, requiring a larger amount of modules, would increase system cost, complexity, integration issues, etc.

Power supply and low RF power unit

A high voltage power supply (HVPS) is required to operate and condition klystrons with proper functional and electrical requirements. Although 5 GHz sources are not fully developed and the location of DEMO, together with its alternating current distribution grid, are not known, a solution close to the one proposed for ITER [159] can be reasonably envisaged. So a single HPVS module is expected to feed four klystrons by means of a multi-secondary transformer which forms the input of a second block based on the pulse step modulation technology, namely a stack of series connected, independent, modular voltage supplies. In such a way, klystron protection from arcs can be performed by fast, solid-state, opening switches like series arrays of insulated-gate bipolar transistors instead of cumbersome crowbars based on mercury-containing ignitrons. All other auxiliary power supplies needed for klystron operation, as well as low power RF units fixing the operational frequency of four LHCD modules and the required phase shift between them, would be of the conventional type.

Such a solution presents several attractive features in terms of performance, modularity, maintainability, flexibility, etc. and it does not need R&D, since most of the components required for its development are already available from industries. After a demanding work of data research from reliability databases, the cumulative failure rates of basic units, constituting the LHCD system, have been calculated in the frame of a preliminary reliability availability maintainability inspectability analysis [160]. As regards HVPS and low power RF unit, final failure rates are 554×10^{-6} and 2.4×10^{-6} hours^{-1} respectively, assuming worst case conditions, an additional 10% increase due to passive components and 70 basic modules for each HVPS. The first value exceeds the maximum failure rate required for the whole LHCD system, that is 10^{-5}, but a large decrease can be achieved if redundant modules are introduced, a prompt substitution in case of fault is foreseen or an accurate maintenance is scheduled.

Main transmission line

The main transmission lines (MTLs) are meant for carrying a large RF power from the generators to the launcher. Despite their design and the components needed to efficiently accomplish this task depend on the particular topology of the system and its I/O requirements, a common layout usually remains true. This includes the following elements:

- Low-loss transmission lines, generally implemented with oversized circular waveguides. They are in charge of the actual energy transport over most of the distance between the generators and the launcher. Oversized waveguides have high power-handling capability and lower ohmic losses in comparison with monomodal guiding structures; as a drawback they allow energy transfer from the mode of interest into spurious (i.e. unwanted propagating) modes.

- Bends. According to the system layout, the path from the generators to the launcher may include a large number of bends, which can backward reflect part of the power and excite potentially detrimental spurious modes. With respect to the latter mechanism, waveguide bends are the most critical component and unconventional solutions must be sought to improve the unsatisfactory performance of standard, smooth-wall, circular curves.

- Mode filters. Even with the most careful design, some unwanted modes are unavoidably excited at waveguide discontinuities such as flanges or bends and, propagating to and fro along the transmission line, may give rise to dangerous trapped mode resonances. Mode filters are conceived to damp the spurious modes, while being ideally transparent to the operational one.

- Adapting devices like splitters, combiners, tapers and mode converters. They are intended to be compliant with I/O requirements, i.e. the outputs of the microwave generators and the input waveguides of the launcher.

Everything has to be monitored, controlled and protected: bi-directional couplers and optical detectors are effective and commonly used tools that can fulfil several task like protecting klystrons from reflected power, detecting arcs or serving for RF phase measurements. Circulators are probably useless since the launcher is based on the PAM concept, but this cannot be confidently said, yet. The possibility of using optical fibres, working in the infrared range, close to the launcher has to be checked according to compliance with ionizing radiation. As for arc detection innovative solutions allowing arc localization (e.g. based on sound detectors or radar techniques) can be possibly investigated together with the most recent suggestions (i.e. bolometry) for the launcher mouth.

The design of high-power RF components for oversized waveguides requires particular attention to avoid parasitic modes and excessive electric field values. Matching conditions between different sections and components of the transmission line must be achieved avoiding metallic posts, irises and H-plane septa that can accidentally generate electrical breakdowns. Furthermore, due to the large amount of transmitted RF power, some devices may undergo overheating and require an active cooling.

Depending on the areas of applicability other than fusion engineering, the aforementioned components have seen a different level of development. For example oversized waveguides and some types of bends are standard devices, while some kinds of power splitters, converters and mode filters have to be designed and built on purpose. The conclusive choice between off-the-shelf and non-standard components requires detailed input data that are not available at this stage. However reasonable assumptions can lead to meaningful remarks which are addressed in section 4.3.

Launcher

The launcher design is relatively clear from the conceptual viewpoint; the direst issue is the choice of materials, which is addressed later on.

4.2.3 Radio-frequency windows

The MTL is usually pressurized with a high electrical strength gas to reduce the risk of breakdown. At the end of the MTLs, in the back-plate of the launcher, RF windows must be hosted to separate the pressurized region of each transmission line from the launcher exposed to the vacuum vessel. Their failure is a catastrophic event in an operating fusion reactor. The function and operational environment of RF windows are very demanding: low reflection and insertion loss, high power-handling capability, excellent mechanical strength, high thermal shock resistance, vacuum tightness and compatibility with irradiation conditions are needed. Vacuum windows must be transparent to RF waves, withstand the static torus overpressure, dissipate the internal microwave heating using a reactor-compatible coolant and not be degraded by exposure to high and medium energy neutrons and gamma rays. These features are required during steady-state operations.

The scientific literature regarding microwave windows is vast, but very few papers focus on the issues in CW lower hybrid systems for fusion reactors. Much work is related to klystron windows, but it mostly concerns short-pulse applications like linear colliders, which do not share the peculiar irradiation matters of high-Q tokamaks. The latter have been addressed at different frequencies within the R&D of the 1 MW, CW window for the ECRF system of ITER. An intense R&D activity is thus mandatory for the RF windows of the LHCD system for DEMO.

Assembly considerations

For high-power applications, cylindrical windows, operating with the TE_{11} mode in circular waveguide are preferred to disks in rectangular waveguide, due to the reduction of the electric field at the critical dielectric-metal seal region [161]. A pillbox window implements this concept: it is made by a dielectric disk inserted in a circular waveguide and two junctions for input/output rectangular waveguides. The metallic frame of the window could be copper, nickel-copper or titanium; the pillbox configuration also facilitates the brazing dielectric-metal. For some ceramics like alumina, having a high yield of secondary electron emission, Ti, Cr203 or particularly TiN coatings can be used to effectively suppress multipactor breakdown phenomena. Attention has to be paid to the film thickness that is a compromise between two counteracting needs: reducing the number of secondary electrons and limiting ohmic losses on electrically conductive films [162].

As far as cooling is concerned, four general classes of high-power, CW windows have been considered for mm-wave applications [163]: distributed, liquid-edge-cooled, gas-surface-cooled single-disk, and liquid-surface-cooled double-disk as reported in Fig. 4.19. For the present application the second solution must be preferred. The distributed window cannot be employed because of its complicated and expensive mechanical structure, high losses and danger of arcing. The gas-surface-cooled single disk is not compatible with the use of SF_6-filled waveguides and liquid-surface-cooled double-disk windows require two disks per barrier and the use of dielectric coolants, which generally do not fulfil safety requirements.

Liquid-edge-cooled single disks can be cryogenically cooled. This option is useful for materials like sapphire, whose loss tangent and thermal coefficient undergo, respectively, large reduction and great enhancement at cryogenic temperatures. Nevertheless this solution is unlikely to be adopted because it entails cumbersome windows requiring dewars (canisters) and insulations, scarcely compatible with the severe space constraints in the rear of

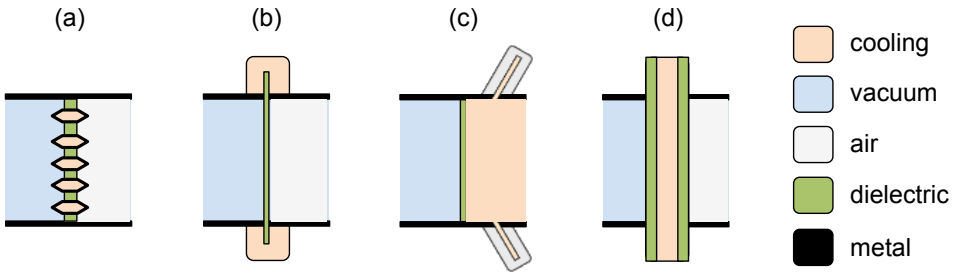

Figure 4.19: General classes of high-power, CW windows: a) distributed window, b) liquid-edge-cooled disk, c) gas-surface-cooled single-disk and d) liquid-surface-cooled double-disk.

the launcher. Water is the favourite candidate among the possible coolants for torus windows: it allows a more compact and reliable design of the component, while being cheap, effective and compatible with the nuclear environment.

Dielectric materials

The low loss tangent dielectric materials either currently used or under active development are the following: alumina, beryllium oxide (BeO), boron nitride (BN), silicon nitride, gold-doped silicon, sapphire and chemical vapour deposition (CVD) diamond. In order to identify the possible candidates for the RF vacuum windows of the DEMO LHCD system, the main parameters of aforementioned materials have been collected through a broad bibliographic investigation and summarized in Tables 4.6 and 4.7 for edge-cooled windows at room temperature.

Polycrystalline aluminium oxide (Al_2O_3) or alumina is a ceramic that can be procured in a variety of different grades, achieving very attractive properties for high-power, shortly pulsed, microwave windows to be installed in klystrons. It was chosen as torus vacuum barrier in some LHCD systems such as FTU (8 GHz), Alcator C-mod (4.6 GHz) and EAST (2.45 GHz). Beryllium oxide, a poly-crystalline, toxic material combining high thermal conductivity with low expansion coefficient, has been often adopted in the

	alumina 99.5% p.c.	beryllia p.c.	BN (CVD) p.c.	silicon nitride comp.
Density [g/cm^3]	3.89	2.85	2.3	3.4
Ultimate bending strength [MPa]	379	140	80	800
Poissons number	0.22	0.3	0.25	0.28
Youngs modulus [GPa]	375	345	70	318
Specific heat capacity [J/(gK)]	0.88	1.05	0.8	0.6
Thermal conductivity [W/(m·K)]	35	260	55	59
Thermal expansion coef. [10^{-6}/K]	8.4	7.2	3	2.4
Dielectric strength [kV/cm]	169	138	374	185
Relative permittivity	9.4	6.7	4.2	7.5
Loss tangent [10^{-4}]	1.1	30	10	19
Failure resistance [10^3W/m]	3.3	10.3	15.7	44.5
Max neutron fluence [n/m^2]	10^{20} [164, 165]	10^{20} [164]	n.a.	$<10^{21}$ [166, 167]
Metallizing/brazing	o.k.	o.k.	o.k.	o.k.
Unit price (200pcs/order) [k$]	< 2	$2 \div 3$	n.a.	$3 \div 3.5$

Table 4.6: Main parameters of window materials at room temperature for an edge-cooled configuration (p.c. = polycrystalline, comp. = compound).

	Au-doped silicon s.c.	sapphire s.c.	diamond (CVD) p.c.
Density [g/cm^3]	2.3	3.98	3.52
Ultimate bending strength [MPa]	1000	400	500
Poissons number	0.1	0.28	0.1
Youngs modulus [GPa]	190	420	1050
Specific heat capacity [J/(gK)]	0.7	0.76	0.52
Thermal conductivity [W/(m·K)]	150	31	1800
Thermal expansion coef. [10^{-6}/K]	2.5	5.8	1.0
Dielectric strength [kV/cm]	n.a.	480	1000
Relative permittivity	n.a.	9.3	5.6
Loss tangent [10^{-4}]	8.6	0.9	0.5
Failure resistance [10^3W/m]	284	3.6	858
Max neutron fluence [n/m^2]	10^{20} [168]	10^{21} [169]	10^{20} [169]
Metallizing/brazing	o.k.	o.k.	o.k.
Unit price (200pcs/order) [k$]	n.a.	$2 \div 3$	> 4

Table 4.7: Main parameters of window materials at room temperature for an edge-cooled configuration (s.c. = single crystal, n.a. = not available).

case of longer pulses, e.g. for the LH launchers in JET (3.7 GHz), Tore Supra (3.7 GHz), KSTAR (5 GHz) and proposed for ITER (5 GHz). Apart from these two materials, the remaining ones have undergone intense research studies mostly in connection with other H&CD systems.

All materials have their own thresholds, beyond which radiation permanently modifies their parameters due to the accumulation of defects and the evolution of microstructures. For ceramics, tolerable irradiation maxima are generally dictated by modifications induced in thermal conductivity and loss tangent, being the most sensitive properties, while other characteristics, like physical dimensions, flexural strength, permittivity and dielectric breakdown strength mostly change at higher displacement damages [170, 171, 169].

Besides irradiation damages, dynamic effects may also occur: the transient degradation in loss tangent can be higher than estimations based on post-irradiation measurements. In this sense the most common mechanisms are the radiation-induced conductivity and radiation-induced electrical degradation. The former, caused by the excitation of valence electrons into the conduction band due to energetic radiation, varies inversely with frequency, hence it is negligible above ion cyclotron frequencies [172]. The same remark holds true for the latter [170], being a controversial topic of difficult understanding and consisting in a severe permanent increase in the electrical conductivity of ceramic insulators during extended irradiation,

when an electric field is applied at the same time. Therefore, at LH frequencies, the loss tangent of a wide range of ceramics is said to increase only slightly during pulsed neutron irradiation at a damage rate of about 10^{-5} dpa/s [173].

Although ceramics behave in a qualitatively similar manner, there are significant quantitative differences, which are strongly affected by factors like material grade, types of impurities, measurement frequency and irradiation conditions. For example a 20% reduction of the thermal conductivity was measured for Al_2O_3 99.5% at fluences of 10^{21} n/m^2 in [174] and 10^{24} n/m^2 in [171], whereas [167] found the same decrease for Al_2O_3 99.8% at 2×10^{22} n/m^2. As a general rule in presence of contradictory results, the most restrictive conditions have been considered, giving preference to the latest, fusion-relevant papers and applying interpolation and extrapolation to derive 5 GHz estimates from available data. Then, tolerable neutron fluences have been determined by the acceptable modifications of thermal conductivity and loss tangent, which generally depend on window design. Since BeO windows can withstand ITER environment without undergoing any change and are compliant with the severe requirements of the LH system, radiation-induced degradation has been regarded admissible when material properties were similar to or better than beryllium oxide. For materials, the unirradiated properties of which were worse than BeO, an allowable variation of 20% has been considered as done in [169].

Accordingly, for alumina 99.5% the tolerable neutron fluence given in [164] for ICRF applications has been adopted after finding confirmation that, at the same fluence, the 5 GHz loss tangent is lower than 10^{-3} [165]. In the case of beryllium oxide, its employment in ITER, together with data reported in [164], guarantees unchanged properties up to 10^{20} n/m^2, which is the expected neutron fluence at the port plug. No data have been found for boron nitride, while scarce information exists for silicon nitride, whose modifications in thermal conductivity and loss tangent have been supposed through rough interpolation and general remarks from [167] and [166], respectively. With reference to gold-doped silicon, interpolated values at 5 GHz can be easily derived from [168], while concerning sapphire and CVD diamond, tolerable fluences indicated for electron cyclotron frequencies have been used in Table 4.7. Sapphire at cryogenic temperatures was the main candidate for EC windows; this fact guarantees that thermal conductivity is unchanged under the given threshold [169] also at room temperature since this parameter generally degrades less at higher temperature [170, 167]. As for loss tangent, it is not expected to be a concern by combining results at different frequencies and temperatures [175, 176, 177] and considering that, in general, neutron irradiation fluences up to about 10^{22} n/m^2 produce only small increases in the loss tangent of Al_2O_3 [170]. In the case of CVD diamond, the limit given in the studies for EC systems is dictated by the degradation of thermal conductivity rather than power loss [178], so even

considering a worse behaviour of the latter at 5 GHz, maximum fluence can be reasonably expected to hold true. Actually there are post-irradiation studies of loss tangent at microwaves but significant differences are reported in [179] between nominally similar samples, however degradations are not dramatic.

Tolerable neutron fluences given in previous tables can be only considered as indicative due to the previous remarks and the following reasons. First of all, some post-irradiation studies made use of fission neutrons, which present significant spectral differences from fusion neutrons [173], and, as pointed out in [172], the changes of some properties, like swelling and dielectric loss, vary with the neutron energy spectrum as a result of the production of different transmutation products. Secondly, irradiation temperatures also play a significant role, mostly with reference to thermal conductivity. Tolerable neutron fluences should refer to the operational window temperature in stationary conditions, which is unknown at the moment since it depends on the window design, materials, cooling system, etc. With reference to the BeO disk with radius of 50 mm for the LHCD of ITER, the calculated temperatures at the centre and at the edge were about 22° C and 180° C, respectively. Fortunately the amount of degradation in thermal conductivity is generally larger for the lower irradiation temperatures [170], [167]. Finally dynamic effects have been considered negligible for LH windows, but a further assessment in this sense is required. Accordingly dedicated experiments at 5 GHz with DEMO-relevant irradiations are beneficial, considering that no window can fail due to the criticality of its role and the difficulty of its replacement.

On the basis of the information summarized in Tables 4.6 and 4.7, we can draw the following conclusions with reference to the material choice. Alumina, boron nitride and silicon nitride must be excluded among DEMO candidates because the low thermal conductivity makes these insulators not suitable for CW operations. The same remark applies to Sapphire at room temperature; this dielectric is acceptable when cryogenically cooled, but this option is not viable in terms of mechanical complexity and space requirements [180]. Among the remaining candidates, Au-doped silicon is too brittle and prone to mechanical cracking according to [163], hence only BeO and CVD diamond are usable. The former is already under intense R&D activity in connection with ITER [181] and can be regarded as a safer, short-term solution. The latter, apart from its cost, exhibits definitely superior characteristics and seems a more appealing, long-term candidate.

Concerning cost estimations, they are rough order of magnitude prices per unit, considering an order of 200 pieces. The unit consists of the ceramic window brazed with metal sleeves, so that welding is up to customers; the pricing for the rest of the structure, i.e. copper, waveguide, flanges, etc., has been estimated in around 200$. Cost estimations are courtesy of KYOCERA Corporation [182] and Altair Technologies, Inc. [183].

Full-wave microwave simulations

Preliminary full-wave RF analyses have been carried out using the typical CVD diamond permittivity and a loss tangent degraded by neutron irradiation. A thin pillbox window, water-cooled at the edge, with a dielectric thickness of 3 mm and a symmetric iris as matching element, is the most promising solution for the vacuum barrier of the LHCD system in DEMO. It can withstand a power of 0.5 MW in CW operation, even with a reflected power of 10%, and sustain a maximum pressure of 0.9 MPa. The thickness, much shorter than the conventional window ($0.5\lambda_{\mathrm{TE11}}/\sqrt{\varepsilon_r}$ long in circular waveguide), significantly reduces the losses and the cost of the disk. Between the two input/output waveguides taken into exam, the WR284 is preferable due to its lower maximum intensity of the E-field, while the WR229 allows exploiting the R&D already performed for the RF windows of ITER.

4.2.4 Passive active multijunction antenna

Passive active multijunction (PAM) antennas have been proven as the most effective and promising launchers for reactor-relevant LHCD systems. Compared to conventional grills, consisting of independently fed (phased) waveguides having RF windows placed near the plasma, the multijunction concept allows a remarkable reduction of reflected power at the expenses of a lower $n_{||}$ flexibility. Among multijunction antennas, i.e. the PAM and the FAM (full active multijunction), the former has some advantages on the latter, albeit its lower directivity and smaller actively radiating surface.

In details, particularly when referring to DEMO, PAM launchers present

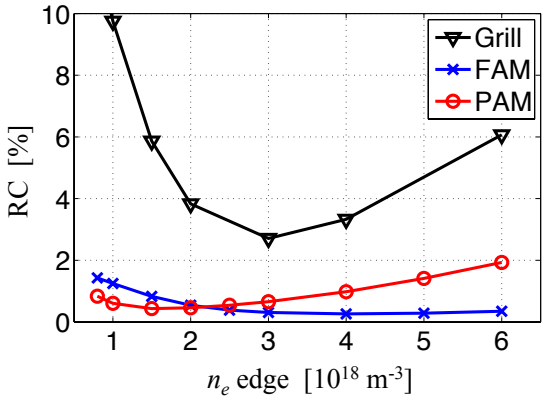

Figure 4.20: Simulations performed with the TOPLHA code for a single row of different FTU launchers, using a standard parabolic density profile, static magnetic field = 5.9 T, frequency = 8 GHz (cutoff density = 0.8×10^{18} m^{-3}), waveguide phasing = -90 deg, giving a peak $n_{||} \cong 1.88$.

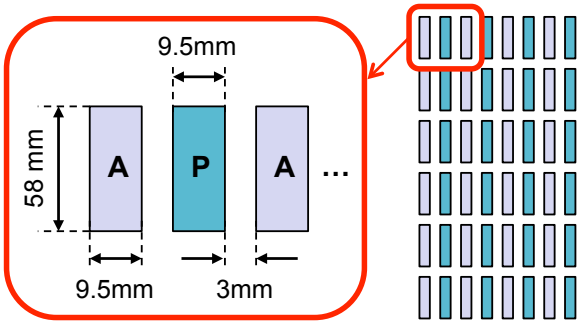

Figure 4.21: Possible module of the LH antenna in DEMO: A and P denote active and passive waveguides, respectively.

the following very attractive features:

- coupling properties are optimized close to the cutoff density. It is clearly shown in Fig. 4.20, where the reflection coefficients predicted by TOPLHA [184] for a conventional grill, a FAM and a PAM launcher are compared. The plot actually refers to 8 GHz antennas designed for FTU and simulated using a typical FTU plasma scenario, but the meaning holds true at 5 GHz as some ITER studies demonstrated.
- efficient heat removal: a large number of vertical cooling ducts can be accommodated just behind passive waveguides; contrariwise, in the FAM concept, horizontal pipes have to be installed in between active waveguides, thus decreasing the radiating surface.
- good neutron shielding due to the very dense structure.
- mechanical robustness

A possible antenna module has been thus conceived as depicted in Fig. 4.21. The waveguide height of 58 mm maximizes the transmitted power density and limits the propagation to the fundamental TE_{10} mode. The wall thickness of 3 mm guarantees enough stiffness and manufacturability. The module represents the part of the launcher fed by a single source, i.e. by 500 kW, and it consists of an array of 6×4 active waveguides, resulting in a maximum power density of 37.8 MW/m^2. The latter value is a safety factor 0.6 lower than the maximum allowed power density (P_d), which is around 64 MW/m^2 according to the scaling law

$$P_s \ [\mathrm{MW/m^2}] = 22.1 f^{0.66}$$

given in [145], where f is the operational frequency in GHz. An internal phasing of -90 deg is considered for the arms of each bi-junction, leading to a power spectrum peaked at $n_{||} = 1.8$, as required. The surface of the

module at the launcher mouth is 0.1×0.366 m^2, implying that a total area of around 1×3.7 m^2 is needed to accommodate 200 modules and deliver something less than 100 MW.

The use of the PAM launchers has been successfully demonstrated in medium-size tokamaks, but their employment in DEMO requires a solution to the most critical issue: the choice of suitable materials. In particular the antenna mouth, facing the plasma, must cope with the harshest environmental conditions in terms of thermal load, maximum tritium retention, erosion rates, bombardment by neutrons and ions. At this stage only a preliminary discussion of the problem, describing the current status, can be given without prescribing conclusive solutions owing to a double lack of information on the side of both material knowledge and DEMO environment.

As for the former, some papers [185] stressed that, for future devices like DEMO, new radiation resistant materials have to be developed and tested under realistic conditions. For example, concerning neutron wall load, due to the lack of an intense 14 MeV neutron source, high-flux fission reactors have often represented the only tools to quantify the n induced material damage. In some cases, monoenergetic ions were employed, but they differ from fusion-born fast neutrons, e.g. in their narrower energy spectrum, and produce different damage profiles. In the future an appropriate neutron facility like IFMIF [186] will provide appropriate radiation environments for material testing. ITER itself will represent an essential testbed, taking into account that current estimations of wall lifetime and tritium retention for ITER are based on extrapolations from present experiments or modeling calculations and imply large uncertainties. For example, quantitative figures concerning the erosion rate of LH launchers cannot be known reliably, since the most advanced LH launcher is the one installed and operating on long pulses in Tore Supra, which is a medium-size tokamak. In general, the materials for the mouth of LH launchers must surely present the following features: compatibility with the plasma, resistance against physical and chemical sputtering, high melting point, good thermal shock resistance, low activation by neutrons, availability and acceptable cost.

Regarding the available information on DEMO, they are only indicative at this stage. Expected thermal fatigue in reactors is no more than twice the one of ITER, namely a heat flux lower than 1 MW/m^2 is expected during normal operation [187]. On the contrary no predictions can be made about thermal shocks, which induce crack formation, vaporization, surface melting, melt layer ejection, and particle emission induced by brittle destruction processes. Plasma disruptions have to be totally avoided or, at most, a maximum number of events much smaller than in ITER, with its 10% of disrupted discharges, can be considered. So the transient heat load in DEMO is mainly associated with energy deposition by edge localized modes, whose occurrence and energy deposition (maybe $\ll 1$ MJ/m^2) are currently unknown. As for neutrons, the outboard neutron wall loading (NWL) in

ITER is 0.78 MW/m^2 for an irradiation of 0.54 full power year (fpy), corresponding to a lifetime of about 4700 hours. Preliminary technical reports about neutron analyses in DEMO foresee enhancement factors of 2 and 3 for NWL and fpy, respectively; moreover blanket exchange is considered extending the lifetime irradiation to 5 fpy.

Coming to the materials for the LH launcher, ITER obviously represents the best starting point. In that case, a water-cooled launcher was designed with its mouth consisted of a short layer of beryllium and the bulk made of stainless steel and CuCrZr. Beryllium is the material chosen for the ITER main chamber because it is an excellent oxygen getter, a good thermal conductor and the lightest metal these wall components can be made of (heavier impurities in the plasma lead to higher cooling due to radiation). Nevertheless its employment in ITER is questionable and must be avoided in DEMO due to its melting point of only 1560 K and the low threshold energies for physical sputtering, compared to elements with higher atomic number. Alternatives to beryllium, already adopted in ITER or suggested for fusion reactors, are carbon-fibre-composites (CFC) or tungsten coatings.

The formers have excellent thermal conductivity and strength; moreover they do not melt, but undergo sublimation at a temperature of about 3825 K. Nevertheless their thermal conductivity experiences a rather strong degradation even after relatively low neutron fluences and, above all, CFC suffer from chemical erosion/sputtering by means of formation of volatile hydrocarbons, whose redeposition generates tritium-containing layers. Tritium retention is the largest problem of CFC because it significantly affects their lifetime: when accumulation reaches the maximum allowable amount (presently 350 gram), a forced shutdown for cleaning or conditioning or replacement is mandatory, limiting the availability of the machine. Due to this reason, the use of CFC divertor plates in ITER is planned just at the beginning of its operation in the non-active phase without tritium. For operation in the active phase, the CFC plates are planned to be replaced with tungsten ones to minimize tritium retention by co-deposition.

The other option is tungsten (W), having a melting point of 3695 K, very attractive thermo-physical properties and small physical sputtering yield, which can be further decreased through a boron coating. Its high thermal conductivity exhibits a much smaller degradation after neutron irradiation and, in contrast to CFC, bombardment by $3 \div 4$ MeV He^{2+} ions did not lead to consequences on the erosion features. The successful operation of ASDEX Upgrade with fully tungsten wall supports the use of this material in a fusion reactor from the viewpoint of erosion and control. With very long pulses and a sufficient clearance between wall and plasma, wall erosion should not be governed by plasma ions, but by the comparatively low flux of energetic charge exchange atoms which would result in very low wall erosion. Moreover the high neutron scattering and capture cross-section of tungsten do not decrease significantly the tritium breeding ratio in a solid

breeder blanket if the thickness of W coating is up to 3 mm. The drawbacks of tungsten are its brittle nature and the fact that it is ductile and easily machinable only above the ductile-brittle-transition-temperature of about 670 K. Then, it is said to be significantly activated during neutron irradiation [185], but information about its behaviour under appropriate radiation environment is scarce. Unlike CFC, it can melt and, due to its high atomic number (74), the maximum allowable W-concentration in the plasma is 1 ppm against a 12% for CFC. Recently efforts have been directed towards self-passivating tungsten alloys, where a small content of other elements allow the enhancement of passive safety in the case of a loss of coolant, while keeping the favourable properties of tungsten. Either silicon or chromium are especially promising as alloying elements because they improve the oxidation resistance. At present, self-passivating W-based alloys are the main candidate for the first wall armour of fusion reactors [188].

With reference to the bulk of the antenna, appealing candidates are the stainless steels, in particular low activation grades with very low content of nickel. More precisely the so called reduced-activation ferritic-martensitic steels show reasonably good thermo-physical and mechanical properties, a low sensitivity to radiation-induced swelling and helium embrittlement under fission neutron irradiation and good compatibility with major cooling and breeding materials [189]. An example is the EUROFER 97 [190], whose electrical resistivity at room temperature is however 50×10^{-8} Ωm, namely about 30 times higher than for copper. The use of some coating, having both high electrical conductivity and low sensitivity to neutrons and ionizing radiation, can be possibly assessed for the waveguides. Nevertheless copper must be absolutely avoided because it undergoes severe degradation under neutron irradiation, mostly as regards its electrical conductivity. Precipitation hardened or dispersion strengthened copper alloys like Cu-Al_2O_3 and CuCrZr solve the problem of copper swelling and loss of electrical conductivity under irradiation: CuCrZr was indeed foreseen for the LH antenna of ITER. Unfortunately these alloys are still too prone to activation and they must be banned in DEMO: if an irradiation condition of 5 years in the first wall is considered, after 100 years these alloys will be still above the high level waste limit. Alternatives have to be investigated starting for example from tungsten, aluminium and gold: they are also activated but were found to loose activation more quickly than copper [191]. As for the technological feasibility of a W coating on a first wall structure of low activation stainless steel, plasma spray coating experiments were carried out on EUROFER. Through the deposition of a mixed interlayer deposited by simultaneous spraying of EUROFER and W powder, excellent adhesion of the subsequently deposited W layer was achieved [187].

Concerning coolant, both water and helium can operate in DEMO environment; the choice between them depends on the required cooling efficiency.

A few words can be finally spent about RF windows: the choice of

material has been already addressed in a section 4.2.3, here the impact of neutron issues on the launcher design is instead discussed. Even taking into account the sole irradiation period till the first shutdown for blanket and divertor exchange, the displacement per atom at the outboard first wall is at least 6 times higher than in ITER. If a LH launcher identical to the one of ITER were used in DEMO, neutrons would surely damage RF windows because, in that design, owing to the severe space requirement, just 400 mm were available for neutron shield, leading to a calculated neutron fluence slightly lower than 10^{20} n/m^2, i.e. barely enough to prevent window damage. Surely space requirements for DEMO will be much less severe than in ITER, but neutron fluxes will be higher too and shorter RF solutions must be designed for the launcher to save room for the neutron shield. Furthermore, unlike EC systems where there is more flexibility in designing the beam path, at LH frequencies doglegs and bends, being beneficial for shielding neutrons, significantly complicate the design.

4.3 Transmission Line of a LH System for DEMO

4.3.1 Guiding structures

Rectangular and circular waveguides stand out against other guiding structures for their low attenuation and high power-handling capability. On one hand they are available as off-the-shelf products in a number of standard dimensions, deterring from the use of unconventional solutions. On the other hand, they must be employed outside the frequency range they are intended to. It follows that waveguides are overmoded and one can benefit from adopting off-the-shelf products just for the straight sections of the transmission line, where the mode conversion, even at flanges, is almost negligible. As for the rest, the designer has to cope with several, usually uncommon, problems, which wipe out the possibility of employing standard products and ask for unconventional solutions and components, as respectively happens for bends and mode filters. As a general rule the number of spurious modes, i.e. propagating modes other than the operational one, has to be reduced as much as possible to limit accidental conversion losses.

Besides rectangular and circular waveguides, there is a third option represented by the so-called Tallguides® [192]. They are precision rectangular oversized waveguides, meant to work with the TE_{01} mode in an overmoded regime and primarily employed in satellite earth station uplinks and radars. Together with their low transmission loss and high power-handling capability, being respectively 10 times lower and 5 times higher than ordinary WR-type waveguide, Tallguides are provided with all necessary transitions, bends, twists and mode suppressors, whose quality control manufacturing standards are certified under ISO 9001:2008.

Among the different options reported in relevant data sheets, the TG215 (inner dimensions = 54.6 mm × 111.8 mm) is the most suitable one for the LHCD of DEMO; its features have been compared at 5 GHz to those of standard circular and rectangular waveguides. Circular waveguides are supposed to work with the TE_{01} mode that is not the fundamental one, but it allows an efficient transmission of high RF power over long distance because its attenuation drops rapidly as the diameter increases, making it the lowest-loss mode. Similarly, rectangular waveguides are supposed to work with the mode that achieves the lowest ohmic losses, namely the TE_{10} mode, which is also the fundamental one.

The comparison is shown in Fig. 4.22 in terms of transmission loss and power-handling capability. The former is expressed through the length of a straight waveguide section, at which the input power is attenuated to 95% by C10100 (also known as OFE) copper. The latter refers to the peak power limit owing to air breakdown at room temperature and sea level. The TG215 exhibits much better properties than the standard rectangular waveguide working in the same frequency band, namely the WR137 with

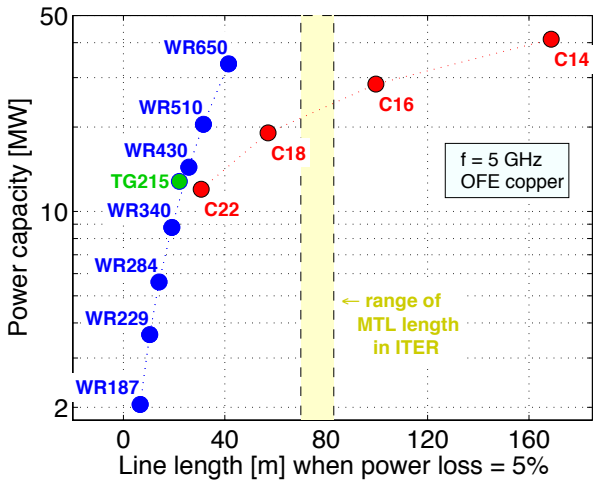

Figure 4.22: y-axis: power-carrying capacity calculated according to [193] when breakdown E-field $= 3 \times 10^6$ V/m, power safety factor $= 2$ and VSWR $= 1.2$. x-axis: straight line length leading to a 5% of attenuation [33] due to C10100 copper (i.e. about 101% IACS). Calculations at 5 GHz for different waveguides identified by their code.

power capacity = 0.7 MW and line length at 5% attenuation = 2.5 m. Nevertheless it does not suffice for the LHCD system in DEMO, when assuming a maximum attenuation of 5% along the transmission lines as a requirement and considering that, in ITER, the LHCD launcher is further than 50 m from the klystrons. Less severe conditions in DEMO than in ITER are unlikely.

Accordingly the use of the C16 results the best trade-off between the needs of reducing the attenuation losses and lowering the number of modes above cutoff at 5 GHz. With this standard waveguide an attenuation loss of 5% is achieved after about 100 m, which represents a good margin for bearing addition losses from other components like flanges, bends and converters. Some margin might be alternatively used to replace copper waveguides with lighter and cheaper aluminium ones allowing line lengths of about 70 m. The number of transmission lines cannot be supposed yet: a MTL consisting in one waveguide per klystron wouldy simplify the design since there would be no need for combining the outputs of two or more RF sources. Nevertheless constraints dictated by space availability could prevent from adopting this solution.

A few words must be spent about the simulation setup for microwave ports with circular cross section, because the correct calculation of the coupling between modes and the proper convergence of the results need all propagating modes to be considered. Unlike rectangular waveguides, in the

	C18	C16	C14
Waveguide radius [mm]	57.3	67.1	78.5
Modes above cutoff	10	15	18
TE_{01} propagation constant [m^{-1}]	80.6	87.8	92.7
TE_{01} guided wavelength [mm]	78	71.6	67.8
TE_{01} attenuation [dB/m]	0.0039	0.0023	0.0013

Table 4.8: Main parameters of some standard circular waveguides at 5 GHz.

circular ones, most of the modes have a corresponding degenerate counterpart, taken with different polarization. It follows that the actual number of orthogonal modes propagating in the C16 at 5 GHz is not 15, but 26, which is almost at the upper limit of what can be currently analysed with commercial simulation tools running on ordinary workstations. Worldwide used softwares like CST MICROWAVE STUDIO (MWS) require plenty of CPU time to solve such overmoded structures and another software like HFSS is even internally limited to support a maximum of 25 modes for each microwave port. The prediction of RF performance for C14-based components may instead require either cutting-edge computational resources or dedicated modelling activity. The main parameters of the C16 waveguide at 5 GHz have been reported in Table 4.8 together with the ones of the C18 and C14 for comparison. For preliminary calculations, one can simulate few modes and get approximate results, but this is not the aim of the present study. Here tricks that allow bypassing the issue, taking advantage of the particular component to be studied, are presented together with possible ways of fully overcoming the problem.

Waveguide compliance with power-handling capability requirements in terms of average and peak power has to be eventually taken into account. Both issues are common matters of high-power, continuous wave transmission lines and conventional solutions exist. On one hand, the average power causes heating by ohmic losses on the conductors, leading to a temperature increase, which puts an upper bound to the power capacity of a waveguide in steady-state conditions. This limit can be enhanced by employing waveguides provided with forced cooling or cooling fins. On the other hand, the peak power, being responsible for arcing phenomena, puts some constraint on waveguide cross-section. This constraint can be reduced, without affecting the transmission properties of the structure, by pressurizing the waveguide at $2 \div 3$ bar with high electrical rigidity gases like dry air or SF_6. The latter is particularly suitable to quench arcs due to its ability to capture electrons and absorb their energy; in addition it can fully recover its insulating properties after the arc extinction, healing by itself the chemical decomposition caused by the discharge.

4.3.2 Bends

A computational trick for bent waveguides consists in employing simulation tools that allow exciting the waveguide port with a single mode, while considering the other propagating modes that flow out of the structure. It means that a single column of the scattering matrix is calculated without encountering convergence issues or accuracy reduction, because the possible conversions of the excited mode into the undesired ones are fully considered. It is worth pointing out that some software only allows the computation of the entire scattering matrix.

The proposed approach is justified by the fact that the main figure-of-merit for bends is their efficiency, i.e., in the present case, the ratio between the output power carried by the TE_{01} mode and the input power of the same mode. In general waveguide curves are assumed to be fed by a pure TE_{01} mode and their behaviour when excited by other modes is a minor concern, which does not lead to design requirements. Just to give an idea of the simulation times to deal with, a solver run of CST MWS for a 90 deg bend with smooth walls and constant curvature radius of 1 m, using standard accuracy and computing a single column of the scattering matrix at 5 GHz, takes about 30 minutes on a desktop computer with a 64-bit quad-core processor at 3.07 GHz and 12 GB of RAM.

Overview of possible candidates

The study of the effect of curvature on the propagation of the TE_{01} mode in waveguides of circular cross-section drew particular attention in the 1950s, when this kind of transmission was a promising candidate for long-distance communication. In that frame much work was produced; it was mainly theoretical since the computer diffusion and the computational electromagnetics were still far from their breakthrough. Most of the alternatives to smooth-wall bends were proposed from the 1950s till the mid of 1960s, when the problem of bends was almost abandoned because optical fibres were proven to be more efficient and cost-effective than oversized circular waveguides. From 1990s on, overmoded waveguides have undergone renewed interest, mostly in connection with linear colliders and large-size tokamaks. In this context, researchers focused on different issues from the ones of 30 years before, since their major objective was (and still is) the efficient transmission of a large amount of energy rather than information. Parameters like power-handling capability of the component, rather than its bandwidth, drove the proposal of other innovative bend concepts. In this situation, full advantage was taken from the recent developments in computational capabilities and numerical techniques.

A wide bibliographic investigation has been carried out and a summary of the different approaches is given in the following.

- **Jouguet angle**. A pioneering paper by Jouguet [194] demonstrated the existence of a critical angle at which the TE_{01} mode totally converts into the TM_{11}, i.e.

$$\theta_c = \frac{\pi}{2.32}\frac{\lambda_0}{a}$$

being a the waveguide radius and λ_0 the free-space wavelength. By doubling this angle a perfect TE_{01} transmission should take place. Such a solution is easy-to-implement, but scientific literature is somewhat contradictory about its effectiveness. On one side experimental verification was given [195], but, on the other side, some studies showed that Jouguet's result only works in case of weak coupling (curvature radius $\gg$ waveguide diameter) [196] and that conductor losses [197], as well as additional parasitic conversions (TE_{01} into TE_{11} and TM_{11} into both TE_{21} and TM_{21}) [198], affect the expected performance.

- **Degeneracy removal**. This approach aims at removing the strong coupling between the TE_{01} and TM_{11} modes due to the fact that they are degenerate. Two techniques are especially effective in degeneracy removal: corrugations and ellipticity [197]. As for the former, the TE_{01} mode propagates in a corrugated waveguide nearly as in the smooth-wall pipe, whereas the TM_{11} mode experiences additional loading due to the radial grooves. With this option, straight and curved waveguide sections can be directly connected through flanges; besides the realization of corrugated waveguides is a standard process. As for the second technique, suitable transitions from circular to elliptical cross-section are necessary and the use of slightly elliptical waveguides throughout the path of the MTL is not suggested because an eccentricity of 0.3 results in a 25% to 35% higher heat loss than in the circular waveguide. Both corrugations and ellipticity were proven to work well when the curvature radius is much greater than the waveguide diameter, while there is no evidence of their effectiveness when the two parameters have comparable values.

- **Normal mode**. This technique [197] consists in transforming the TE_{01} mode into a normal mode of the curved region, which can propagate ideally uncoupled across bends of arbitrary length, e.g. the TM_{11} mode with polarization perpendicular to the bending plane. This concept relies on standard, smooth-wall, round curves, but it asks for mode transducers. For example half a cylinder of low-loss dielectric material with ε_r close to one can accomplish the required conversion. Alternatively two Jouguet-angle bends can perform it if placed out of the plane of the main curve. Similar solutions in a single plane need instead a rotation of the polarization, achievable with a section of elliptical waveguide or longitudinal, diametrical, dielectric sheets.

- **Dissipation**. If an infinite number of ideal TM_{11} mode absorbers were inserted along a bend, the TE_{01} bend loss would approach zero. Dissipative structures acting on the TM_{11} produce a similar effect [197]. Examples are longitudinal diametrical resistive sheets, longitudinal resistive rods and closely spaced copper rings in a lossy housing.

- **Constant wavefront**. Efficient bends can be realized if the wavefront of the TE_{01} remains radial with respect to the centre of curvature [199]. Two practical implementations of this concept were proposed: a suitable variation of the permittivity of the dielectric medium inside the waveguide over its cross-section and a variation of the surface reactance of the guide around its circumference, e.g. with circumferential dielectric-loaded grooves hosting coaxial modes. The first option has to be ruled out because of the aforementioned reason, while the second one can be taken into account for a deeper assessment.

- **Longitudinal slots**. A curved waveguide structure with negligible coupling between the TE_{01} mode and other propagating modes can be achieved by means of longitudinal shallow corrugations [200]. They lower the cutoff frequencies of TE modes, reducing the coupling to the TM_{11} mode, whose propagation can be avoided by a proper choice of the waveguide radius. As a drawback, the condition of large bending radius compared to waveguide diameter has to be fulfilled to attain satisfactory performance. Furthermore the reduction of waveguide cross-section implies the use of tapers and the increase of power density.

- **Mitre bend**. Although mitre bends are mostly employed at mm-waves, they have been adopted at lower frequencies too. In [201], a profiled mirror working at 11.424 GHz with ultra-high power (about 600 MW) has been designed for a smooth-wall circular waveguide operating with the TE_{01} mode. In that circumstance the use of mode converters was proposed so that the 21% of the power impinging the mirror is carried by the TE_{02}: this condition allows to have both the E-field and its derivative equal to zero at the wall. Even without using converters, tapers are probably required to reach a quasi-optical operational regime (waveguide radius $\gg$ wavelength, at least a factor 4), where mitre bends can exhibit satisfactory performance [202]. A remarkable advantage of mitre bends is their compactness.

- **Curvature profile**. A variation of the curvature profile across the bend can adjust mode conversion and recombination, giving high performance. It was proven using different design techniques with 90 deg bends for corrugated waveguides at 28 GHz, achieving efficiency of 98.7% [203], and for smooth-wall waveguides at 10 and 34.272 GHz, with efficiencies of 99.98% [204] and 99.9% [205], respectively. In the

latter case, the curve was manufactured and successfully tested. The method does not need tapers since waveguide cross-section does not change. So far it has been applied to higher frequencies, less propagating modes and larger curvature radii than the ones of the LHCD for DEMO, for which its viability has to be verified.

- **Mode recombination**. After calculating the eigenfunctions in a modified cross-section, the bend can be designed so that the phasing between modes at the end of the curve is the same as at the beginning. This approach was applied to a 90 deg bend at 11.424 GHz [206] by introducing two septa and choosing curvature radius and waveguide cross-section (i.e. diameter, septa width and thickness) that give negligible mode conversion. A solution based on the same concept and working at the same frequency was developed making use of a rectangular cross-section [207], where only 4 modes can propagate and their in-phase recombination at the end of the curve is used. Both curves employed adiabatic tapers and worked with a single curvature radius.

- **Rectangular cross-section**. An appealing solution consists in exploiting an E-plane bend in rectangular waveguide [208]. A single mode, exhibiting high transmission efficiency across E-plane bends, is supposed to propagate across the curved path, giving high performance components which do not depend on either angle or curvature radius, but require complicated mode converters. The proposed option foresaw the use of the TE_{20} mode in the bent rectangular waveguide plus two tapers and two converters, based on a cross-shaped section.

Solutions combining more techniques have been also proposed, e.g. a bend with elliptical cross-section and segmentation into several parts, whose lengths and curvature radii were optimized [205]. Considering the huge amount of specific options and general approaches, an exhaustive benchmark is very demanding; to assess different concepts, a priority based on their appeal has been thus fixed. For example, the presence of either dielectric-filled or cumbersome converters should be avoided in the LHCD system for DEMO. Dielectrics, resistive or conductive structures inside the waveguide introduce additional losses and increase the risk of electric discharge, while bulky transitions complicate the side-by-side integration of the transmission lines. Hence the lowest priority has been assigned to solutions based on such approaches or suspected of being ineffective or unsuitable for high-power operation. The device bandwidth was not considered in this rating because the LHCD system for DEMO is an extremely narrow-band application. Furthermore, the actual operative frequency is expected to be almost identical to the nominal one because the low RF power unit (i.e. the driver) sets it, while the klystron simply acts like an amplifier.

Assessment of the most appealing candidates

The effectiveness of the aforementioned approaches has been often demonstrated both theoretically and experimentally only in the most suitable working conditions for each particular technique, so as to highlight its strength. Generally these conditions correspond to curvature radii much larger than waveguide diameters, while, in practical problems, a point of concern is the need of bending oversized waveguides over curvature radii almost comparable to the waveguide diameter.

At this stage no information is available about the MTL layout of the LHCD system in DEMO; hence the present study deals with 90 deg curves, being the most common and attended angle in the scientific literature. As for curvature radii, five different values, ranging from 200 mm to 1000 mm with steps of 200 mm, have been considered. Energy travels from the generators to the antenna through several waveguides, which must be arranged in an array, so, by considering an external radius of 100 mm for the connecting flanges, the minimum inter-axis distance between adjacent waveguides is around 200 mm [209]. This is shown in Figure 4.23, where two possible integration schemes are depicted: the one relies on straight waveguides with identical length and bends with different curvature radius, while the other is the contrary. The latter approach occupies more room, but it requires designing and manufacturing a single, modular bend, usable for any waveguide of the array.

Three curve concepts have been assessed in addition to the standard

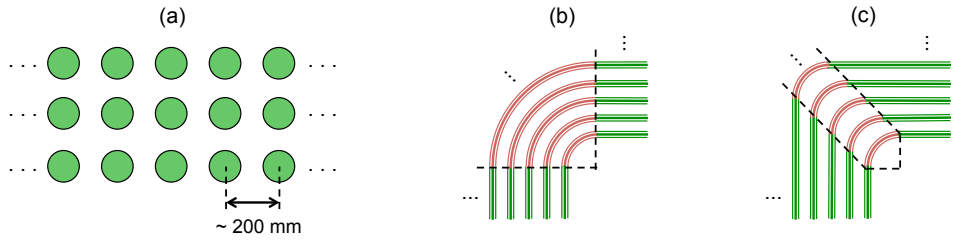

Figure 4.23: (a) Beam of waveguides arranged in a rectangular array; (b) bends with constant length of the straight sections; (c) bends with constant length of the curved sections.

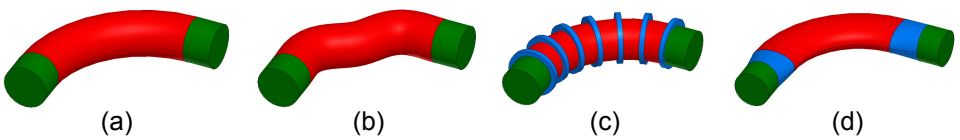

Figure 4.24: Types of bends: standard (a), with shaped curvature (b), with corrugations (c) and with elliptical cross-section (d).

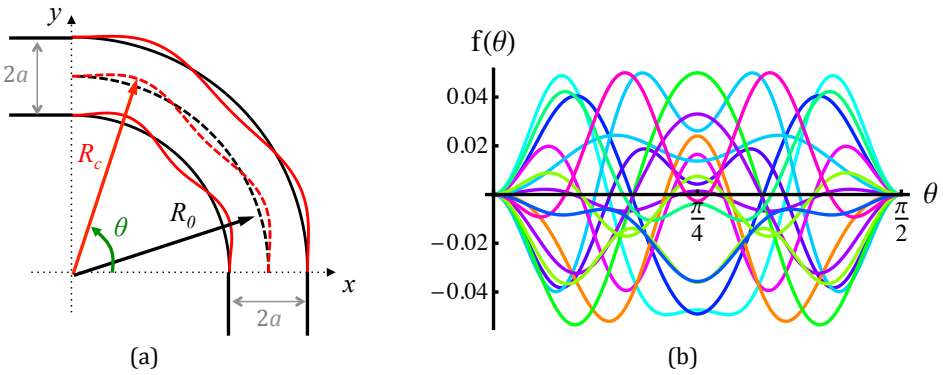

Figure 4.25: (a) Reference system of the curve. (b) Plots of several f(θ) for a cosine series of 4 coefficients with random values.

bend with smooth wall and constant curvature radius; all configurations are shown in Figure 4.24. As explained previously, they have been selected among many candidates according to some criteria like manufacturability and compliance with high-power requirements. For each approach the transmission efficiency has been calculated with CST MWS through a two-steps optimization. A first optimizer (usually the particle swarm optimization) or an extensive parametric analysis is applied to the whole feasibility domain, running the simulations with low accuracy to reduce the computation time. Then a deterministic algorithm, i.e. the trust region framework, is launched with standard accuracy inside a close neighbourhood of the optimum found at the previous step.

The first type of bend is based on a C16 waveguide with a shaped curvature profile: the curvature radius is left free to vary along the bend. Its profile has been optimized, keeping fixed the input and output coordinates and discarding unfeasible shapes under the simulation or manufacturability viewpoint. With the notation of Fig. 4.25, the curve profile is expressed mathematically as follows

$$\begin{cases} x = R_c(\theta)\cos(\theta) \\ y = R_c(\theta)\sin(\theta) \end{cases} \qquad \text{with} \qquad R_c = R_0[1 + \mathrm{f}(\theta)]$$

where the case with f(θ) = 0 corresponds to the standard rounded curve. Several mathematical representations of the function f(θ) have been tried, e.g. Chebyshev polynomials, Fourier series, splines and Lagrange interpolation with different samplings (equidistant nodes, Chebyshev nodes, artificial zeros). The most suitable one resulted the development as a bilateral Fourier series with real coefficients according to the following equation:

$$\mathrm{f}(\theta) = \sum_{n=-N}^{N} c_n \mathrm{e}^{\imath 4n\theta} = c_0 + 2c_1\cos(4\theta) + 2c_2\cos(8\theta) + \ldots + 2c_N\cos(4N\theta)$$

which reduces to a cosine series after enforcing the condition $c_{-n} = c_n$, being mandatory to achieve both symmetrical bends with respect to their bisector and soft variation at the boundaries. Some plots of this function with $N = 4$ and random values of the coefficients are given in Fig. 4.25b; only 3 out of 4 coefficients are free to vary because $\mathrm{f}(\theta)$ must vanish at the boundaries:

$$\mathrm{f}(0) = \mathrm{f}(\pi/2) = 0$$

to assure continuity with input/output straight waveguides. This results in the following condition relating the coefficients:

$$c_0 = 2(c_1 + c_2 + c_3)$$

The success of the Fourier representation over its competitors can be explained by referring to its nature, namely to the fact that its coefficients are related to the variation speed of the function across the bend. In other words, the more coefficients are used, the sharper variations are permitted; the truncation order of the series together with a limitation on coefficient amplitudes thus allow the attainment of a feasible design. In the present case a truncation order of 2 has been adopted for curvature radii of 200 mm and 400 mm, while an additional coefficient has been considered from 600 mm to 1 m; these numbers as well as upper and lower bounds to coefficient values have been empirically derived.

The second bend option consists of a corrugated waveguide, implementing the approach of degeneracy removal. For this kind of curves, the parameters that have been used for the optimization are the corrugation depth, width and period.

The last bend concept under consideration is the waveguide having elliptical cross-section. It requires the design of transitions to pass from a circular to an elliptical waveguide; these parts have been realized through an adiabatic transformation of the cross-section. After some preliminary full-wave analyses, the ellipse came out to be more effective when minor and major radii respectively lay on and out of the bending plane. These two parameters, together with the length of the two adiabatic tapers at the input and output of the bend, have been used as optimization domain.

The outcomes of the optimization are shown in Figure 4.26 in terms of bend efficiency, together with a side enlargement in dB scale of the values at the highest curvature radius. Standard curves with smooth wall behave like mode converters for the considered angle and waveguide radius. Among the alternatives taken into consideration, corrugated waveguides stand out as the most promising option with efficiencies ranging from 90% at a curvature radius of 200 mm to 99% at 1 m. Such results suggest that a minimum curvature radius of 1 or 0.8 m can be attained at most. The major drawbacks of corrugated waveguide are their weight and cost, which are significantly

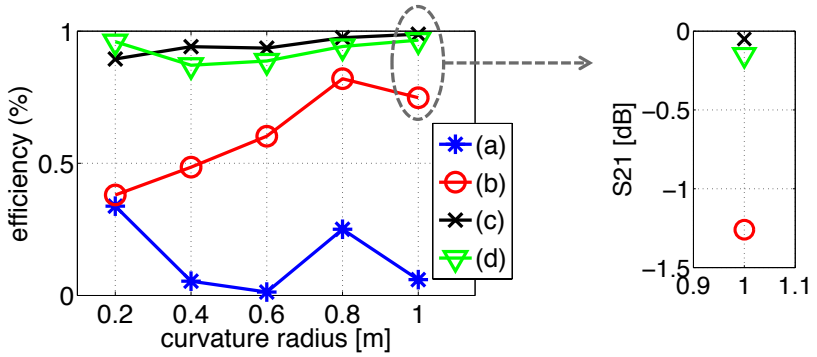

Figure 4.26: Comparison of the TE_{01} transmission efficiency for smooth-wall (a), shaped (b), corrugated (c) and elliptical (d) bent waveguides.

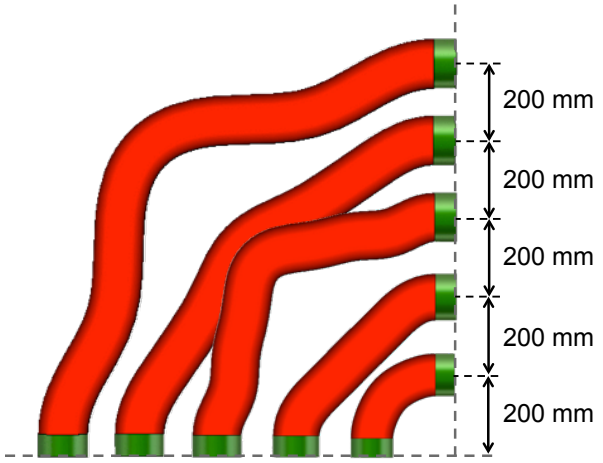

Figure 4.27: Arrangements of the bends with optimized curvature profiles for an inter-axis distance of 200 mm between waveguides.

raised by the presence of grooves. In comparison to a smooth-wall waveguide, corrugations require higher conductor thickness, i.e. few millimeters more than the corrugation depth or an even larger margin in the case of pressurized waveguides to avoid deformations. Bends with elliptical cross-section also exhibit good results, but they present the disadvantage of requiring two transitions for each curve. Moreover the higher the eccentricity, the higher the intensity of the electric field along the shorter axis.

In addition to the RF performance and issues like manufacturability, weight, etc., an important factor to be considered is the possibility of assembling the curves side-by-side in the waveguide beam going from the generators to the antenna. This is a major concern when using the approach of Fig. 4.23b adopted in ITER. As example, bends with profiled curvature

could not be arranged side-by-side with a pitch of 200 mm, but their minimum spacing depends on their profile. For each 0-th order curvature radius, the optimum values of the coefficients change, leading to different, quite convoluted shapes that overlap as depicted in Fig. 4.27. As for the other bends, different curvature radii always lead to different optimal dimensions, but without implying integration problems. For the considered geometries, optimized corrugations never exceeded 10 mm, thus laying behind the flanges, while, as regards to elliptical waveguides, the situation is slightly more critical because, in some cases, the cross-sections of adjacent vertical waveguides come almost to touch each other.

Bend based on corrugated waveguides

Two alternative configurations of bend with corrugated waveguide have been also compared. As shown in Fig. 4.28a, they have either ring- or radial-type corrugations, which have been optimized for different curvature radii, assuming that, along the waveguide axis, corrugation width and distance are equal. The geometry with the lowest bending radius was optimized with the two-steps approach previously described, whereas only a local optimizer was run for next configurations, whose curvature radius progressively increases with steps of 37 mm. The Trust Region Framework algorithm is launched within a close neighbourhood of the optimal point found for the last optimized geometry.

Results are plotted in Fig. 4.28b showing that efficiencies higher than 97% cannot be achieved for bending radii smaller than 800 mm. The two configurations exhibit almost identical performance in terms of efficiency, so that the choice between the two options is mainly dictated by their ease of manufacturing.

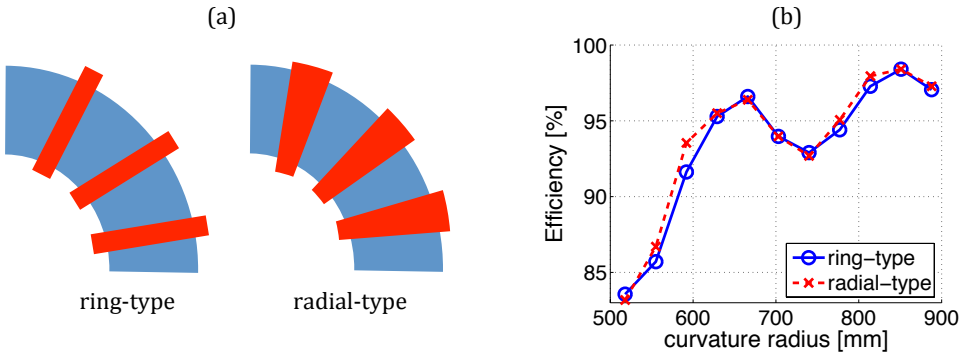

Figure 4.28: (a) Corrugation with constant width (ring-type) and with constant angular width (radial-type); (b) transmission efficiency of bends with different kinds of corrugations.

4.3.3 Converters

Assuming the use of 5 GHz, 500 kW, CW klystrons with output in WR187 and of RF windows with input in WR229, two converters are required to pass from the $TE^{\square}_{10}$ mode in rectangular waveguide to the TE°_{01} mode in circular waveguide at the beginning of the MTL and to perform the inverse transformation at its end. The combiners for the double output of the klystron into a single WR187 have been already developed

Possible candidates to attain the required conversion are the King-type,

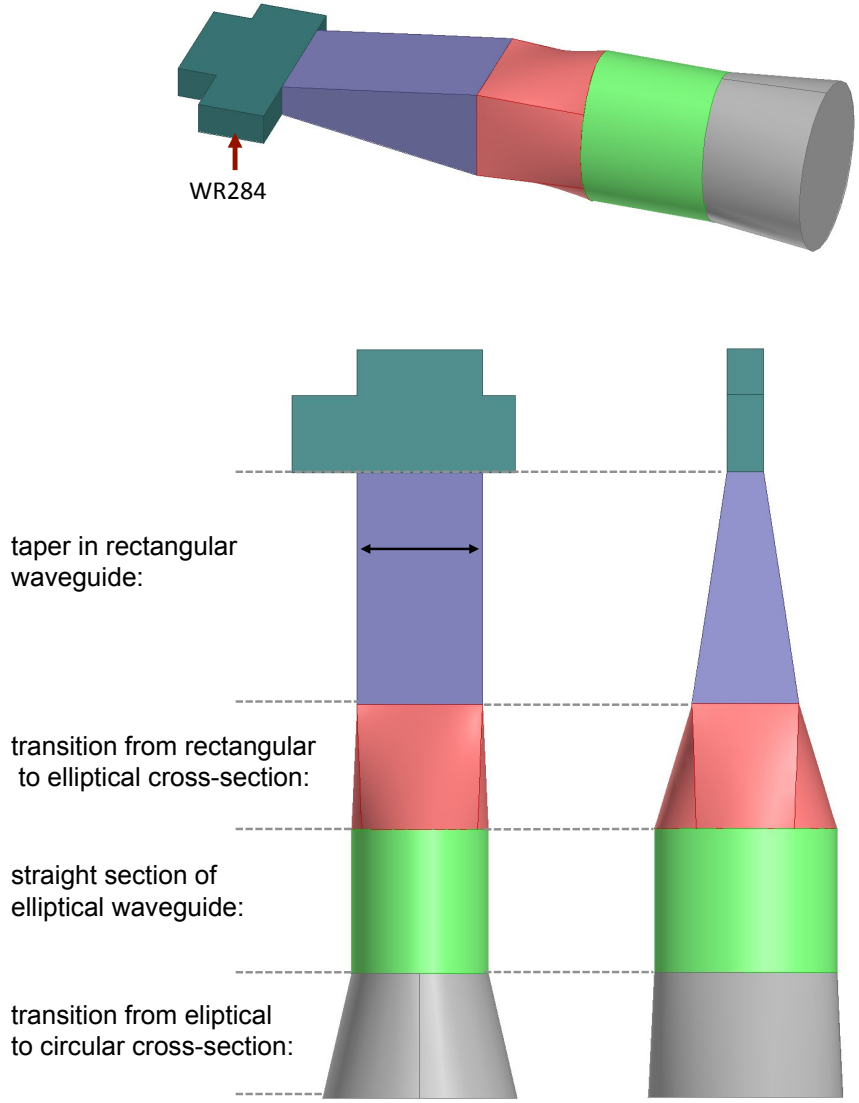

Figure 4.29: Geometry of the $TE^{\square}_{10}$ to TE°_{01} mode converter.

the Southworth-type, the coaxial wrap, the modified Southworth-type and the Marie converters. With the intent of reducing component size, a combination of different approaches, consisting of a right-angle step and a gradual transition from rectangular to circular waveguide passing through an elliptical cross-section, has been analysed. The geometry is shown in Fig. 4.29. After an intense optimization, acceptable performance was attained with a relatively short device (total length ∼0.57 m), showing the feasibility of this concept. Only the case with the WR229 was considered because, at the klystron output, the transition from WR187 to WR229 can be realized with an adiabatic taper. In such a way, a single bi-directional converter can be employed at both the beginning and the end of the MTL.

The CEA-ENEA-IPR proposal

A joint activity between ENEA, CEA and IPR was proposed for the development of two converters and a 90 deg corrugated bend to be tested at high power [210]. The task is aimed at verifying the technological readiness of such components of the MTL for reactor-relevant LH systems and providing a benchmark for the employed RF design tools. The prototypes, to be designed (ENEA), manufactured (IPR) and tested (CEA) up to 600 kW for 1000 s, are scaled mock-ups at 3.7 GHz, a frequency that allows the use of test facilities available at CEA-Cadarache. The main specifications are

- I/O interfaces: at one side, WR284 (72.136 x 34.036 mm^2) operating with the TE_{10} mode; at the other side, circular waveguide with a diameter of 181.24 mm. The latter value is obtained by multiplying the diameter of the C16 standard waveguide (134.112 mm) for the scaling factor 5/3.7 and rounding the result (90.6162 mm) to the 2nd decimal digit.
- RF generator: klystron TH2103C [211], frequency = 3700 ± 2.5 MHz.
- Curvature radius ≤ 1500 mm; a trench of 2200 mm in the experimental layout sets an upper bound to the available space for the components under test.
- Materials: bend in ETP copper ($\sigma = 58$ MS/m), converters in aluminium ($\sigma = 35.6$ MS/m).

Two commercial softwares have been adopted for the design: CST MWS 2014 and HFSS v.13, exploiting symmetry planes.

With reference to the converter design, the following objectives have been considered:

- conversion efficiency $\geq 98\%$ from $TE_{10}^{\square}$ to TE_{01}° ($S_{21} > -0.09$ dB);
- reflection coefficients ≥ -30 dB (VSWR < 1.07).

Results from the different electromagnetic solvers are coherent. The four corners of the rectangular waveguide at the input junction (Fig. 4.29) can be rounded to reduce the risk of voltage breakdown without affecting RF performance. The geometrical parameters have been optimized to achieve a conversion efficiency of −0.087 dB; average losses for an input power of 600 kW are 967 W and the spurious mode with highest amplitude is the TE°_{41} (−18.7 dB).

As regards the bend, a simulated transmission efficiency of at least 99% ($S_{21} > 0.0436$ dB) was chosen as target. Such performance was found to be achievable only with a bending radius of 1400 mm or larger, which also assures very low reflection of the TE_{01} mode. Some spurious modes are also reflected back, but, in the optimized configuration, the total power coming back to the input port is always lower than −30 dB. A higher level of spurious modes is instead delivered at the output port, mostly in the form of the TE_{11}, TM_{11} and TE_{41} modes; the latter in particular is around −24 dB according to CST MWS. HFSS predictions of transmission efficiency are more pessimistic than CST MWS: 98.2% against 99.8%. Losses calculated with CST MWS are lower than HFSS results, while predicted maximum E-field is rather similar. Anyhow, predicted values are acceptable.

Ohmic losses cause heating by Joule effect, which, in turn, causes the mechanical deformation of the curve. This phenomenon has been approximately investigated with CST MWS by using a conservative convective heat transfer coefficient of 4 W/(m^{2}K) for solid curves with a copper thickness of 5 mm, assuming an ambient temperature of 293 K. Thermal conductivities of air and copper are 0.026 and 401 W/(m·K), respectively. Outward boundary conditions for the heat flux were assigned to the domain box except for the faces in correspondence of the input/output waveguides, where

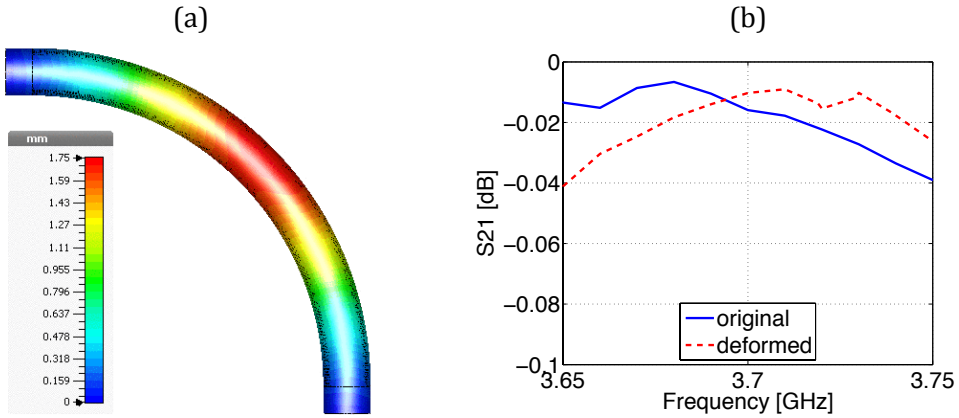

Figure 4.30: Magnitude of the mechanical displacement (a) and TE_{01} transmission (b) with and without deformation due to heating by ohmic losses.

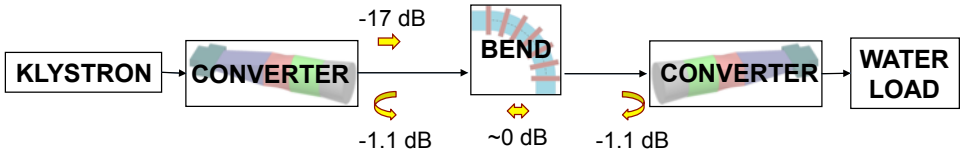

Figure 4.31: Layout of a high-power test bench; values refer to the TE_{41}.

adiabatic conditions were adopted. The mechanical deformation associated with the temperature increase is calculated keeping fixed the positions of the input/output ports. The displacement is essentially radial with the magnitude depicted in Fig. 4.30, where the transmission efficiency recalculated in the deformed structure is also given.

The onset of trapped mode resonances instead represents a major concern of the experimental test setup, the schematic layout of which is given in Fig. 4.31. If a mixture of TE_{01} (-0.09 dB) and TE_{41} (-18.7 dB) is considered at the input of the bend, the variation of maximum electric field and ohmic loss is actually negligible, even considering the worst phasing conditions between the two modes. Nevertheless the TE_{41} passes almost intact across the bend ($S_{21} \approx -0.058$ dB) and undergoes high reflection at the output converter ($S_{11} \approx -1.1$ dB). The net effect is that the spurious mode travels back and forth across the bend setting up a standing wave pattern. The end-to-end microwave system (two converters + bend) behaves like a resonator for the TE_{41} mode, the amplitude of which grows till a saturation level set by the reflectivity of the converters. This phenomenon, known as trapped mode resonance, may be dangerous since it entails an increase of the maximum electric field as well as of ohmic losses.

If the end-to-end microwave system (two converters + bend) is modelled like a simple resonator, the maximum electric field can be estimated as

$$E^{\max} = \frac{E_0}{1-r} \qquad \text{with} \quad r = \sqrt{R \cdot R}$$

where E_0 is the initial E-field amplitude injected by the first converter and R is reflectivity of the converter for the TE_{41} mode. By replacing previous numbers, an amplification $E_{\max}/E_0$ of 4.47 is obtained. This value could be reduced by employing a mode filter, e.g. inserted between the bend and a converter. To a first approximation, if the mode filter attenuates the TE_{41} mode by $A = 0.4$, we have

$$r = \sqrt{R \cdot A \cdot R \cdot A}$$

and the field amplification reduces to 1.45, i.e. a factor 3 lower than without filter. Hence mode filters can attain significant effects even without achieving total absorption and their employment along the transmission lines of reactor-relevant LH systems is required.

4.3.4 Mode filters

Waveguides based on corrugations, partially filled with absorbing material, must be preferred to damp unwanted modes leaving untouched the inner part of the waveguide. The geometry of such a filter for circular waveguide is sketched in Fig. 4.32. Corrugations are defined by four parameters: width w_c, period p_c, depth of their vacuum region h_{cv} and absorber depth h_{ca}. The first two parameters are essentially determined by a trade-off between two counteracting needs, namely maximizing the absorption of unwanted modes and leaving the TE_{01} mode as untouched as possible. The latter two dimensions instead mostly affect the damping behaviour of the device.

The LH systems of present-day tokamaks are not equipped with mode filters because they have shorter and essentially straight transmission lines: the lengths of the MTL are about 20, 30 and something more than 30 meters in Tore Supra, FTU and JET, respectively. Despite the increasing attention recently paid to these components [212, 209], the scientific literature on the topic is scarce and the lack of specific tools as well as simple design formulas is still an issue.

An R&D activity is needed, aimed at (i) investigating the peak and average power handling capability of these components and (ii) studying the relation between RF performances and corrugation geometrical dimensions. As for the former item, a multi-physics analysis with COMSOL Multiphysics has been carried out, showing that, in stationary conditions and natural convection, excessively high temperatures (> 1000 K) are reached for a small amount of power (1%) carried by spurious modes. Heat exchangers and forced cooling are thus mandatory to dissipate microwave heating.

Concerning the second task, a good figure-of-merit is the absorption of a given mode when passing through the filter; the full scattering matrix has to be computed to derive the absorption. A modelling activity has been thus undertaken, following the modal approach of section 3.4, to overcome intrinsic limitations of tools based on volumetric electromagnetic solvers.

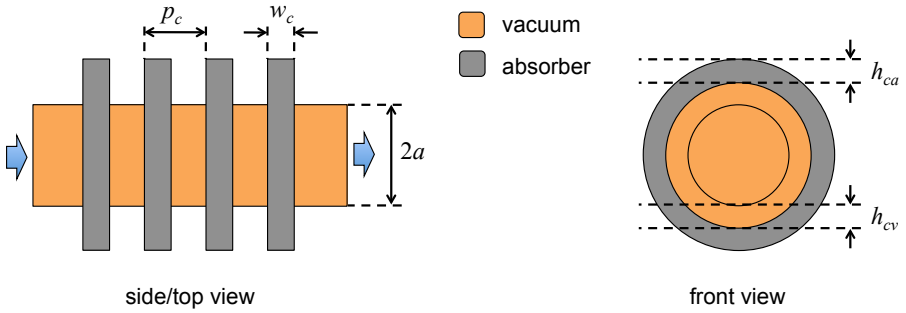

Figure 4.32: Geometry of a mode filter for circular waveguide operating with the TE_{01} mode.

Materials

The choice of the absorbing materials that partially fills filter corrugations can be reasonably addressed toward silicon carbide, as proposed for the same component of the ITER LHCD system. silicon carbide (SiC) is a non-oxide ceramic. The high thermal conductivity coupled with low thermal expansion and high strength gives this material exceptional thermal shock resistant qualities. Furthermore it experiences no phase transitions that would cause discontinuities in thermal expansion: sublimation temperature is approximately 2700 °C. It also has other exclusive properties such as high hardness, chemical stability, oxidation resistance, high erosion resistance, high electric field breakdown strength and high maximum current density. All of these quantities make SiC a perfect candidate for high power, high temperature electronic devices: it can be used up to 1600 °C [213, 214].

The employment of SiC as microwave absorber stands out to be a well-documented application within the scientific literature [215, 216]. Pure silicon carbide actually presents low dielectric properties that give barely the capacity to dissipate microwave power: $\varepsilon_r = 8.32$ and $\tan\delta = 0.12$ at 10 GHz as reported in [217]. This limit can be overcome by using diverse techniques such as surface modification by electroless nickel plating [218] and doping procedures by combustion [219] or laser-induced gas-phase reaction [220]. Synthesized nano-SiC power can indeed enhance real and imaginary electric permittivity to a great extent. Here, SiC is assumed to have $\varepsilon_r = 13.5$ and $\tan\delta = 0.44$, being the same dielectric properties used in [160]. The remaining part of the filter can be made of copper.

Modelling

The starting point consists in expressing the fields in the four regions indicated in Fig. 4.33 with Roman numerals. The first two are homogeneous semi-infinite circular waveguides, where the electromagnetic field can be

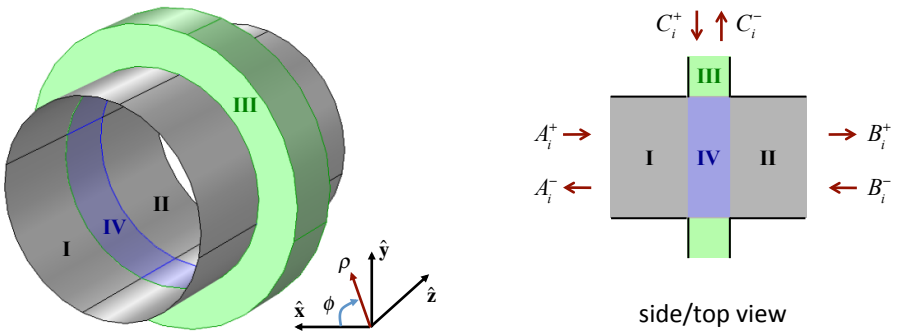

Figure 4.33: Geometry of a circular waveguide with a concentrical junction.

written like a summation of TE and TM modes similarly to (3.21) but using cylindrical coordinates:

$$\begin{aligned}\mathbf{E}^{\mathrm{I,II}} &= \sum_{i=1}^{N_1} \mathrm{f}_i^{\mathrm{I,II}}(z)\,\mathbf{e}^{\mathrm{I}}_{\mathbf{t}_i}(\rho,\phi) + \mathrm{g}_i^{\mathrm{I,II}}(z)\,\mathbf{e}^{\mathrm{I}}_{\mathbf{z}_i}(\rho,\phi) \\ \mathbf{H}^{\mathrm{I,II}} &= \sum_{i=1}^{N_1} \mathrm{g}_i^{\mathrm{I,II}}(z)\,\mathbf{h}^{\mathrm{I}}_{\mathbf{t}_i}(\rho,\phi) + \mathrm{f}_i^{\mathrm{I,II}}(z)\,\mathbf{h}^{\mathrm{I}}_{\mathbf{z}_i}(\rho,\phi)\end{aligned} \tag{4.5}$$

The functions $\mathrm{f}(z)$ and $\mathrm{g}(z)$ are defined as in (3.22) and (3.23) with w_c in place of a_c, while the field components and the eigenfunctions are given in (3.24) and (2.42), respectively.

In region III, the electromagnetic field can be written as a summation of TE^z and TM^z modes, corresponding to direct and reflected radial waves, i.e. waves that travel in the $\pm\rho$ direction. The field variation in radial direction is expressed with the j-th order Hankel functions of the 1st and 2nd kind, while the propagation constants are

$$\beta_\rho = \pm\sqrt{\omega^2\mu\varepsilon - \left(\frac{p\pi}{w_c}\right)^2} \tag{4.6}$$

Modes are defined by the following potential functions

$$F_{zqp} = \left[C^+_{qp}H^{(1)}_q(\beta_\rho\rho) + C^-_{qp}H^{(2)}_q(\beta_\rho\rho)\right]\cos(q\phi)\sin\left(\frac{p\pi}{w_c}z\right) \tag{4.7}$$

for TE modes with $q = 1, 2, 3, \ldots$ and $p = 1, 2, 3, \ldots$, and

$$A_{zqp} = \left[C^+_{qp}H^{(1)}_q(\beta_\rho\rho) + C^-_{qp}H^{(2)}_q(\beta_\rho\rho)\right]\cos(q\phi)\cos\left(\frac{p\pi}{w_c}z\right) \tag{4.8}$$

for TM modes with $q = 0, 1, 2, \ldots$ and $p = 0, 1, 2, \ldots$. By inserting the latter equations inside the general formulas relating fields to vector potentials [221] and introducing proper normalization factors, the expression of the electromagnetic field in region III is obtained. By characterizing the equations with the data of an absorbing material in place of vacuum, the fields in the lossy dielectrics can be also written.

For region IV, according to the resonator method, the superposition of three suitably chosen standing wave solutions is considered:

$$\begin{aligned}\mathbf{E}^{\mathrm{V}} &= \mathbf{E}^{\mathrm{V}(1)} + \mathbf{E}^{\mathrm{V}(2)} + \mathbf{E}^{\mathrm{V}(3)} \\ \mathbf{H}^{\mathrm{V}} &= \mathbf{H}^{\mathrm{V}(1)} + \mathbf{H}^{\mathrm{V}(2)} + \mathbf{H}^{\mathrm{V}(3)}\end{aligned} \tag{4.9}$$

where the sets are defined similarly to (3.25).

Once the field expressions for all the four regions are available, the tangential components of their electric and magnetic fields have to be matched

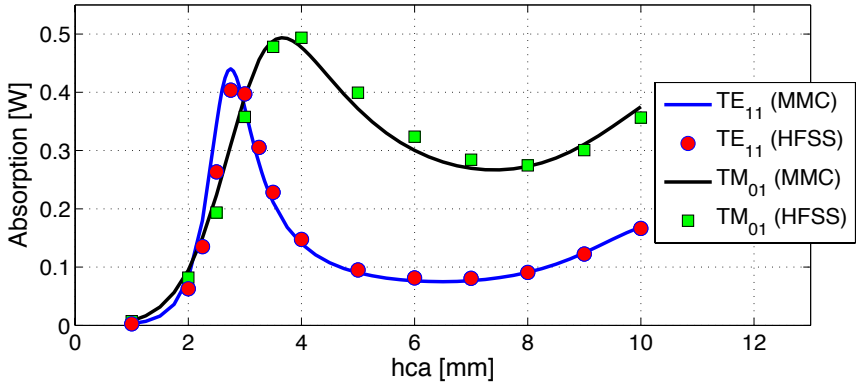

Figure 4.34: Absorption versus h_{ca} for two modes at 5 GHz in a filter with one corrugation, $a = 25$ mm, $w_c = 5$ mm, $h_{cv} = 10$ mm, input power = 1 W per mode, SiC as absorber.

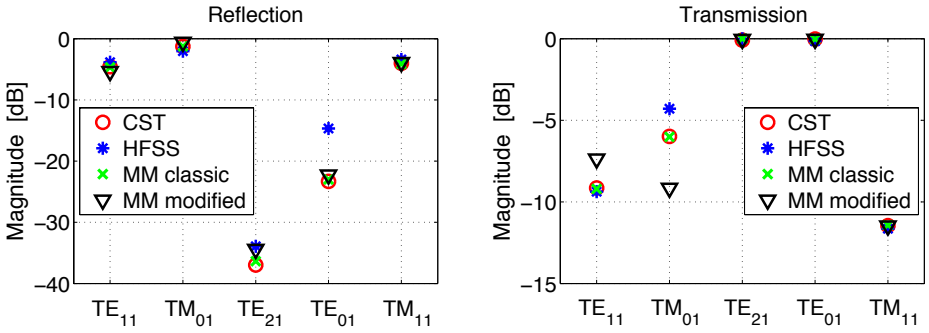

Figure 4.35: Comparison between the reflection and transmission self-terms of the scattering matrix, computed by different tools at 5 GHz for the geometry of Fig. 3.5.

along the three boundary interfaces. The enforcement of mode orthogonality allows obtaining a linear system, from which the relationship between the modal amplitude coefficients of the three semi-infinite waveguides can be derived to result in the generalized scattering matrix of the structure. If the corrugation ended with a conductor or it were partially filled with an absorber, further equations would be added to the linear system.

The aforementioned model has been coded in MATHEMATICA and validated against other tools for simple structures working at 5 GHz. A preliminary benchmark with HFSS has been carried out in terms of absorbed power, considering a circular waveguide with $a = 25$ mm and a single corrugation with $w_c = 5$ mm and $h_{cv} = 10$ mm. The waveguide only supports two propagating modes: the TE_{11} and the TM_{01}. The absorber depth h_{ca} has been varied; the comparison in Fig. 4.34 reveals a very good agreement.

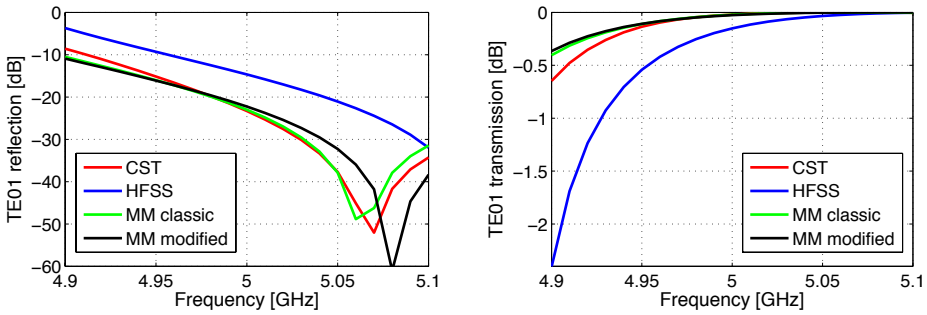

Figure 4.36: Comparison between the frequency behaviour of S_{11} and S_{21} for the TE_{01} mode, computed by different tools for the geometry of Fig. 3.5.

Tool	**# cores**	**user time [s]**
CST (frequency solver)	2	11344
HFSS v.11	1	4443
Standard mode-matching	1	230
Modified mode-matching	1	2850

Table 4.9: Solver times [s].

Then the cascade of scattering matrices has been coded and the test geometry of Fig. 3.5 has been simulated. The comparison has been carried out in terms of the scattering parameters $S_{1:i,1:i}$ and $S_{2:i,1:i}$, namely by feeding a port with the i-th mode and looking at both ports the wave amplitude of the same mode. The outcome is shown in Fig. 4.35: apart from a couple of transmission coefficients, the proposed method, indicated as "MM modified", presents a good agreement with the most reliable results, i.e. the ones from the standard mode-matching technique and CST MWS. The latter always agree, while HFSS simulations stopped without reaching convergence after 15 adaptation passes. The cross-terms of the scattering matrix, namely the coupling between modes in reflection and transmission, were not compared because they are less significant.

A frequency sweep has been also performed with the same tools. Results are overlapped in Fig. 4.36 for the reflection and transmission coefficients of the TE_{01} mode. HFSS misses the resonance that the other tools find at slightly different frequencies; indeed its calculations were stopped after 15 adaptive steps without reaching the convergence. A denser or adaptive sampling of the frequency band would significantly improve the curve, but the constant frequency step of 10 MHz was chosen to better compare the computation times of the tools. Relevant data, obtained with an INTEL® Core™ 2 Duo at 2.53 GHz and a RAM of 4 GB, are reported in Table

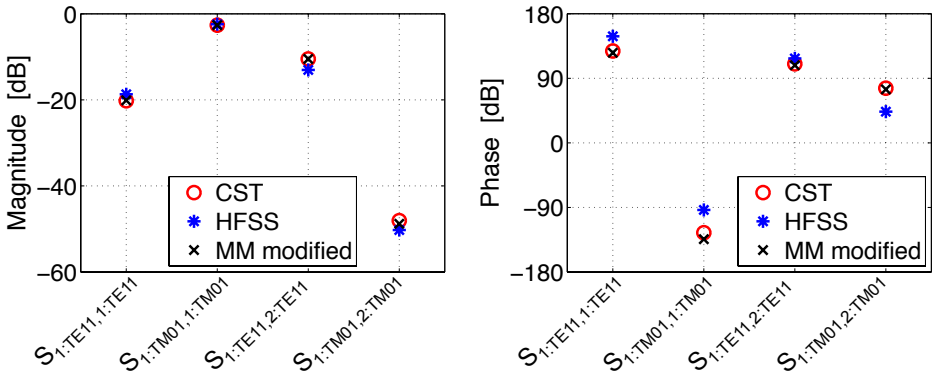

Figure 4.37: Comparison between the scattering parameters $S_{(port):(mode),(port):(mode)}$, computed by different tools at 5 GHz for a filter with 4 corrugations and parameters as in Fig. 4.34.

4.9: modal approaches outrank volumetric solvers. Moreover they exhibit a better scaling with the electrical dimensions of the structure, looking very promising for larger geometries than the present example. The fastest technique is the standard mode-matching because the integrals in its formulation were put in closed form; nevertheless this method cannot be directly applied to dielectric-filled corrugations. The modified mode-matching can be used instead for mode filters; the code we used here can be greatly improved looking for a symbolic solution of the integrals to bypass their numerical integration. In general, the development of a code allows possibilities of enhancement which are not allowed in commercial tools, like for example the parallelization or the seamless integration with advanced optimizers.

A last benchmark has been carried out using a geometry similar to the fist test of Fig. 4.34, but with 4 corrugations. The coupling between modes is negligible so only the self-terms of the scattering matrix have been compared in terms of both magnitude and phase. As shown in Fig. 4.37, a very good agreement has been obtained, mostly between CST MWS and our method, whereas HFSS presents minor deviations, despite the convergence was reached for this structure. The mean square errors relevant to the amplitude of the scattering parameters of the 4×4 matrix are 5.6×10^{-7} and 5.6×10^{-3} for CST MWS and HFSS, respectively.

The validation was aimed at proving the viability of the modal approach for mode filters based on corrugated circular waveguides. The purpose has been accomplished, but it is worth pointing out that the modal analysis is not intended to utterly replace commercial CADs. The latter are multi purpose simulation tools preserving a larger flexibility in drawing geometries as well as high accuracy and reliability; they are mostly useful after a preliminary optimization for fine adjustments.

Conclusions

We have considered both radiating and guiding structures, where the electromagnetic field is expressed through the eigenmodes of the wave equation in those specific geometrical systems. Although the structures that have been considered present substantial differences and are conceived for distinct applications, they share the common feature of being studied taking full advantage of their modal behaviour. The latter has been successfully exploited to build up effective tools for the analysis and design of these devices and to acquire insight on their physical mechanisms.

More precisely, as far as the design of antennas working with lattice modes is concerned, the eigenfunctions of the Bloch waves have been considered rather than their eigenvalues as usually done so far. The key concepts of these antennas have been illustrated by referring to the square lattice of dielectric rods that, in its two-dimensional approximation, can be effectively addressed by means of a cylindrical wave approach. Antennas working with modes in either the dielectric or the air band have been presented, demonstrating that lattices with very low index contrast can be profitably employed if the electric field pattern of particular eigenmodes is exploited in a proper fashion. Common materials of 3D printers such as ABS, can be thus used to realize cheap, easy-to-fabricate periodic structures, able to shape the emission of primary radiators with low directivity.

Despite such materials exhibit high loss tangent, antennas relying on the eigenmodes of the air band achieve high radiation efficiency, being the electric field mostly localized outside the dielectric cylinders. This property has been highlighted by comparing this kind of structures with the resonator antennas for both triangular and square arrangements of Alumina rods. In this benchmark, two-dimensional and finite-height geometries have been considered, showing that the method based on Bloch waves is more directive for compact structures, whereas the other method is more suitable to low-profile configurations.

In EBG antennas based on Bloch waves, the position of the source plays a major role. The amplitude of the excited modes is proportional to the eigenfunction of their electric field taken at the point where the radiator is placed. A code implementing the PWE method has been enhanced to address these mechanisms. When working at the lower edge of the air band in

square lattices of dielectric cylinders in a vacuum, two degenerate modes can propagate; their excitation can be controlled by playing with the position of the source within the primitive cell of the lattice. Two configurations of a dual-feed antenna based on this behaviour have been analysed in terms of radiation and electrical properties. The EBG structure improves the radiation performance of the primary radiators while keeping them rather uncoupled, although they are less than a wavelength apart. Possible future developments of this type of antenna are the study of TE modes, triangular lattices or complementary structures with air holes in a dielectric background.

With reference to metallic waveguides, we have addressed extreme operational regimes, where the number of propagating modes is higher than usual. The performance of these devices is hard to be predicted with the common algorithms of computational electromagnetics that mesh the simulation domain. We have thus reported the solid mathematical framework that is at the basis of two successful modal approaches, i.e. the coupled-mode theory and the mode-matching method. To the best of our knowledge, both techniques have been enhanced to perform calculations beyond the state of the art.

The coupled-mode theory can effectively deal with variations in the waveguide cross-section under the approximation of small perturbation compared to waveguide size and wavelength. This approach is suitable to study Bragg reflectors and cavities based on such mirrors in highly oversized guiding structures. In particular, a rigorous calculation of diffractive and ohmic quality factors is described; it provides more reliable and accurate results in comparison to approximate formulas reported in literature.

The mode-matching method can perform full-wave calculations of the Bragg resonator if single excitation modes are considered, but it is less suitable than the coupled-mode theory when beat-wave converters must be analysed. We have mostly proven its effectiveness, in combination with the resonator technique, to address corrugation-based mode filters. The calculation of the scattering parameters reduces to the evaluation of the closed-form expressions of the surface integrals and some matrix algebra operations. Compared to a commercial solver, the semi-analytical modal approach allows a shorter execution time, facilitating the use of global optimization techniques such as the PSO as shown with several examples. Simple models of a corrugation have been built up to acquire a better understanding of the physical phenomena that take place and to provide guidelines for designers. Slot position and cross-section determine the excitation of the corrugations, while their behaviour as absorbers can be expressed through an analytical matrix term. A careful investigation of this term, aimed at identifying new, enhanced configurations, represents a possible continuation of this work.

Finally some fields of application where previous approaches are useful have been presented. In details, the development of a 250 GHz cyclotron auto-resonance maser has been considered by detailing the design of the

resonant cavity based on Bragg reflectors. The dependences on geometrical dimensions and mode order have been clarified before choosing for the project a resonator with total length of 690 mm, diameter of 15 mm and Q-factor of 4000 for the TE_{82} mode.

Then the technological needs and issues, associated with the development of a lower hybrid (5 GHz) system for reactor-relevant tokamaks, have been discussed. The materials of the launcher, facing the harshest nuclear environment, represent the most critical engineering issues. Some components of the main transmission lines also require substantial research and development, despite significant steps in these direction have been already performed and presented in this dissertation. In particular some prototypes of converters and bends must be built and tested at high-power, while mode filters still need the enhancement of their numerical modelling.

Symbols and Acronyms

2D	two-dimensional
3D	three-dimensional
ABS	acrylonitrile butadiene styrene
CAD	computer-aided design
CARM	cyclotron auto-resonance maser
CD	current drive
CEA	commissariat à l'energie atomique et aux energies alternatives
CFC	carbon-fibre-composites
CVD	chemical vapour deposition
CW	continuous wave
CWA	cylindrical wave approach
DEMO	demonstration power plant
E-field	electric field
EBG	electromagnetic bang-gap
EC	electron cyclotron
ECCD	electron cyclotron current drive
ECRF	electron cyclotron resonance frequency
ECRH	electron cyclotron resonance heating
EFBC	electric field boundary condition
EFDA	European fusion development agreement
ELM	edge-localized mode
ENEA	Italian national agency for new technologies, energy and sustainable economic development
ENZ	epsilon near zero
ETP	electrolytic-tough-pitch
FAM	full active multijunction
FDTD	finite-difference time-domain
FEM	finite element method
FIT	finite integration technique
FTU	Frascati tokamak upgrade

FWHM	full width half maximum
GSM	generalized scattering matrix
H-field	magnetic field
H&CD	heating and current drive
HPBW	half-power beam width
HVPS	high voltage power supply
I/O	input and output
IBZ	irreducible Brillouin zone
ICRF	ion cyclotron resonance frequency
IFMIF	international fusion materials irradiation facility
IPR	Indian institute for plasma research
ITER	international tokamak experimental reactor
LH	lower hybrid
LHCD	lower hybrid current drive
MASER	microwave amplification by stimulated emission of radiation
MFBC	magnetic field boundary condition
MHD	magnetohydrodynamics
MM	mode-matching
MTL	main transmission line
MWS	MICROWAVE STUDIO
NWL	neutron wall loading
OFE	oxygen-free electronic
PAM	passive active multijunction
PEC	perfect electric conductor
PI	parametric instability
PMC	perfect magnetic conductor
PWE	plane wave expansion
R&D	research and development
RF	radio-frequency
SLL	side lobe level
SOL	scrape-off layer

Bibliography

[1] J. D. Joannopoulos, S. G. Johnson, J. N. Winn, and R. D. Meade, *Photonic Crystals: Molding the Flow of Light*, 2nd ed. Princeton University Press, 2008.

[2] E. Yablonovitch, "Inhibited spontaneous emission in solid-state physics and electronics," *Phys. Rev. Lett.*, vol. 58, no. 20, pp. 2059–2062, May 1987.

[3] P. de Maagt, R. Gonzalo, Y. C. Vardaxoglou, and J.-M. Baracco, "Electromagnetic bandgap antennas and components for microwave and (sub)millimeter wave applications," *IEEE Trans. Antennas Propag.*, vol. 51, no. 10, pp. 2667–2677, Oct. 2003.

[4] K. Yasumoto, *Electromagnetic Theory and Applications for Photonic Crystals*, ser. Optical Science and Engineering. Taylor & Francis, 2010.

[5] E. R. Brown, C. D. Parker, and E. Yablonovith, "Radiation properties of a planar antenna on a photonic-crystal substrate," *J. Opt. Soc. Am. B*, vol. 10, no. 2, pp. 404–407, Feb. 1993.

[6] W. Leung, R. Biswas, S.-D. Cheng, M. Sigalas, J. McCalmont, G. Tuttle, and K. M. Ho, "Slot antennas on photonic band gap crystals," *IEEE Trans. Antennas Propag.*, vol. 45, no. 10, pp. 1569–1570, Oct. 1997.

[7] M. Thèvenot, A. Reineix, and B. Jecko, "A dielectric photonic parabolic reflector," *Microw. Opt. Tech. Lett.*, vol. 21, no. 6, p. 411414, Jun. 1999.

[8] R. Coccioli, F.-R. Yang, K.-P. Ma, and T. Itoh, "Aperture-coupled patch antenna on UC-PBG substrate," *IEEE Trans. Microw. Theory Tech.*, vol. 47, no. 11, pp. 2123–2130, Nov. 1999.

[9] F. Yang and Y. Rahmat-Samii, "A low profile circularly polarized curl antenna over an electromagnetic bandgap (EBG) surface," *Microw. Opt. Tech. Lett.*, vol. 31, no. 4, p. 264267, Nov. 2001.

[10] ——, "Reflection phase characterizations of the EBG ground plane for low profile wire antenna applications," *IEEE Trans. Antennas Propag.*, vol. 51, no. 10, pp. 2691–2703, Oct. 2003.

[11] ——, *Electromagnetic Band Gap Structures in Antenna Engineering*, ser. The Cambridge RF and Microwave Engineering Series. Cambridge University Press, 2008.

[12] J.-C. Iriarte, I. Ederra, R. Gonzalo, Y. Brand, A. Fourmault, Y. Demers, L. Salgetti-Drioli, and P. de Maagt, "EBG superstrate array configuration for the WAAS space segment," *IEEE Trans. Antennas Propag.*, vol. 57, no. 1, pp. 81–93, 2009.

[13] A. Weily, L. Horvath, K. Esselle, B. Sanders, and T. Bird, "A planar resonator antenna based on a woodpile EBG material," *IEEE Trans. Antennas Propag.*, vol. 53, no. 1, pp. 216–223, Jan. 2005.

[14] S. Enoch, G. Tayeb, P. Sabouroux, N. Guérin, and P. Vincent, "A metamaterial for directive emission," *Phys. Rev. Lett.*, vol. 89, p. 213902, Nov. 2002.

[15] M. Qiu and S. He, "High-directivity patch antenna with both photonic bandgap substrate and photonic cover," *Microw. Opt. Tech. Lett.*, vol. 30, no. 1, pp. 41–44, Jul. 2001.

[16] H.-Y. Yang, "Finite difference analysis of 2-D photonic crystals," *IEEE Trans. Microw. Theory Tech.*, vol. 44, no. 12, pp. 2688–2695, Dec. 1996.

[17] K. Elmahgoub, F. Yang, and A. Elsherbeni, *Scattering Analysis of Periodic Structures Using Finite-Difference Time-Domain Method*, ser. Synthesis lectures on computational electromagnetics. Morgan & Claypool Publishers, 2012.

[18] R. Coccioli, T. Itoh, and G. Pelosi, "A finite element-generalized network analysis of finite thickness photonic crystals," in *IEEE MTT-S*, vol. 1, Jun. 1997, pp. 195–198.

[19] M. N. Vouvakis, Z. Cendes, and J.-F. Lee, "A FEM domain decomposition method for photonic and electromagnetic band gap structures," *IEEE Trans. Antennas Propag.*, vol. 54, no. 2, pp. 721–733, Feb. 2006.

[20] R. Garnier, A. Barka, and O. Pascal, "FEM eigenmode solver for EBG band diagram computation," in *Proc. of the 5th European Conference on Antennas and Propagation (EUCAP)*, Apr. 2011, pp. 650–654.

[21] J. B. Pendry and A. MacKinnon, "Calculation of photon dispersion relations," *Phys. Rev. Lett.*, vol. 69, pp. 2772–2775, Nov. 1992.

[22] A. Reynolds, U. Peschel, F. Lederer, P. Roberts, T. Krauss, and P. de Maagt, "Coupled defects in photonic crystals," *IEEE Trans. Microw. Theory Tech.*, vol. 49, no. 10, pp. 1860–1867, Oct. 2001.

[23] M. Hosseini, D. Klymyshyn, and G. Wells, "A circuit model for the design of self-excited EBG resonator antennas with miniaturized unit cells," *IEEE Antennas Wireless Propag. Lett.*, vol. 13, pp. 1279–1283, 2014.

[24] S. Martin, I. Martinez, J. Turpin, D. Werner, E. Lier, and M. Bray, "The synthesis of wide- and multi-bandgap electromagnetic surfaces with finite size and nonuniform capacitive loading," *IEEE Trans. Microw. Theory Tech.*, vol. 62, no. 9, pp. 1962–1972, Sep. 2014.

[25] K. Yasumoto, H. Toyama, and T. Kushta, "Accurate analysis of two-dimensional electromagnetic scattering from multilayered periodic arrays of circular cylinders using lattice sums technique," *IEEE Trans. Antennas Propag.*, vol. 52, no. 10, pp. 2603–2611, Oct. 2004.

[26] F. Frezza, L. Pajewski, and G. Schettini, "Characterization and design of two-dimensional electromagnetic band-gap structures by use of a full-wave method for diffraction gratings," *IEEE Trans. Microw. Theory Tech.*, vol. 51, no. 3, pp. 941–951, Mar. 2003.

[27] L. Pajewski, L. Rinaldi, and G. Schettini, "Enhancement of directivity using 2D-electromagnetic crystals near the band-gap edge: a full-wave approach," *Prog. Electromagn. Res.*, vol. 80, pp. 179–196, 2008.

[28] E. Lucas and T. Fontana, "A 3-D hybrid finite element/boundary element method for the unified radiation and scattering analysis of general infinite periodic arrays," *IEEE Trans. Antennas Propag.*, vol. 43, no. 2, pp. 145–153, Feb. 1995.

[29] C. Kyriazidou, H. Contopanagos, W. M. Merrill, and N. Alexpoulos, "Artificial versus natural crystals: effective wave impedance of printed photonic bandgap materials," *IEEE Trans. Antennas Propag.*, vol. 48, no. 1, pp. 95–106, Jan. 2000.

[30] M. Sarnowski, T. Vaupel, V. Hansen, E. Kreysa, and H. Gemuend, "Characterization of diffraction anomalies in 2-D photonic bandgap structures," *IEEE Trans. Microw. Theory Tech.*, vol. 49, no. 10, pp. 1868–1872, Oct. 2001.

[31] Martinez *et al.*, "Manufacturing tolerance analysis, fabrication, and characterization of 3-D submillimeter-wave electromagnetic-bandgap crystals," *IEEE Trans. Microw. Theory Tech.*, vol. 55, no. 4, pp. 672–681, Apr. 2007.

[32] CST Computer Simulation Technology AG, "CST MICROWAVE STUDIO," https://www.cst.com/.

[33] R. Collin, *Foundations for Microwave Engineering*, ser. IEEE Press Series on Electromagnetic Wave Theory. Wiley, 2001.

[34] MATLAB, *version 7.12.0 (R2011a)*. Natick, Massachusetts: The MathWorks Inc., 2011.

[35] L. Li, "Use of Fourier series in the analysis of discontinuous periodic structures," *J. Opt. Soc. Am. A*, vol. 13, no. 9, pp. 1870–1876, Sep. 1996.

[36] ——, "Fourier modal method for crossed anisotropic gratings with arbitrary permittivity and permeability tensors," *J. Opt. A–Pure Appl. Op.*, vol. 5, no. 4, p. 345, 2003.

[37] M. Abramowitz and I. A. Stegun, *Handbook of Mathematical Functions with Formulas, Graphs, and Mathematical Tables*, 9th ed. New York: Dover, 1964.

[38] V. Jandieri, K. Yasumoto, and Y. Liu, "Directivity of radiation of a dipole source coupled to cylindrical electromagnetic bandgap structures," *J. Opt. Soc. Am. B*, vol. 29, no. 9, pp. 2622–2629, Sep. 2012.

[39] COMSOL Inc., "COMSOL Multiphysics," https://www.comsol.it/.

[40] M. Thèvenot, C. Cheype, A. Reineix, and B. Jecko, "Directive photonic-bandgap antennas," *IEEE Trans. Microw. Theory Tech.*, vol. 47, no. 11, pp. 2115–2122, Nov. 1999.

[41] E. Arnaud, R. Chantalat, M. Koubeissi, T. Monediere, E. Rodes, and M. Thèvenot, "Global design of an EBG antenna and meander-line polarizer for circular polarization," *IEEE Antennas Wireless Propag. Lett.*, vol. 9, pp. 215–218, 2010.

[42] Y. Ge, K. Esselle, and T. Bird, "The use of simple thin partially reflective surfaces with positive reflection phase gradients to design wideband, low-profile EBG resonator antennas," *IEEE Trans. Antennas Propag.*, vol. 60, no. 2, pp. 743–750, 2012.

[43] F. Frezza, L. Pajewski, E. Piuzzi, C. Ponti, and G. Schettini, "Advances in EBG-resonator antenna research," in *International Symposium on Antennas and Propagation (ISAP)*, 2012, pp. 1301–1304.

[44] ——, "Radiation-enhancement properties of an X-band woodpile EBG and its application to a planar antenna," *International Journal of Antennas and Propagation*, vol. 2014, no. 5, 2014.

[45] H. Contopanagos, N. Alexopoulos, and E. Yablonovitch, "High-Q radio-frequency structures using one-dimensionally periodic metallic films," *IEEE Trans. Microw. Theory Tech.*, vol. 46, no. 9, pp. 1310–1312, Sep. 1998.

[46] C. Cheype, C. Serier, M. Thèvenot, T. Monédière, A. Reineix, and B. Jecko, "An electromagnetic bandgap resonator antenna," *IEEE Trans. Antennas Propag.*, vol. 50, no. 9, pp. 1285–1290, Sep. 2002.

[47] S. Enoch, G. Tayeb, and D. Maystre, "Dispersion diagrams of bloch modes applied to the design of directive sources," *Prog. Electromagn. Res.*, vol. 41, pp. 61–81, 2003.

[48] S. Ceccuzzi, L. Pajewski, C. Ponti, and G. Schettini, "Directive propagation in two EBG structures: a comparison," in *Proc. of the International Microwave Symposium (IMS)*, Seattle, USA, Jun. 2013.

[49] ——, "Comparison between two methods for directivity enhancement of antennas through 2-D EBGs," in *Proc. of the 34th Progress In Electromagnetics Research Symposium (PIERS)*, Stockholm, Sweden, Aug. 2013.

[50] ——, "Directive EBG antennas: A comparison between two different radiating mechanisms," *IEEE Trans. Antennas Propag.*, vol. 62, no. 10, pp. 5420–5424, Oct. 2014.

[51] F. Frezza, L. Pajewski, and G. Schettini, "Periodic defects in 2D-PBG materials: full-wave analysis and design," *IEEE Trans. Nanotechnol.*, vol. 2, no. 3, pp. 126–134, Sep. 2003.

[52] Y. J. Lee, J. Yeo, R. Mittra, and W. S. Park, "Application of electromagnetic bandgap (EBG) superstrates with controllable defects for a class of patch antennas as spatial angular filters," *IEEE Trans. Antennas Propag.*, vol. 53, no. 1, pp. 224–235, Jan. 2005.

[53] R. Woode, E. Ivanov, M. Tobar, and D. Blair, "Measurement of dielectric loss tangent of alumina at microwave frequencies and room temperature," *Electron. Lett.*, vol. 30, no. 25, pp. 2120–2122, Dec. 1994.

[54] G. Akishin *et al.*, "Composition of beryllium oxide ceramics," *Refract. Ind. Ceram.+*, vol. 51, no. 5, pp. 377–381, Jan. 2011.

[55] T. Moreno, *Microwave Transmission Design Data*, ser. Microwave Library. Artech House, Inc., 1989.

[56] D. Sievenpiper, L. Zhang, R. F. J. Broas, N. Alexopolous, and E. Yablonovitch, "High-impedance electromagnetic surfaces with a forbidden frequency band," *IEEE Trans. Microw. Theory Tech.*, vol. 47, no. 11, pp. 2059–2074, Nov. 1999.

[57] F. Yang and Y. Rahmat-Samii, "Microstrip antennas integrated with electromagnetic band-gap (EBG) structures: a low mutual coupling design for array applications," *IEEE Trans. Antennas Propag.*, vol. 51, no. 10, pp. 2936–2946, Oct. 2003.

[58] I. Ederra, B. Pascual, A. Labajos, J. Teniente, R. Gonzalo, and P. de Maagt, "Experimental verification of the reduction of coupling between dipole antennas by using a woodpile substrate," *IEEE Trans. Antennas Propag.*, vol. 54, no. 7, pp. 2105–2112, Jul. 2006.

[59] A. Weily, T. Bird, and Y. Guo, "A reconfigurable high-gain partially reflecting surface antenna," *IEEE Trans. Antennas Propag.*, vol. 56, no. 11, pp. 3382–3390, Nov. 2008.

[60] S. Muhammad, R. Sauleau, and H. Legay, "Small-size shielded metallic stacked Fabry-Perot cavity antennas with large bandwidth for space applications," *IEEE Trans. Antennas Propag.*, vol. 60, no. 2, pp. 792–802, Feb. 2012.

[61] R. Hashmi, B. Zeb, and K. Esselle, "Wideband high-gain EBG resonator antennas with small footprints and all-dielectric superstructures," *IEEE Trans. Antennas Propag.*, vol. 62, no. 6, pp. 2970–2977, Jun. 2014.

[62] B. Riddle, J. Baker-Jarvis, and J. Krupka, "Complex permittivity measurements of common plastics over variable temperatures," *IEEE Trans. Microw. Theory Tech.*, vol. 51, no. 3, pp. 727–733, Mar. 2003.

[63] G. Reiter, "Generalized telegraphist's equation for waveguides of varying cross-section," *Proc. of the IEE - Part B: Electronic and Communication Engineering*, vol. 106, no. 13, pp. 54–61, 1959.

[64] J. Shafii and R. Vernon, "Mode coupling in coaxial waveguides with varying-radius center and outer conductors," *IEEE Trans. Microw. Theory Tech.*, vol. 43, no. 3, pp. 582–591, Mar. 1995.

[65] L. Solymar, "Spurious mode generation in nonuniform waveguide," *IRE Trans. Microw. Theory Tech.*, vol. 7, no. 3, pp. 379–383, Jul. 1959.

[66] A. Yariv, *Quantum Electronics*. John Wiley & Sons, Incorporated, 1975.

[67] V. Bratman, G. Denisov, N. Ginzburg, and M. Petelin, "FEL's with Bragg reflection resonators: Cyclotron autoresonance masers versus ubitrons," *IEEE J. Quantum Electron.*, vol. 19, no. 3, pp. 282–296, Mar. 1983.

[68] R. B. McCowan, A. W. Fliflet, and S. H. Gold, "Multimode analysis of Bragg reflectors for cyclotron maser applications," Naval Research Laboratory, Tech. Rep. AD-A276509, 1991, nRL-MR-6777.

[69] C. K. Chong *et al.*, "Bragg reflectors," *IEEE Trans. Plasma Sci.*, vol. 20, no. 3, pp. 393–402, Jun. 1992.

[70] P. Zambon and P. van der Slot, "Design of a 30 GHz bragg reflector for a Raman FEL," *Nucl. Instrum. Meth. A*, vol. 341, no. 1-3, pp. 484–488, 1994.

[71] B. Kulke, M. Caplan, and R. Stever, "250 GHz cold tests for the LLNL CARM experiment," in *Conference Record of the 1991 IEEE Particle Accelerator Conference, Accelerator Science and Technology*, May 1991, pp. 763–765 vol. 2.

[72] R. B. McCowan, A. W. Fliflet, S. H. Gold, V. L. Granatstein, and M. C. Wangh, "Design of a waveguide resonator with ripled wall reflectors for a 100 GHz CARM oscillator experiment," *Int. J. Electron.*, vol. 65, no. 3, pp. 463–475, 1988.

[73] Wolfram, "Mathematica," http://www.wolfram.com/mathematica/.

[74] A. Yariv, "Coupled-mode theory for guided-wave optics," *IEEE J. Quantum Electron.*, vol. 9, no. 9, pp. 919–933, Sep. 1973.

[75] R. Mittra, "Relative convergence of the solution of a doubly infinite set of equations," *J. Res. Natl. Inst. Stand. Technol.*, vol. 67D, no. 2, pp. 245–254, Mar. 1963.

[76] ANSYS, "HFSS," http://www.ansys.com/.

[77] J. A. Ruiz-Cruz, J. R. Montejo-Garai, and J. M. Rebollar, "Computer aided design of waveguide devices by mode-matching methods," in *Passive Microwave Components and Antennas*, V. Zhurbenko, Ed. InTech, Apr. 2010.

[78] F. Arndt, I. Ahrens, U. Papziner, U. Wiechmann, and R. Wilkeit, "Optimized E-plane T-junction series power dividers," *IEEE Trans. Microw. Theory Tech.*, vol. 35, no. 11, pp. 1052–1059, Nov. 1987.

[79] J. Wade and R. H. Macphie, "Conservation of complex power technique for waveguide junctions with finite wall conductivity," *IEEE Trans. Microw. Theory Tech.*, vol. 38, no. 4, pp. 373–378, Apr. 1990.

[80] K.-P. Ma, K. Hirose, F.-R. Yang, Y. Qian, and T. Itoh, "Realisation of magnetic conducting surface using novel photonic bandgap structure," *Electron. Lett.*, vol. 34, no. 21, pp. 2041–2042, Oct. 1998.

[81] M. de Cos, F. Las Heras, and M. Franco, "Design of planar artificial magnetic conductor ground plane using frequency-selective surfaces for frequencies below 1 GHz," *IEEE Antennas Wireless Propag. Lett.*, vol. 8, pp. 951–954, Aug. 2009.

[82] R. Cairns and A. Phelps, *Generation and Application of High Power Microwaves*, ser. Scottish Graduate Series. Taylor & Francis, 1997.

[83] M. Thumm and W. Kasparek, "Passive high-power microwave components," *IEEE Trans. Plasma Sci.*, vol. 30, no. 3, pp. 755–786, Jun. 2002.

[84] J. Wesson and D. Campbell, *Tokamaks*, ser. International Series of Monographs on Physics. OUP Oxford, 2011.

[85] T. Wangler, *RF Linear Accelerators*, ser. Physics textbook. Wiley, 2008.

[86] J. Benford, "Space applications of high-power microwaves," *IEEE Trans. Plasma Sci.*, vol. 36, no. 3, pp. 569–581, Jun. 2008.

[87] B. Zohuri, *Directed Energy Weapons Technologies.* CRC Press, 2012.

[88] L. Roselli, S. Kawasaki, and F. Alimenti, "Guest editorial [special issue on wireless power transfer]," *IEEE Trans. Microw. Theory Tech.*, vol. 62, no. 4, pp. 889–891, Apr. 2014.

[89] H. Butterweck, "Mode filters for oversized rectangular waveguides," *IEEE Trans. Microw. Theory Tech.*, vol. 16, no. 5, pp. 274–281, May 1968.

[90] A. Bécoulet *et al.*, "Steady state long pulse tokamak operation using Lower Hybrid Current Drive," *Fusion Eng. Des.*, vol. 86, no. 68, pp. 490–496, 2011.

[91] A. Cullen, R. Reitzig, and P. Robson, "Further considerations of overmoded rectangular waveguide for high-power transmission," *Proc. of the Institution of Electrical Engineers*, vol. 112, no. 7, pp. 1301–1310, Jul. 1965.

[92] H.-J. Butterweck and F. de Ronde, "Oversized rectangular waveguide components for mm waves," in *G-MTT International Microwave Symposium Digest*, May 1967, pp. 35–38.

[93] J. Neilson, "Analysis and design of high-power overmoded components," in *IEEE MTT-S*, vol. 2, Jun. 2004, pp. 1017–1020.

[94] N. Marcuvitz and I. of Electrical Engineers, *Waveguide Handbook*, ser. IEE electromagnetic waves series. McGraw-Hill, 1951.

[95] Y. Qin and Y. Yang, "Improved slotted-filter for over-mode rectangular waveguide," in *Proc. of the 4th International Conference on Millimeter Wave and Far Infrared Science and Technology*, Aug. 1996, pp. 218–221.

[96] S. Meschino, S. Ceccuzzi, F. Mirizzi, L. Pajewski, and G. Schettini, "Microwave components for the lower hybrid transmission line of ITER," in *Proc. of the Asia-Pacific Microwave Conference (APMC)*, Dec. 2010, pp. 1320–1323.

[97] S. Ceccuzzi *et al.*, "Mode filters for oversized transmission lines," *Fusion Eng. Des.*, vol. 86, no. 68, pp. 909–912, 2011.

[98] A. Wexler, "Solution of waveguide discontinuities by modal analysis," *IEEE Trans. Microw. Theory Tech.*, vol. 15, no. 9, pp. 508–517, Sep. 1967.

[99] G. Conciauro, M. Guglielmi, and R. Sorrentino, *Advanced modal analysis: CAD techniques for waveguide components and filters*, ser. v. 1. Wiley, 2000.

[100] R. Thabet and L. M. Riabi, "Rigorous design and efficient optimization of quarter-wave transformers in metallic circular waveguides using the mode-matching method and the genetic algorithm," *Prog. Electromagn. Res.*, vol. 68, p. 1533, Sep. 2007.

[101] M. Fahmi, J. Ruiz-Cruz, R. Mansour, and K. Zaki, "Recent advances in filter topologies and realizations for satellite communications," *J. Commun. Netw.*, vol. 13, no. 6, pp. 625–632, Dec. 2011.

[102] C. Tomassoni, S. Bastioli, and R. Sorrentino, "Generalized TM dual-mode cavity filters," *IEEE Trans. Microw. Theory Tech.*, vol. 59, no. 12, pp. 3338–3346, Dec. 2011.

[103] C. Bachiller *et al.*, "Hybrid mode matching method for the efficient analysis of metal and dielectric rods in H plane rectangular waveguide devices," *IEEE Trans. Microw. Theory Tech.*, vol. 58, no. 12, pp. 3634–3644, Dec. 2010.

[104] A. Pellegrini, A. Monorchio, G. Manara, and R. Mittra, "A hybrid mode matching-finite element method and spectral decomposition approach for the analysis of large finite phased arrays of waveguides,"

IEEE Trans. Antennas Propag., vol. 62, no. 5, pp. 2553–2561, May 2014.

[105] T. Sieverding and F. Arndt, "Field theoretical CAD of open or aperture matched T-junction coupled rectangular waveguide structures," *IEEE Trans. Microw. Theory Tech.*, vol. 40, no. 2, pp. 353–362, Feb. 1992.

[106] Z. Jiang and Z. Shen, "Mode-matching analysis of large aperture coupling and its applications to the design of waveguide directional couplers," *IEE Proc.-H*, vol. 150, no. 6, pp. 422–428, Dec. 2003.

[107] F. M. Vanin, F. Frezza, and D. Schmitt, "Computer-aided design of Y-junction waveguide diplexers," *Prog. Electromagn. Res. C*, vol. 17, pp. 203–218, 2010.

[108] Y. Tao, Z. Shen, and G. Liu, "Closed-form expressions for the equivalent circuit model of square-waveguide T-junctions and its application in ortho-mode transducer design," *IEEE Trans. Microw. Theory Tech.*, vol. 58, no. 5, pp. 1167–1174, May 2010.

[109] M. Leroy, "On the convergence of numerical results in modal analysis," *IEE Proc.-H*, vol. 31, no. 4, pp. 655–659, Jul. 1983.

[110] G. Eleftheriades, A. Omar, L. Katehi, and G. Rebeiz, "Some important properties of waveguide junction generalized scattering matrices in the context of the mode matching technique," *IEEE Trans. Microw. Theory Tech.*, vol. 42, no. 10, pp. 1896–1903, Oct. 1994.

[111] ITER Organization, "ITER the way to energy," http://www.iter.org/.

[112] J. Kennedy and R. Eberhart, "Particle swarm optimization," in *Proc. of the IEEE International Conference on Neural Networks*, vol. 4, Nov. 1995, pp. 1942–1948.

[113] ENEA-GRID, "CRESCO: Computational research center for complex systems," http://www.cresco.enea.it/.

[114] V. Erckmann and U. Gasparino, "Electron cyclotron resonance heating and current drive in toroidal fusion plasmas," *Plasma Phys. Control. Fusion*, vol. 36, no. 12, p. 1869, 1994.

[115] T. Luce, "Applications of high-power millimeter waves in fusion energy research," *IEEE Trans. Plasma Sci.*, vol. 30, no. 3, pp. 734–754, Jun. 2002.

[116] ITER Physics Expert Group on Energetic Particles, Heating and Current Drive and ITER Physics Basis Editors, "Chapter 6: Plasma auxiliary heating and current drive," *Nucl. Fusion*, vol. 39, no. 12, p. 2495, 1999.

[117] E. Poli *et al.*, "Electron-cyclotron-current-drive efficiency in DEMO plasmas," *Nucl. Fusion*, vol. 53, no. 1, p. 013011, 2013.

[118] S. Kern *et al.*, "Experimental results and recent developments on the EU 2 MW 170 GHz coaxial cavity gyrotron for ITER," in *EPJ Web of Conferences*, vol. 32, 2012, p. 04009.

[119] S. Ceccuzzi *et al.*, "CARM: A THz source for plasma heating," in *Proc. of the 38th International Conference on Infrared, Millimeter, and Terahertz Waves (IRMMW-THz)*, Mainz, Germany, Sep. 2013.

[120] I. Spassovsky *et al.*, "CARM: A THz source for plasma heating," in *Proc. of the 6th UK, Europe, China Millimeter Waves and THz Technology Workshop (UCMMT)*, Rome, Italy, Sep. 2013.

[121] S. Ceccuzzi *et al.*, "MM-wave cyclotron auto-resonance maser for plasma heating," *AIP Conf. Proc.*, vol. 1580, no. 1, pp. 558–561, 2014.

[122] G. Dattoli *et al.*, "The gyratron, CARM and FEL devices: an analytical unified formulation for the small signal analysis," in *Proc. of the 10th International Vacuum Electron Sources Conference (IVESC)*, Saint Petersburg, Russia, Jun. 2014.

[123] S. Ceccuzzi *et al.*, "Initial steps towards a bragg-reflector for a 250 GHz CARM experiment," in *Proc. of the 9th International Workshop Strong Microwaves and Terahertz Waves: Sources and Applications*, Nizhny Novgorod, Russia, Jul. 2014, pp. 209–210.

[124] A. A. Tuccillo *et al.*, "CARM as possible alternative source for EC systems: R&D in ENEA frascati," in *Proc. of the US-EU-JPN Workshop on RF Heating Technology*, Sedona, AZ, USA, Sep. 2014.

[125] L. Amicucci *et al.*, "The ENEA CARM source for nuclear fusion: Project status and perspectives," in *Proc. of the 39th International Conference on Infrared, Millimeter, and THz Waves (IRMMW-THz)*, Tucson, AZ, USA, Sep. 2014, pp. 1–2.

[126] M. Gasparotto, "Present status of the FTU: Frascati Tokamak Upgrade," in *Proc. of the IEEE Thirteenth Symposium on Fusion Engineering (SOFE)*, vol. 1, Oct. 1989, pp. 509–514.

[127] A. A. Tuccillo *et al.*, "Deliverable of EFDA task: WP11-DAS-HCD-LH:01-02-03 "Assessment of LHCD for DEMO"," ENEA, Tech. Rep. RT-MAG-EFDA-LH-02_V1, Sep. 2012.

[128] ——, "Deliverable of EFDA task: WP12-DAS-HCD-LH "Assessment of LHCD for DEMO"," ENEA, Tech. Rep. RT-MAG-EFDA-LH-03_V0, Apr. 2013.

[129] ——, "Deliverable of EFDA task: WP13-DAS-HCD-LH "Assessment of LHCD for DEMO"," ENEA, Tech. Rep. RT-MAG-EFDA-LH-04_V0, Mar. 2014.

[130] C. Gormezano *et al.*, "Chapter 6: Steady state operation," *Nucl. Fusion*, vol. 47, no. 6, pp. S285–336, Jun. 2007.

[131] J. Decker *et al.*, "Calculations of lower hybrid current drive in ITER," *Nucl. Fusion*, vol. 51, no. 7, p. 073025, Jul. 2011.

[132] T. Suzuki *et al.*, "Experimental investigation and validation of neutral beam current drive for ITER through ITPA joint experiments," *Nucl. Fusion*, vol. 51, no. 8, p. 083020, Aug. 2011.

[133] F. Alladio *et al.*, "Heating experiments on the FT tokamak in the lower hybrid frequency range," *Plasma Phys. Control. Fusion*, vol. 26, no. 1A, pp. 157–164, Jan. 1984.

[134] N. Fisch, "Theory of current drive in plasmas," *Rev. Mod. Phys.*, vol. 59, no. 1, pp. 175–234, 1987.

[135] D. Moreau and C. Gormezano, "Lower hybrid current drive in TORE SUPRA and JET," *Plasma Phys. Control. Fusion*, vol. 33, no. 13, pp. 1621–1638, Nov. 1991.

[136] T. Watari, "Review of Japanese results on heating and current drive," *Plasma Phys. Control. Fusion*, vol. 35, no. A, pp. 181–198, Dec. 1993.

[137] M. Porkolab *et al.*, "Observation of lower-hybrid current drive at high densities in the alcator C tokamak," *Phys. Rev. Lett.*, vol. 53, no. 5, pp. 450–453, Jul. 1984.

[138] G. Hoang *et al.*, "A lower hybrid current drive system for ITER," *Nucl. Fusion*, vol. 49, no. 7, p. 075001, Jul. 2009.

[139] A. Tuccillo *et al.*, "Progress in LHCD: a tool for advanced regimes on ITER," *Plasma Phys. Control. Fusion*, vol. 47, no. 12B, pp. 363–377, Dec. 2005.

[140] ——, "On the use of lower hybrid waves at ITER relevant density," in *Proc. of the 24th IAEA Fusion Energy Conference*, San Diego, California, USA, Oct. 2012.

[141] R. Cesario *et al.*, "Current drive at plasma densities required for thermonuclear reactors," *Nat. Comm.*, vol. 1, no. 55, pp. 274–281, Aug. 2010.

[142] P. Lallia, "A LHR heating slow wave launching structure suited for large toroidal experiments," in *Proc. of the 2nd Topical Conference on RF Plasma Heating*, Lubbock, Texas, USA, 1974, pp. C3–1–C3–6.

[143] D. Moreau, "Lower-hybrid current drive experiments in TORE SUPRA," *Phys. Fluids B*, vol. 4, no. 7, pp. 2165–2175, Feb. 1992.

[144] P. Bibet, X. Litaudon, and D. Moreau, "Conceptual study of a reflector waveguide array for launching lower hybrid waves in reactor grade plasmas," *Nucl. Fusion*, vol. 35, no. 10, pp. 1213–1223, Oct. 1995.

[145] V. P. Ridolfini *et al.*, "LHCD and coupling experiments with an ITER-like PAM launcher on the FTU tokamak," *Nucl. Fusion*, vol. 45, no. 9, pp. 1085–1093, Sep. 2005.

[146] A. Ehedhal *et al.*, "Validation of the ITER-relevant passive-active-multijunction LHCD launcher on long pulses in tore supra," *Nucl. Fusion*, vol. 50, no. 11, p. 112002, Nov. 2010.

[147] G. V. Pereverzev and P. N. Yushmanov, "ASTRA Automated System for TRansport Analysis," IPP, Tech. Rep. 5/98, Feb. 2002.

[148] A. R. Esterkin and A. D. Piliya, "Fast ray tracing code for LHCD simulations," *Nucl. Fusion*, vol. 36, no. 11, pp. 1501–1512, Nov. 1996.

[149] R. Cesario and A. Cardinali, "Parametric instabilities excited by ion sound and ion cyclotron quasi-modes during lower hybrid heating of tokamak plasmas," *Nucl. Fusion*, vol. 29, no. 10, pp. 1709–1720, Oct. 1989.

[150] M. Irzak and O. Shcherbinin, "Theory of waveguide antennas for plasma heating and current drive," *Nucl. Fusion*, vol. 35, no. 2, pp. 1341–1356, Nov. 1995.

[151] A. Cardinali *et al.*, "Assessment of the LH wave for demo in pulsed and steady state scenario," *AIP Conf. Proc.*, vol. 1580, pp. 454–457, 2014.

[152] E. Barbato and F. Santini, "Quasi-linear absorption of lower hybrid waves by fusion generated alpha particles," *Nucl. Fusion*, vol. 31, no. 4, pp. 673–685, Apr. 1991.

[153] E. Barbato and A. Saveliev, "Absorption of lower hybrid wave power by α-particles in ITER-FEAT scenarios," *Plasma Phys. Control. Fusion*, vol. 46, no. 8, pp. 1283–1297, Aug. 2004.

[154] M. Goniche *et al.*, "Operational issues at high lower hybrid power density in JET: Waveguide conditioning and arc detection," *Plasma Phys. Control. Fusion*, vol. 54, no. 7, p. 074002, Jul. 2012.

[155] K. Rantamäki *et al.*, "LH wave coupling over ITER-like distances at JET," *AIP Conf. Proc.*, vol. 933, pp. 261–264, May 2007.

[156] M. Porkolab, S. Bernabei, W. M. Hooke, and R. W. Motley, "Observation of parametric instabilities in lower-hybrid radio-frequency heating of tokamaks," *Phys. Rev. Lett.*, vol. 38, no. 5, p. 230233, Jan. 1977.

[157] H. Do *et al.*, "Test result of 5 GHz, 500 kW CW prototype klystron for KSTAR LHCD system," *Fus. Eng. Des.*, vol. 86, no. 6-8, pp. 992–995, Oct. 2011, proc. of the 26th Symposium of Fusion Technology (SOFT), Sep.–Oct. 1st, 2010, Porto, Portugal.

[158] S. Lenci, E. L. Eisen, and K. Lind, "Development of a 250 kW CW, 4.6 GHz klystron for plasma heating," in *IEEE International Vacuum Electronics Conference*, Palo Alto, CA, USA, Apr. 2009, pp. 379–380.

[159] P. K. Sharma *et al.*, "Proposed high voltage power supply for the ITER relevant lower hybrid current drive system," *Fus. Eng. Des.*, vol. 86, no. 6-8, pp. 819–822, Oct. 2011, proc. of the 26th Symposium of Fusion Technology (SOFT), Sep.–Oct. 1st, 2010, Porto, Portugal.

[160] F. Mirizzi, "Prolegomena to the RAMI analysis of a conceptual LHCD system for DEMO," *Fus. Eng. Des.*, vol. 88, no. 68, pp. 887 – 890, 2013, proc. of the 27th Symposium On Fusion Technology (SOFT); Liège, Belgium, Sep. 2012.

[161] R. Bierce, W. Fowkes, and J. Jasberg, "Window materials design and properties for use in high power klystrons," *IEEE Trans. Nucl. Sci.*, vol. 12, no. 3, pp. 180–184, Jun. 1965.

[162] Y. Saito, "Surface breakdown phenomena in alumina rf windows," *IEEE Trans. Dielectr. Electr. Insul.*, vol. 2, no. 2, pp. 243–250, Apr. 1995.

[163] M. Thumm and W. Kasparek, "Passive high-power microwave components," *IEEE Trans. Plasma Sci.*, vol. 30, no. 3, pp. 755–786, Jun. 2002.

[164] L. Heikinheimo *et al.*, "Dielectric window for reactor like ICRF vacuum transmission line," *Fus. Eng. Des.*, vol. 55, no. 4, pp. 419–436, Sep. 2001.

[165] R. Heidinger, "Design parameters of ceramic insulator materials for fusion reactors," *J. Nucl. Mater.*, vol. 179-181, no. Part 1, pp. 64–69, Mar.-Apr. 1991.

[166] S. N. Buckley and P. Agnew, "Radiation-induced changes in the dielectric properties of insulating ceramics at icrh frequencies," *J. Nucl. Mater.*, vol. 155-157, no. Part 1, pp. 361–365, Jul. 1988.

[167] L. L. Snead, S. J. Zinkle, and D. P. White, "Thermal conductivity degradation of ceramic materials due to low temperature, low dose neutron irradiations," *J. Nucl. Mater.*, vol. 340, no. 2-3, pp. 187–202, Apr. 2005.

[168] J. Molla, R. Vila, R. Heidinger, and A. Ibarra, "Radiation effects on dielectric losses of Au-doped silicon," *J. Nucl. Mater.*, vol. 258-263, no. Part 2, pp. 1884–1888, Oct. 1998.

[169] R. Heidinger, M. Rohde, and R. Spörl, "Neutron irradiation studies on window materials for EC wave systems," *Fus. Eng. Des.*, vol. 56-57, pp. 471–476, Oct. 2001.

[170] L. W. Hobbs, F. W. C. Jr., S. J. Zinkle, and R. C. Ewing, "Radiation effects in ceramics," *J. Nucl. Mater.*, vol. 216, pp. 291–321, 1994.

[171] C. Hazelton, J. Rice, L. L. Snead, and S. J. Zinkle, "Effect of neutron radiation on the dielectric, mechanical and thermal properties of ceramics for rf transmission windows," *J. Nucl. Mater.*, vol. 253, pp. 190–195, Mar. 1998.

[172] T. Shikama and G. P. Pells, "A comparison of the effects of neutron and other irradiation sources on the dynamic property changes of ceramic insulators," *J. Nucl. Mater.*, vol. 212-215, no. Part 1, pp. 88–89, Sep. 1994.

[173] S. J. Zinkle and E. R. Hodgson, "Radiation-induced changes in the physical properties of ceramic materials," *J. Nucl. Mater.*, vol. 191-194, no. Part A, pp. 58–66, Sep. 1992.

[174] M. Rohde and B. Schulz, "The effect of the exposure to different irradiation sources on the thermal conductivity of Al_2O_3," *J. Nucl. Mater.*, vol. 173, no. 3, pp. 289–293, 1990.

[175] J. D. Fowler Jr., "Radiation-induced rf loss measurements and thermal stress calculations for ceramic windows," *J. Nucl. Mater.*, vol. 123, no. 13, pp. 1359–1364, May 1984.

[176] R. Heidinger and F. Kniger, "Investigations on advanced ceramics for window applications in radiofrequency heating concepts," *J. Nucl. Mater.*, vol. 155157, Part 1, pp. 344–347, Jul. 1988.

[177] R. Heidinger, "Dielectric measurements on sapphire for electron cyclotron wave systems," *J. Nucl. Mater.*, vol. 212215, Part B, pp. 1101–1106, Sep. 1994.

[178] M. Thumm, "MPACVD-diamond windows for high-power and long-pulse millimeter wave transmission," *Diam. Relat. Mater.*, vol. 10, no. 910, pp. 1692–1699, Sep.–Oct. 2001, proc. of the 7th International Conference on New Diamond Science and Technology (ICNDST-7).

[179] R. Heidinger, A. Ibarra, and J. Molla, "Pre- and post-irradiation studies on mm-wave losses in reference window materials for electron cyclotron wave systems," *J. Nucl. Mater.*, vol. 258263, Part 2, pp. 1822–1826, Oct. 1998.

[180] R. Heidinger, G. Dammertz, A. Meier, and M. Thumm, "CVD diamond windows studied with low- and high-power millimeter waves," *IEEE Trans. Plasma Sci.*, vol. 30, no. 3, pp. 800–807, Jun. 2002.

[181] J. Hillairet *et al.*, "Design and tests of 500 kw RF windows for the ITER LHCD system," 2015, in Press.

[182] "Kyocera corporation," http://global.kyocera.com/index.html.

[183] "Altair technologies, inc." http://www.altairusa.com/index.php.

[184] D. Milanesio *et al.*, "TOPLHA: an accurate and efficient numerical tool for analysis and design of LH antennas," *Nucl. Fusion*, vol. 52, no. 1, p. 013008, Jan. 2012.

[185] J. Linke, "Plasma facing materials and components for future fusion devices–development, characterization and performance under fusion specific loading conditions," *Phys. Scr.*, vol. T123, pp. 45–53, 2006.

[186] P. Garin, "IFMIF specifications from the users point of view," *Fus. Eng. Des.*, vol. 86, pp. 611–614, Oct. 2011.

[187] H. Bolt *et al.*, "Materials for the plasma-facing components of fusion reactors," *J. Nucl. Mater.*, vol. 329-333, no. A, pp. 66–73, Aug. 2004.

[188] P. Lopez-Ruiz, N. Ordás, S. Lindig, F. Koch, I. Iturriza, and C. García-Rosales, "Self-passivating bulk tungsten-based alloys manufactured by powder metallurgy," *Phys. Scr.*, vol. T145, p. 014018, Dec. 2011.

[189] K. Ehrlich, "Materials research towards a fusion reactor," *Fus. Eng. Des.*, vol. 56-57, pp. 71–82, Oct. 2001.

[190] K. Mergia and N. Boukos, "Structural, thermal, electrical and magnetic properties of Eurofer 97 steel," *J. Nucl. Mater.*, vol. 373, no. 13, pp. 1–8, Feb. 2008.

[191] B. Bromberger *et al.*, "Monte-Carlo simulations of neutron-induced activation in a fast-neutron and Gamma-based cargo inspection system," *J. Instrum.*, vol. 7, no. 03, p. C03024, Mar. 2012, proc. of the

2nd International Workshop on Fast Neutron Detectors and Applications, Ein Gedi (Israel), November, 2011.

[192] "Antennas for communications, "Tallguide, ultra low transmission loss waveguide"," http://www.tallguide.com/.

[193] H. Barlow, "The relative power-carrying capacity of high-frequency waveguides," *Proc. of the IEE - Part III: Radio and Communication Engineering*, vol. 99, no. 57, pp. 21–27, Jan. 1952.

[194] M. Jouguet, "Effect of curvature on the propagation of electromagnetic waves in guides of circular cross sections," *Cables et Transmission*, vol. 1, no. 2, pp. 133–153, Jul. 1947.

[195] G. Sims, "The influence of bends and ellipticity on the attenuation and propagation characteristics of the H01 circular waveguide mode," *Proc. of the IEE - Part IV: Institution Monographs*, vol. 100, no. 5, pp. 25–33, Oct. 1953.

[196] W. Albersheim, "Propagation of TE01 waves in curved wave guides," *Bell System Technical Journal, The*, vol. 28, no. 1, pp. 1–32, Jan. 1949.

[197] S. E. Miller, "Notes on methods of transmitting the circular electric wave around bends," *P. IRE*, vol. 40, no. 9, pp. 1104–1113, Sep. 1952.

[198] B. Katsenelenbaum, *Theory of Nonuniform Waveguides: The Cross-section Method*, ser. IEE electromagnetic waves series. Institution of Electrical Engineers, 1998, ch. Chapter 5: Bent waveguides.

[199] H. Barlow, "Propagation of the circular H01 low-loss wave mode around bends in tubular metal waveguide," *Proc. of the IEE - Part B: Radio and Electronic Engineering*, vol. 104, no. 16, pp. 403–409, Jul. 1957.

[200] J. Davies, "An investigation of some waveguide structures for the propagation of circular TE modes," *Proc. of the IEE - Part C: Monographs*, vol. 109, no. 15, pp. 162–171, Mar. 1962.

[201] M. Shapiro and R. Temkin, "High power miter-bend for the next linear collider," in *Proc. of the Particle Accelerator Conference*, vol. 2, 1999, pp. 836–838.

[202] K. Patel, V. Dwivedi, Y. Kosta, and H. Pandya, "Modeling of a smooth wall circular waveguide miter bend using waveguide gap theory," *International Journal of Advanced Engineering Technology*, vol. 1, pp. 17–26, Apr. 2010.

[203] B. Plaum, D. Wagner, W. Kasparek, and M. Thumm, "Optimization of waveguide bends and bent mode converters using a genetic algorithm," in *Proc. of the 25th International Conference on Infrared and Millimeter Waves*, Sep. 2000, pp. 219–220.

[204] G. Denisov and D. Sobolev, "A method of waveguide mode converter synthesis," in *Proc. of the Joint 30th International Conference on Infrared and Millimeter Waves and 13th International Conference on Terahertz Electronics (IRMMW-THz)*, vol. 2, Sep. 2005, pp. 600–601.

[205] A. Vikharev, G. Denisov, S. Kuzikov, and D. Sobolev, "New TE01 waveguide bends," *J. Infrared Millim. Te.*, vol. 30, no. 6, pp. 556–565, 2009.

[206] C. Nantista, N. Kroll, and E. Nelson, "Design of a 90 deg; overmoded waveguide bend," in *Proc. of the Particle Accelerator Conference*, May 1993, pp. 983–985.

[207] S. G. Tantawi, "A novel circular TE01-mode bend for ultra-high-power applications," *Journal of Electromagnetic Waves and Applications*, vol. 18, no. 12, pp. 1679–1687, 2004.

[208] J. Waarren, "Compact bend for TE01 mode circular overmoded waveguide," Sep. 1992, US Patent 5,151,673.

[209] F. Mirizzi and S. Ceccuzzi, "Optimized bends and mode filters for the main transmission lines of the ITER-like LHCD system," in *Proc. of the IEEE/NPSS 24th Symposium on Fusion Engineering (SOFE)*, Chicago, USA, Jun. 2011, pp. 1–5.

[210] M. Goniche *et al.*, "CEA/ENEA/IPR joint proposal for the development of oversized components for transmission lines of a reactor-relevant LHCD system," May 2014, tech. proposal.

[211] A. Beunas *et al.*, "High-power CW klystron for fusion experiments," *IEEE Trans. Electron Devices*, vol. 56, no. 5, pp. 864–869, May 2009.

[212] F. Mirizzi, P. Bibet, and S. Kuzikov, "The main microwave components of the LHCD system for ITER," *Fusion Eng. Des.*, vol. 6668, pp. 487–490, 2003, 22nd Symposium on Fusion Technology (SOFT).

[213] G. Harris and INSPEC (Information service), *Properties of Silicon Carbide*, ser. EMIS datareviews series. INSPEC, Institution of Electrical Engineers, 1995.

[214] Ioffe Physico-Technical Institute, "New semiconductor materials. characteristics and properties," http://www.ioffe.ru/SVA/NSM/, electronic archive.

[215] H. Abderrazak and E. S. B. H. Hmida, *Properties and Applications of Silicon Carbide*, ser. IEE electromagnetic waves series. InTech, Apr. 2011, ch. Chapter 16: Silicon Carbide: Synthesis and Properties, prof. Rosario Gerhardt (Ed.).

[216] B. Zhang, J. Li, J. Sun, S. Zhang, H. Zhai, and Z. Du, "Nanometer silicon carbide powder synthesis and its dielectric behavior in the GHz range," *J. Eur. Ceram. Soc.*, vol. 22, no. 1, pp. 93–99, Jan. 2002.

[217] D. Zhao, H. Zhao, and W. Zhou, "Dielectric properties of nano Si/C/N composite powder and nano SiC powder at high frequencies," *Physica E*, vol. 9, no. 4, pp. 679–685, Apr. 2001.

[218] G. Zou, M. Cao, H. Lin, H. Jin, Y. Kang, and Y. Chen, "Nickel layer deposition on SiC nanoparticles by simple electroless plating and its dielectric behaviors," *Powder Technol.*, vol. 168, no. 2, pp. 84–88, Oct. 2006.

[219] X.-L. Su, W.-C. Zhou, F. Luo, Z.-M. Li, and D.-M. Zhu, "A cost-effective approach to improve dielectric property of SiC powder," *J. Alloy Compd.*, vol. 476, no. 12, pp. 644–647, May 2009.

[220] D.-L. Zhao, F. Luo, and W.-C. Zhou, "Microwave absorbing property and complex permittivity of nano SiC particles doped with nitrogen," *J. Alloy Compd.*, vol. 490, no. 12, pp. 190–194, Feb. 2010.

[221] C. Balanis, *Advanced Engineering Electromagnetics*, ser. CourseSmart Series. Wiley, 2012.